Electron Microscopic Investigation of Interfaces in Materials for Orthopedic Applications

by

Valarie Ilene Benezra

Bachelor of Science in Chemistry
University of Michigan

Submitted to the Department of Materials Science and Engineering
in Partial Fulfillment of the Requirements for the Degree of

Doctor of Philosophy
in Materials Science

at the

MASSACHUSETTS INSTITUTE OF TECHNOLOGY
SEPTEMBER 1998

Signature of Author _____
Department of Materials Science and Engineering
August 7, 1998

Certified by _____
Linn W. Hobbs
John F. Elliott Professor of Materials
Thesis Supervisor

Accepted by _____
Linn W. Hobbs
John F. Elliott Professor of Materials
Chair, Departmental Committee on Graduate Students

Electron Microscopic Investigation of Interfaces in Materials for Orthopedic Observations

by
Valarie Ilene Benezra

Submitted to the Department of Materials Science and Engineering on August 7, 1998 in partial fulfillment of the requirements for the degree of Doctor of Philosophy in Materials Science in the Department of Materials Science and Engineering.

Abstract

About 250,000 people undergo knee and hip arthroplasty each year in North America alone, with hundreds of thousands more receiving joints over the rest of the world. Two factors are key to the success of these implants: first, the quality of attachment of the prosthetic joint to the patient's bone, and second, the low generation of wear particles as the components of the prosthesis articulate against each other.

This thesis is a study of both of these factors. First, the mechanism of bone apposition to hydroxyapatite (HA) coatings on Ti-6Al-4V was investigated via transmission electron microscopy (TEM). In this section of the study, Ti alloy cylinders were coated with HA by two different methods to yield three types of coatings - annealed and unannealed plasma-spray (PSHA) coatings and an annealed ion-beam assisted deposited (IBAD-HA) coating. These cylinders were implanted in trabecular bone in dogs from periods ranging from 3 hours to 14 days. Mechanical testing indicated that the bone/implant interface with the PSHA coated implants was significantly stronger than that with the IBAD-HA coated or uncoated Ti alloy implants. However, there were no differences in the degree of bone apposition to the three HA-coated materials; thus indicating that bone apposition is not a sufficient indicator of mechanical integrity of the bone/HA interface.

In the second section of this study, the microstructural factors contributing to the observed wear properties of the oxide on Zr-2.5Nb were investigated via TEM. Zr-2.5Nb barstock which had been rotary-forged to impart an anisotropic microstructure was sectioned and oxidized in dry air at 600°C and 635°C for a variety of times ranging from 30 minutes to 40 hours. Cross-sections across the oxide/metal interface were observed via TEM. The oxide scale comprises primarily monoclinic zirconia, with small amounts of tetragonal zirconia. Evidence of a mixed oxide phase, $6ZrO_2 \cdot Nb_2O_5$, was also observed. The microstructure of this oxide is dependent on oxidation temperature, the microstructure of the underlying metal, and oxide depth. Two oxide microstructures originating from beta-Zr grains in the alloy were also identified.

A third study concerned the architecture and microstructure of naturally-derived and synthetic bone substitute materials (BSMs). While BSMs are used clinically to promote healing in large bone defects, they were useful to this study as a control for the organization of mineral in mature bone. Low voltage high resolution scanning electron microscopy (LVHRSEM) enabled observations of the three dimensional architecture of these materials which were then correlated with TEM observations. The crystallites in an anorganic bovine-derived BSM were organized in a hierarchical fashion which paralleled the organization of collagen. In contrast, the synthetic materials were organized in an isotropic network. The difference in organization was attributed to the formation of the mineral matrix of bone on an anisotropic collagen template.

Thesis Supervisor: Linn W. Hobbs
Title: John F. Elliott Professor of Materials

Quotations relevant to polishing titanium rod (and TEM samples), oxidized zirconium, and the color of electrons:

One day a committee of elders will come to my door and tell me it is time to perform the ritual of the polished stick....Here's the way it works....You are taken to a nice place, where it is all quiet and serene and Zen. You are cared for. Fed well. And often affirmed. Your task is simply this: to spend a week polishing a stick. They give you some sandpaper and lemon oil and rags. And, of course, the stick -- a nice but ordinary piece of wood. All you have to do is polish it. As well as you can. Whenever you feel like it. That's it: *polish the stick.*

At the end of the week the elders will return. They will gravely examine your work...."No stick was ever polished quite like *this*!" they will exclaim....Be proud, stick polisher! This is really something. And, it is enough.

Oh, don't I wish.

Robert Fulghum [1]

"This must be the land of OZ," said Dorothy, "and we are surely getting near the Emerald City."

"Yes," answered the Scarecrow. "Everything is green here..."

L. Frank Baum, *The Wizard of Oz*, 1900

On the completion of the doctoral degree:

...The earth is all before me. With a heart
Joyous, nor scared at its own liberty.
I look about; and should the chosen guide
Be nothing better than a wandering cloud,
I cannot miss my way. I breathe again!

William Wordsworth, *The Prelude*, 1805

This is the day which G-d has made: let us be glad and celebrate in it!

Psalm 118

Table of Contents

List of Figures

List of Tables

Acknowledgments

This thesis has my name on it, but none of it would have happened without the help of a lot of other people:

My family - Dr. Mom and Dad and Stacy and Jenn and Dave and Shawn - thanks for being there and for understanding when it took three days for me to call back!

My other family - Mom and Dad and Andrew and Eric and John and Carol for making me one of the family and for Neil

My pre-husband, Neil. "You keep on asking me if we should make this official. Are you asking me if we should we make this official?"

All the roommates - Sitta (Wo bist du?); Jenn Healey, helping the Media Lab take over the Boston Pops; Rose, my domestic partner and partner in party-planning and all around friend (That one's a beer!); pre-Rabbi Ensign Michelle, co-founder of the Prescott St. *minyan*; Judah - when you are famous, can I say I picked blueberries with you? Debbie, not a roommate but a symbiote - Bei mir bistu sheyn!.

Everyone at MIT Hillel and the MIT Folk Dance Club and Harvard Hillel and the Porter Square *Minyan* and the Tremont St. shul.

All my friends in Boston - When I get out of the cave I will see you all again!

My advisors - Linn Hobbs - Thanks for your advice and for being there at thesis time. Myron Spector - thanks for all the help, especially when I had no clue in which direction to go next.

My committee - Ned Thomas and Ioannis Yannas, for making sure all the conclusions matched all the data.

All the people who made the implant experiment possible - Brian Wong; Francis, Frank, and Diane from the VA Hospital in Jamaica Plain; Dr. Cui for sending me e-mail and materials from China; Dr. Hsu - not only for the surgeries but for the rides and for being cheerful at 8am and for being such an amazing teacher. It was an exhilarating six weeks!

Gordon Hunter and Marc Long for all the advice and encouragement on the oxidized zirconium and to Gordon especially for spending three hours giving me rewrites on the OZ chapter over the phone

Everyone at the Brigham - especially Sandra and Dr. Shortkroff for all their advice; Anuj for continuing the BioOss work; Peg and Karen for all their help and patience

The Yannas group and office - Lila, Donna, Mark, Toby, Sunil - we had a great time at the Biomaterials meetings and I appreciate you letting me crash in your lab! Libby and Bernie - we miss you! Stacy, Dawn, and Cyndi - good luck with everything! Howie - thanks for letting me tag along on your surgeries!

The Hobbs group, now and then - Sreeram and Lu-Chang for making sure I knew everything I needed before they up and left; Julia for advice and support and letting me yell and for all the help getting the draft out and for saving my skin by helping get the final copy out - you could play the market with your karma account; Stephan for all the help on the MPC poster; Meri for always smiling and for running that in situ experiment for me; All the UROPS - Lan, Matt, Wendy, Vicky, Emma - it was nice to have help - it was even nicer to have company in the lab; Anabela, because of whom I can make a French braid; Phyllis for keeping me sane and letting me steal office supplies and for listening when I went off on some irrelevant topic.

The (other) office mates - Mike for listening and advising and for seeing right through things; Kevin, Beth and Lynne - you weren't around much for one reason or another, but it was sure nice to chat with someone between samples!

EM types - Pat Reilly for all her help and patience and advice and for knowing exactly what the problem was; David B. for help and good conversation; Tony G.-R. for letting me steer the STEM and for telling me how the FEGSEM really works - "Of course, electrons are green"; Mike F. for teaching me a lot more than electron microscopy (and a lot of that, too); Nick P. for all his help in the facility and in the lab

Others - Natasha Chang for teaching me all I know about wear, Fred Wilson for knowing everything, John DiFrancesco for just popping over to fix things, Fred Cote for all his help while I spend three days polishing titanium rod in his machine shop, Pat Kearney and Yin-Lin Xie for all their help in the prep lab, Hal Ackler for proving that one person can make a difference (and for making the difference that saved me from months of darkroom time), everyone at the Central Machine Shop, especially Peter Morley - those guys can do *anything*! Libby and Tim from the surface facility for all their help. Pedro and Sandra from the Architecture Cafe for saying Hi and keeping me supplied with cereal and croissants.

And all the sources of funding - the Office of Naval Research (Graduate Fellowship), John F. Elliott Chair, William Branstrom Fellowship, Department of Materials Science and Engineering, Smith and Nephew, Inc., BioKinetix Foundation, Brigham Orthopedic Foundation. The CMSE and Biology Department Electron Microscopy Facilities and the CMSE Surface Analysis Facilities are supported in part by grants from the NSF.

Chapter 1

Introduction

1.1 Materials Concerns in Joint Arthroplasty

Prosthetic hips and knees are currently implanted in about 240,000 patients every year in North America [2, 3]. Candidates for joint arthroplasty include patients who exhibit excessive pain or dysfunction in either the hip or knee due to fracture of the femoral head, arthritis, or other conditions [2, 3]. Hip replacement can take two forms: total arthroplasty (THA) and hemiarthroplasty. The former involves replacement of both the femoral head and the acetabular cup in the pelvis (Figure 1.1). Following hemiarthroplasty, the prosthetic hip, or, more precisely, the prosthetic femoral head, articulates against the patient's own acetabulum, which is not replaced. Both the tibial and femoral surfaces are always replaced in total knee arthroplasty (TKA); however, the surgeon must determine what to do with the patella and the various ligaments and tendons. These can be left intact, replaced with prosthetics, or removed entirely [3].

Many devices have been proposed for repair or replacement of both the hip and the knee. The prosthetic design for the hip most commonly used today incorporates a ball component which is attached to the femur via a stem which is inserted into the marrow cavity. This results in a two part materials problem for the femoral component of hip prostheses (see below), and the ball and the stem are frequently produced from different materials [4]. The femoral component of the prosthetic knee is a plate which replaces the

entire articular surface of the femur. Ultra high molecular weight polyethylene (UHMWPE; MW > $6*10^6$, -[CH_2CH_2]-)has long been the material of choice for both the tibial component in TKA and the acetabular component in THA (Figure 1.1).

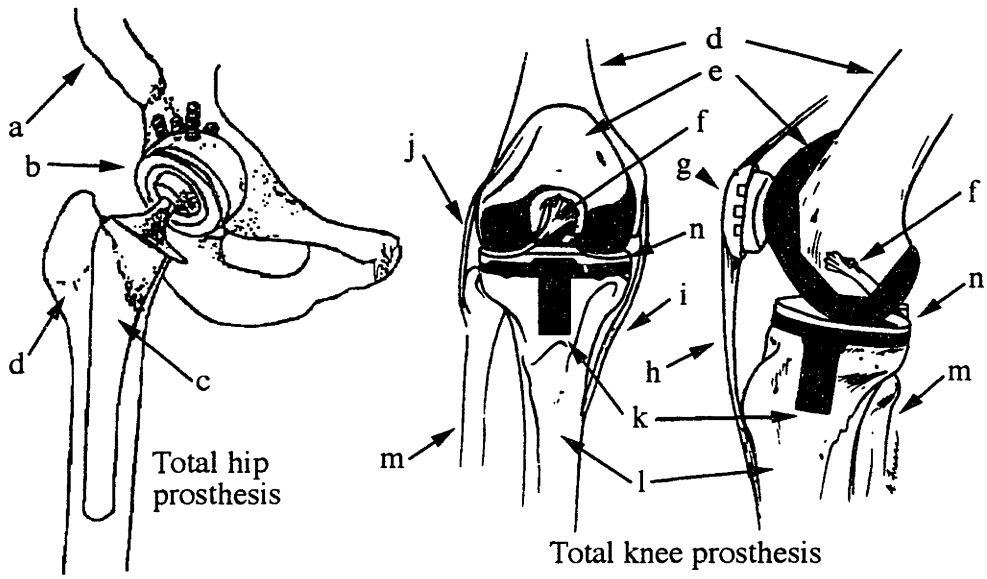

a: pelvis; b: acetabular component of hip prosthesis and prosthetic ball (attached to femoral component of hip prosthesis); c: prosthetic stem (femoral component of hip prosthesis); d: femur; e: femoral component of knee prosthesis; f: cruciate ligaments; g: UHMWPE (patellar) button; h: patellar tendon; i: medial collateral ligament; j: lateral collateral ligament; k: tibial component of knee prosthesis; l: tibia; m: fibula.

Figure 1.1 (Left) Drawing of cementless total (right) hip replacement, showing screws used to fix prosthetic acetabulum; (Middle and Right) Frontal and lateral views of cemented total (right) knee replacement, showing retention of the cruciate and collateral ligaments and replacement of the patella with polyethylene button. Adapted from [2, 3].

The materials requirements for the prosthetic stem in hip arthroplasty include high compressive and bending strength and low elastic modulus. In addition, the surface of the material must facilitate the formation of an interface with the surrounding bone which will resist high shear stresses, which can exceed four times body weight during walking and other daily activities [2, 5]. The most common stem materials are Ti-6Al-4V and cobalt-chromium, with Young's moduli of 105 and 230 GPa, respectively. In contrast, the cortical bone surrounding the implant has a modulus of 30 GPa; the cancellous bone at the

ends of the femur has a modulus of 3 GPa. The difference in modulus results in stress shielding of the bone: stresses on the leg are not conducted from the implant to the surrounding bone in a physiological fashion. This lack of mechanical stress on the bone tissue results in the reduced activity of osteoblasts, cells responsible for bone formation. In the presence of normal bone resorption by osteoclasts, this reduced osteoblastic activity results in a net loss of bone mass. The decrease in bone density puts the patient at risk for both fracture and prosthesis failure, which would necessitate a revision arthroplasty to replace the prosthetic hip [2]. While similar requirements exist for TKA, stress shielding is less in evidence, and the prosthesis geometry minimizes the forces that are transmitted to the interface of the bone and the prosthesis [3].

The most common attachment vehicle for both THA and TKA is poly(methyl methacrylate) (PMMA), which serves as a "bone cement," providing mechanical fixation by both penetrating the interstices of the surrounding bone and adapting to surface features of the metallic stem. One of the problems with bone cement is that particles of PMMA break off of the bulk and are endocytosed by macrophages, cells whose role it is to remove loose debris normally dislodged in the body. These macrophages release chemical regulators which promote bone resorption by activating osteoclasts, thereby reducing the density of the bone adjacent to the implant stem [2]. Fracture at either the bone/PMMA or implant/PMMA interface may lead to micromotion of the implant within the bone. Localized stresses resulting from this motion can exceed the compressive strength of the bone, resulting in pressure necrosis. The damaged bone is resorbed, increasing bone porosity, reducing the integrity of the bone/implant interface, and, eventually, leading to fibrous tissue encapsulation of the implant [6]. This tissue cannot form a robust interface between the implant material and bone, and the implant eventually fails outright or is replaced because the increased micromotion is excessively painful to the patient [6].

Porous coatings were developed as an alternative attachment vehicle to increase the mechanical strength of the interface. These coatings, either cobalt-chromium alloy or titanium beads, provide macropores a few hundred micrometers in diameter into which bone can grow, creating a mechanically interlocked interface [7]. Fracture along this interface is difficult because the fracture lines must either follow the tortuous path of the surface or extend across the bone. Typically, pores greater than 100 micrometers are required to allow viable bone ingrowth [8]. There is also a theoretical limit to the ultimate interfacial strength of these systems [6]. Osteoconductive materials, which promote bone growth along their surface (such as the apatites under investigation here), have been applied as coatings onto the metal beads comprising porous coatings. This approach has been shown by some to increase the strength of attachment to porous-coated implants, perhaps by promoting the initial growth of bone into the pores [9].

Many investigators feel that an attachment vehicle which can facilitate both mechanical and chemical bonding will increase the strength of the interface between the implant and bone even further. Such materials would not only encourage bone deposition along the surface of the implant (i.e., osteoconduction) but serve also as a template for bone growth directly on their surface, resulting in a chemical adhesion [6]. Coatings incorporating both macroporous and osteoconductive materials have also been developed [10].

While many calcium phosphate ceramics have been developed as bone bonding materials, the most common coating for orthopedic implants continues to be plasma-sprayed hydroxyapatite (PSHA). Hydroxyapatite, $Ca_{10}(PO_4)_6OH_2$, is a synthetic material which mimics bone mineral, or biological apatite. The difference between the synthetic and biological materials is extensive substitution of carbonate (CO_3^{2-}) for phosphate *in vivo*. These coatings have been shown to facilitate bone growth on the surface of both hip and dental implants, with interfacial strengths too great to be explained by mechanical bonding

alone [11]. Indeed, the first goal of this study is to distinguish the roles of mechanical and chemical bonding in the interfacial strength between bone and HA.

The above discussion has focused on issues of implant fixation. It should be noted that research to improve fixation has concentrated on hip replacement; initial fixation is less of a concern in TKA [3]. A primary issue in TKA, and one which also applies to THA, is wear, especially the influence of geometry, materials, and surgical technique on tribology [12, 13].* Excessive wear of either the femoral or tibial component in both cemented and cementless TKA and THA can lead to bone resorption similar to that resulting from particles of bone cement as described above [15-17]. The materials requirements for the articulating surfaces in joint arthroplasty include high compressive and shear strength and high wear resistance, in addition to requirements for biocompatibility which apply to all biomaterials. In the hip, the tribology requirements for the ball also depend on whether it will articulate on the patient's acetabulum or a prosthetic acetabulum.

UHMWPE is universally used as the tibial articulating surface in both THA and TKA. This hydrophobic polymer exhibits two primary wear mechanisms. Plastic strain can accumulate due to cyclic loading of the joint prosthesis and result in debris generation. Because this occurs on the scale of the microscopic asperities on the surface of the material, it results in generation of small wear particles on the order of a micrometer in size. As this deformation spreads into the sub-surface of the material, larger particles are produced as a result of delamination wear [18, 19]. Which of these two mechanisms will predominate depends on surface roughness of the articulating material, but, in general, reducing surface roughness also reduces wear [20, 21]. Different prosthesis designs and UHMWPE manufacturing techniques can result in greatly varying degrees of wear [22-24].

Other wear mechanisms occurring in this system provide further insight into the interaction of the articulating surface with UHMWPE. Oxidative wear of metallic

* Wear is defined as the damage due to material loss at the surface of a component which articulates against other moving parts [14].

counterfaces both produces particles of metal oxides and roughens the surface of the metal, increasing both two-body and three-body abrasive wear [25]. Adhesive wear increases inversely with surface hydrophilicity. UHMWPE sticks to the relatively hydrophobic passive oxides on Co-Cr or Ti-alloy surfaces, resulting in shearing of the material [25]. The coefficient of friction of the UHMWPE/counterface system also influences adhesive wear [26]. As the counterface is scratched due to the above mechanisms, abrasive processes also contribute to polyethylene wear [25].

In contrast, inert surfaces such as alumina and zirconia are more hydrophilic, cannot undergo oxidative wear, and are more resistant to three-body wear in general [25]. As a result, ceramic materials would be expected to perform better in wear tests against UHMWPE. Moreover, they can be produced with smoother surface finishes than is possible for metals [27]. Experiments with both alumina and zirconia (PSZ) have demonstrated superior wear properties in comparison to stainless steel and cobalt-chromium alloys [28-32].

While ceramics are more resistant to abrasion, they are not always able to resist the high compressive forces being transmitted through the leg [33]. Indeed, the low fracture toughness of alumina limits its usefulness in TKA [28]. Thus, just as an attachment vehicle for the hip was developed which combined the desired bulk properties of a metal (toughness) with the surface properties of a ceramic (osteoconductivity), a material for the articulating component is required which combines the toughness of a metal with the wear resistance of a ceramic surface.

One concern which arises in the use of a ceramic coating instead of a sintered ceramic head is scale integrity. Detachment of the oxide will both roughen the surface and produce particles which can promote three-body wear and particle disease. In addition, residual stresses in an oxide coating or scale derived from oxidation will influence the nucleation and propagation of cracks which could lead to spalling. However, the oxide

scale formed on zirconium is highly resistant to spalling. This has led to the widespread use of various zirconium alloys for pressure tubes in Canadian CANDU nuclear reactors [34]. Moreover, the oxide on zirconium is stable and adherent when articulated against UHMWPE [35]. In addition, high compressive stresses in the oxide layer, resulting in part from the high Pilling-Bedworth ratio of the zirconium/zirconia system (1.57), can discourage the nucleation and propagation of cracks, especially along the curved surfaces of the prosthetic knee [35, 36]. While the origins of oxide stresses in oxidized zirconium (OZ) have not been extensively characterized, a number of factors have been identified which contribute to oxide stresses in other systems such as Ni/NiO. These include epitaxic phenomena such as the motion of interface dislocations, specimen geometry, the difference in thermal expansion coefficients between the oxide and the metal, changes of either oxide or metal composition during oxidation, and grain boundary oxidation [37-39].

The favorable wear properties of OZ result partially from the oxide microstructure. This is controlled not only by the oxidation conditions, but by the thermal history of the metal substrate, which influences oxide structure [35, 40, 41]. However, most studies of OZ microstructure have been conducted within the nuclear power industry and have not been related to tribology. A second goal of this thesis is to investigate the relationship between the microstructure of OZ and its tribology.

Bone substitute materials (BSMs) answer an orthopedic need related to that addressed by joint arthroplasty, *viz* the replacement of an injured section of bone. While the prostheses described above replace joints and facilitate the patient's motion, bone substitute materials have both a short- and long- term structural function. In situations where a gap of more than a few millimeters is formed in bone, due to either injury or surgery, BSMs facilitate bone regeneration and provide mechanical stability during healing [42]. Over the last 20-30 years, a number of synthetic and natural bone substitute materials has been developed for clinical use [42, 43]. These materials have high osteoinductive

potential, not only in wound sites but in implant sites, especially in the sinus cavity, where an increased density of bone is needed for implant fixation [44-47].

These materials are also useful in non-clinical applications for studies of bone structure. Whole bone is difficult to study, and most researchers either use partially mineralized tissue or demineralized bone to study the organization of collagen and apatite in bone. By studying anorganic bone, it is possible to both investigate mineral architecture in bone and establish a control to which other bony deposits, such as those on hydroxyapatite coatings, can be compared. Moreover, an understanding of the architecture of bone mineral can provide insights into the mechanical and chemical properties of bone and facilitate the development of new BSMs.

1.2 Outline

This thesis comprises three related studies of the microstructure of orthopedic biomaterials. Chapter Two is a study of the architecture of naturally derived and synthetic BSMs. The goals of this study were twofold. The first was to determine the relationship between the microstructure of the mineral and organic matrices in whole bone; the second was to provide a control for the study of mineral deposits on hydroxyapatite coatings in Chapter Three.

Chapter Three is a study of bone bonding to HA-coated Ti-6Al-4V. The primary goal of this study was to distinguish the roles of mechanical and chemical bonding in the interfacial strength between bone and HA. A second goal of this study was to outline a mechanism for biological apatite deposition at that interface.

Chapter Four is a study of the microstructure of oxidized zirconium. Its primary goal was to investigate the relationship between the microstructure of OZ and its tribology. A second goal of this study was to look at the variation of oxide microstructure with respect to that of the underlying oxide.

Chapter Five develops relationships among the themes of the three previous chapters, presents a conclusion, and suggests directions for future research.

Chapter 2

Architecture and Microstructure of Bone Substitute Materials

2.1.1 Architecture of bone mineral and collagen

The mineral phase of bone imparts to the tissue its compressive, shear, and inflectual strengths and moduli of elasticity and serves as an important depot for calcium and macro-molecular soluble regulators. The mechanical, solubility, and protein adsorption properties of bone are critically dependent on the molecular structure and morphology of the individual apatite crystallites, which in turn result from the coordinated arrangement of apatite crystallites on a collagen template; collagen constitutes the fibrous component of what can be viewed as a fiber-reinforced ceramic composite. The apatite crystallites, in turn, are composed of a defect-structure hydroxyapatite which incorporates about 9% carbonate in the phosphate sites [48, 49]. The carbonate substitution also changes the morphology of the apatite crystallites. While hydroxyapatite (space group $P6_3/m$)has a hexagonal unit cell and naturally forms rod-like crystals with equivalent (100) and (010) faces, carbonate-substituted apatite forms more plate-like crystallites [50]. There are two possible mechanisms for carbonate substitution in the HA lattice:

$$CO_3^{2-} \xrightarrow{HA} CO_{3_{PO_4}}^{\bullet} + \frac{1}{2}V_{Ca}^{'} \qquad \text{(Eqn. 2.1)}$$

$$CO_3^{2-} + V_{OH}^{\bullet} \xrightarrow{HA} CO_{3_{PO_4}}^{\bullet} \qquad \text{(Eqn. 2.2)}$$

Carbonate substitution leads to changes in crystallite morphology resulting from changes in the relative surface energies of the various crystallographic planes. As carbonate content is increased, HA crystallites gradually adopt a plate-like morphology instead of the hexagonal rod morphology typical of pure HA [50]. Investigations of crystallographic modification of HA and other calcium phosphates during annealing indicates that high temperature and vacuum annealing tends to lead to decomposition, while low temperature annealing in air or moist environments leads to increased phase purity [51-54]. This may indicate that the mechanism in Equation 2.2 is more likely, but detailed study would be required to confirm this.

What we know of the association of the mineral crystallites and collagen fibers has come primarily from transmission electron microscopy [55-61]. Information obtained from tilt experiments and high-resolution lattice imaging coupled with selected area electron diffraction has provided evidence that the crystallites have a plate-like character, with the crystallographic **c**-axis of the hexagonal unit cell aligned along the long axis of the associated collagen fibril [62, 63]. Studies have also demonstrated that the platelets are produced by a preferred crystal growth in the **a-c** crystallographic plane [59, 64-68]. More recently, advances in tomographic reconstruction of micrographs obtained using high-voltage electron microscopy have provided three-dimensional reconstructed images of plate-like apatite crystallites in calcifying tendon and in newly forming bone [69-71]. Previous studies of collagen have shown that collagen molecules are organized in fibrils with a 67 nm stagger among parallel collagen molecules. The "hole zones," the spaces between the ends of the collagen fibrils, stain preferentially, leading to the periodic structures observed in TEM of stained sections.

By combining high-voltage TEM images of thick sections of partially mineralized turkey tendon, Landis, et al. were able to arrive at a model for the early deposition of apatite crystallites in collagen (Figure 2.1). According to the tomographic observations, apatite crystallites nucleate in the hole zones and grow in a plate-like morphology in between the collagen molecules within the fibril, creating a layered structure of collagen molecules interleaved with apatite crystallites [72].

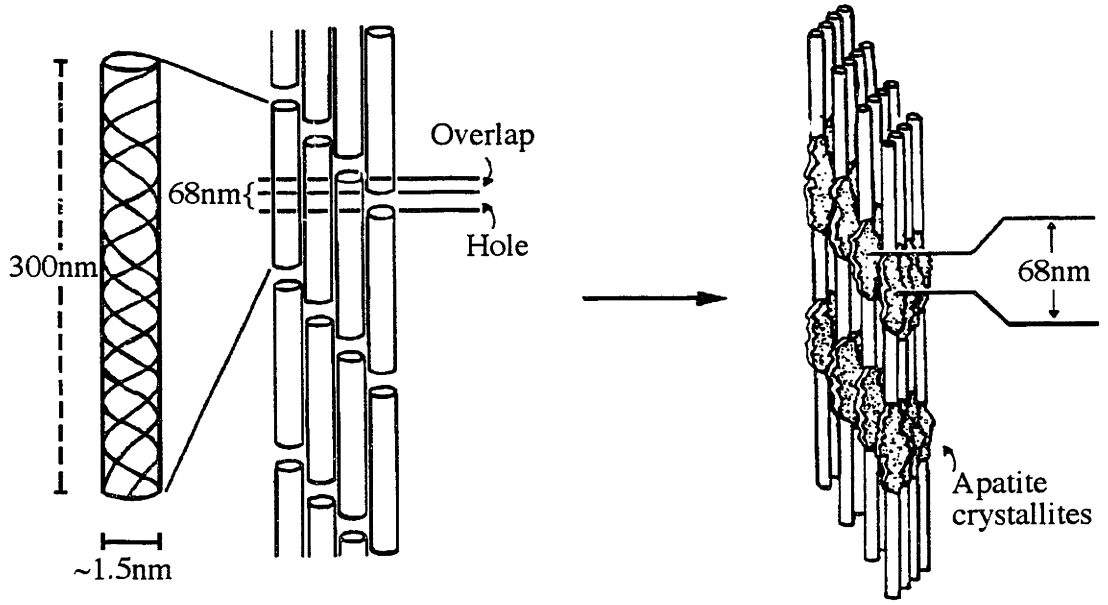

Figure 2.1: Model of initial deposition of apatite in collagen fibrils. Adapted from [59, 71].

There are two schools of thought concerning the locus of apatite mineral. The first maintains that the mineral is located exclusively within the collagen fibrils. This hypothesis is supported by observations of pickerel and herring bone [61, 73]. When observed in cross section, mineral was observed only within the collagen fibrils. Within individual collagen fibrils, periodic bulges were seen every 68 nm, corresponding to the periodicity of the hole zones and indicating that these zones were the primary locus of mineral [74]. In

addition, the crystallite nucleation and growth rates were independent among collagen fibrils [61, 73].

A second model maintains that there is extrafibrillar mineral. According to this model, mineralization begins at structures called matrix vesicles, which form between the collagen fibrils [60]. The fibrils then start to mineralize at their periphery, followed by mineralization of the fibril interior [75]. In one study, Fourier transform analysis of electron micrographs apparently revealed non-periodic apatite deposits within mineralized turkey tendon which are presumably located in the interstices within fibril bundles and fascicles. This extrafibrillar matrix would then provide mineral continuity among the mineralized fibrils [76]. However, the Fourier analysis does not definitively locate these non-periodic deposits with respect to the collagen fibrils. Indeed, even the non-periodic appearance of these deposits depends on the image contrast conditions, which do not appear to have been carefully controlled in this particular study.

These two models are not necessarily incompatible [77]. Recent work has more carefully elaborated the role of matrix vesicles in initial mineralization and their association with the collagen fibrils [69, 78-81]. Indeed, the initial mineral deposits in cartilage more closely resemble the extrafibrillar matrix vesicles than periodic collagen-mediated deposits, and similar structures have been observed in poorly mineralized turkey tendon [79, 81, 82]. In addition, TEM of the cement line in remodeling bone also reveals structures similar to the matrix vesicles described above, and they have also been observed at wound sites in rat tibiae [83, 84]. Moreover, data showing that collagen comprises only 40% of the volume of wet bone supports the theory of a continuous mineral matrix which includes both intrafibrillar and extrafibrillar mineral - as much as 75% of the mineral in bone may be extrafibrillar [85]. Additionally, three-dimensional analysis utilizing serial sectioning and tomography has demonstrated that the controversy between the two models may result from the traditional dilemma of TEM: how to relate a two dimensional image back to a three

dimensional structure. That is, information which is missing (because the feature in question is just outside of the TEM section) or obscured (because of over-projection of adjacent, higher contrast features) may have led previous observers to miss features such as matrix vesicles [86]. While matrix vesicles may not be easily visible by tomography, surface deposits of mineral have been observed [87].

Scanning electron microscopy has also been of great value in providing information about the three-dimensional architecture of bone down to the micrometer level [88, 89]. The use of this method for obtaining information about individual crystallites has been complicated by the necessity to apply electrically conductive coatings that, while relatively thin, still could obscure features of the crystallites [90]. In whole bone, the presence of the organic phase of bone generally impedes identification of the morphological features of the individual apatite crystallites, partially due to the sensitivity of collagen to dehydration [88, 89].

2.1.2 Objectives

The objective of this investigation was to employ low-voltage high-resolution scanning electron microscopy (LVHRSEM) to investigate the morphology and organization of apatite crystallites in mature bone. Anorganic bovine bone was studied in this investigation to allow the examination of the mineral phase after removal of the organic matter. TEM examination of the samples both confirmed the identification of features observed in the SEM and allowed comparison to earlier studies of bone mineral architecture. It also enabled comparisons with observations of whole bone. That TEM observations of mineral in whole bone and in anorganic bone are similar indicates that the removal of collagen did not introduce artifacts into the SEM observations (see below).

To demonstrate how the interaction of collagen and apatite results in the architecture and crystal structure of bone mineral, two synthetic bone substitute materials,

OsteoGraf/LD-300 (OL) and OsteoGen (OG), were also studied. Clinically, synthetic materials have the same advantages as naturally derived bone substitute materials and provide an alternative to allograft or autograft bone. Their value in this study derives from their failure to replicate potentially important chemical (*e.g.*, carbonate content), ultrastructural and architectural features of bone mineral that influence the incorporation and remodeling of the graft and its effects on the remodeling of surrounding bone [91]. According to the manufacturers' brochures, OL is designed for high porosity and solubility, while OG is optimized for low solubility, high porosity, and purity of the apatite phase [92, 93].

2.2 Materials and Methods

2.2.1 Naturally derived and synthetic bone substitute materials

Anorganic bovine cortical and trabecular bone (BioOss™) (BO) was obtained from Geistlich Biomaterials (Wollhusen, Switzerland). The trabecular bone had been fragmented into 1 mm pieces composed of a few trabeculae; the cortical bone was in blocks 10-20 mm on a side and about 5 mm thick. Fragments about 1-5 mm^3 were broken from the blocks for SEM observation. Both the fragments of cortical BioOss and particles of trabecular BO were mounted on 10-mm diameter aluminum SEM stubs with carbon tape. OsteoGraf/LD-300 (OL; CeraMed, Lakewood, CO) and OsteoGen (OG; Impladent, Holliswood, NY) were mounted on 10 mm Al stubs with carbon tape and left uncoated. All HA materials were observed in a JEOL 6320 FEGSEM operating at 1kV with a working distance between 2 and 4 mm to minimize charge accumulation. Other operating voltages were also used for observation, but without improvement in image quality or the degree of charge accumulation. Fracture surfaces of the trabecular BioOss were also observed. Images were collected and some signal averaging performed using image

processing package provided by JEOL for the microscope. Final contrast and brightness adjustments were made using Adobe Photoshop.

Individual pieces of trabecular BioOss (BO), OL, and OG and 1 mm^3 chips of cortical BioOss were also prepared for TEM. The trabecular bone fragments were dehydrated prior to embedding in graded solutions of ethanol and water. Both dehydrated and untreated fragments of cortical BioOss were prepared. Dehydration was performed by immersion in 70%, 80%, 90%, and neat (3x) ethanol for 10 minutes each. All samples were incubated in 3:1, 2:1, 1:1, and 1:2 solutions of acetone and Spurr's Resin (Polysciences, Warrington, PA) for 8 hours each, and then incubated in neat Spurr's Resin for 8 hours before being cured for 24 hours at 60°C. Spurr's resin was prepared with 10 g vinylcyclohexene dioxide (VCD), 5 g diglycidyl ether of polypropylene glycol (DER-736), 26 g nonenyl succinic anhydride (NSA), and 0.4 g dimethylaminoethanol (DMAE). After measuring the components, the mixture was folded for 5 min. before use. Extra resin was stored, covered, in a fume hood for no more than 48 hrs.

Silver to gray sections cut at room temperature using an ultramicrotome (Reichert Ultracut S, Leica, Nußloch, Germany) were collected on 400 mesh copper grids which had been immersed in a solution of double sided tape (a source of polyisobutylene) and xylene and dried. Carbon was evaporated onto the sections, which were then viewed in JEOL 200CX, JEM 2010, Akashi EM-002B TEMs, all operated at 200kV. Stereoimaging was performed in the JEOL 200CX instrument by rotating the sample between -20 and +20 degrees and taking pictures at 5 or 10 degree intervals. Pictures taken before and after the tilt series at 0 degrees of tilt were used to evaluate the extent of beam damage to the samples. A cooled CCD camera (Gatan, Warrington, PA) was used to collect high resolution images in the JEM2010. To highlight the crystalline regions of the sample, the images were Fourier filtered using Digital Micrograph, a software package provided by Gatan for the CCD camera. In the resulting image, contrast from the aperiodic sections of

the sample (mostly epoxy) had been filtered out. Crystallographic modeling and simulation of the electron diffraction patterns of the hydroxyapatite unit cell was performed with the simulation software Cerius^2 (Molecular Simulations, Inc., San Diego, CA). The scattering factors for hydroxyapatite were not significantly different for x-rays or electrons.

2.2.2 TEM of whole canine bone

Trabecular bone was cut from the distal femur of an adult mongrel dog. The tissue was placed in ethylene glycol until it could be dissected. It was cut into 1 mm^3 blocks using a Dremel™ tool fitted with a ceramic cut-off tool. The blocks were agitated in ethylene glycol for 24 hours and then transferred to ethanol and stored in a refrigerator for at least 48 hours. Samples for TEM were cleared in propylene oxide three times (five minutes each) and embedded in Spurr's resin. The Spurr's resin was prepared as above, except that 4.5 g of DER 736 was used to produce a somewhat harder block. Samples were incubated with agitation in 1:3, 1:2, 1:1, and 2:1 solutions in propylene oxide for 24 hours each. They were then placed under vacuum in neat Spurr's for 24 hours and embedded in BEEM capsules with fresh resin for 24 hours at 60°C. Samples were microtomed and carbon coated as above. They were viewed in the same JEOL 200CX TEM as the BioOss samples.

2.3 Results

Several levels of mineral architecture in BioOss were observed in the SEM: the organization of individual apatite crystallites in fibrils, the aggregation of parallel fibrils into columnar networks, and the meshing of these networks to form interlocking structures which reflect the lamellar organization of bone (Figure 2.2). In both trabecular and cortical material, the mineral is arranged in fibrils which parallel the fibrillar architecture of collagen [94]. These fibrils aggregate into columns which form into larger structures,

accommodating cells and other micrometer scale features of bone. Figure 2.2 shows a hole to the right of the micrograph which may be a canaliculus, one of the channels which contain cell processes; osteocyte lacunae were also observed. The terraced fracture surface exposed the cross section of the networks, which exhibited microporosity reminiscent of the individual fibrils (Figure 2.3). While the cross section revealed the cylindrical nature of the mineral fibrils, it also showed continuity of the apatite crystallites among the fibrils. Thus, individual fibrils were not just loosely associated but incorporated into a single mineralized network.

The fracture surface of the cortical BioOss also showed structures which corresponded to the fracture surfaces of bone lamellae [56, 88]. In Figure 2.4, the surface of the sample was oriented at an angle to the plane of the micrograph, which shows several layers of lamellae. The arrows indicate crystallites approximately perpendicular to the fracture plane. The bright lines correspond to the actual fracture surface. Fractured surfaces of trabecular BioOss also exhibited layered structures (Figure 2.5). In general, fracture surfaces of the cortical BioOss were more highly mineralized than the trabecular surfaces. The fibrillar organization of the material was less evident, due to the high density of mineralization in the more mature interior regions of the trabeculae.

The average width of the mineral fibrils was 65-80 nm, comparable to the average diameter of collagen fibrils (Figure 2.6). The fibrils were composed of individual crystallite "beams." These beams appeared to form a continuous network along the fibrils. Less highly mineralized fibrils exhibited a periodic ladder-like arrangement of crystallites (Figure 2.6), with the "rungs" oriented roughly perpendicular to the long axis. Thus, crystallites running parallel to the collagen fibrils were connected by crystallites running perpendicular to the collagen fibrils.

Higher resolution SEM micrographs also show individual plates of hydroxyapatite crystallites (Figure 2.7). The large depth of field and high resolution available in the FEG-

SEM enables one to distinguish the individual plates of hydroxyapatite, even those which extend several nanometers into the sample. Individual crystallites can be observed oriented both relatively parallel to the plane of the micrograph and at a significant angle to it.

TEM likewise revealed structures of plate-like bone crystallites aggregating into interpenetrating networks. The plate-like morphology of the crystallites was confirmed via stereoimaging. As shown in Figure 2.8, crystallites were oriented both parallel and perpendicular to the plane of the section. Those crystallites oriented relatively parallel to the plane of the section were viewed as plates; those viewed on edge appeared as rods (see discussion). The crystallites ranged from 30-120 nm in length, 6-9 nm in thickness, and 20-60 nm in width. No significant differences in crystallite width were found among crystallites of trabecular, cortical, or dehydrated cortical BO. The maximal lengths observed in the dehydrated cortical samples were about 50 nm longer than in the undehydrated samples.

Crystallites were frequently observed aggregated in parallel networks at least several micrometers in length and 60 to several hundred nanometers across. Forks and branches which appeared in the wider networks of crystallites imply that the networks are composed of aggregates of thinner networks (Figure 2.8). Also to be noted is the similarity in magnification between Figure 2.6 and Figure 2.8. The crystallite fibrils viewed with a three dimensional perspective in the SEM are shown in cross-section -- at the same magnification -- in the TEM.

Within the crystallite networks, crystallites were observed in discrete aggregates oriented perpendicular to the long axis of the network and distributed along it with an average periodicity of 65 +/- 4 nm (n=7) (Figure 2.9). At first glance, the micrographs resemble published micrographs of mineralized collagen [79]; however, no protein was present in this material, as evidenced by elemental analysis [42, 95]. Similar aggregates of crystallites oriented on edge were also observed. Within these aggregates, crystallites were

oriented parallel to each other. Other cross-sections of crystallites showed aggregates oriented in a staggered arrangement. In both cases, the collagen molecules are hypothesized to run parallel to the long axis of the crystallites, with the organization of the crystallites reflecting that of the hole zones in the collagen fibril. Similar structures were observed in TEM images of whole bone (Figure 2.10).

The ladder-like features observed in the FEGSEM were not observed as such in the TEM. Figure 2.11 shows several parallel cross-sections of crystallite fibrils. These fibrils were composed of crystallites arranged almost exclusively on edge or parallel to the plane of the TEM section. Notably, the two arrangements of crystallites (on edge or parallel to the section) do not alternate. This provides two possible explanations for the "ladders" seen in the SEM. The first is also the simpler of the two. The rungs of the ladders as seen in SEM are crystallites oriented with their flat faces parallel to the surface of the BioOss. The surface of the sample is not perpendicular to the beam, so the crystallites tend to have a measured periodicity closer to 50 nm than to 65 nm. They appear as rungs rather than as dense networks because the hole zones in the collagen are arranged such that parallel crystallites are arranged in stacks. The sides of the "ladders" are composed of crystallites arranged with their edges oriented parallel to the surface of the sample. In the TEM, these networks appear denser, and they appear as solid networks in the SEM.

This explanation, while it may be supported by the micrographs, is somewhat unsatisfying. There is no reason why the crystallites viewed on edge in the TEM should form a continuous network when observed in the SEM when the crystallites viewed in plan view do not. Careful examination of the periodic aggregates of crystallites oriented parallel to the TEM section reveals that these networks are also probably continuous and that the variation in contrast results from a variation in length among the individual crystallites. Moreover, further examination of Figure 2.11 reveals crystallites which appear to be situated between the crystallite networks. These crystallites form in between the fibrils,

connecting them to each other. This, then, is a possible explanation for the variation in density among the mineral fibrils as viewed in the SEM. The denser fibrils are the actual mineral fibrils; the crystallites forming the "rungs" connect the mineral fibrils to each other and account for interfibrillar mineral continuity. It should be noted that direct evidence of mineral continuity, such as grain boundaries, were not observed in the TEM after extensive searching.

The growth habit of the crystallites was revealed via lattice resolution imaging in both high- and low-resolution TEM (Figure 2.12). These images also confirm that the individual crystallites comprise single crystals of apatite. The lattice fringes were indexed and their angle to the long axis of the crystallite measured. This angle was compared to the actual orientation of the plane in question with the **c** crystallographic axis of hydroxyapatite. The {h00} planes are parallel to the **c** axis, while (00l) planes are perpendicular to it. Figure 2.12 reveals that the (001) planes are oriented perpendicular to the long axis of the crystallites. This orientation is consistent with alignment of the long axis of the crystallites along the **c** crystallographic axis of hydroxyapatite (Figure 2.12).

Selected area electron diffraction patterns from clusters of crystallites viewed both on edge and in plan view were also consistent with preferential crystal growth and network alignment along the **c**-axis (Figure 2.9). The crystallites viewed on edge had their long axes oriented roughly parallel to one another. The crystallites in plan view comprised part of a network which is lying diagonally across the micrograph. The long axis of the crystallites appeared to be oriented along the network. The partial arcs included by the (002) and (004) rings reveal the orientation of the **c** axis of the crystallites included in the micrographs (Table 2.1). The section of the (310) ring appearing in the pattern is also oriented at 90 degrees to the (002) reflections. Because the **c** and **c*** (in reciprocal space) axes are parallel to one another and perpendicular to (001) in the rhombohedral system, these features, combined with the orientation of the (001) reflections perpendicular to the

direction of the long axis of the crystallites, indicate that the crystallite long axis corresponds to the [001] direction. It should be noted that the same is not true of the {100} and <100> families of planes and directions.

Selected Scattering Planes in Hydroxyapatite

d (Å)	Intensity	hkl
8.17	12	100
4.07	10	200
3.88	10	111
3.44	40	002
3.17	12	102
3.08	18	210
2.81	100	211
2.78	60	112
2.72	60	300
2.63	25	202
2.26	20	310
2.14	10	311
1.98	30	222
1.89	16	312
1.84	40	213
1.81	20	321
1.78	12	410
1.75	16	402
1.75	16	303
1.72	20	004

Table 2.1: Selected scattering planes and intensities from hydroxyapatite [96].

The synthetic materials, in contrast, had a much simpler architecture than that of the BioOss. At low magnification, LVHRSEM revealed that the OL has a regular but somewhat rough surface punctuated by both small nodules and pits (Figure 2.13). At higher magnification, the nodules were shown to be composed of individual apatite crystallites (Figure 2.14). These crystallites appeared to be rod-like in morphology and were arranged end-to-end in a random network to form the bulk material (Figure 2.15).

The OG also had a relatively rough surface (Figure 2.16). However, any nodules and pits in this surface were about the same size as the crystallites which comprised the bulk. As in the OL, these nodules were composed of small rod-like crystallites oriented end-to-end in a random network (Figure 2.17). However, the network was not as uniform as that in OL. In some areas, several crystallites appeared to be mutually aligned in a row. Similar features were also observed in TEM (Figure 2.18). However, they were typically separated by several hundred nanometers.

It is important to note that these samples were not fractured for SEM observations. Thus, the micrographs do not reveal the interior structure but instead show the surface of the as-received material. On first inspection of the SEM micrographs, it appears as though the crystallites of OG were arranged in nodules which are interconnected to form the bulk material. However, TEM did not confirm the presence of secondary organization in OG as it did for BO. The size of the crystalline aggregates viewed in the SEM did not match any features observed in the TEM, with the exception of the widely scattered linear arrays of crystallites. Even in a random array of crystallites, it is likely that there would be a few linear structures. Indeed, the end-to-end organization of apatite crystallites in bone shows that a linear arrangement is not energetically impossible. In this case, however, it is more likely that the surface irregularities are due to mechanical interactions (adhesion, friction) between individual particles of OG in the sample vial.

TEM of OL and OG also revealed a random network of crystallites (Figures 2.19, 2.20). Crystallites of both materials range in length up to 80 nm; OL crystallites were approximately 30 nm wide, OG crystallites about 20 nm. In addition, the rod-like morphology of the crystallites was confirmed by the uniform shape of the crystallite cross sections as viewed in TEM. Some of the crystallites were oriented on end, and their cross sections exhibited the hexagonal facetting typical of hydroxyapatite. This rod-like

morphology also indicates that the crystallites were primarily composed of hydroxyapatite, without extensive carbonate substitution [50].

In addition, the SAED patterns of both materials, which each incorporated about 100 scattering objects, include a complete (002) ring, indicating that the **c**-axis of the crystallites is randomly oriented (Figures 2.19, 2.20). Because the **a** and **b** axes of hydroxyapatite are crystallographically equivalent, the long axis of the rod-like crystallites must be parallel to the **c**-crystallographic axis. HRTEM confirms that this is indeed the case. The (002) plane, which is perpendicular to [001], was oriented perpendicular to the long axis of the crystallites (Figures 2.21, 2.22).

All three HA materials exhibited extensive beam damage. The carbonate, phosphate, and hydroxyl groups render HA susceptible to radiolysis. This results in amorphization of the HA in isolated regions which resemble voids because of their contrast with the remaining crystalline material. While bone mineral (carbonated apatite) is relatively stable for up to about 20 minutes under the electron beam under normal viewing conditions at about 100,000x magnification, both OL and OG show extensive damage within about 5 minutes.

2.4 Discussion

Identification of features of mineral architecture in whole bone tissue is difficult. Studies of bone architecture tend to employ demineralized bone or partially mineralized fibrous tissue such as tendon [97]. Neither of these materials can provide a model of the organization of mineral in mature bone. However, anorganic bone can be used to characterize the architecture and microstructure of the bone mineral matrix if care is taken not to alter the bone mineral matrix during processing. Methods for the removal of collagen from bone are at least a hundred years old [42]. The first chemical methods for removing collagen were developed in the 1950s [98]. Since then, not only ethylenediamine

but also hydrazine and other chemicals have been used to chemically denature and remove the collagen matrix, in addition to anhydrous thermal methods [42, 89].

Previous work has shown that preparation of ultra-thin sections using processing of bone specimens through aqueous solutions can alter the crystalline phase [99, 100]. In the present study, it is possible that the chemical method used for the removal of the organic matter altered in some way the apatite crystallites. That the crystallites seen in the specimens in this study displayed ultrastructural features similar to those seen in other TEM investigations of bone specimens prepared using anhydrous methods suggests that the fundamental morphology of the crystallites and their arrangement is not remarkably altered by the processing employed in this investigation [61, 71, 78]. Specifically, the identification of periodic arrangements of bone mineral in both unstained whole bone specimens and BO indicates that the mineral architecture of bone is not collapsed by the removal of the organic component. In addition, infrared spectroscopy of BioOss shows peaks corresponding to carbonate, indicating that the apatite in BO is similar in composition to that in bone, and the XRD patterns from bone and BioOss are also similar [95]. Moreover, little or no difference in crystallite size was found between cortical BO and dehydrated BO (that is, bone crystallites which had been further exposed to a water/ethanol solution). This indicates that the crystallite size is not altered so dramatically through exposure to solvents that either the arrangement of those crystallites in anorganic bone with respect to each other or even the dimensions of the individual crystallites are significantly different from that in whole bone.

The choice of anorganic bone as a model of bone mineral architecture is further validated by comparison of our observations with previous studies of biological apatite crystallites. The periodic aggregates of crystallites with a 64 nm spacing consistent with the banding of collagen supports other TEM investigations which have asserted that the crystallites form within spaces provided by the staggered arrangement of the tropocollagen

molecules in the collagen fibril [71, 101]. Small angle x-ray studies also suggest that the mineral nucleates in the hole zones of the collagen fibrils. While these observations also seem to indicate that the crystallites are needle-like rather than platelike, they also allow the possibility of plate-like aggregates of crystallites [102]. TEM observations of mineral crystallites have tended to show plate-like crystallites [59, 63, 78, 101]. While rod-like structures are also observed, further observations reveal that they are actually plate-like crystallites viewed on edge, as shown by use of a tilting stage. The higher contrast of the rod-like structures with respect to plate-like structures implies that the plates are not merely aggregates of rod-like crystallites; the continuity of lattice fringes over several tens of nanometers confirms that they are indeed single crystals [63]. Finally, studies of both isolated apatite crystallites and partially mineralized tissue have shown an [001] direction parallel to the long axis of the crystallites [55, 62, 71].

Thus, while anorganic bone was originally developed as a bone "substitute" material [42], it also is useful for non-clinical research applications. Specifically, because the structure of the mineral is not sensitive to dehydration, unlike that of collagen, anorganic bone is useful for elucidating three-dimensional structure via SEM, which is operated under high vacuum conditions. The advent of high-resolution SEM using a field emission gun (FEGSEM) has enabled architectural study of bone mineral architecture at a resolution previously available only via TEM.

Unlike conventional TEM or SEM, the FEGSEM does not rely upon thermionic emission for the production of electrons. Rather, a large electric field is generated at the source, which emits electrons via tunneling. Because field emission is more efficient than thermionic emission, source brightness is much higher. Probe current is a function of both brightness and spot size; thus, an increase in brightness is accompanied by a reduction in spot size, increasing resolution. Thus, the FEGSEM can achieve resolution comparable to that available in TEM while maintaining the depth of field which is the hallmark of SEM.

In addition, the reduced voltage of the electrons (1 kV versus 20-40 kV in conventional SEM and 200 kV in TEM) reduces the voltage at which the ratio of the outgoing secondary electrons and the incoming primary electrons is unity. This precludes charge accumulation at the surface and obviates the need for carbon or gold coating of samples. The decreased energy of the electrons also reduces beam penetration into the sample, ensuring that only surface features are viewed in the microscope.* Thicker gold coatings with finite grain sizes can obscure nanometer size features, neutralizing the advantages of high resolution SEM [89]. The ability to view samples without a coating hence facilitates the high-resolution observation of highly porous or irregular surfaces.

Thus, the combined use of TEM and FEGSEM in this study enabled the comparison of two-dimensional and three-dimensional views of a given object at the same magnification and the correlation of SEM and TEM observations. The crystallites viewed in the TEM can be seen directly in three dimensions in the SEM micrographs, providing morphological information which was only implied by the change in crystallite projection with tilt in the TEM. The plate-like nature of the crystallites also explains the wide range of crystallite dimensions observed in TEM. Only crystallites oriented perfectly parallel to the TEM section are viewed full size; the measured dimensions decrease as the angle of tilt increases within the section. While this foreshortening precludes the use of traditional statistical methods to determine average grain dimensions, observation of a large number of crystallites can provide an indication of the maximum dimensions they achieve.

SEM observations show the crystallites aggregating into ladder-like structures. In TEM, the cross sections of these structures present themselves as aggregates of small crystallites arranged in networks with a 65 nm periodicity; this is in agreement with neutron diffraction studies of fully mineralized collagen [104]. These networks were probably

* Monte Carlo simulations on aluminum spheres indicate that the reduction in penetration is about a factor of 10 for a voltage decrease from 30 to 5kV [103].

oriented parallel to the collagen fibers which had previously been chemically removed from the sample but which had the same periodic structure and width [101]. The observed series of networks lying parallel to each other in the TEM then correspond to longitudinal cross-sections of the columnar aggregates of fibrils. These networks are connected to each other by individual crystallites, visible in the TEM, which correlate with the "rungs" of the ladder-like structures observed in SEM. Just as the fibrils viewed in the SEM micrographs do not always lie parallel to one another, so too are the networks in the TEM oriented over a large range of solid angles [105].

The two microscopy methods are complementary, each confirming the interpretations of observations made in the other instrument and allowing the extension of observation to both grosser and finer scales. The highest level of hierarchy observed in SEM -- the aggregation of fibrils into lamellae -- is too large to observe in the TEM because the lamellae are several micrometers across [59]. Conversely, the individual crystallites, which are only 2-4 nm thick, are the smallest objects which can be viewed in the SEM. While the SEM cannot provide further information about crystallite microstructure, electron diffraction in the TEM allows identification of the **c** axis of HA with respect to the image. Thus, TEM observations reveal the crystallites as single crystals with the long axis parallel to [001] and the long axis of the mineral fibrils.

In addition to confirming elements of crystallite organization, TEM is also useful for confirmation of crystallite size. Because of the large depth of field available in the FEGSEM, entire crystallites can be resolved, even when they are highly tilted with respect to the beam; however, their dimensions can be distorted by 50% or more [90]. In the TEM, while foreshortening certainly occurs, it is limited by the thickness of the sections, and it is possible to get a estimate of the greatest possible dimensions, if not average dimensions [106].

The combination of TEM and FEGSEM has also allowed observations of more densely mineralized tissue than was previously possible. While existing models of bone mineral organization are not able to describe the arrangement of apatite crystallites in fully mineralized tissue, they do imply that the arrangement of mineral crystallites within the collagen matrix should reflect the architecture of that matrix. The mineral contribution to this correspondence was directly observed in this study. Just as the collagen molecules organize into fibrils, the mineral crystallites were observed arranged into fibril-like structures. The collagen fibrils arrange themselves in larger bundles and lamellae which are paralleled by the arrangement of mineral fibrils into columnar bundles and lamellae.

In addition, this study directly confirms the presence of extrafibrillar mineral, resolving the question in the literature of apatite is deposited outside of the collagen fibrils. Crystallites observed between the crystallite fibrils provide evidence that the mineral phase of bone, like the collagen matrix, is continuous. That anorganic bone specimens retain approximately one-third of their compressive strength also points to some type of chemical bonding among the crystallites [107]. This hypothesis is also supported by the observation that unsintered BioOss particles are not powders but macroscopic fragments or blocks. Bone is not a mineral-reinforced fibrous matrix; it is instead composed of two interwoven matrices, with the first serving as a template for the formation of the second.

Combination of the observations of this study with the model proposed by Landis and Weiner (cf. Figure 2.1) thus leads further development of a model of bone mineral architecture. Figure 2.25a reproduces the two-dimensional portion of Figure 2.1, this time to scale. Once drawn to scale, it is easy to see the how the staggered arrangement of hole zones and overlap zones leads to the periodicity viewed in stained collagen samples in the TEM. However, because the collagen molecules are arranged in a near-hexagonal arrangement with respect to each other, there are two possibilities for the arrangement of the hole zones with respect to each other [59, 104, 108]. Figure 2.25a demonstrates that a

collagen molecule is just longer that four periods (of 67 nm) as viewed in TEM. Let the sections of the molecule described by the four periods be numbered 1-4. If the stagger in the collagen molecule occurs along both lateral axes of the collagen lattice (the third, longitudinal, axis is the length of the molecules), then the hole zones will be isolated from one another, as shown in Figures 2.25b and 2.26a. If the stagger occurs along one axis but not the other, then the hole zones will be contiguous, as shown in Figures 2.25c and 2.26b [108]. Which one of these models describes the three-dimensional arrangement of collagen has not been clearly established, but evidence from analytical studies of the types of cross-links within collagen fibrils favors the model illustrated in Figure 2.26b [59, 104]. However, the choice of Figure 2.26a or b does not actually influence the description of the arrangement of apatite within the collagen matrix presented in this study for several reasons.

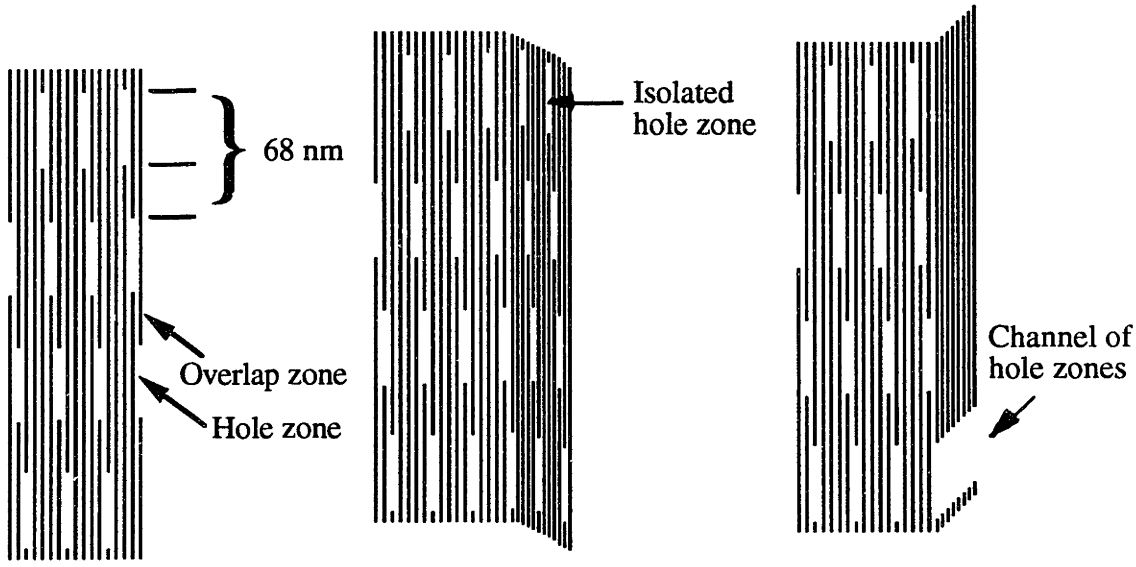

Figure 2.25: a) Two dimensional view of a collagen fibril. b,c) Two 3D views of a collagen fibril, corresponding to the cross-sections discussed in Figure 2.26. Scale: 1 mm = 4 nm, but the collagen molecules are 0.1 mm wider than they ought to be; the height of the figure is 1 cm less than the full length of a single collagen molecule.

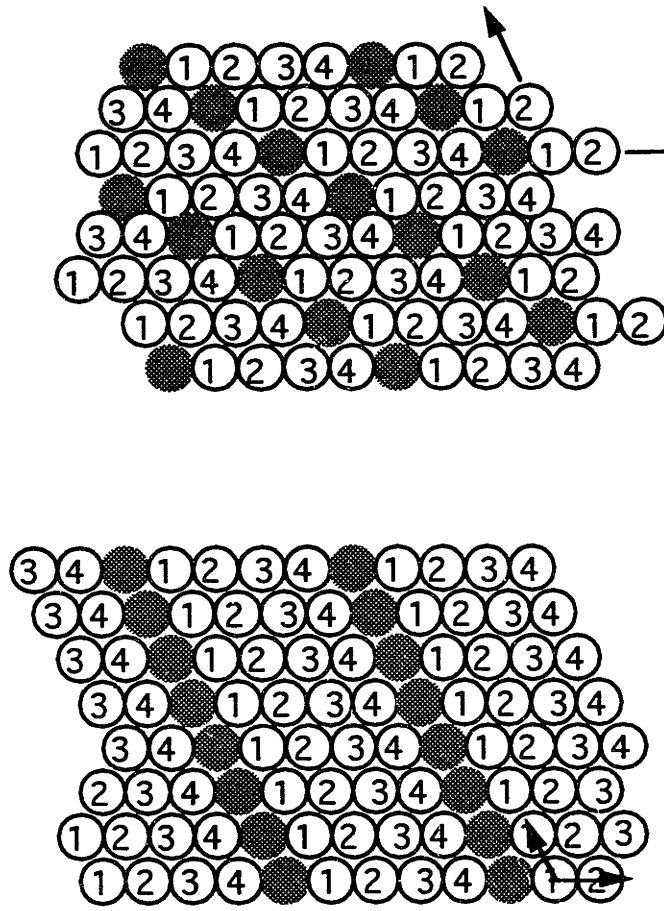

Figure 2.26: Cross-sectional diagrams of a collagen fibril, adapted from [108]; the space filling model is not drawn to scale: a) Diagram assuming staggered arrangement of collagen molecules in both dimensions of the hexagonal lattice, shown by arrows. b) Diagram assuming staggered arrangement of collagen molecules in only one dimension, shown by the horizontal arrow. The numbers 1-4 describe four sections of an individual collagen molecule, which is just longer than four 67 nm periods of a collagen fibril.

The first reason is that the apatite crystallites are definitely larger than the hole zones. Crystallites longer than 40 nm will extend out of the hole zones into the overlap zones. However, the observed thickness of the crystallites is only 2-4 nm, so they will fit between the layers of collagen molecules, which are 4 nm apart [70]. Second, only two or

three of the 30-60 nm wide crystallites will fit within the diameter of the 40-80 nm wide collagen fibrils. This is in contradiction to Figure 2.1. If the hole zones are arranged in channels, then the crystallites will fit in the channels. If the hole zones are isolated, the crystallites will simply grow in between the rows of collagen molecules.

In addition, both of the models in Figure 2.26 are consistent with the arrangement of crystallites observed in Figures 2.9-11 -- within a given crystallite fibril, the crystallites are all parallel to one another. In 2.26a, the proximity of the hole zones to each other creates a preferred direction of crystallite growth, even though the crystallites have to grow through the intermolecular spaces. The alignment of the holes makes the structure more "flexible" along the diagonals described by the hole zones. Similarly, if the hole zones are contiguous, then stereochemical influences would favor initial growth parallel to the channels created by the hole zones. However, this would not preclude later growth of crystallites at an angle to the hole zone channels as the collagen fibrils became more completely mineralized, and obliquely oriented crystallites have been proposed contributors to intrafibrillar mineral continuity. Indeed, the periodic arrangements of crystallites are not the only arrangement of crystallites viewed in the TEM micrographs in this study - denser arrangements of crystallites tend not to exhibit this periodicity (cf. Figure 2.8). This further indicates that apatite crystallites are oriented in directions which are not parallel to each other or to the proposed hole zone channels.

If the ends of the collagen molecules do not limit the growth of the crystallites, one might question what does stop crystallite growth before the maximum. While this thesis cannot answer that specific question, it does establish that a portion of the of the crystallites in an given collagen fibril do not achieve the maximum possible length. If all the crystallites achieve lengths of 120 nm (the maximum observed), then they will appear to form a continuous network when observed via TEM because the length of a hole zone and its two adjoining overlap zones is only 94-98 nm (Figure 2.27). Indeed, the longer

crystallites in the collagen fibril probably contribute to mineral continuity within the fibril. The periodic networks were visible in the TEM because their constituent crystallites tended to be closer to 60 nm in length, although some of the crystallites were longer. Thus, the variation of crystallite lengths in the TEM is not only a function of foreshortening. Careful measurements of individual apatite crystallites will be required to clearly establish their size distribution.

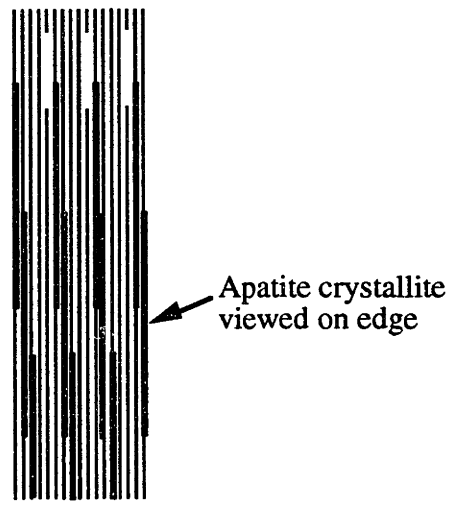

Figure 2.27: Two dimensional view of a collagen fibril with 120 nm crystallites oriented on edge in each hole zone (cf. Figure 2.25), showing that long crystallites will appear as continuous networks.

This study shows that the hierarchical organization of bone mineral is a result of the nucleation of bone on a collagen template which is also organized in a hierarchical manner. In contrast, while the synthetic materials are formed via a proprietary process, it is clear that this process involves nucleation of apatite in an isotropic environment to produce an isotropic, random arrangement of crystallites. This may lead to differences in cellular interactions between the synthetic and naturally derived materials. Osteoblasts can migrate along the surface of and within particles of deprotonated cancellous bone mineral easily

because it has the same internal surface area per unit mass as bone, facilitating deposition of bone within the packed implant material [44]. However, this does not necessarily lead to differences in the effectiveness of synthetic and naturally derived apatite [44, 109].

The biological processes involved in deposition also result in a difference in composition between the synthetic and the naturally derived hydroxyapatite. Apatite in bone has extensive carbonate substitution, whereas synthetic apatites have a composition closer to that of stoichiometric hydroxyapatite. This leads to the difference in crystallite shape observed via TEM; apatite crystallites become more plate-like in morphology with increasing carbonate substitution [50]. The chemical difference does not, however, necessarily lead to differences in crystalline fraction because the percent crystallinity can be controlled via processing [43, 92].

The differences in chemistry, crystallography, and crystallite organization between synthetic and naturally derived apatites do not necessarily result in differences in clinical performance. Interestingly, researchers have found both OsteoGen and BioOss inappropriate as fillers in dental pulp [47, 110]. Furthermore, both materials have been extremely successful as intra-osseous materials [42, 44-46, 109, 111, 112]. After implantation, bone forms over the surface of both types of implants within two weeks [44]. However, the mechanism of resorption and bone apposition to the two types of materials could be different [42].

Following page

Figure 2.2: a) LVHRSEM micrograph of anorganic trabecular bone, showing the organization of bone mineral into fibrils, shown here from the side b) a schematic describing the various features.

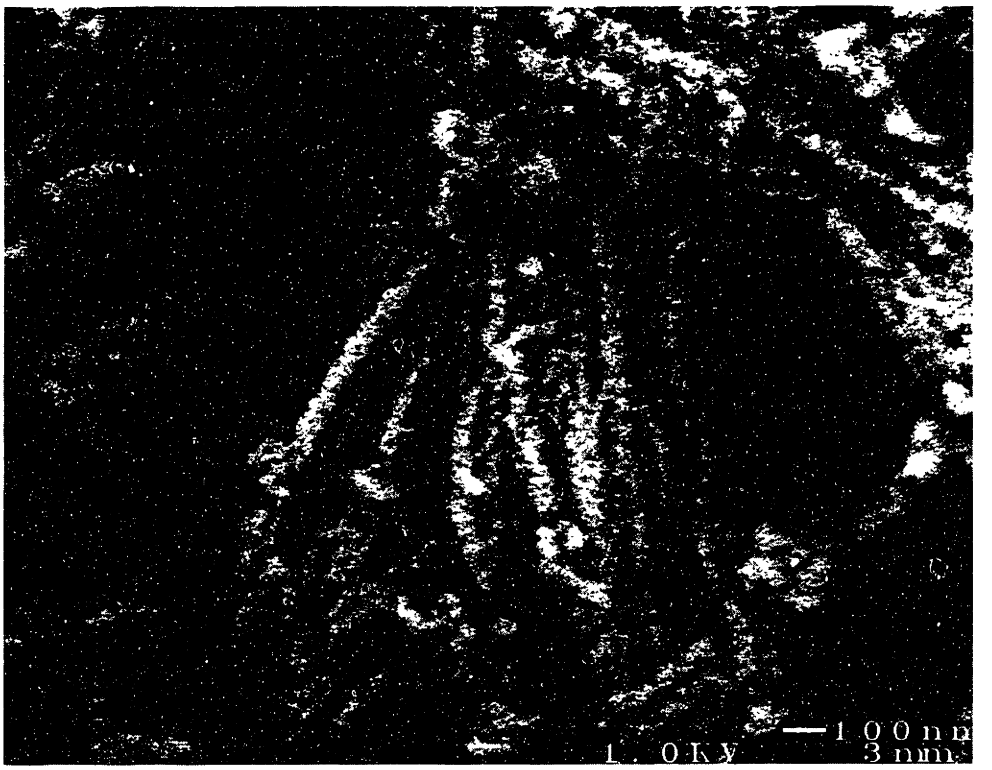

Figure 2.2a

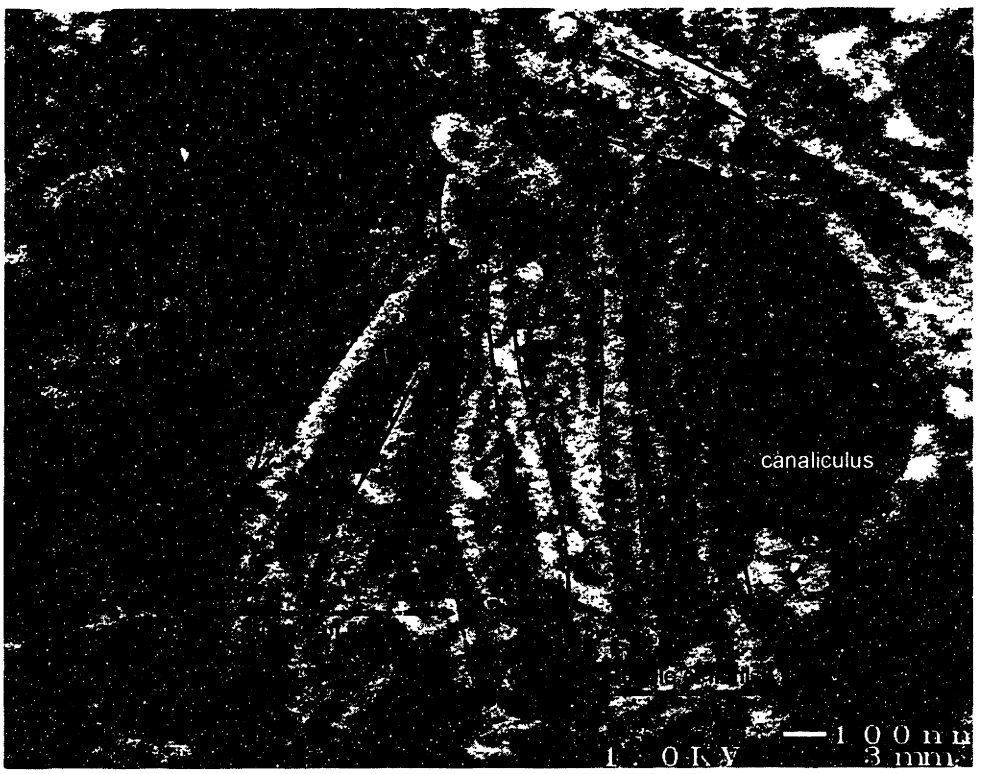

Figure 2.2b

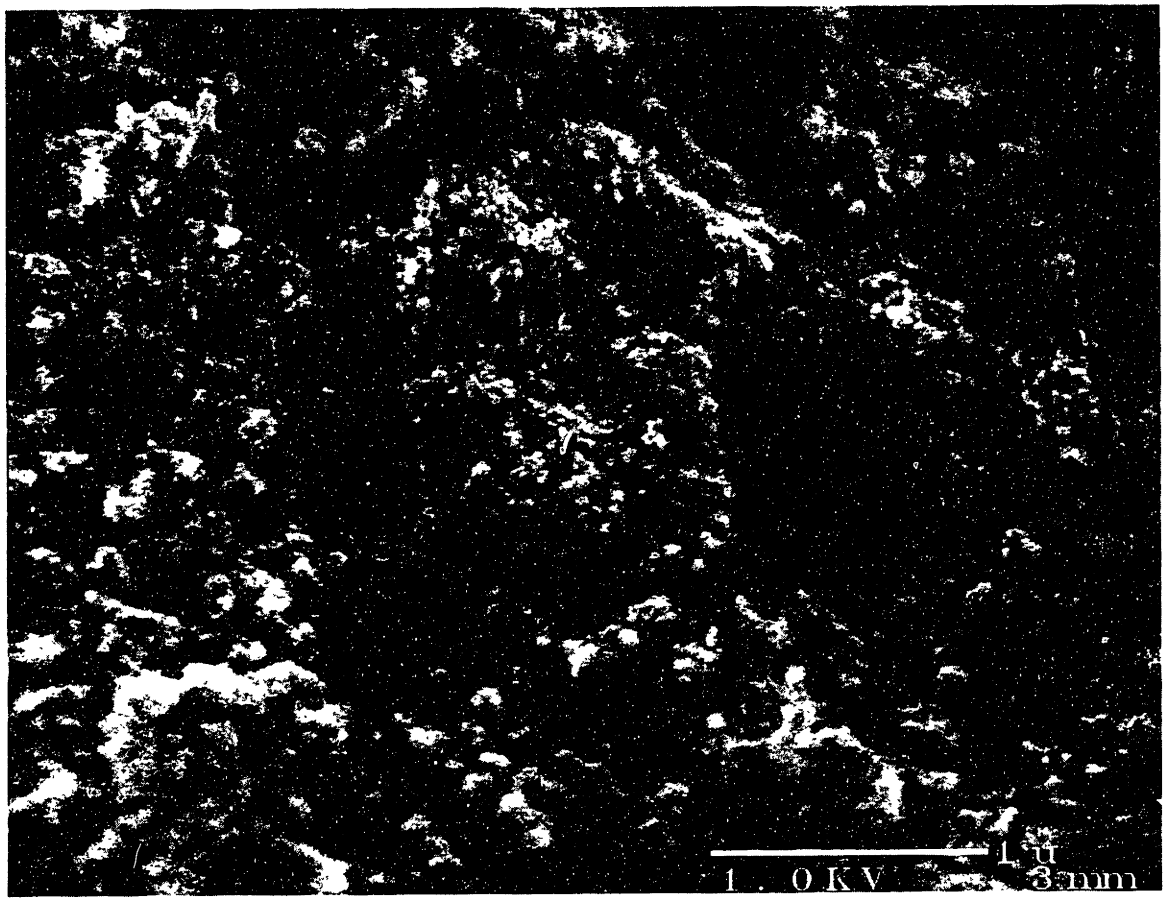

Figure 2.3: LVHRSEM micrograph of anorganic trabecular bone, showing the mineral fibrils both on end and from the side.

Following page

Figure 2.4: LVHRSEM micrograph of anorganic cortical bone, showing layers of lamellae composed of apatite networks running roughly parallel to each other within the lamellae (arrows).

Figure 2.5: LVHRSEM micrograph of a fracture surface in anorganic trabecular bone, showing layered structures akin to the lamellae in Figure 2.4.

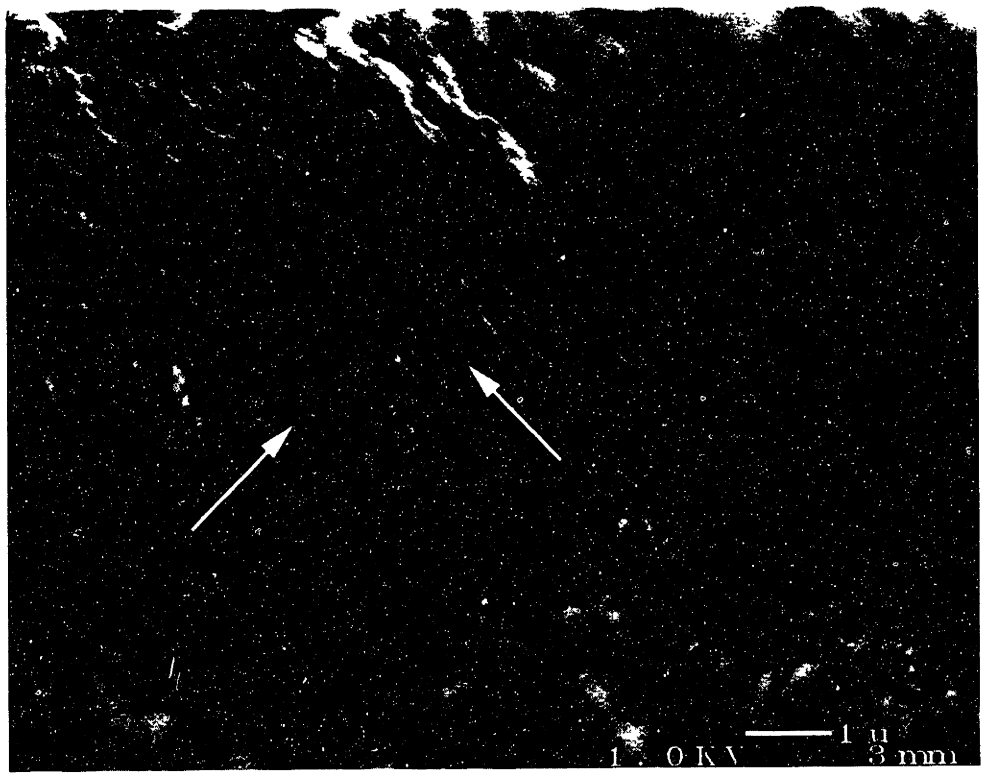

Figure 2.4

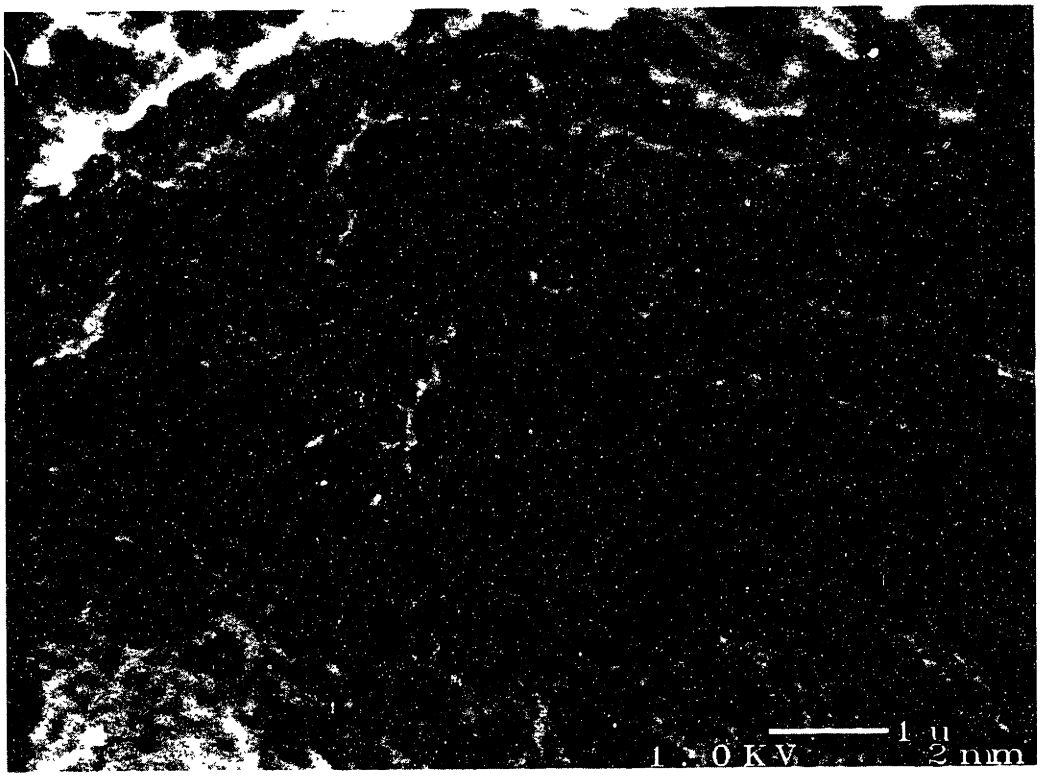

Figure 2.5

Following page

Figure 2.6: LVHRSEM micrograph of anorganic trabecular bone, a higher magnification view of Figure 2.2, showing a interfibrillar crystallites in a ladder-like arrangement connecting mineral fibrils to each other (arrows).

Figure 2.7: FEGSEM image of anorganic cortical bone, showing individual plate-like crystallites.

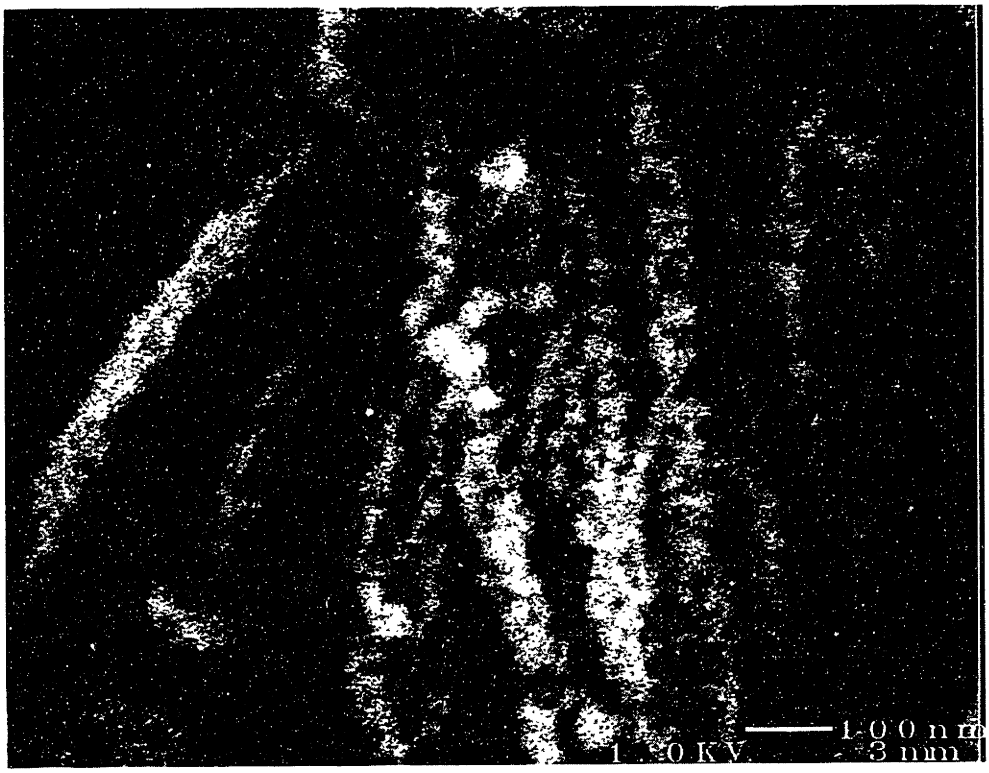

Figure 2.6

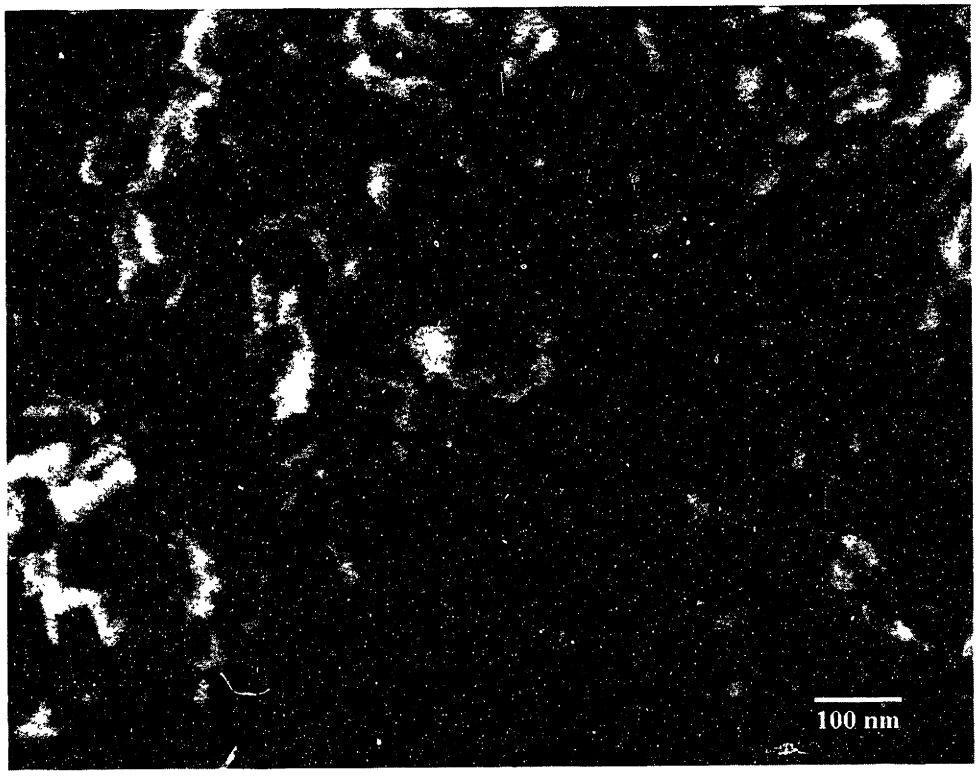

Figure 2.7

Following page

Figure 2.8: a) TEM image of anorganic trabecular bone, showing cross-sections of mineral fibrils composed of individual apatite crystallites b) A schematic showing the various fibrils.

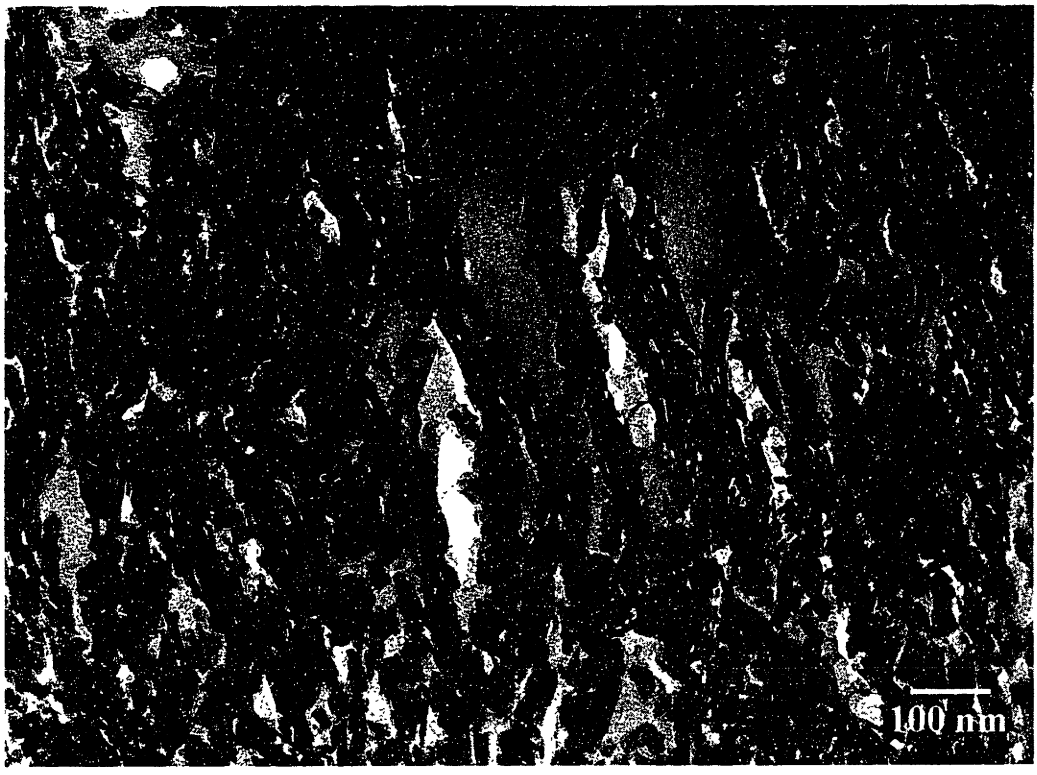

Figure 2.8a

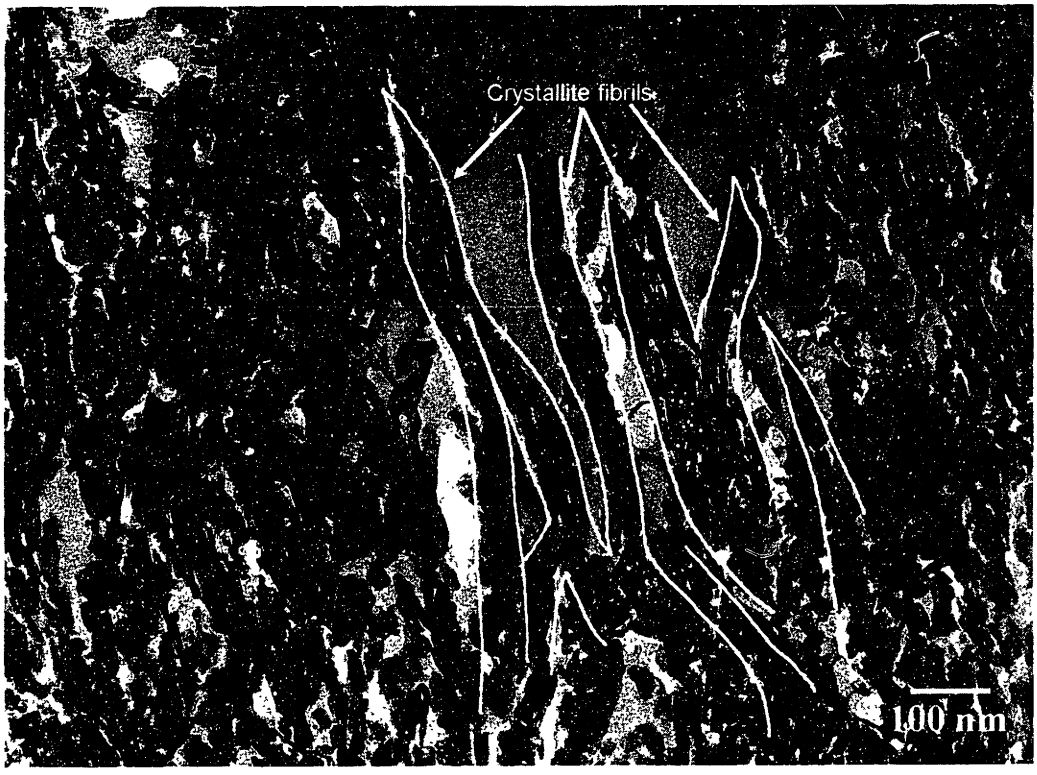

Figure 2.8b

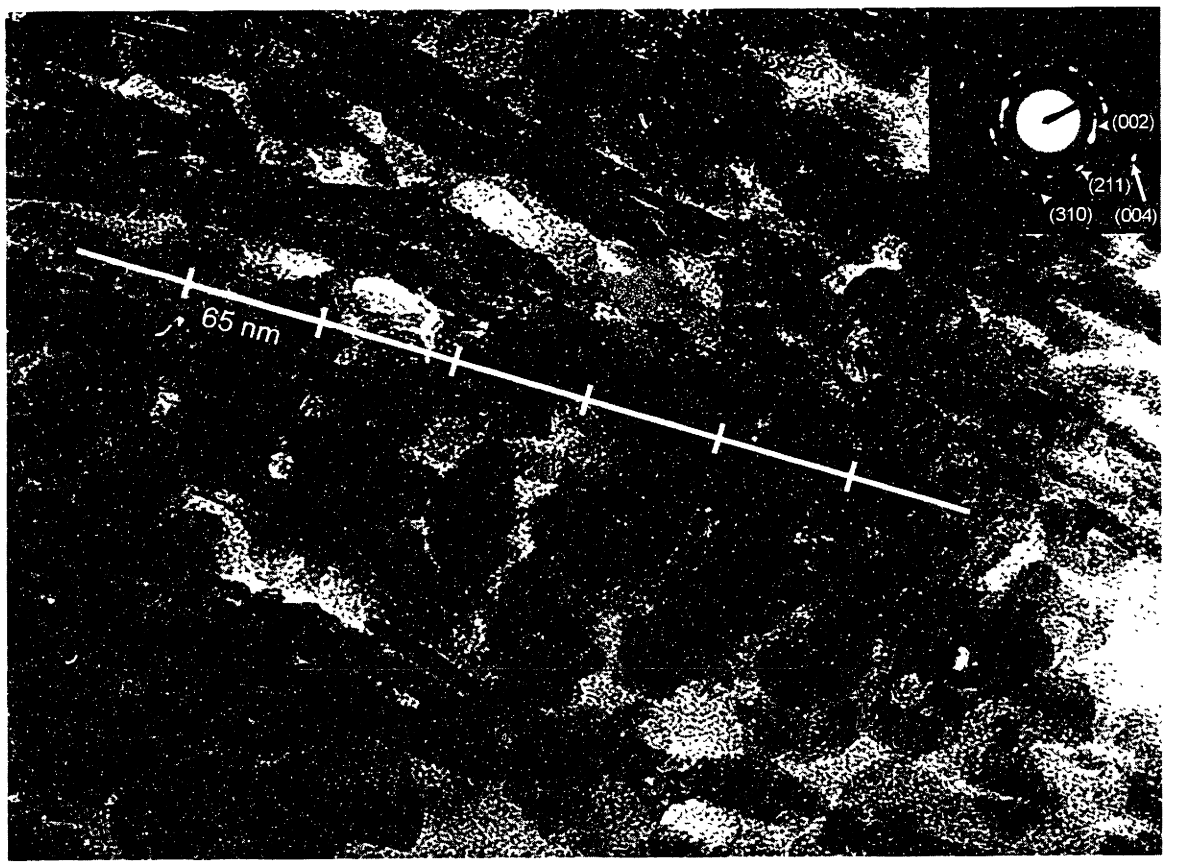

Figure 2.9: TEM image of anorganic trabecular bone, showing an arrangement of crystallites. The SAED pattern shows short arcs corresponding to (002) and an incomplete ring corresponding to (211).

Following page

Figure 2.10: TEM micrograph of whole bone (unstained) showing periodic aggregates of crystallites similar to those observed in Figure 2.11.

Figure 2.11: TEM image of anorganic trabecular bone, showing several parallel networks of crystallites.

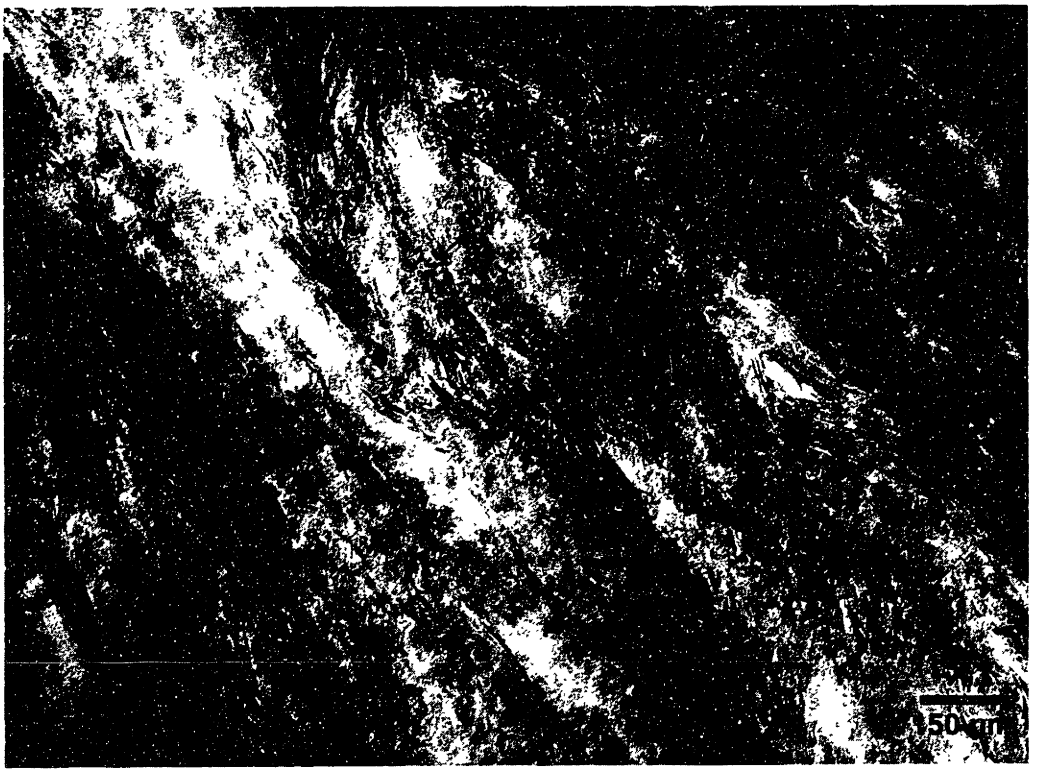

Figure 2.10

Figure 2.11

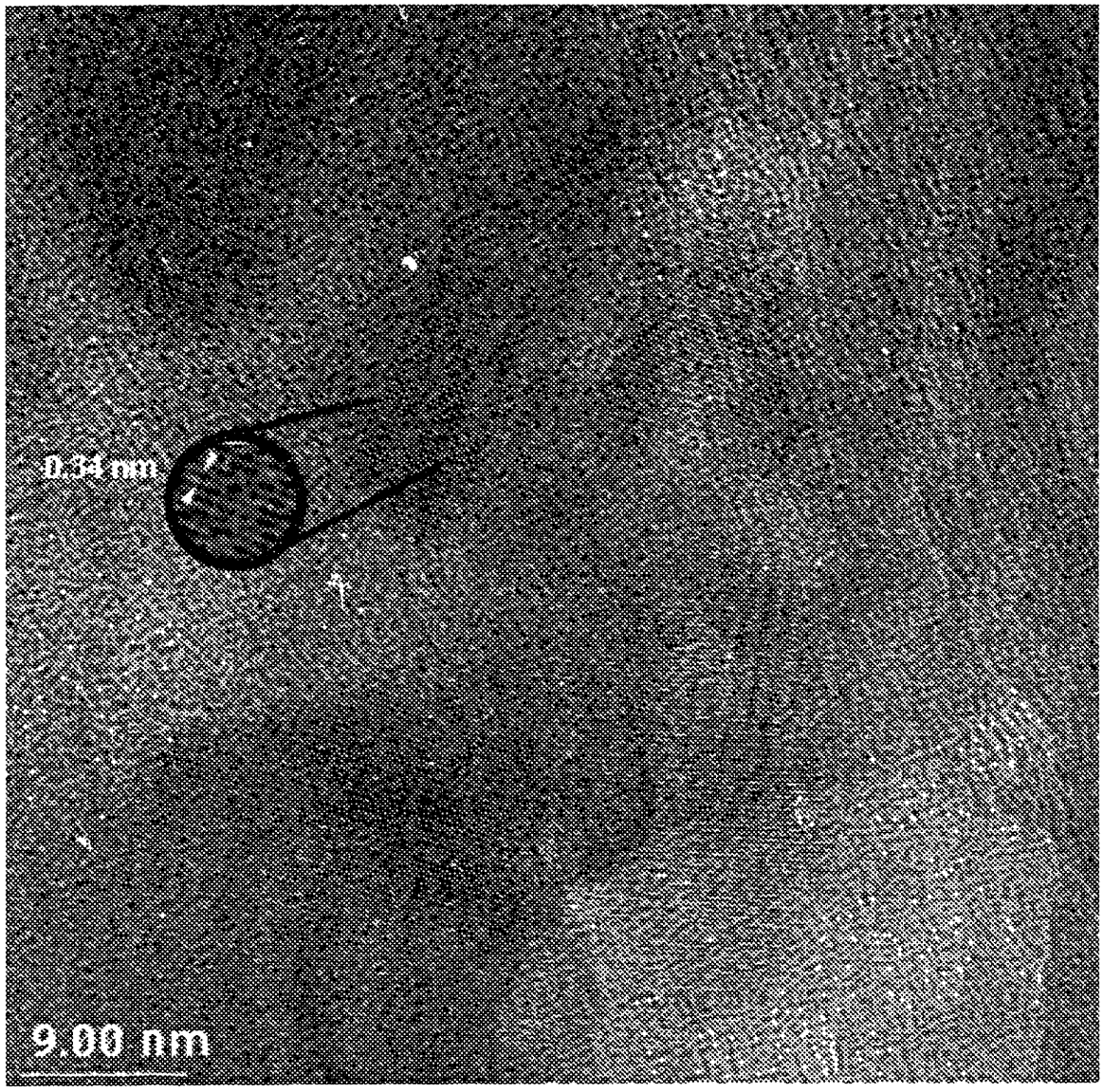

Figure 2.12: a) HRTEM image of anorganic trabecular bone, showing (002) lattice fringes (highlight); b) (Following page) Image a) after fast Fourier transform (FFT), showing the dimensions of the mask used for the "reverse" FFT; c) Image (a) after Fourier filtering, revealing the (002) lattice fringes perpendicular to the long axis of the crystallites.

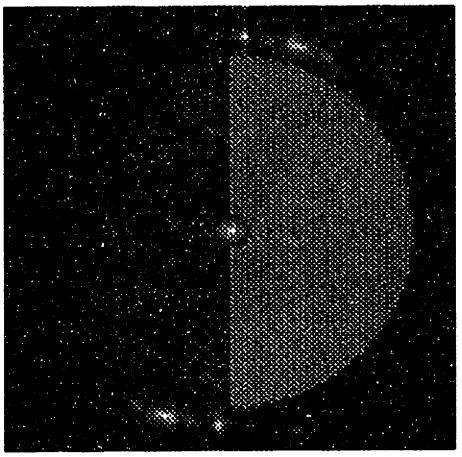

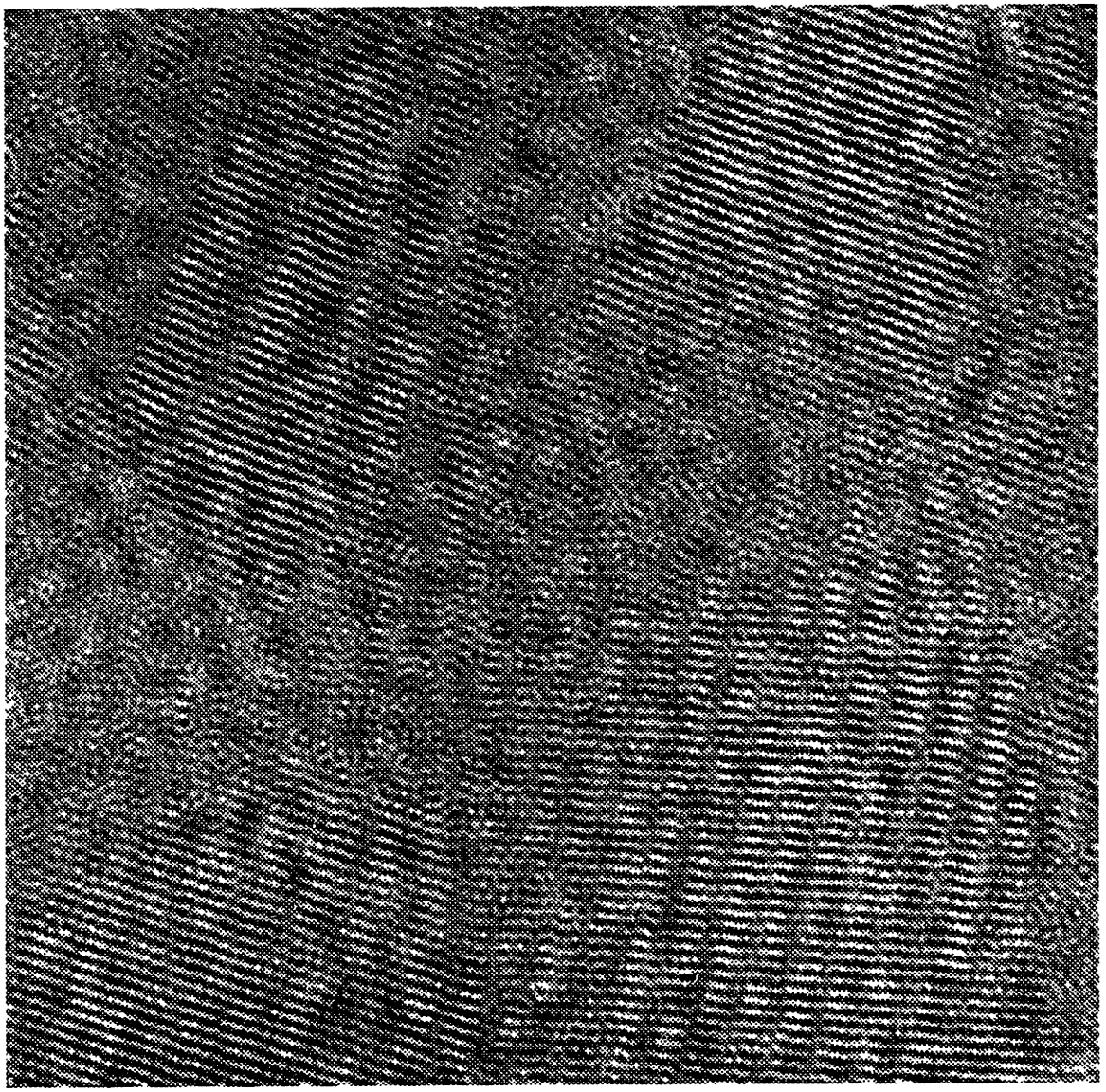

Following page

Figure 2.13: Low magnification LVHRSEM image of the surface of a particle of OsteoGraf/LD300™.

Figure 2.14: LVHRSEM image of OsteoGraf/LD300™ showing the constituent crystallites.

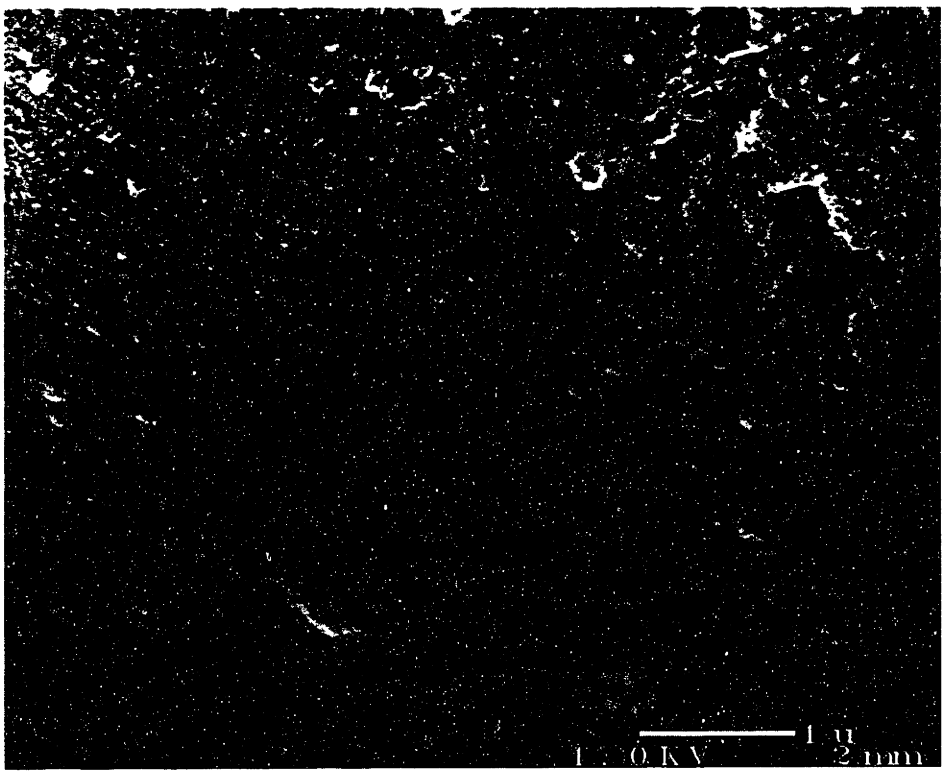

Figure 2.13

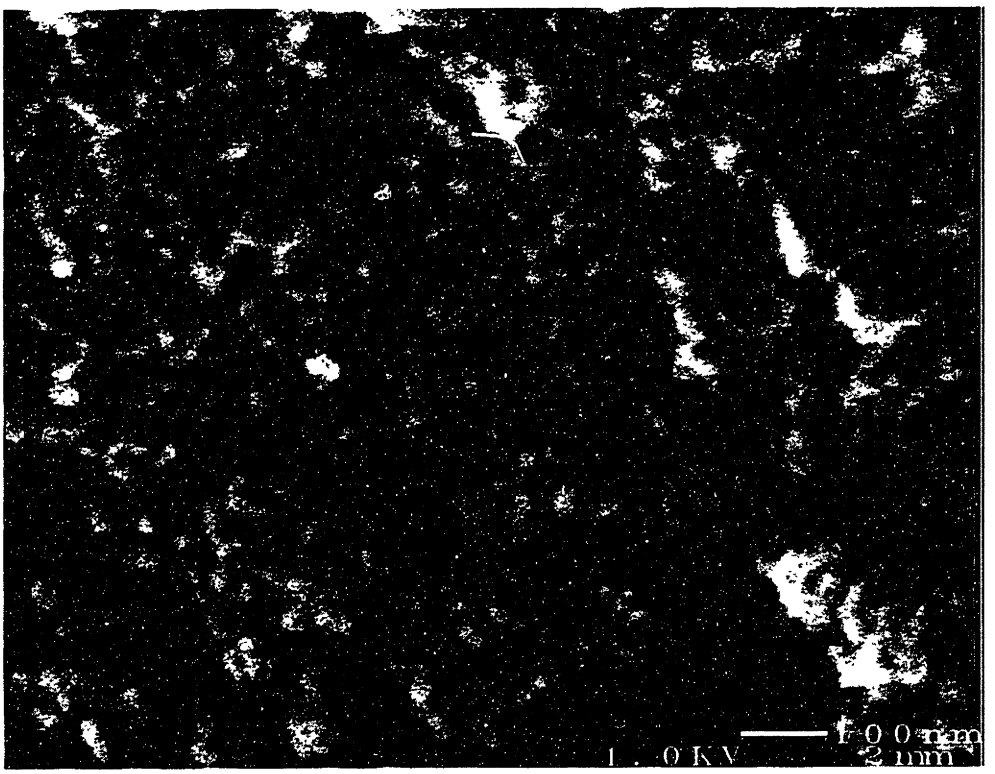

Figure 2.14

Following page

Figure 2.15 - TEM micrograph of OsteoGraf/LD300™, revealing that the material is composed of small crystallites arranged in a random network.

Figure 2.16: Low magnification LVHRSEM image of the surface of a particle of OsteoGen™.

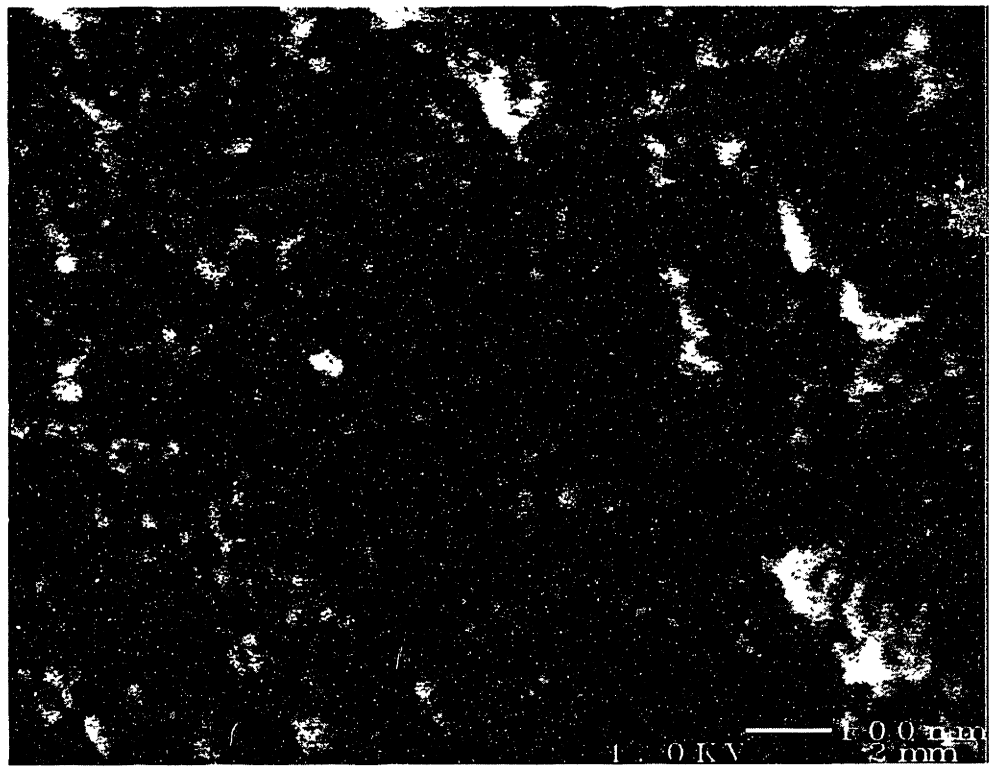

Figure 2.15

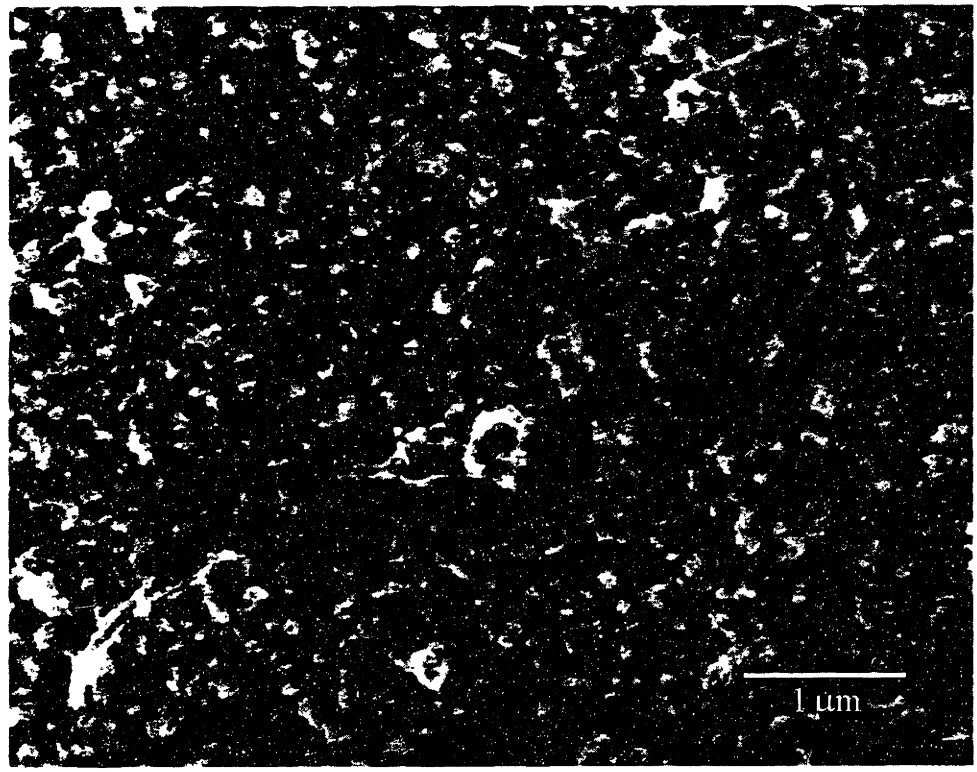

Figure 2.16

Following page

Figure 2.17: LVHRSEM image of OsteoGen™ showing the constituent crystallites.

Figure 2.18: TEM image of OsteoGen™, showing isolated linear arrangements of crystallites (arrows).

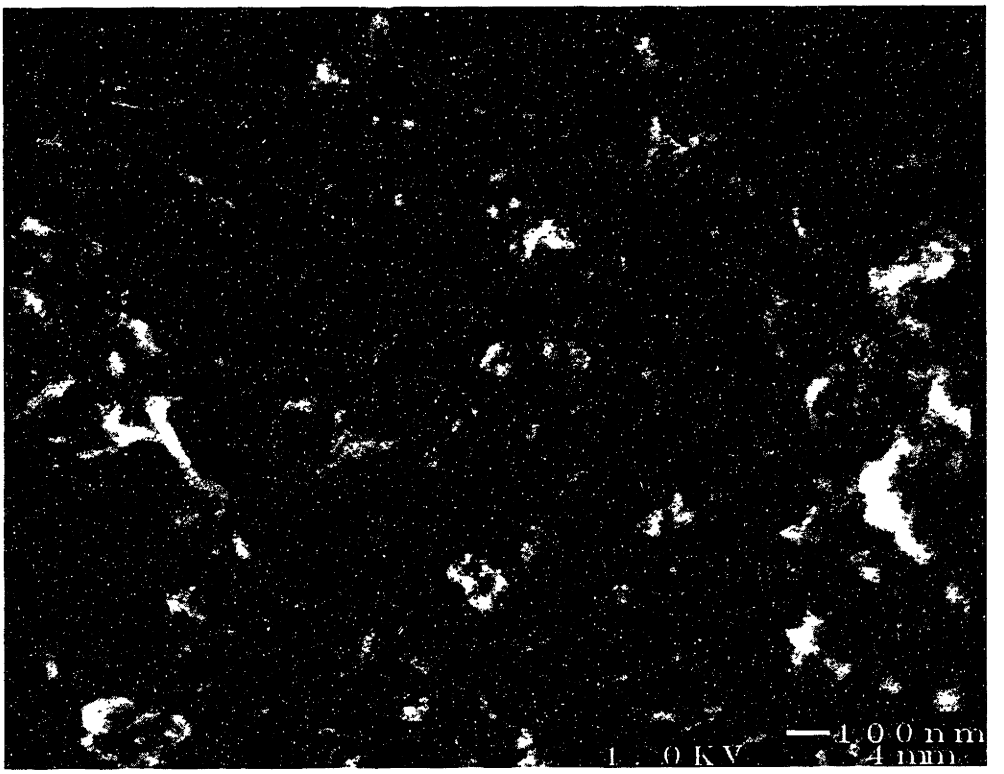

Figure 2.17

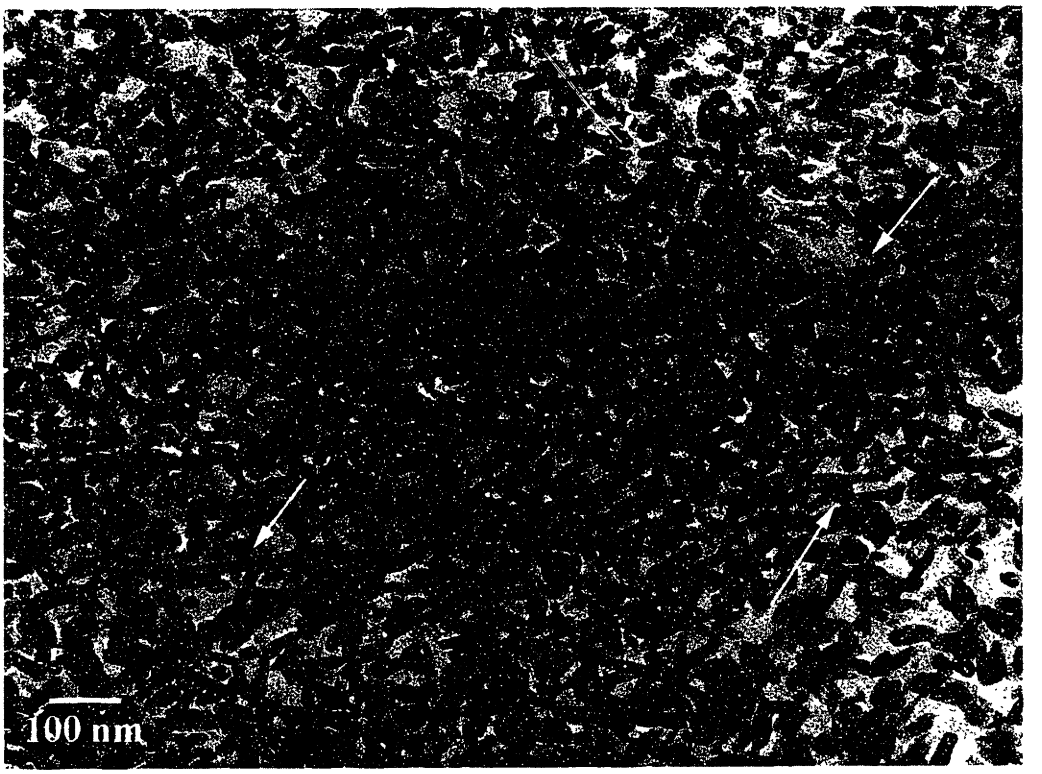

Figure 2.18

Following page

Figure 2.19: TEM image of OsteoGraf/LD300™ and SAED pattern showing rings corresponding to (002) and (211) (inset). The arrows indicate crystallites which exhibit facetting.

Figure 2.20: TEM image of OsteoGen™ and SAED pattern showing rings corresponding to (002) and (211) (inset). The arrows indicate crystallites which exhibit facetting.

Figure 2.19

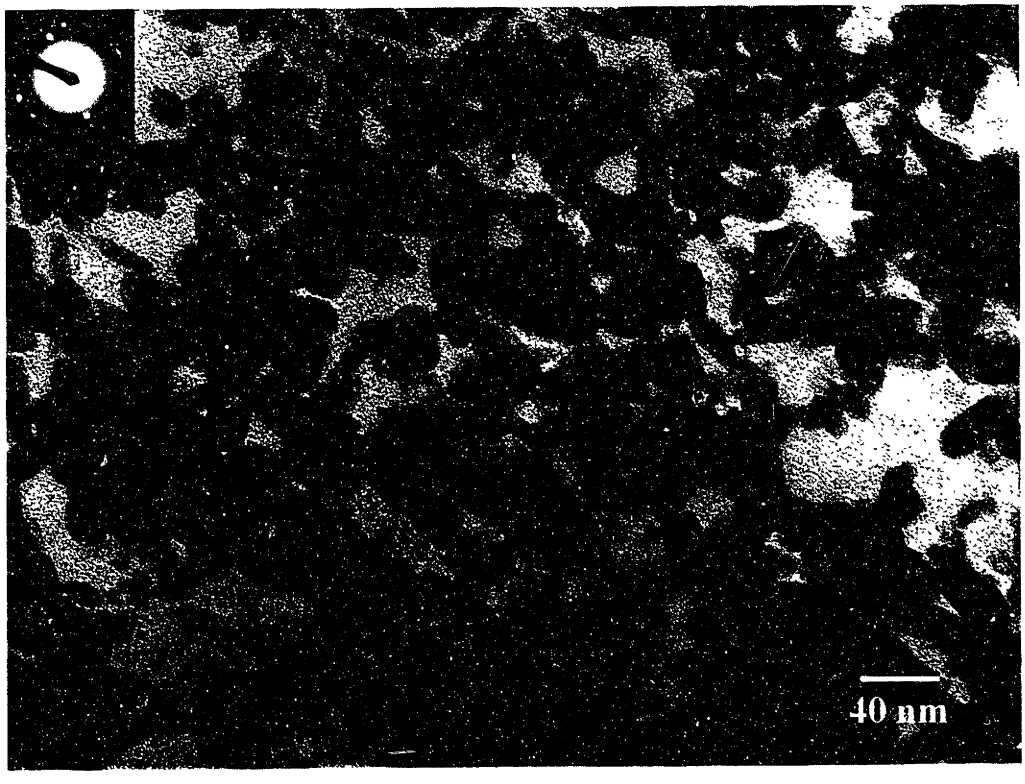

Figure 2.20

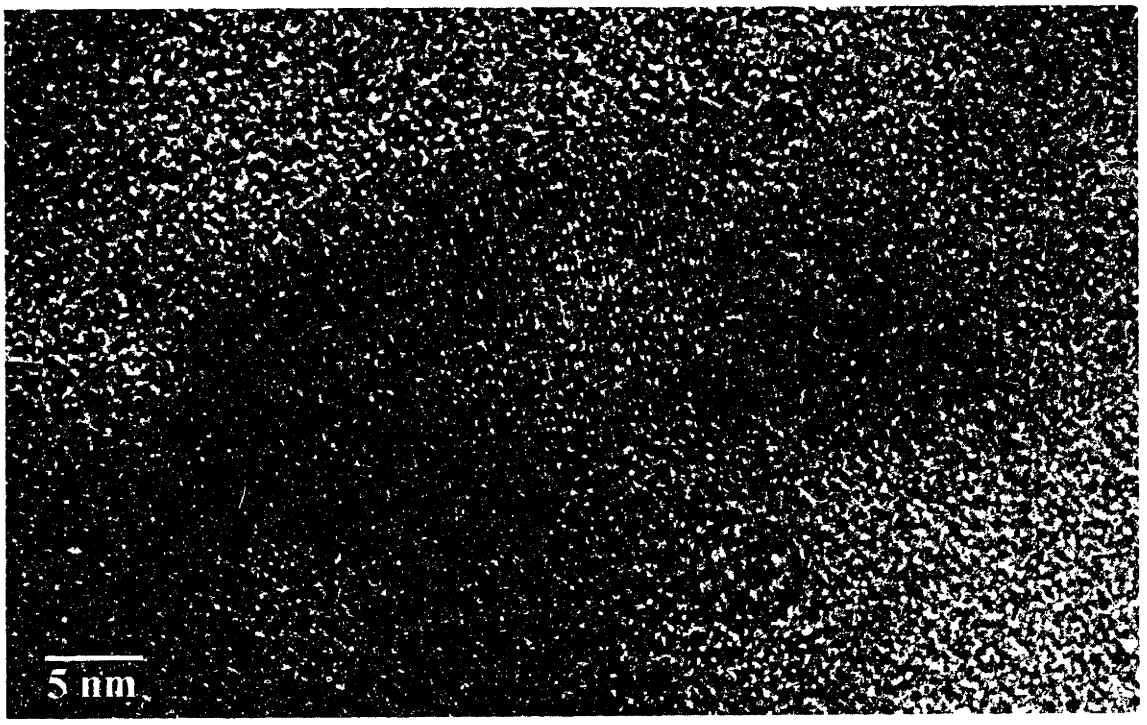

Figure 2.21: HRTEM image of an OsteoGraf/LD300™ crystallite, showing (002) lattice fringes running perpendicular to the long axis of the crystallite.

Figure 2.22: HRTEM image of an OsteoGen™ crystallite, showing (002) lattice fringes running perpendicular to the long axis of the crystallite.

Chapter 3

Bone Adhesion to Hydroxyapatite Coatings

3.1.1 Bone bonding to calcium phosphate coatings

Biological apatite deposition has been observed on a variety of calcium phosphate ceramics *in vivo*, including hydroxyapatite (HA) and β-tricalcium phosphate (β-TCP) in both osseous and non-osseous sites [113]. These deposits are not seen on sintered HA particles within 7 days of implantation, but within 10 days both a surface apatite layer and small calcification globules can be observed [114]. Mineral deposits are also observed within hours of implantation of PSHA-coated (PSHA) rods in cancellous bone [115, 116]. The globular deposits of apatite crystallites observed on PSHA are similar to those observed in mineralizing cartilage [117].

After 2 weeks, 85% of the surface of PSHA-coated Ti-6Al-4V rods implanted in cancellous bone is apposed by bone [118]. Bone also proliferates over the surface of rods implanted in cortical bone within 3 weeks [119]. An intervening layer of organic material sometimes appears between sintered HA and bone [120, 121]. Other groups report a collagen-free transition layer [122, 123], and some see direct attachment of the bone to the HA without an intervening layer [124]. Neo et al. report bone growth on sintered HA both with and without an intervening apatite layer [125]. The observed transition layer appears to be composed of proteoglycans, glycosaminoglycans, and apatite crystallites [121, 123]. Apatite crystallites have been observed as little as 20 nm from the HA surface [126].

The deposition of biological apatite and the formation of a bone/HA bond seem to depend on the dissolution of the coating and the reprecipitation of carbonated apatite [123, 127-129]. The degree of dissolution/reprecipitation observed is a function of both the composition and the degree of crystallinity of the surface [114, 127]. The rate of *in vitro* dissolution and reprecipitation decreases with increasing crystallinity [127]. Cell cultures on plasma-sprayed HA coatings of differing crystallinities displayed increased biological mineralization in conjunction with reduced crystallinity [130]. However, the predictions of the *in vitro* solubility and precipitation tests do not always correlate with observations during experiments conducted *in vivo*. Apatite deposition is observed on relatively crystalline materials such as sintered HA, and *in vivo* tests showed no significant difference in the interfacial shear strengths of sintered and PSHA coatings [114, 131]. Indeed, solubility may not necessarily relate to bone bonding *in vivo*; tetracalcium phosphate is significantly more soluble than plasma-sprayed hydroxyapatite, yet they have similar bone bonding potential [132, 133]. Heat treatment tends to increase phase purity and decrease solubility, but a heat-treated PSHA rod actually exhibited increased bone apposition at 12 weeks with respect to untreated rods [134-138].* There may be other mechanisms by which crystalline materials can stimulate precipitation besides calcium and phosphate ion release, and there is some evidence that bone bonding may depend more on precipitation onto a calcium phosphate-based (Ca/P) coating [114, 132].

The mechanism by which dissolution accelerates bone apposition to Ca/P coatings is not known in detail. However, the commonly proposed theory that the extra supersaturation resulting from dissolution may accelerate precipitation of carbonated apatite from solution is unlikely, especially as HA typically does not induce calcification in non-osseous sites [139]. Instead, the calcium and phosphorous released from the implant is quickly diluted by the surrounding fluid [129]. However, nearby cells may acidify the

* It should be noted that this may only be true for low temperature heat treatments of HA, which degrades at temperatures greater than 850°C [51, 53, 137].

local environment in response to the increased concentration of calcium and phosphate, promoting the dissolution and reprecipitation of HA [140].

Surface roughness may also have an effect on the integrity of the bone/coating interface by facilitating mechanical interlocking between the bone and the grooves (either nanoscale or microscale) of the coating. This is certainly the case for metallic implants -- grit-blasted cpTi implants tend to promote bone apposition, while polished implants induce fibrous encapsulation [141]. Increasing roughness increases the amount of bone apposition, especially in combination with acid etching [142]. However, this does not indicate a simple effect of smooth versus rough surfaces -- cells cultured on smooth polystyrene produced more mineralized tissue than on roughened polystyrene [143]. The mechanical strength of the interface of bone with HA-coated titanium was not significantly different than that with a rough titanium surface, although the coating did increase the amount of bone apposition [144]. Another study comparing PSHA to arc-deposited titanium showed similar results [145]. On the other hand, HA coatings do seem to increase bone ingrowth and interfacial strengths in both porous and textured titanium implants [9, 146, 147].

One theory is that HA increases initial bone apposition and ingrowth through chemical interactions, but the mechanical interlocking between the implant and bone provides a much stronger interface [148]. The idea of a chemical effect is also supported by observations that the interfacial strengths of bone with HA and alumina are the same at 12 weeks but that HA leads to a stronger bond at 4 weeks [149]. Interestingly, in the same study, no significant differences were seen between sintered and plasma-sprayed HA implants, despite an order of magnitude difference in surface roughness [149]. That highly crystalline HA does not exhibit degraded osteoconduction with respect to more soluble HA materials indicates that it may act as a mechanical template, even on the micrometer scale, for new bone and not only as a chemical promoter of bone growth [9, 149]. Some go so

far as to say that mechanical interdigitation on the 1-2 micrometer scale is the only contributor to bone bonding and that there is no chemical bonding at all [150].

Nevertheless, HA does not appear to be required for bone bonding, and several groups report bone apposition to the surface of metallic implants. Depending on the shape of the implant, bone apposes between 40 and 70% of the surface of the titanium 5 months post-implantation [151]. Others observe bone apposition to transcortical cpTi-coated polycarbonate implants with an intervening 20 nm thick collagen-free layer of proteoglycans [152-154]. An intervening "electron dense" layer between implant and bone similar to those observed on ceramic implants is also observed on commercial cpTi dental implants [155]. This layer is about 50 nm wide and is composed of mineralized tissue. However, others report direct apposition of mineralized collagen to cpTi implants in a transcortical model [156, 157]. Nevertheless, Jansen et al. suggest that a very precise interference fit between the implant and the bone is required to achieve direct bone apposition to the implant. For this reason, they recommend the use of coated implants, which can induce bone growth over a small bone-implant gap [157]. However, other groups find that cpTi implants in cortical bone show reduced interfacial shear strengths in comparison to ceramic coated implants and observe a layer of fibrous tissue, possibly scar, between the bone and the implant [119, 154].

Bone bonding to titanium appears to depend on both the time scale observed and surface finish. Steinemann et al. measure tear-off forces three months after both rough and porous Ti was implanted comparable to the compressive strength of trabecular bone. However, they note that interfacial strengths do not increase until after three months. Indeed, for the first 20 days after implantation, the interface with porous coated titanium has no mechanical strength, and other stabilization is required for the system [158, 159]. This time delay supports the theory that HA chemically promotes early deposition of bone matrix [157].

3.1.2 Plasma spraying and ion beam assisted deposition

A plasma is a high-energy, high-temperature (>20,000 K) phase including an appreciable amount of ionized atoms. For coating, a plasma is generated in a small cylindrical chamber with an anode at one end and a cathode at the other. As electrons are accelerated through the chamber, they collide with gas atoms which are being pumped into it, ionizing the atoms. The additional electrons contribute to the process, increasing the conductivity of the gas. This induces a discharge between the electrodes, further increasing current flow. The ionized atoms move towards the anode, which has a small orifice. As the plasma emerges, a powder is injected into it. The plasma both partially melts the particles and propels them towards the substrate, where they splat and cool [160].

A number of variables influence the morphology, composition, and microstructure of the coating. These include the powder size distribution and composition, gas pressure and plasma velocity, substrate angle and surface finish, and a number of other variables [160]. This experiment is not designed to test the effects of these variables. It should be noted that the company which sprayed the rods for this experiment has optimized its process to enhance several coating properties, including adhesion to the Ti-alloy substrate. Many researchers have also conducted studies on how to optimize the composition and interfacial strengths of the coatings [51, 53, 136, 137, 161-165].

The primary reason so much research has focused on coating techniques is that plasma-sprayed coatings frequently do not adhere to the underlying substrate. The strength of the HA/bone interface is meaningless if the HA coating is not adherent to the substrate. In addition to modifications of the PS coatings, a number of researchers have investigated other coating techniques, including arc and pulsed-laser deposition [148, 166]. One technique which has recently been adapted for HA is ion-beam assisted deposition (IBAD).

IBAD coatings have increased interfacial strengths with respect to PSHA coatings but can be prepared with similar compositions [167].

The principle behind IBAD is that ion bombardment of a growing film changes the properties of that film. In this case, a plasma, similar to that generated during plasma spraying, is generated in a small chamber. It leaves the chamber through a mesh grid which spreads the beam and is incident on the same target as the deposited material. The coating can be deposited through a variety of methods; electron beam evaporation and ion beam sputtering are the most common. The incident ion beam interacts with the newly-deposited material in several ways. The ions can collide both elastically and inelastically with the adatoms (deposited material), causing physical displacement and electronic excitations. The ion beam has enough energy to sputter the coating, reducing the deposition rate. It can produce localized composition gradients, disorder precipitates, or intermix deposited layers. For some materials below a critical temperature, amorphization can result. Defect generation resulting from the incident ion beam can also modify the local composition [168].

These interactions have several effects on the coating. Coatings produced via IBAD are denser than conventional coatings. The beam influences grain nucleation, growth, and texture and increases the width of interfacial amorphous layers in thin films. Importantly, the incident ion beam can modify interfacial stresses in the films by annealing out defects, relaxing stresses, and changing the impurity concentration in the film. In addition, it can increase the chemical bonding between the coating and the substrate. Both of these effects improve coating adhesion. IBAD also results in a smoother coating surface. Most of these effects can be related to displacement of adatoms, via sputtering or elastic collisions, by the ion beam [168].

The most important effect of the beam in HA coatings appears to be interfacial mixing during initial coating deposition [169]. This results in a large interfacial layer about

27 nm thick, compared to less than 1 nm for thermally deposited coatings [167]. IBAD-HA coatings have nearly twice the adherent strength of sputtered coatings and can be produced on as-received or even polished surfaces, without the need for grit-blasting the surface (see below) [167]. The as-deposited coatings are amorphous and incorporate some carbonate [167, 169].

3.1.3 Objectives

The mechanism of bone deposition on HA coatings has not been extensively investigated. One of the goals of this project is to elucidate a sequence of early bone deposition events. By characterizing the events at the surface of an PSHA-coated implant, we will clarify some of the design goals for future improvement of these implants whether by replacing the substrate with a more flexible material or by changing the HA deposition technique to increase the strength of attachment between the coating and the substrate. In addition, we will also compare the PSHA to other coatings.

As discussed above, surface chemistry and roughness both appear to play important roles in the deposition of biological apatite on a substrate [114, 170]. However, the nature of these roles has not been characterized, and the minimum amount of texture required for a given surface to be biologically recognized as "rough" has not been described. In this study, the chemistry and surface roughness of HA coated Ti-6Al-4V rods were varied independently. Comparison of completely smooth ("mirror finish") rods coated with HA to PSHA-coated rods enabled us to evaluate the effect of surface finish for a given surface chemistry. In addition, use of annealed PSHA rods enabled study of the chemical influences on bone apposition, independent of surface finish.

3.2 Preliminary Investigation

3.2.1 Preparation of samples including the bone/HA interface for TEM

A preliminary TEM study of bone apposition to PSHA was conducted using samples generated in a previous study for SEM observation. Of primary concern in this initial study was the development of a TEM preparation method which would include both the metal/HA interface and the HA/bone interface. Specifically, one goal of this study was to evaluate the feasibility of ion milling as a sample preparation technique for implanted rods. Of course, the initial mechanism of bone bonding to PSHA coatings was also of interest. Still, this study provided some initial insights into the complexity of TEM preparation of the cylindrical explants.

Several groups have used TEM to study the attachment of bone to HA *in vivo*. Many of these groups used blocks of various calcium phosphate ceramics, including HA and tricalcium phosphate; most, with the notable exceptions of Tracy and Doremus in 1984 and Jarcho in 1977, use a diamond knife or ultramicrotomy to achieve final sample thinning [113, 114, 124, 125, 171]. TEM sample preparation with an HA-coated metal rod is somewhat more difficult, and most groups studying these systems either used light microscopy exclusively or separated the ceramic/bone section of the sample from the metal by cryofracture or by sawing the desired area out of the specimen [10, 119, 132, 151, 170]. While studies of implants at later stages of bone development, greater than 3 or 8 weeks, show maturing bone which has commenced remodeling, studies at earlier time points do reveal deposition of bone matrix components [114]. At no time did any of these previous studies find fibrous material apposing the HA instead of bone.

3.2.2 Methods

ELI-grade Ti-6Al-4V rods (ASTM F136-92; "extra low interstitial"), 5 mm in diameter and 10 mm long, were plasma-spray coated with hydroxyapatite (BioInterfaces,

San Diego, CA). These were pre-treated according to the procedure described by Prabhakar and implanted in the medial aspect of the distal femur and the proximal tibia of two legs of 10 adult Beagle dogs, for a total of 40 implants [172]. There were two groups of dogs which were sacrificed either 6 or 14 days post-operatively. Implants in the contralateral limb of each dog were left in the leg for 3 hours or 2 days, respectively. After sacrifice, the implants were removed together with the surrounding bone intact and fixed in formalin. Undecalcified specimens were dehydrated in graded acetone solutions and embedded in poly(methyl methacrylate) [172]. These samples were cross-sectioned and mounted on acrylic slides for SEM. In addition, several unimplanted rods were embedded in Araldite resin and prepared for TEM.

The sample preparation technique was based on that developed by Lan Hoang and Bruce Pint. A trephine drill lubricated with 1000 grit SiC slurry was used to cut 3 mm grooves in the sections into which steel rings were attached using Hardman Green epoxy (Belleville, NJ). If the titanium fell out of the sample, as it did if the cross section was drilled completely through, the epoxy was also used to fill the gap. The resulting 3 mm discs were removed from the cross section by polishing the back (undrilled) side by hand on 320 grit SiC paper until the grooves were visible and then on 600 grit SiC paper until the samples were freed. Individual samples could then be prepared for TEM observation. A single sample was mounted drilled side up on a platen with crystal bond (Aremco, Ossining, NY) and polished by hand on 600 grit SiC paper lubricated with 1000 grit SiC slurry until the entire sample was visible. It was then polished to a 1 μm finish with 6 and 1 μm diamond pastes (Buehler, Lake Bluff, IL) on the back side of photographic film. A final polish on nylon improved the quality of the finish. The sample was then remounted polished side down and polished on 600 grit SiC paper lubricated with 1000 grit SiC slurry until it was 100 μm thick. It was then polished with 6 μm diamond paste as for the first side until it was about 50 μm thick and with 1 μm paste until it was between 30 and 40 μm

thick. Frequently, polishing had to be stopped before the final sample thickness was achieved to ensure sample integrity. A copper slot grid was attached to the sample with Hardman Green epoxy and the sample removed from the platen. The sample was then ion-milled to electron transparency on a Gatan Model 600 Dual Ion Mill operated at 6 kV and 1 mA. The sample was mounted on a cold stage which was thermally connected a liquid nitrogen. The stage kept the temperature of the sample close to room temperature during milling. In addition, the stage was inclined between 12 and 15 degrees to the argon plasma during milling. The samples were milled until the bone had been eroded back to the HA interface. The sample recovered 6-days post-implantation was prepared by Lan Hoang, a UROP (1993-1994) in the Hobbs group. One unimplanted HA specimen was ground using a tripod polisher and diamond papers, as described in Appendix A. It was not wedge polished; final thinning was performed in the ion mill (see Appendix A). Samples were coated with ~10 nm evaporated carbon prior to observation in the TEM. TEM and selected area electron diffraction (SAED) were performed on JEOL 200CX TEM operated at 200kV. Stereoimaging was performed by taking a series of pictures of the sample at approximately 5 degree intervals for a total rotation of 40 degrees. High resolution electron microscopy (HRTEM) was performed on an Akashi EM 002-B instrument operated at 200kV.

3.2.3 Results

Biological apatite deposits appeared as small clusters of crystallites, about 4 nm in width, on the HA surface within three hours of implantation (Figure 3.1). The crystallites were randomly organized, and the clusters had no definite shape. In general, the crystallites appeared needle-like in morphology, and stereomicroscopy confirmed mostly needle-like, as opposed to plate-like, crystallites. However, smaller, plate-like crystallites

were also observed (Figure 3.2). The crystallites did not appear to be directly associated with the apatite coating; the coating was not identified in the micrographs

As healing progresses, more needle-like crystallites were deposited on the surface, and the nodules became larger, denser, and somewhat circular in cross-section. By 6 days, fully developed nodules were observed both in isolation and in clusters, with an average diameter of 200 nm (Figure 3.3). The constituent crystallites were 3-10 nm wide and reach lengths of up to 70-100 nm. Diffraction pattern for these samples included the 211 rings typical of hydroxyapatite.

At 14 days post-implantation, both the nodular networks and more oriented networks were observed. The nodular networks observed were about the same size at those observed at 6 days . The oriented networks (Figure 3.4) were much more extensive, exceeding 800 nm in length, but incorporated crystallites of about the same size. The diffraction pattern of this network at 14 days showed sharp rings corresponding to the 002, 211, and 410 reflections, indicating the presence of larger crystallites. In addition, the arc in the 002 rings indicates a preferred orientation of the crystallites along the **c** axis typical of apatite crystallites.

In order to obtain additional information about the crystallinity of the biological apatite, we used high resolution TEM to image the crystalline lattice fringes. Figure 3.5 shows (211) lattice fringes in the plasma spray coating on the controls. Figure 3.6, taken from a 3 hour specimen reveals the crystallinity of the fibrils. The figure shows two crystallites, exhibiting (002) and (300) lattice fringes.

TEM of the unimplanted controls showed no fiber-like crystallites similar to those observed in the implanted samples. Individual grains or splats appeared to be 200-300 nm across. In some grains, (100) lattice fringes were observed (Figure 3.7). Almost all the samples exhibited extensive electron and ion beam damage in the form of voids. In Figure 3.7, the voids observed within these coatings are bounded by (100) lattice fringes. The

hexagonal shape of some of the voids indicates that they may also be bounded by (110) planes in the HA lattice. That the voids exhibited facetting typical of the HA system indicates that they may be amorphized areas within the coating [173]. In the implanted specimens, areas extending over at least 350 nm and exhibiting lattice fringes corresponding to (111) planes were also observed, showing that extensive areas of the coating remain intact after short implantation times.

In order to better define the morphology of the individual crystallites, we tilted the sample in the electron microscope and obtained micrographs at various orientations. We then viewed pairs of micrographs in a stereoviewer. During tilting, the projection of some of the fibers remained relatively constant, indicating a needle-like morphology. Others displayed altered projected widths, indicating a more plate-like morphology. While the fibers were certainly not cylindrical, the two short dimensions did not appear to be very different. The 3D structure of individual crystallites was difficult to distinguish in the stereoimages; however, when traced outlines of the crystallites were superimposed on each other, it was evident that the apparent orientation of the crystallites with respect to each other changed as the sample was rotated, confirming the observations made in the stereoimages.

3.2.4 Discussion of preliminary results

SEM observations of these samples showed that only 20% of the HA surface was apposed by bone at 6 days. At 14 days, the apposition peaked, with about 80% of the surface in contact with trabecular bone [118]. However, our TEM observations show that mineral deposition is not a strictly linear process which proceeds uniformly over the entire implant surface. While organized, parallel networks of biological apatite are not observed until 14 days post-implantation, the initial globular apatite deposits continue to be observed

in samples from 3 hours to two weeks after implantation. Mineral deposition is continually initiated at sites along the implant surface, even as mature bone develops at other sites.

Both the crystallites and the nodules have the same size and shape as those in the initial apatite deposits in mineralizing cartilage. In contrast, initial mineral deposits in type I collagen in bone tend to nucleate as plate-like crystals in the hole zones of the collagen. While our TEM samples were unstained, these data seem to imply that the original deposition at the surface of the implant is not mediated by type I collagen. This conclusion is also supported by observations of a collagen-free electron-dense zone between HA-containing implants and bone [122, 123]. Moreover, previous immunohistochemical studies in our group have shown that at 6 days post-implantation, the coating-bone interface stains selectively for fibronectin, laminin, and collagen Type IV, proteins associated with wound healing. Less staining is observed for osteopontin and vitronectin, proteins associated with the organic matrix of bone [115]. The deposition of apatite at the surface appears to coincide with the inflammatory and initial wound healing response at the implant site, preceding the migration of osteoblasts and the production of collagen.

The ion-mill protocol summarized here was designed to minimize thermal and radiation damage to the sample. Radiation damage in both the TEM and the ion mill is exhibited by void formation in the sample. The cold stage keeps the sample at about 0°C during milling. While ion-milling under these conditions did not damage the samples significantly, ion-milled material tended to sputter back on to the samples. As one might expect, poorly crystalline bone, ceramic HA, and metallic titanium mill at different rates. The bone tended to mill out of the sample and the titanium did not mill significantly. Moreover, this technique has several other drawbacks. The preliminary polishing steps are not particularly efficient. Typically, only one sample can be prepared per week, and about half of the samples which were attempted for this study had to be discarded or showed nothing of interest in the TEM. Most notably, no satisfactory samples were prepared from

specimens recovered two days post-implantation. In addition, the titanium tended to fall out of the sample during preparation. When it was not lost, the Ti and the softer regions of the sample tended to polish at different rates, leading to gouging in the bony areas of the sample. Perhaps most importantly, the limited electron transparent area in the samples prevented identification of the HA/bone interface. While a variety of interesting features was observed, their proximity to the HA coating could not be determined.

In summary, biological apatite begins depositing within three hours of implantation of plasma spray coated HA, suggesting a role in modifying the surface for bone bonding. The nodular aggregates of apatite recall the initial calcium deposits in mineralizing cartilage. The small bundles of apatite fibers develop into mature bone over time, and this phenomenon can be observed in TEM samples prepared by ion-milling instead of microtomy. However, ion milling is not a very useful technique for the preparation of large numbers of implants for TEM observation.

Following page

Figure 3.1: TEM image of PSHA-coated Ti-6Al-4V recovered three hours after implantation in canine trabecular bone.

Figure 3.2: TEM image of PSHA-coated Ti-6Al-4V recovered three hours after implantation in canine trabecular bone, showing biological apatite crystals oriented both on edge (needle-like morphology) and parallel to the plane of the sample (plate-like morphology).

Figure 3.1

Figure 3.2

Following page

Figure 3.3: TEM image of PSHA-coated Ti-6Al-4V recovered six days after implantation in canine trabecular bone.

Figure 3.4: TEM image of PSHA-coated Ti-6Al-4V recovered two weeks after implantation in canine trabecular bone. The diffraction pattern shows arcs corresponding to (002) and rings corresponding to (211) and (410), indicating the presence of larger crystallites exhibiting a preferred orientation.

Figure 3.3

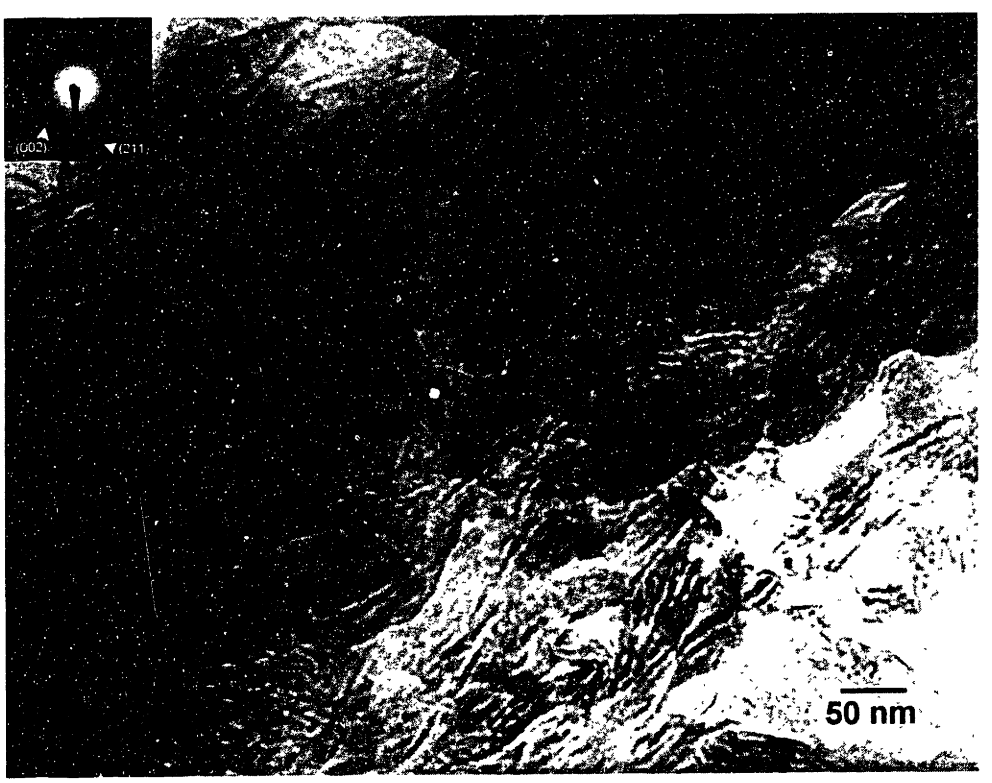

Figure 3.4

Following page

Figure 3.5: High resolution TEM image of the PSHA coating on Ti-6Al-4V, including the (211) lattice fringes.

Figure 3.6: High resolution TEM image of apatite crystallites deposited near a PSHA-coated Ti-6Al-4V rod three hours after implantation in canine trabecular bone. The white arrows indicate the (002) lattice fringes (3.41 Å); the black arrows indicate (300) lattice fringes (2.72 Å).

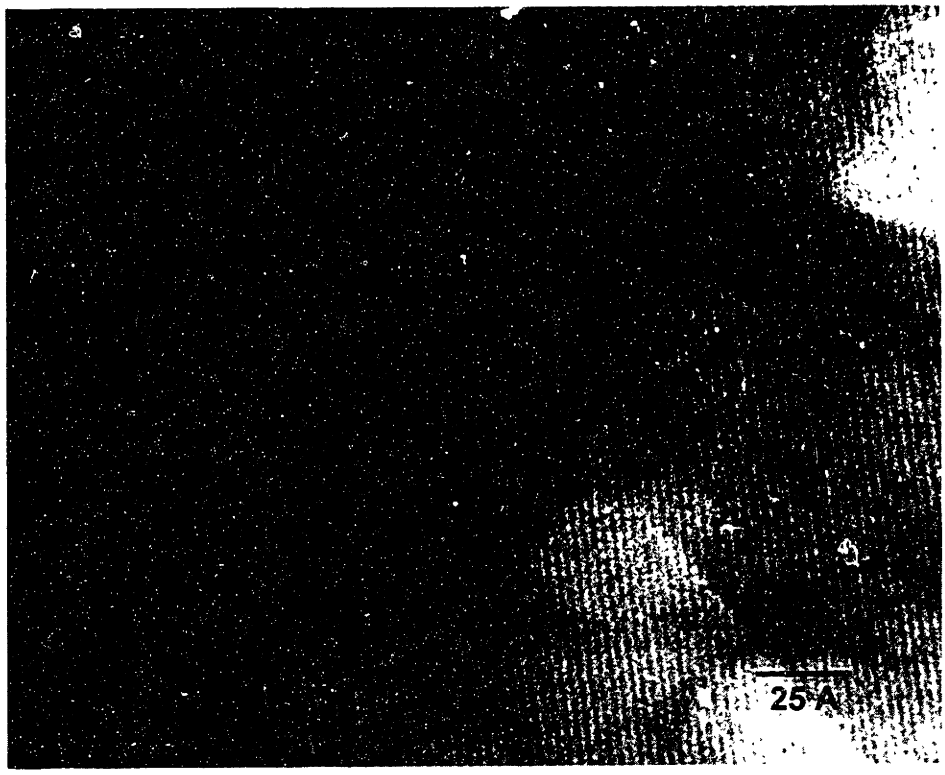

Figure 3.5

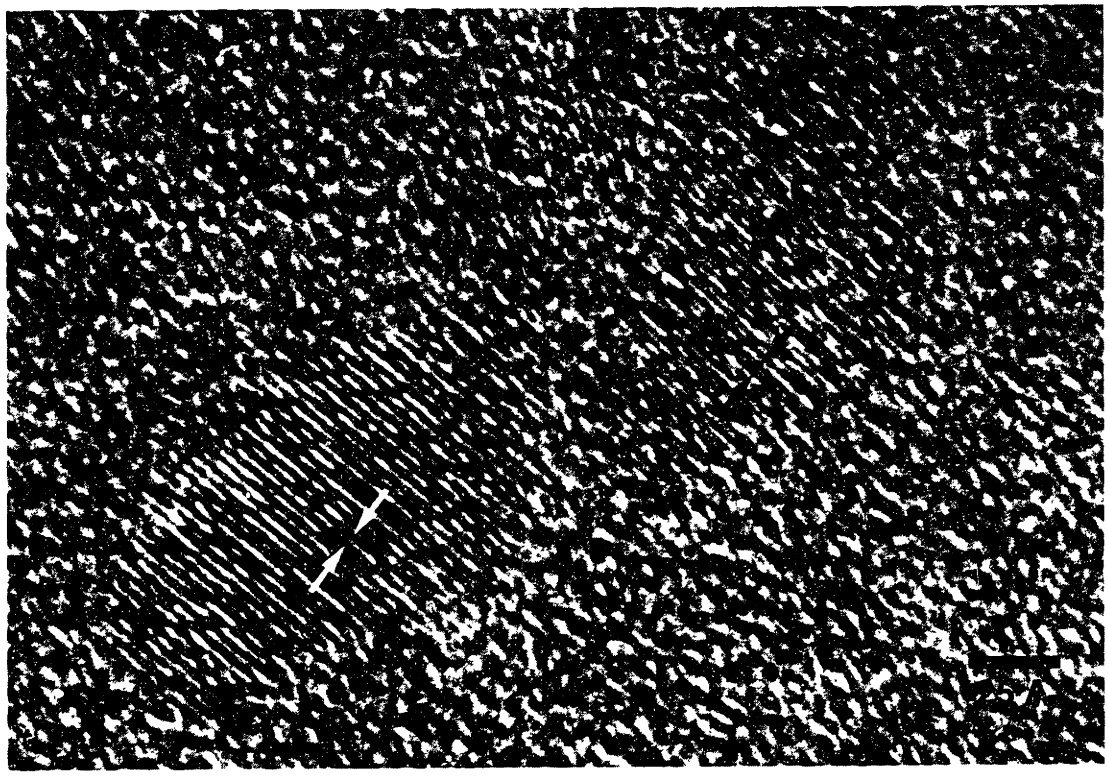

Figure 3.6

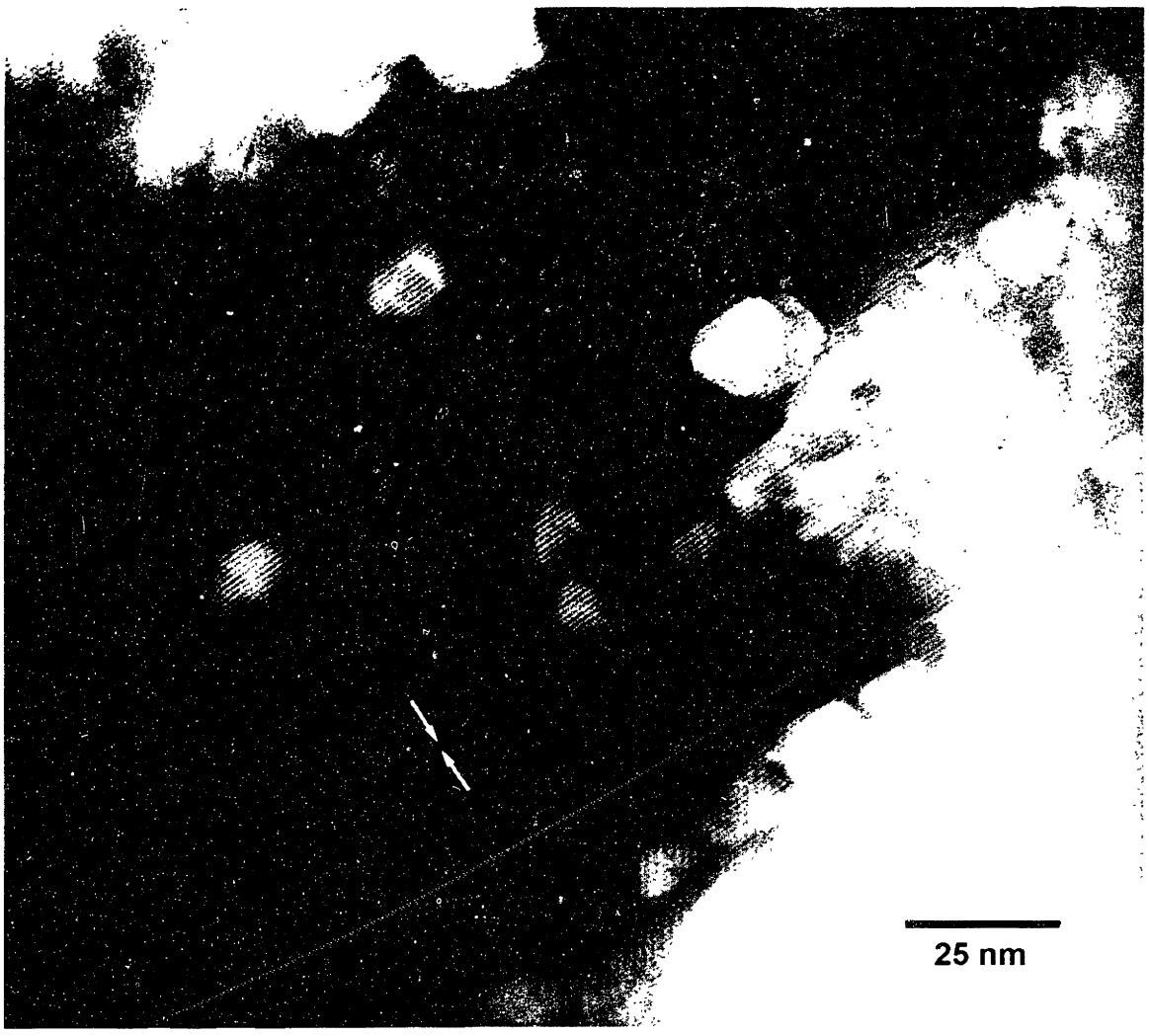

Figure 3.7: TEM image of the PSHA coating on Ti-6Al-4V. The voids present (black arrows) are bounded by the (100) lattice fringes (white arrows).

3.3 Materials

3.3.1 Preparation of implant materials

Ti-6Al-4V ELI grade (ASTM F136-92) rod 6.41 mm in diameter was obtained from Titanium Industries (Parsippany, NJ). This was machined into 12.5 mm long rods for plasma-spraying. The rods were plasma sprayed by Bio-Coat, Inc., (Southfield, MI) except for a 3-4 mm length at one end, which was left uncoated. Some of the plasma spray rods were later annealed in air to increase the coating crystallinity. The rods were stood on end in a crucible in a furnace which was ramped from room temperature to 600°C at 4 degrees/minute and held for 42 minutes (0.7 hours). The furnace cooled to 200°C after about 4 hours, at which time the furnace door was left ajar until the temperature reached 25°C.

Ti-alloy rod from the same source was also polished in preparation for HA coating via IBAD. The rod was mounted in a lathe and polished with 360, 400, 500, and 600 grit SiC paper, followed by 2/0 and 3/0 SiC paper. A Dremel™ tool equipped with a cotton-tipped rod was used to polish the rod with 600, 800, 1000, and 1200 grit SiC grease. This left a long period irregularity (about 5 mm) in the surface of the material. A delrin bushing was used to mount the rod in a collet to protect the finish while the rod was being cut. The rod was cut into 12.5 mm cylinders, which were then cleaned in toluene and acetone and expressed to Dr. Fu-Zhai Cui, Tsinghua University, China, to be coated [167]. The rods were annealed in air at MIT; they were stood on end in a crucible in a furnace which was ramped to 400°C at 4 degrees/minute. The furnace was then cooled to about 200°C over three hours, at which time the furnace door was left ajar until the temperature reached 25°C.

Ti-alloy rods machined into 12.5 mm cylinders were also used as an uncoated control in this experiment. These were degreased and cleaned by sonicating in toluene, 1,1,2-trichloro-1,1,2-trifluoroethane, acetone, neat ethanol (twice), and distilled water (twice) for five minutes each.

Polyethylene cylinders 6.41 mm in diameter and 4 mm long were machined for use as spacers in the distal femoral sites. These were cleaned by a quick rinse in 1,1,2-trichloro-1,1,2-trifluoroethane, acetone, and water. They were dried under vacuum for several hours and sterilized in steam for 30 minutes.

All metallic implants were sterilized in ethylene oxide vapor for 12 hours.

3.3.2 Surface characterization

The percent crystallinity and calcium phosphate phases present were characterized by x-ray diffraction. A Rigaku RU-300 rotating (copper) anode diffractometer with 0.5 degree dispersion and scatter slits and a 0.3 degree receiving slit was used to collect XRD data. Typical spectra were read at 0.02° intervals at 2°/second. The HA phases in the coatings were identified. The total area under the spectrum trace between 2θ=25° and 36.5° was integrated. The area under the spectrum trace resulting from "diffraction" from the amorphous fraction of the material was identified and integrated separately. The ratio of these two areas is the fraction of amorphous material in the coating; subtraction from unity yields the fraction of crystalline material. Instead of wide angle XRD, glancing angle XRD (GAXRD) was performed on the IBAD-HA samples due to the thin nature of the coatings. A 5 mm height-limiting slit was used to reduce background. These data were not considered appropriate for calculation of percent crystallinity.

Surface roughness was determined quantitatively via profilometry. Roughness was measured in duplicate on three rods from each sample group on a Tencor P10 Profilometer. The scan speed was 5 μm/s, the sampling rate was 50 Hz, and a 45 μm waviness filter was used to smooth the data following collection. Data were collected over a 501 μm trace. All measurements were performed parallel to the axis of the cylindrical samples. The software which drives the profilometer can perform a variety of calculations on the data. However, it cannot perform calculations on saved data. Because the initial

calculations for most of the samples did not include one of total path length, the total distance traversed by the probe over the length of the scan, a statistical measurement of the path length was not possible. Instead, path length measurements from titanium alloy and an annealed PSHA-coated sample were used to approximate the path lengths for the uncoated and PSHA-coated samples, respectively, and the path length measurement from a polished Ti-alloy rod was used to approximate that for the IBAD-HA coated samples.

The actual surface area was calculated by squaring the path length measured via profilometry. This calculated surface area was actually normalized to a square, the sides of which were the length of the profilometry scan. The total area of the coated area of the implant was calculated using measurements of the length and diameter of the coated section of the rods; the actual surface area was calculated by multiplying this by the normalized surface area.

Qualitative observations of the coating surfaces were made in an Electroscan Model E-3 ESEM operated at 30 keV. Samples were left uncoated and were observed at relatively short working distances (2-4 mm) with a medium sized condenser lens (50 % total lens current).

Coating solubility was measured via a simple solubility test. Three rods from each sample set (IBAD-HA, unannealed IBAD-HA, PSHA, annealed-PSHA, and uncoated Ti alloy) were immersed in 0.05 M Tris (Tris(hydroxymethyl)aminomethane) (Sigma, St. Louis, MO) adjusted to pH 7.4 at 37°C. The buffer was prepared in distilled/filtered water (18 MΩ, Millipore filtration system). Ten microliter aliquots were removed after 15, 30, and 60 minutes and 1, 2, and 3 days. The 15 minute data were discarded because the samples became cross-contaminated during mixing.* These were combined with 1 mL of a standard reagent from Sigma to form a calcium-arsenazo III complex which could then be

* The directions from Sigma indicate that, after adding the sample, the reagent should be mixed by inversion and agitation. Agitation is sufficient; the samples should not be inverted unless capped cuvettes are being used.

characterized by UV-VIS spectrophotometry. Because of the small sample volumes, special 1 mL polystyrene cuvettes were used for spectrophotometry. Solutions were mixed in the cuvettes by agitation for 5 minutes, and all spectra were taken within an hour of collecting the aliquots. A Cary 5E UV-Vis spectrophotometer was used to determine the concentration of the calcium-arsenazo III complex. Spectra were read between 550 and 700 nm with respect to 50 mM Tris buffer; the intensity at 650 nm was used for calculations. The background was read with two empty cuvettes.

A standard from Sigma (2.5 mM Ca) was used to calibrate the spectrophotometer, and all measurements were compared to a blank (10 μL of 50 mM Tris in 1 mL reagent). The standard was diluted to 0.25, 0.50, 1.25, and 2.0 mM. A calibration curve was constructed by measuring the absorbance of the arsenazo III complex with 10 microliter aliquots from each of these solutions, in addition to aliquots of a blank (0 mM) and the undiluted standard (2.5 mM), and a 20 microliter aliquot of the standard (5 mM). Absorbance was measured with respect to water, and 18MΩ (filtered) water was used for all dilutions. The calibration curve was linear but flat; the absorbance for the 5 mM sample was not twice that of the 2.5 mM standard (Figure 3.8).

Even though the total volume of buffer decreased by 10 μL after every measurement, the concentrations were not normalized. The resultant error was less than 5%. In addition, the calibration curve was only measured once. The absorbance of the standard varied by less than 5% each day of the experiment, that of the blank by less than one percent.

The lower absorption limit of the polystyrene cuvettes is 340 nm. Sigma produces a reagent for measuring phosphorus in solution by UV-Vis spectrophotometry; the absorbance of these the reagent-phosphate complex (a molybdate complex) is measured at 340 nm. The cuvettes actually have significant absorbance at 340 nm; while it would be interesting to determine the amount of dissolved phosphorus, fused silica cuvettes should

be used to do the experiment. For this experiment, it was decided that the expense was not worth the potential data.

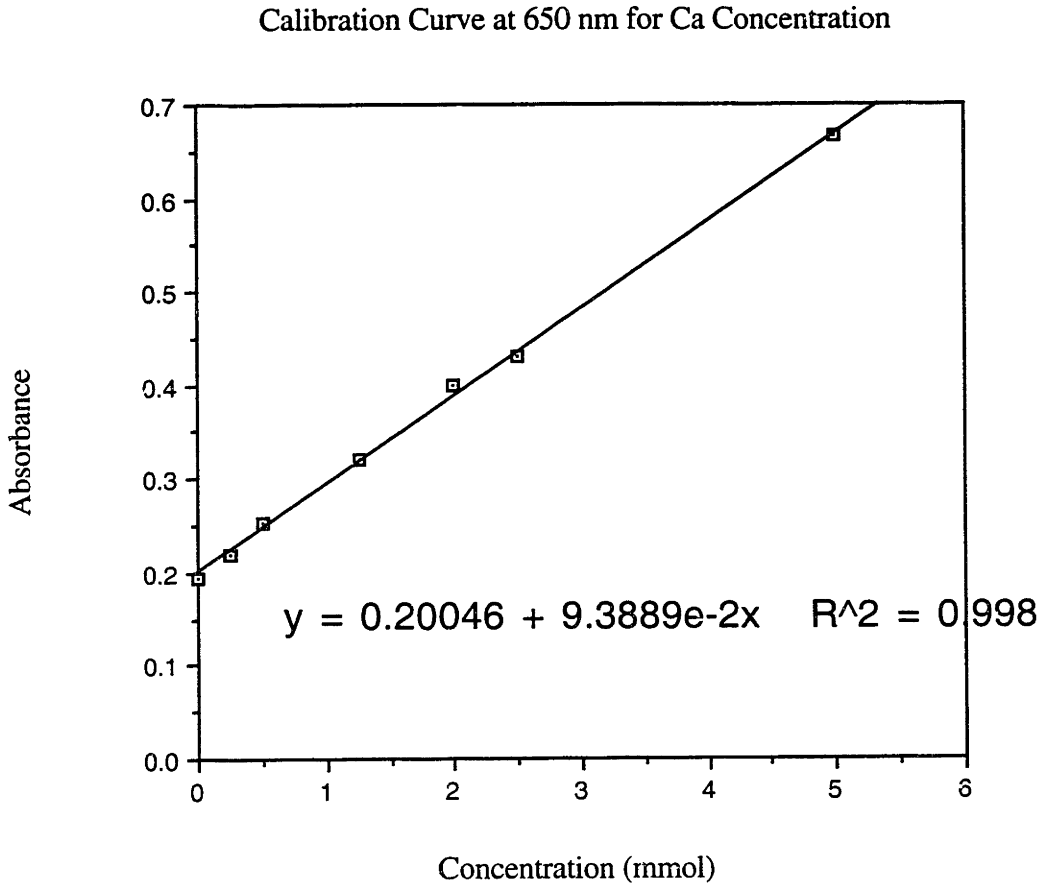

Figure 3.8: Calibration curve for absorbance of Ca-arsenazoIII complex at 650 nm.

3.3.3 Characterization results

Figure 3.9 shows a photograph of the four types of samples used in this experiment. The IBAD coating is very thin and appears only as an interference pattern on the surface of the rod. However, the difference in roughness between the IBAD-HA coated rod and the others is evident. The other interesting observation is the blue color of

the annealed PSHA rods. The uncoated surface of the Ti-alloy oxidized during annealing, resulting in a thin coating of a blue oxide, probably TiO_2+Al_2O_3. The annealed IBAD-HA coated rods were indistinguishable from the unannealed rods to the naked eye, and the time and temperature of annealing were not sufficient for significant amounts of titania to form.

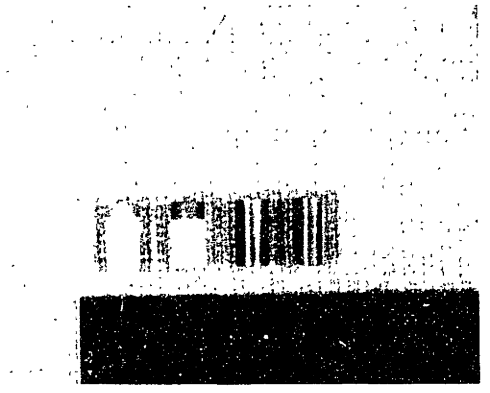

Figure 3.9: Photograph of HA-coated Ti-6Al-4V rods before implantation in canine trabecular bone From left to right, PSHA, annealed-PSHA, IBAD-HA, uncoated Ti-6Al-4V.

Figure 3.10 shows the roughness of the various samples used in this experiment. The roughness of the IBAD samples was not significantly different from that of the polished Ti-alloy rod precursors or following annealing ($p > 0.05$, Student's t-test). The IBAD rods were substantially smoother than materials used for "smooth" samples in other experiments, typically machine-finished titanium [170, 174]. In addition, the total coated areas of the PSHA-coated (2.4-2.5 cm^2) and IBAD-HA coated (2.6-2.7 cm^2) samples were not substantially different, despite the difference in surface roughness, because the entire length of the PSHA-coated rods was not coated.

The variation in roughness among the samples is also evident from ESEM observations of their surfaces (Figure 3.11). At lower magnification, the globular surface of the PSHA coated samples is a dramatic contrast to the tiny polishing tracks on the IBAD-HA coated rods and the machine marks on the uncoated Ti-alloy. Only at higher

magnification is the IBAD-HA coating evident as small globules approximately 200 nm across. The size of the globules is the same order of magnitude as the roughness, as measured by profilometry. It should be noted that the presence of discrete globules in the ESEM does not indicate that the coating is not continuous. Similar contrast can result from texture in the surface of the coating, which would lead to charging of the small ridges along the samples. The only other notable feature were the cracks in the PSHA coatings. Cross-sectional ESEM views of the samples did not reveal whether they extend to the alloy surface; it is likely that if they did, they would take a more tortuous, three-dimensional route than could be imaged on a two-dimensional cross-section.

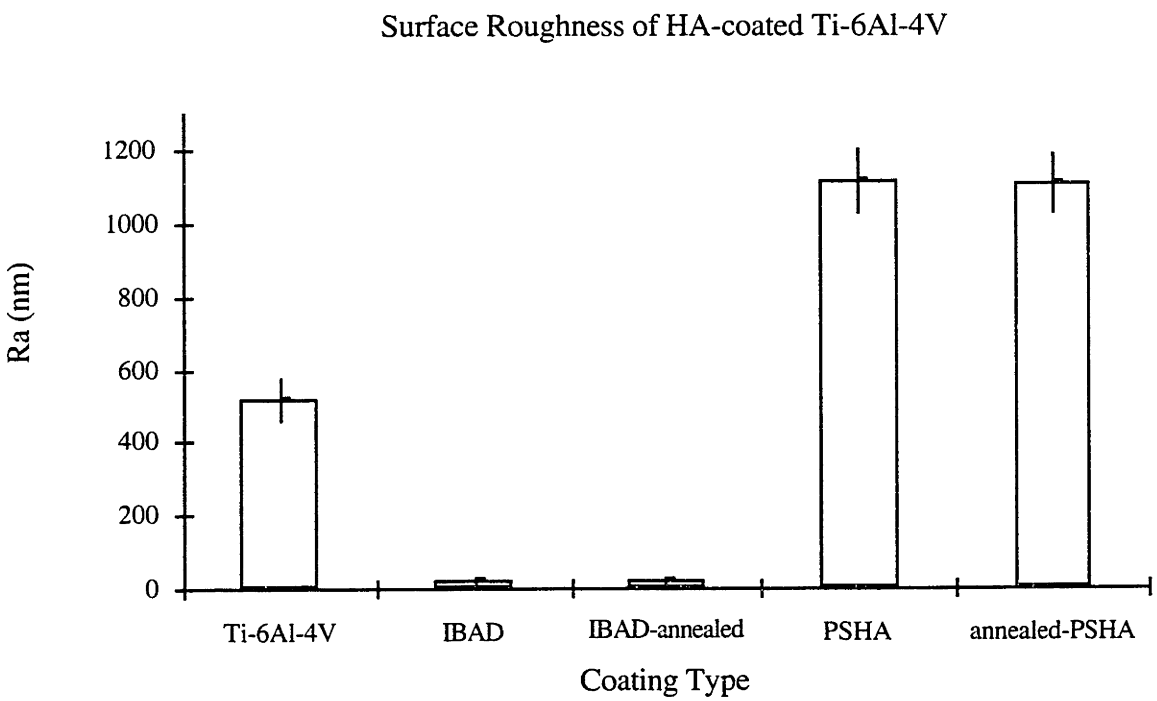

Figure 3.10: Roughness of HA coated rods used in *in vivo* bone bonding experiments and *in vitro* solubility experiments. The error bars indicate standard deviation, n=3.

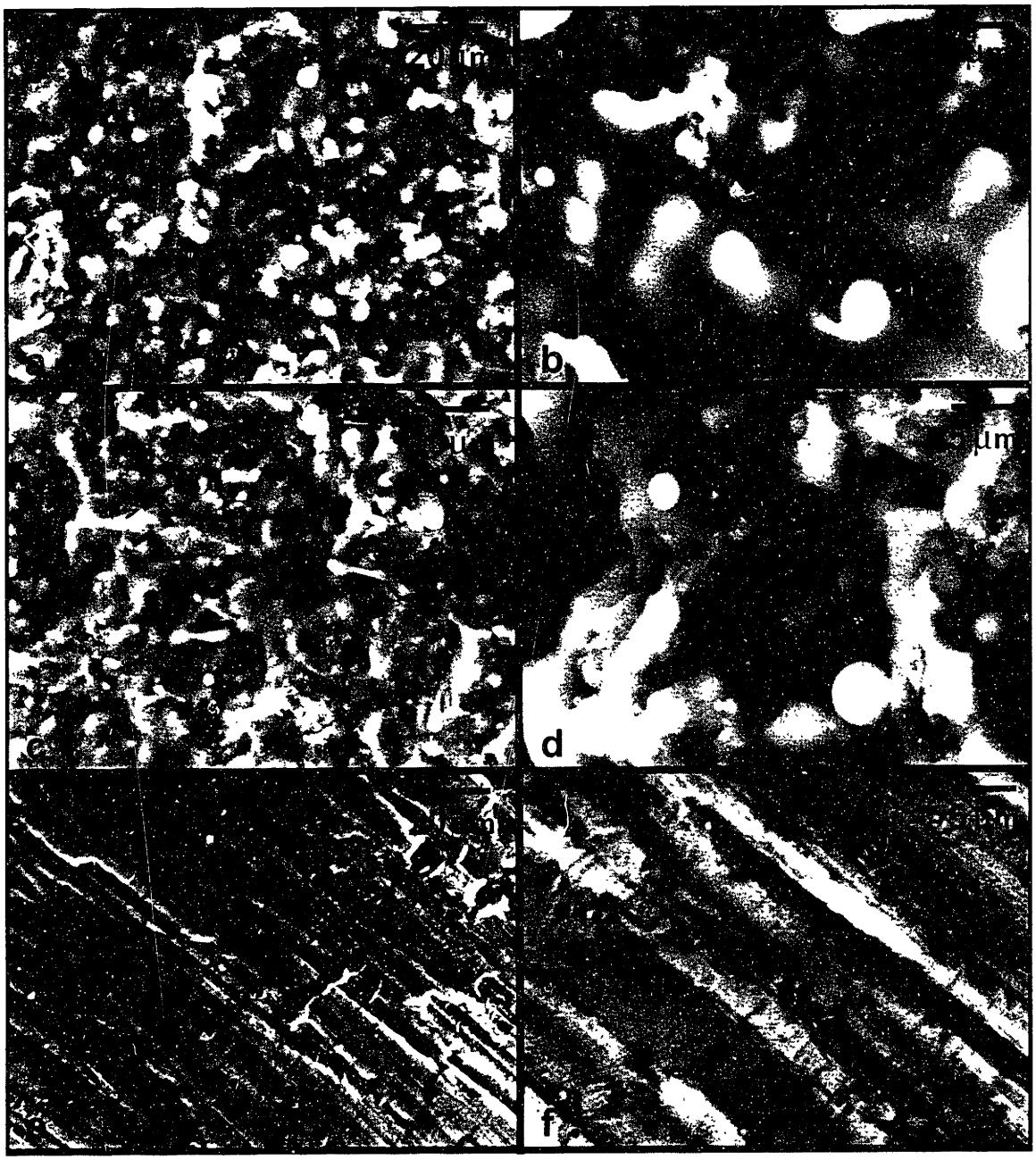

Figure 3.11a: ESEM micrograph of the surfaces of some of the implants used in this experiment: a,b)PSHA; c,d)annealed-PSHA; e,f)Ti-6Al-4V.

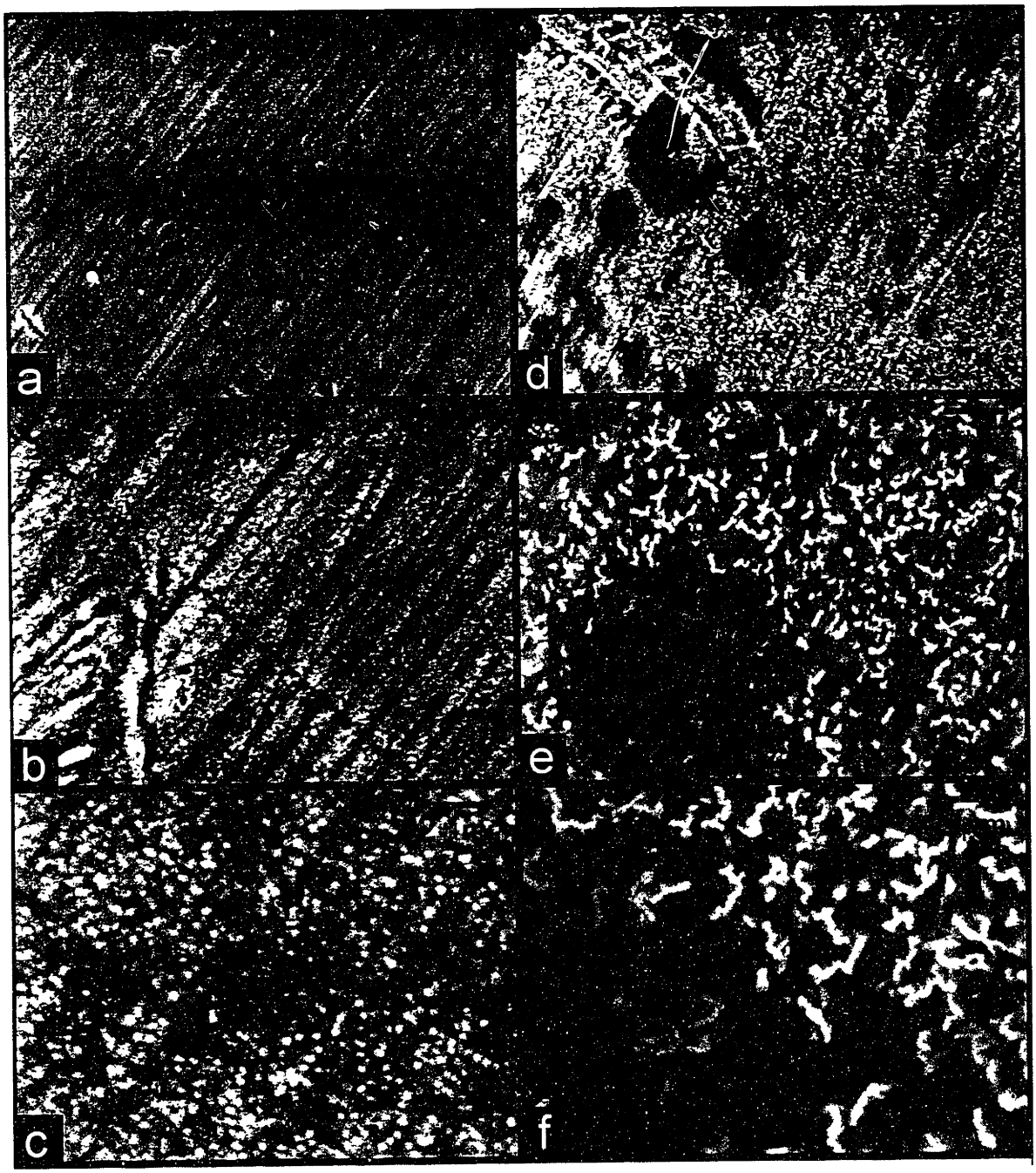

Figure 3.11b: ESEM micrographs of the surfaces of the unannealed (a,b,c) and annealed (d,e,f) IBAD-HA coated rods used in this experiment. The areas indicated by * in (b) and (e) are enlarged in (c) and (f), respectively.

After annealing, the PSHA samples did not look significantly different in the ESEM, although they were significantly more crystalline (Student's t-test, $p < 0.05$, n=3) according to XRD measurements (69.7 +/- 4.8% crystalline before annealing versus 91.9 +/- 1.4% afterwards) (Figure 3.12a,b). XRD spectra from both annealed and unannealed PSHA-coated rods show a small peak at 31° corresponding to β-whitlockite, a $Ca_3(PO_4)_2$ phase. In contrast, the surface of the IBAD-HA coated samples did change significantly, even though the surface roughness did not increase significantly ($p > 0.05$, Student's t-test). Unfortunately, it was not possible to reliably determine the percent crystallinity of the annealed IBAD-HA coated samples. However, glancing and wide angle XRD measurements did show the development of peaks at 32°, 32.3°, and 33.2°, corresponding to the (211), (112), and (300) reflections from HA. Before annealing, only a broad peak was observed in glancing angle XRD spectra, and there was no visible peak in wide angle spectra (Figure 3.13a,b). The high contrast features visible in the ESEM increased to about 1 μm in length, and there were large patches 5-20 μm across with lower concentrations of this feature, which also had duller contrast. As before, this does not indicate that the coating was not continuous.

In the solubility experiment, the initial quick release of calcium and subsequent plateau are expected from prior experiments in the literature (Figure 3.14) [128]. The unannealed IBAD-HA coating is supposed to be completely amorphous [175], yet the PSHA coatings released more calcium into solution. On the other hand, the low calcium release from the annealed IBAD-HA coatings reveal an effect of heat treatment on the solubility of the IBAD-HA coatings. In general, it appears that for the PSHA coatings, coating crystallinity has a small effect on coating solubility. The high variability in the release from the annealed-PSHA coatings is somewhat anomalous; the last point may result from the release of a large particle of the coating. The high surface area would promote

quick dissolution and raise the concentration of dissolved calcium more quickly than dissolution from the surface of the coating.

The low solubility of the annealed IBAD-HA coating was somewhat discouraging. It was hoped that the annealing protocol would result in a coating which showed Ca release characteristics similar to that of the unannealed PSHA coating. It unfortunately appears that this coating is much less soluble than either the unannealed or annealed PSHA coatings. Thus, in this experiment, the effects of surface chemistry and surface roughness were not tested independently.

Following the solubility tests, the rods were allowed to dry, and their surface roughnesses were measured as before. The surface roughnesses were not significantly different from those measured before the experiment, but the individual sample populations did exhibit a somewhat higher standard deviation.

Following pages:

Figure 3.12a: XRD spectrum from a PSHA coating on a Ti-6Al-4V rod before heat treatment; a broad peak corresponding to aperiodic calcium phosphate is centered at 2theta = 32°. b) XRD spectrum from an annealed-PSHA coating on a Ti-6Al-4V rod, showing the reduction in intensity of the broad peak visible in Figure 3.12a. The small peak at 31° corresponds to β-TCP.

Figure 3.13a: GAXRD spectrum from an IBAD-HA coating on a Ti-6Al-4V rod. The 4 strong peaks indicate scattering from the titanium alloy; the broad peak centered at 30° corresponds to aperiodic calcium phosphate. b) GAXRD spectrum from an annealed IBAD-HA coating on a Ti-6Al-4V rod, showing the development of peaks corresponding to HA.

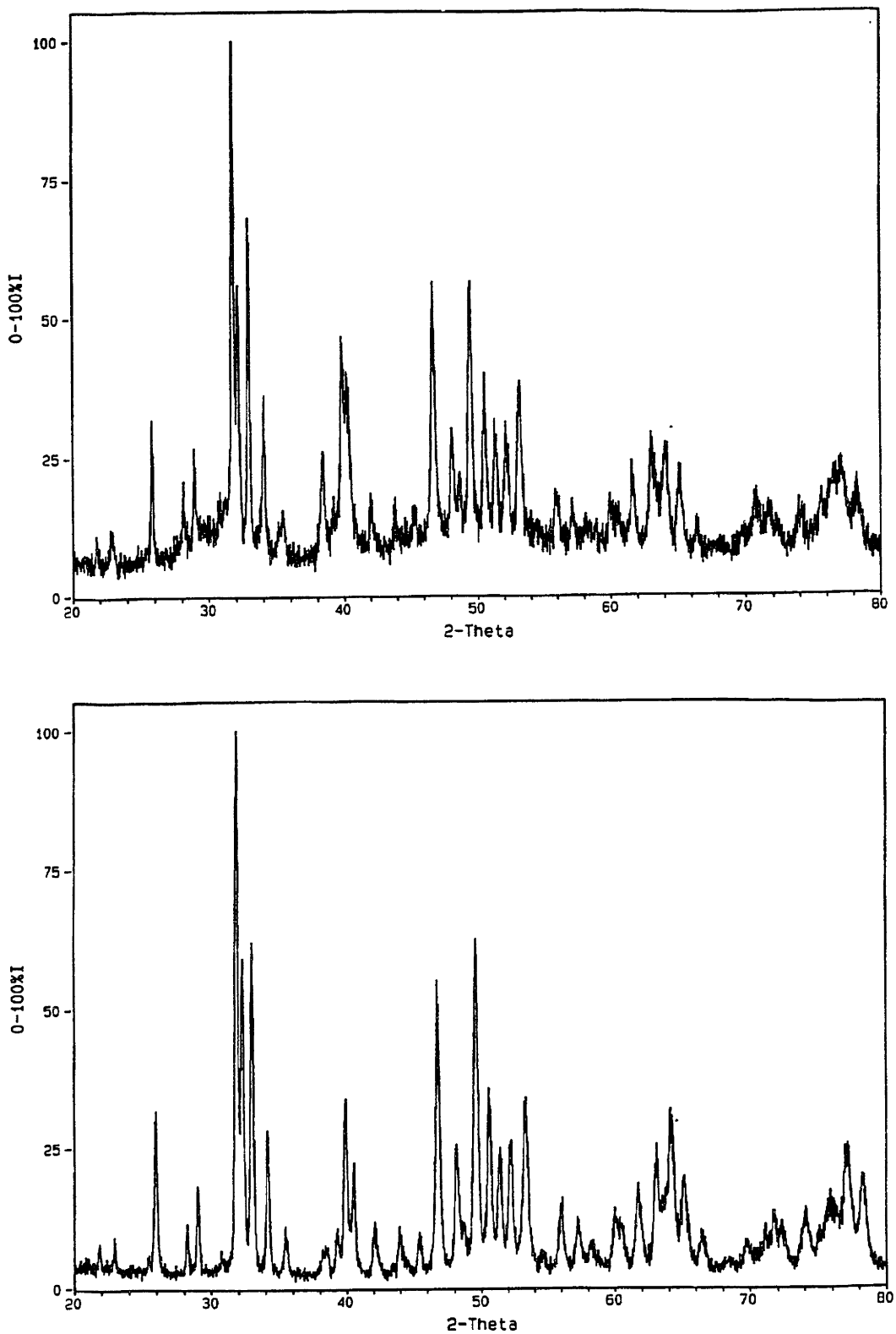
100
75
50
25
0
0-100%I
20
30
40
50
60
70
80
2-Theta
100
75
50
25
0
0-100%I
20
30
40
50
60
70
80
2-Theta

Figure 3.12

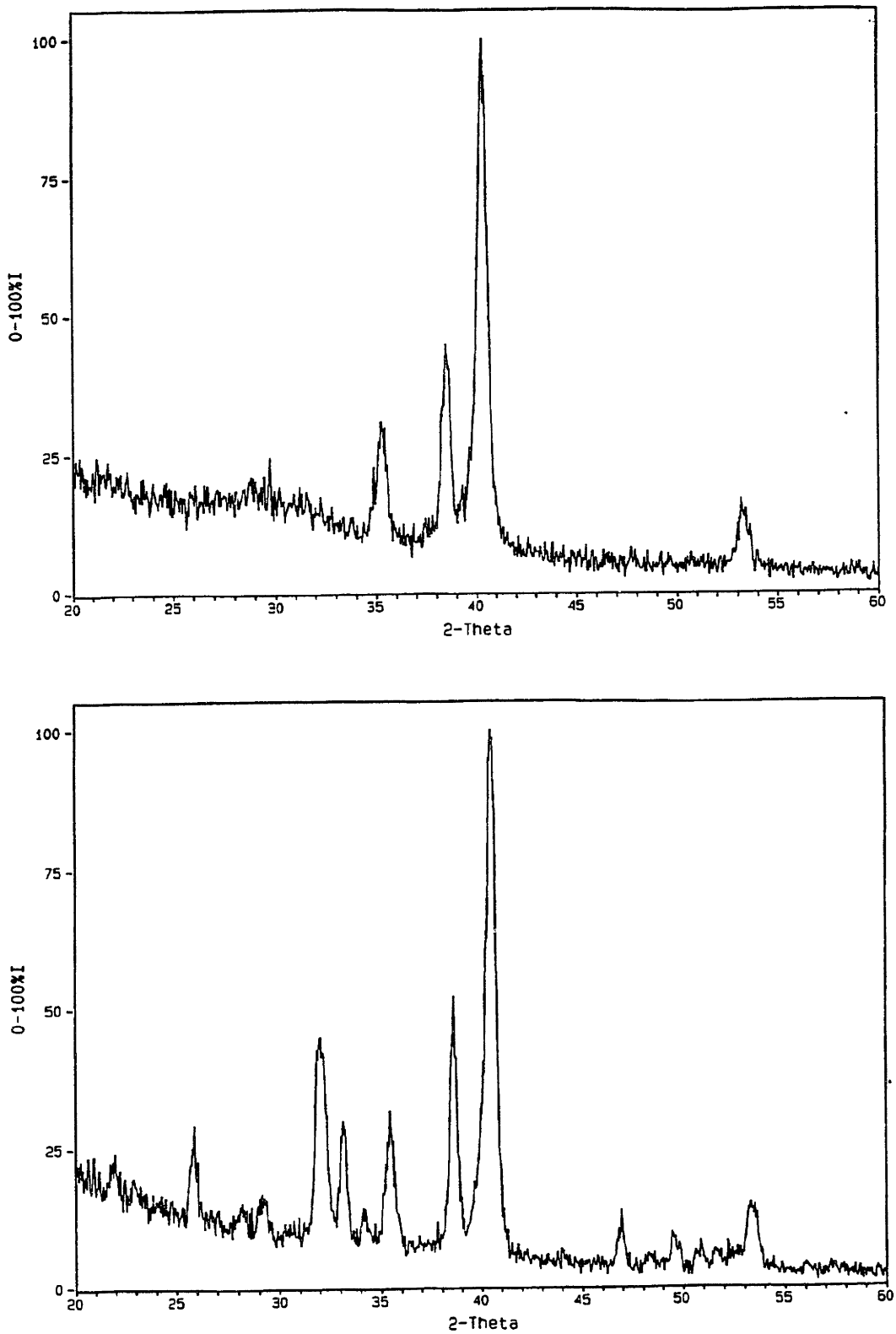
100
75
50
25
0
0-100%I
20
25
30
35
40
45
50
55
60
2-Theta
100
75
50
25
0
0-100%I
20
25
30
35
40
45
50
55
60
2-Theta

Figure 3.13

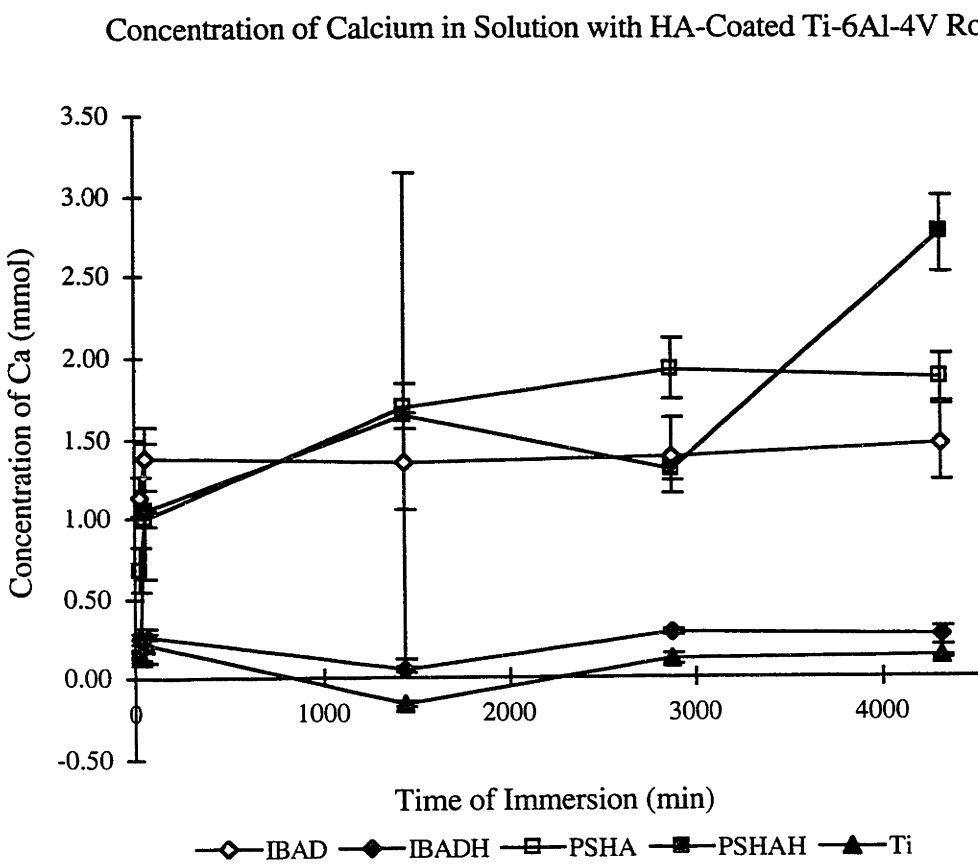

Figure 3.14: Concentration of calcium released from HA-coated Ti-alloy rods in pH 7.4 buffer. The error bars indicate standard deviation; n=3. IBAD=unannealed IBAD-HA; IBADH=annealed IBAD-HA; PSHAH=annealed PSHA; Ti=Ti-6Al-4V

3.4 *In Vivo* Experimental Methods

3.4.1 Surgical procedure

The samples were implanted in the proximal and distal femora and proximal tibiae of adult mongrel dogs (60-80 lbs.) for periods ranging from 3 hours to 10 days (Table 3.1). There were three samples for TEM/SEM preparation at each time period for each sample group (PSHA, annealed-PSHA, IBAD-HA, and Ti-alloy). There were only two

titanium samples in the three hour group (see below). There were also four samples for mechanical testing in each sample group (10 days post-implantation). All 10-day samples were implanted in the left leg. In four dogs, a second surgery was performed after a week, and samples implanted in the right distal femur and proximal tibia to be recovered three days post-implantation. In two dogs, samples were implanted in the right proximal and distal femur and the right and left proximal tibiae three hours prior to sacrifice. Aseptic procedures were not used to implant the 3-hour samples; the dogs were left anesthetized for the implantation time and then sacrificed.

Surgical Matrix for Implantation of HA-Coated Ti-6Al-4V Rods in Dogs

Dog #, procedure	Proximal femur	Distal Femur	Proximal Tibia
3004, surgery 1 3004, surgery 2	HA - 10DM (2)	IBAD - 10DM, 10DH Ti - 3D (2)	Ti - 10DH Ti - 3D
3018, surgery 1 3018, surgery 2	HA - 10DH (2)	IBAD - 10DM, 10DH HA - 3D (2)	HA - 10DM HA - 3D
3007, surgery 1 3007, sacrifice	HA* - 10DM, 10DH HA - 3H (2)	Ti - 10DM, 10DH IBAD - 3H (2)	HA(L),IBAD(R) 3H
3014, surgery 1 3014, surgery 2	HA - 10DM, 10DH	IBAD - 10DM, 10DH HA* - 3D (2)	HA* - 10DM HA* - 3D
3050, surgery 1 3050, sacrifice	HA* - 10DM, 10DH HA* - 3H (2)	Ti - 10DM, 10DH Ti - 3H (2)	HA*(L) 3H, HA(R) 3D†
3049, surgery 1 3049, surgery 2	HA* - 10DM, 10DH	Ti - 10DM (2) IBAD - 3D (2)	IBAD - 10DM IBAD - 3D

† PSHA sample implanted in right proximal tibia for three days seven days after first surgery; annealed-PSHA sample implanted with other three hour samples.

Table 3.1: Surgical schedule for implantation of samples. HA=PSHA; HA*=annealed PSHA; IBAD=IBAD-HA; Ti=uncoated Ti-6Al-4V; 10DH=10 days, for TEM/SEM observation; 10DM=10 days, for mechanical testing; 3D=3 days; 3H=3 hours.

In all cases, two implants were placed in the femoral sites and one in the tibial sites. In the distal femur, a polyethylene spacer was used to separate the samples. No spacer was used in the proximal femur because there was not enough trabecular bone to appose the entire surface of the two samples otherwise. Consequently, only PSHA-coated samples were implanted in the proximal femur, and the uncoated end of one of the samples served

as a spacer. One of the 3-day PSHA samples was implanted in the condylar notch instead of in trabecular bone in the distal femur; one of the 3-hour Ti samples (Dog 3050) was replaced with a fourth 3-day PSHA sample to make up for the improperly placed one. No infection was observed in any of the implant sites at sacrifice. The surgical protocol is detailed in Appendix B.

3.4.2 Embedding and fixation

Following sacrifice, the implanted ends of the leg bones were exposed and sawed off. Tissue containing only samples for SEM/TEM preparation was placed in ethylene glycol; tissue containing samples for mechanical testing was wrapped with gauze sponges soaked in saline. The mechanical testing procedure is given below. The tissue containing samples for SEM/TEM preparation was trimmed using a coping saw and a Dremel™ tool equipped with a ceramic cutoff wheel until the ends of the Ti-alloy rod were visible and the rod was surrounded by a sheath of tissue 1-2 mm thick. During trimming, the tissue was not supported by the actual rod but by the tissue surrounding the rod to prevent shear at the implant/bone interface. A small portable vice proved very useful for supporting the samples. The trimmed samples were fixed in ethylene glycol for 24 hours from the time of trimming (which may have been as much as twelve hours from the time of sacrifice), 6 hours of which were under vacuum. The samples were agitated when not under vacuum. Following fixation, the samples were rinsed in neat ethanol twice for 5 minutes and then twice in propylene oxide (Ted Pella, Reading, CA) for five minutes each. They were then infiltrated with Spurr's resin (Polysciences and Ted Pella) over several days, as follows. The samples were agitated in 1:3, 1:2, 1:1, and 2:1 solutions in propylene oxide for 23 hours each and then vacuum infiltrated with neat Spurr's for 23 hours. They were cured in fresh Spurr's for 23 hours at 60°C. In some cases, the samples were left in neat Spurr's for several days after infiltration but before curing for convenience. In these cases, the

Spurr's was changed for fresh resin at least every 48 hours. Spurr's resin was prepared with 10 g VCD, 4.5 g DER-736, 26 g NSA, and 0.4 g DMAE (see Chapter 2). After measuring the components, the mixture was folded for 5 min. before use. Extra resin was stored, covered, in the hood for no more than 48 hrs.

The first set of samples (Dog 3004) was set in glass vials. It has so far been impossible to get the samples out of the vials because the Spurr's is highly adherent to the glass. The rest of the implants were set in polypropylene Nalgene™ beakers, which separated from the epoxy easily. In all cases the samples were embedded while standing upright in the beakers. One of the titanium samples separated from the tissue during trimming; the tissue and the titanium were embedded separately.

The embedded samples were trimmed with a hack saw and polished on 120 grit SiC paper until the two faces were parallel to each other and to the axis of the embedded rod. The blocks were then sliced on a diamond saw. The 10-day PSHA and annealed PSHA-coated samples were sliced on a Struer Accutom-2™ diamond saw; all other samples were sliced on a Buehler low speed saw. All the saws were cooled with water. At least three slices measuring between 400 and 600 μm were cut. The first and third slices were dedicated to ESEM observation and histology, the second was dedicated to TEM preparation.

3.4.3 TEM preparation

Samples for TEM were first freeze-fractured to remove the titanium alloy rod from the sample. A 0.25" nut from a Swage™ fitting was chilled in liquid nitrogen for at least five minutes. The thickness of the slice to be fractured was recorded, following which the sample slice was chilled in liquid nitrogen for at least two minutes. The slice was placed on the nut such that the edge of the titanium lay across the hole in the nut. A file and a small hammer were used to tap out the titanium. The epoxy usually fractured into two or more

pieces. Slivers about 1 mm square and several millimeters long were cut using a Dremel™ tool equipped with a ceramic cutoff wheel and embedded in Spurr's resin in BEEM vials (Ted Pella) as described above. For the PSHA and annealed-PSHA samples, the slivers were examined to ensure that there was some HA on the tissue before infiltration. The coating frequently appeared to separate from the rest of the tissue during embedding; the IBAD-HA coating was identified by this separation. Fortunately, the coating had not actually separated during infiltration; TEM observation revealed that in most cases there was still tissue attached to the coating.

Silver to gold sections cut via ultramicrotomy were collected on Parlodion coated grids (Ted Pella) and coated with a thin layer of evaporated carbon. While microtomy was somewhat difficult (the bone and coatings continually fell out of the sections) a 5 degree knife angle and a very steep meniscus in the water trough gave satisfactory results. In addition, the knife should be cleaned frequently to remove any particles of material which may adhere to it.

The samples were viewed in a JEOL 200CX TEM at 200kV. If both the coating and some apposing tissue were visible in the TEM, the samples were stained with uranyl acetate and lead citrate. The grids were placed sample side down on individual drops of 4% uranyl acetate in 30% ethanol in water for 15 minutes in a petrie dish in a light-tight box. They were then rinsed 10 times each in each of three beakers of distilled water and allowed to dry. The grids were then placed sample side down on individual drops of 2% lead citrate in water for 10 minutes and rinsed in a similar fashion. To prevent precipitation of the lead from solution, a few NaOH pellets were placed in both the petrie dish and the first beaker of water to neutralize carbonic acid (formed from carbon dioxide). Microscopy was again performed as above. Samples from all the time periods for the coated rods were observed; the IBAD coating could not be located in the three hour and three day samples, so no observations were made. Up to about 0.3 mm of the coating was present in any

given section. XEDS analysis was performed in the JEM 2010. Samples should be pumped down with the diffusion pump in the 2010 before being inserted into the column (and exposed to the ion pump).

An umimplanted PSHA rod was prepared for TEM observation as well. This sample was embedded in LR White epoxy (Polysciences) and prepared as described in Appendix C, except that the titanium separated from the coating while the samples were being trimmed for reembedding. The microtomed samples were viewed in the JEM 2000FX.

3.4.4 Histology

PSHA-coated, IBAD-coated, and Ti-alloy rods recovered 10 days post-implantation were observed with light microscopy to confirm the identification of bone in the ESEM (see below). Slices were mounted on acrylic cards with KrazyGlue™. They were polished on 600 grit SiC paper lubricated with water on a mechanical polishing table until they were about 120 μm thick. They were then polished by hand on the same piece of somewhat worn SiC paper using 1000 grit SiC slurry as a lubricant. Samples were stained with Harris' hematoxylin and eosin according to the protocol in use in the Orthopedic Research Laboratory at Brigham and Women's Hospital, Boston, MA. Samples were stained in hematoxylin for 30 minutes, rinsed in water, acid alcohol, and dilute ammonia, and then stained in eosin for 1 minute, rinsed in water, and allowed to air dry.

3.4.5 ESEM observation

All environmental SEM (ESEM) observations were performed on an Electroscan Model E-3 ESEM operated at 25 keV. Samples were coated with a relatively thick layer of evaporated carbon (several thousand Ångstroms) to increase contrast. A relatively long working distance (~10 mm) and small condenser (65% total lens current) also increased

the contrast between the newly deposited mineral and the PSHA coatings. The total perimeter observed and the total perimeter apposed by bone were measured by hand for each micrograph. At least nine micrographs were taken for each sample; the interval between them was at least twice the arc length of the titanium rod shown in any given micrograph. The micrographs for any given sample were all taken at the same magnification, between 155 and 265x. Higher magnifications were used to confirm the apposition of apatite on the coating. The 10-day and 3-day samples were all observed, with the exception of those from Dog 3004. If the interface between the tissue and the coating could not be clearly seen, the sample was polished, re-coated, and observed again.

3.4.6 Mechanical testing

All mechanical testing was done the same day as sacrifice. The samples were trimmed with a coping saw and a Dremel™ tool equipped with a ceramic cut-off tool until the faces of the specimen were parallel to the ends of the rod and 1-2 mm of the rod was exposed. The specimens were leveled by eye with a small level. The specimens were then set on a 3/4" nut from a Swage™ fitting on an Instron Model 8521 which was fitted with a 10 kN load cell. The appropriate strain rate was determined by testing a dummy sample, a Ti-alloy rod embedded in Spurr's resin. A strain rate of 10 mm/min was considered appropriate. However, the first sample, a PSHA coated sample, failed in a few seconds, so the strain rate for the rest of the samples was reduced to 1 mm/min. One of the Ti-alloy samples (Dog 3049) failed during trimming.

All specimens were stored in ethylene glycol in a refrigerator following fracture. At a later date, the bone surrounding the implant was cut in half without disturbing the implant and the two halves pulled away from each other. Observations of the fracture faces were recorded. In addition, photographs were taken of the fracture surfaces and the length of the unexposed section of the samples were measured. For the samples with plasma-sprayed

coatings, the surface included both the HA-coating and grit-blasted titanium. Even though the contribution of the Ti surface was probably less than that of the HA-coated surface, it was included equally in the calculation of the failure strength.

The failure weights (in pounds) were normalized and converted to pressure (in kPa). The Student's T-test was used to determine whether there were significant differences between results from the IBAD-HA and Ti-alloy samples and between the untreated and annealed-PSHA samples. Analysis of covariance (ANOVA) was used to determine whether there was significant effect of coating type on the mechanical strength of the interface.

3.5 Results

3.5.1 Quantitative results

Figure 3.15 shows the shows the strength of the coating/bone interface *in vivo*. ANOVA showed a significant effect of coating type on mechanical integrity ($p < 0.05$), but there is no significant difference between the two HA coatings or between the IBAD-HA coating and the uncoated Ti-alloy. One of the annealed-PSHA samples demonstrated negligible interfacial strength (see below). Both a Q test and the ASTM T_n Test for outlying results were performed to determine whether to reject the result [176]. The Q value lay between the critical values for 90 and 96% confidence; T_n was just greater than the critical value for 95% confidence. Because the result in question was actually due to poor bone bonding and not to a flaw in the conduct of the mechanical test, the result was retained and is incorporated into the plot below.

Figure 3.16 shows typical fracture faces for each of the four sample groups. The IBAD and Ti-alloy samples fractured at the tissue/implant interface. Small amounts of tissue were occasionally adherent to the rod following fracture. For both of these sample groups, the face of the tissue appeared smooth and red following fracture. The PSHA

samples appeared to fracture either at the coating/tissue surface or within the coating. In general, the fracture appeared to take a somewhat tortuous route and may have included the tissue, the tissue/coating interface, the bulk coating, and the coating/metal interface. The apposing tissue exhibited texture similar to that of sliced bone. As noted above, one of the annealed (heated) PSHA samples exhibited little interfacial strength in contact with bone. Examination of this sample revealed that it had indeed not attached to the bone; the fracture surface included the tissue and the tissue/coating interface. The tissue surface was closer in appearance to that apposing the Ti-alloy and IBAD samples and less like that apposing the other HA-coated samples.

The histological results do not parallel the mechanical test results. There was no significant difference (ANOVA, $p > 0.05$) in bone apposition to the three HA-coatings after 3 or 10 days (Figure 3.17). The Ti-alloy samples were not included in the ANOVA calculation because there was only one sample in the group. A second sample was observed; however, the Ti-alloy rod had come out of the sample during trimming, so it was not possible to measure the extent of bone apposition. However, significant amounts of tissue resembling that which apposed the HA-coated rods, either originating at a trabecula and extending from it in a thin ribbon or independent of trabeculae, were not observed. Significant areas of all three coatings were apposed by apatite tissue, and cellular lacunae are visible via SEM (Figure 3.18).

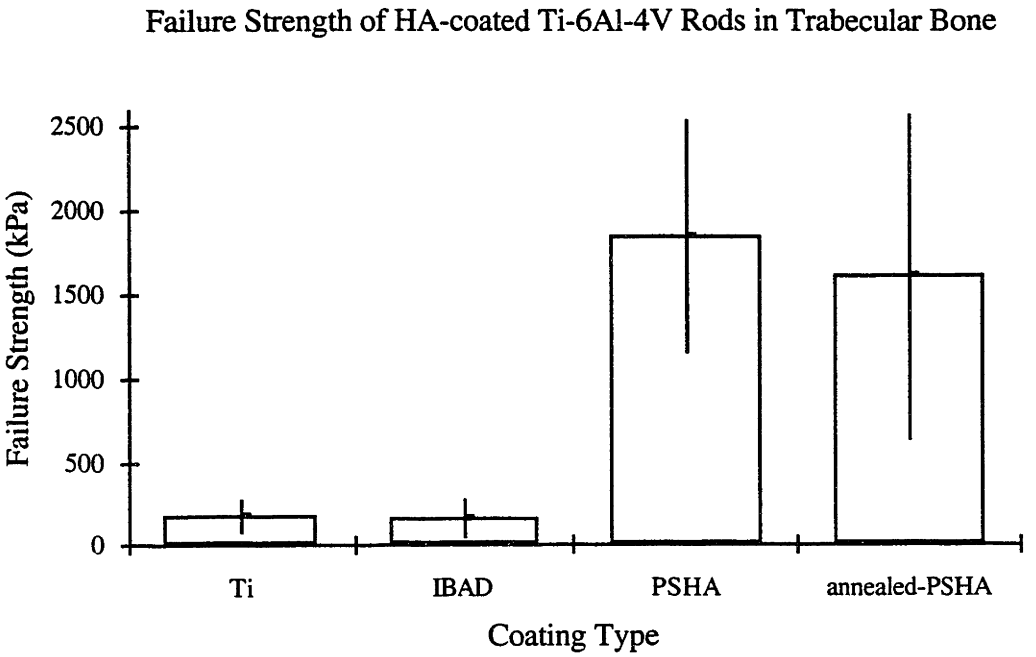

Figure 3.15: Interfacial strength between trabecular bone and various HA-coatings on Ti-6Al-4V 10 days post-implantation. The error bars indicate standard deviation; n=4 except for the uncoated Ti-alloy (n=3).

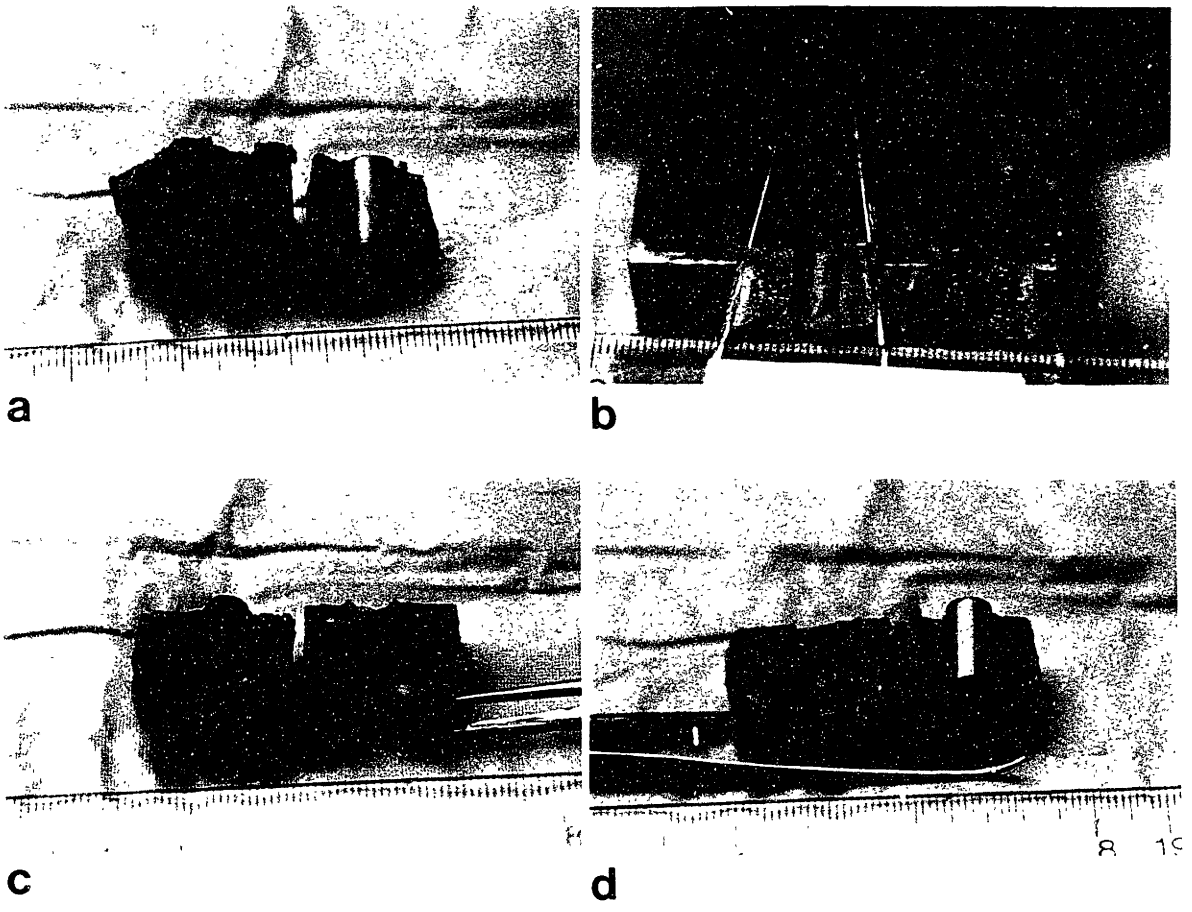

Figure 3.16: Photographs of fracture faces of mechanical test samples. A - IBAD-HA; B - PSHA; C - annealed-PSHA, D - uncoated Ti-4Al-6V

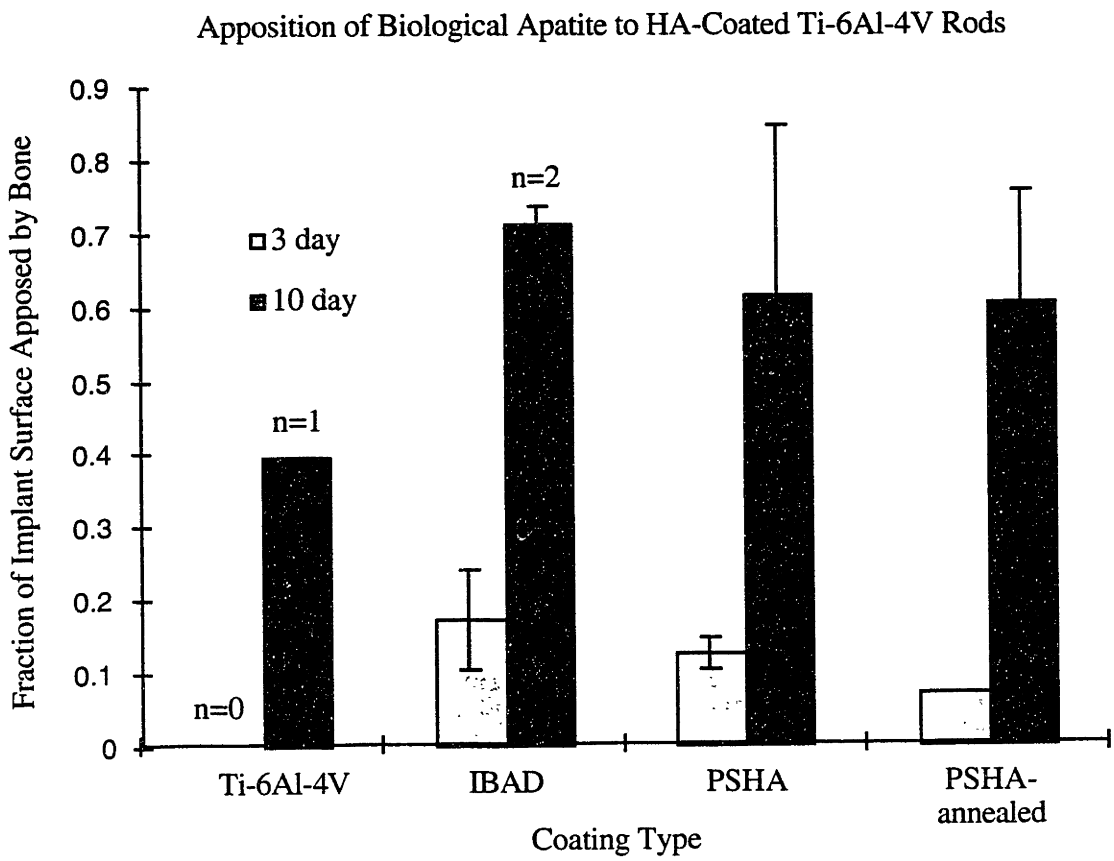

Figure 3.17: Fraction of implant surface apposed by bone after 3 and 10 days *in vivo*. The error bars indicate standard deviation, which is 0.02 for the PSHA-annealed groups at three days. Except where indicated, n=3.

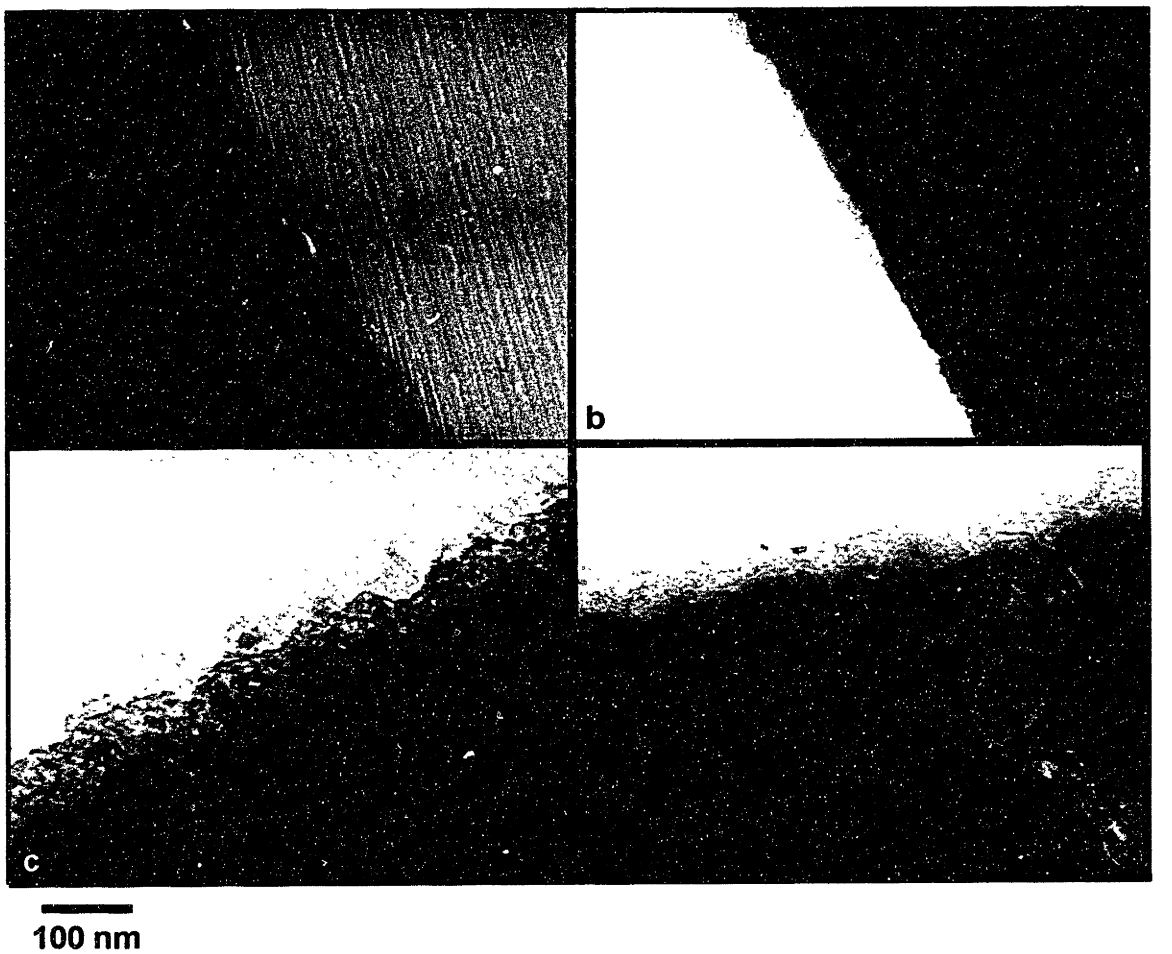

Figure 3.18: Sample ESEM micrographs of the interface between bone and the four HA-coated surfaces: a) uncoated Ti; b) IBAD-HA; c) PSHA; d) annealed-PSHA.

3.5.2 Microscopic observations of apatite deposits on HA-coated samples

The HA coatings and the biological apatite deposits were easily distinguished by the size and shape of the constituent crystallites. While unimplanted PSHA coatings were observed, because the samples were prepared without the Ti-alloy substrate, it was not possible to identify the inner and outer surfaces of the coating. However, observations of the controls did aid identification of the coating in the implanted samples. Both large (about 300 nm long) and small (about 50 nm long) crystallites were observed in the PSHA coatings (Figure 3.19). Because statistical analyses were not performed, this does not necessarily imply a bimodal distribution of crystallite sizes in the coatings. Indeed, ESEM observations of the coating surface (cf. Figure 3.11) indicate that a bimodal distribution is somewhat unlikely. In common with the biological apatite deposits, the crystallites were 2-3 times as long as they were wide. However, they appeared to have an aspect ratio more closely related to those of the synthetic bone substitute materials described in Chapter 2 than to those of the plate-like biological apatite deposits described below. Surprisingly, the IBAD-HA coating had a microstructure similar to that of the PSHA-coatings (Figure 3.20). The portion of the coating retained in the fracture section is about 0.5 μm wide, somewhat thinner than the whole coating, but is composed of blocky crystallites similar to those observed in the plasma-sprayed coatings.

After three hours *in vivo*, few features were distinguishable on the unstained samples aside from the coating. Staining revealed a wide variety of features. In both the PSHA and annealed-PSHA samples, small plate-like crystallites were observed both in the vicinity of the coating and apparently attached to it (Figures 3.21, 3.22). There appeared to be a lower number density of crystallites associated with the annealed-PSHA coating. A 100 nm "border" was also observed surrounding much of the annealed PSHA coating (Figure 3.22).

Deposits on the untreated PSHA coating also exhibited two other microstructures after three hours. The first comprised a speckled network of Ångstrom-scale features; the second was somewhat diffuse but included larger features tens of nanometers in size (Figures 3.23, 3.24). Selected area electron diffraction patterns of both features exhibited a broad ring corresponding to (211) in hydroxyapatite. XEDS of the diffuse features revealed calcium and phosphorus. The former microstructure probably does not result from the release of small calcium phosphate particles from the coating because this feature is still present both three and 10 days post-implantation in the IBAD-HA samples. It may, however, result from the precipitation of calcium phosphate onto any proteins which may have already been deposited near the coating. Immunogold staining could confirm this (see below). However, this is also a common microstructure in TEM micrographs published in the literature, and authors do not call any special attention to it [58, 121, 177]. The morphology of the latter microstructure is consistent with other observations of poorly crystalline calcium phosphate (CaP) [178]. Both the identification of Ca and P through elemental analysis and observations of discrete apatite crystallites within these deposits at later time points indicate also suggest that diffuse microstructure comprises an amorphous CaP phase (see below and discussion).

Larger crystallites can also be observed within the morphologically indistinct deposits on unannealed PSHA coatings after three days (Figure 3.25). After three days *in vivo*, apatite deposits on the annealed-PSHA coating increased in number density to the level exhibited by deposits on the unannealed-PSHA coatings after three hours (Figure 3.26), but the morphologically indistinct deposits were not observed. The 100 nm border is still present in both unstained and stained samples. However, the border also exhibited a second microstructure after staining (Figure 3.27). The stain revealed a series of tiny equiaxed dots along the edge of the border and aggregates of small dots within it. In addition, small circular aggregates of the small dots are also observed, ranging from 20-60

nm in diameter. Electron dense globules without dots are also observed over the same size scale; they are seen in conjunction with areas of the border which do not stain as highly (Figure 3.28). The change in microstructure with the intensity of the stain probably indicates that these small dots are actually artifacts.

Small apatite crystallites were observed in deposits on the unannealed-PSHA coating after 10 days (Figure 3.29). In Figure 3.29, larger, higher contrast crystallites were also included in these deposits, which again show some resemblance to the morphologically indistinct deposits observed in Figure 3.23. In addition, deposits composed primarily of larger crystallites were observed (Figure 3.30). Randomly arranged arrays of crystallite deposits were also observed on the annealed-PSHA coatings after 10 days (Figure 3.31). As in the preliminary study, the crystallites appear needle-like in morphology. However, crystallites observed with lower contrast and more diffuse edges again demonstrate the plate-like morphology of the crystallites.

The most surprising feature observed in the apatite deposits formed on the annealed-PSHA coatings after 10 days was periodic aggregation of crystallites (Figure 3.32). These aggregates are directly apposed to the PSHA coating and were oriented perpendicular to its surface (Figure 3.33). The periodicity of these aggregates was 62-66 nm, comparable to the periodicity of collagen described in Chapter 2 (cf. Figure 2.10). Within the aggregates, the crystallites were aligned with their long axes parallel to the long axis of the aggregate, perpendicular to the surface of the coating. While the crystallites oriented parallel to the plane of the section illustrate the periodic arrangement more clearly than those oriented on edge, within one of the aggregates the crystallites are arranged almost in an end-to-end fashion (Figure 3.33).

Features similar to those described above, with the exception of the borders observed on the annealed-PSHA samples after three days, were observed in the IBAD samples after three days. However, because the coating could not be located within the

section, these features could not be located with respect to it. The primary features observed after 10 days on the IBAD samples were the diffuse aggregates of small apatite crystallites (Figure 3.34). While the apatite deposits directly apposed the coating, the inner layer of the deposits have a morphology closer to the morphologically indistinct CaP deposits seen on the PSHA coatings at earlier time periods. The outer levels of the deposits, farther from the coating, included a higher proportion of larger, higher contrast crystallites.

3.6 Discussion

While many interesting features were observed over the course of this study, perhaps the most notable observation was the lack of the globular aggregates of crystallites which had been observed after both 6 and 14 days in the preliminary study. Their existence may indicate that the globular aggregates are formed farther from the implant/bone interface than the range observed in this study. Such aggregates were not observed in either anorganic or whole bone, further indicating that the globules are part of the biological response to the coating and must be located relatively close to it. However, the globular deposits are associated with earlier stages of bone apposition; thus, it is unlikely that they would be observed in the vicinity of the more developed apatite networks observed after 10 days.

However, many observations were made during this study which explained observations made in the preliminary study, and vice versa. For example, in the preliminary study, the HA coating could be identified only by the relatively large size of its constituent grains. Smaller grains, larger than the apatite deposits, were also observed. In informal group discussions, these were actually hypothesized to be either apatite deposits or fragments of bone remaining from the surgical procedure. However, in this study, the PSHA coating exhibited a large distribution of grain sizes (see Figures 3.20 and 3.11).

Observations of small crystallites the HA coatings indicate that the small grains observed in the preliminary study were part of the HA coating. They were not observed in conjunction with biological apatite deposits because the implant/bone interface had been milled through.

This points out a very important characteristic of this study: all the features discussed above have been located with respect to the HA coating. Indeed, identification of the coating was essential to TEM observations; where the coating could not be identified, it was impossible to identify deposits either directly adjacent to it or micrometers away from it. To perform TEM observations of the Ti-alloy implants, for example, it would be necessary to include the implant in the TEM specimen. While the specimen preparation method in this study first removed the Ti-alloy from the explanted samples, a method for preparing microtomed samples including the Ti-alloy is described in Appendix C.

The mechanical integrity of the bone/PSHA interface after 10 days, 1.6-1.8 MPa, is about half that of trabecular bone, about 3.3 MPa [179]. This is in keeping with reports that the maximum percentage of bone apposition, 80%, is achieved 14 days post-implantation. In this study, the maximum bone apposition observed was only 60-70%. As more bone apposes the implant, the mechanical strength of the entire bone/implant system increases.

The most confusing result in this experiment was definitely that from the solubility experiment. The variability of the calcium release from the annealed-PSHA coatings indicates that they were probably not significantly less soluble than the untreated PSHA coatings. In addition, the untreated PSHA coatings were more soluble than the unannealed IBAD coatings. In this experiment, at least, an increase in coating crystallinity did not result in an increase in solubility. As long as some portion of the coating is amorphous, it will release Ca. That the annealed-IBAD coating was almost completely insoluble may further indicate that it was almost completely crystalline. While the annealing protocol described by Cui et al. is supposed to result in a partially amorphous coating, the increased

cooling time in this experiment following anneal may have allowed the coating to completely crystallize [167, 180].

Given the benefit of hindsight, the decision to do a simplified solubility experiment was probably not the best. However, on a gross scale, it did reveal the difference in chemistry between the PSHA and IBAD-HA coatings. As discussed below, that it was impossible to determine exactly the crystallinity of the IBAD-HA coatings in this experiment may also have proven detrimental to the experimental design. Future investigators are encouraged to produce a number of coatings on flat substrates to be processed in parallel with the cylindrical implants. The added surface area (and thus sampling volume) should increase the scattered intensity in x-ray diffractometry to the point where a crystallinity determination is possible.

One hypothesis in this experiment was that a difference in calcium release from a coating would influence the degree of bone apposition and the mechanical integrity of the interface. The results from the solubility experiment seem, at first glance, to support that conclusion. That there was no difference in the mechanical integrity of the bone/implant interface between the two PSHA coatings but a significant difference between them and the (annealed) IBAD-HA coated implant seems to indicate that a difference in calcium release leads to a difference in mechanical strength.

There are two problems with this conclusion. First, there was no significant difference in bone apposition among the three HA-coated implants. In fact, the IBAD-HA coated implants exhibited greater (although not significantly so) apposition than either of the PSHA-coated implants. Moreover, the IBAD-HA implants were completely smooth, while the PSHA-coated implants were quite rough. Indeed, the experiment was originally designed so that the annealed-PSHA coating would be a rough, insoluble coating and the IBAD-HA coating would be a smooth, soluble coating. That was unfortunately not the case.

Thus, one must rely on the difference in PSHA-coating crystallinity and the difference in mechanical integrity between the rough and smooth PSHA coatings to draw any conclusions at all. The result is actually quite powerful: *bone apposition is not a sufficient indicator for mechanical integrity of the interface between biological tissue and an HA-coated implant.* This conclusion is further supported by TEM observations of apatite crystallites directly apposed to the IBAD-HA coating after 10 days. While both SEM and TEM observations showed extensive apposition of biological apatite to the coatings, the IBAD-HA demonstrated significantly less mechanical stability.

In this study, bone apposition may also have been correlated with the presence of an HA coating, but the results were not significant. However, multiple studies comparing HA-coated and uncoated metallic surfaces have already demonstrated that the chemical interaction of an HA coating with its surroundings *in vivo* is crucial to the formation of a stable bond between tissue and an HA coated implant, and, in this study, the interface between a Ti-alloy rod and bone was shown not to be particularly stable after 10 days [131, 181]. Thus, this study indicates that bone may appose an HA coating regardless of solubility (that is, the coating is osteoconductive), but that something extra is required to provide mechanical integrity. The lack of both calcium release and implant/bone mechanical integrity in both the IBAD-HA coated and uncoated Ti-alloy samples indicates that that something may be related to calcium release from the coating. The uncoated Ti-alloy controls are also somewhat smoother than the PSHA-coated samples, so there is the possibility that there is a threshold roughness for formation of a strong mechanical bond. However, that grit-blasted cpTi implants do not demonstrate superior short-term mechanical stability *in vivo* indicates that this is probably not the case [181].

Other studies also indicate that some level of calcium release may be required for short term mechanical integrity of implants. After four weeks, no significant difference in interfacial strength was observed between PSHA and smoother, less soluble sintered HA

implants, yet PS-alumina coated implants demonstrated significantly less mechanical integrity in a transcortical model [149]. Klein et al. show that heat treatment of a PSHA coating has a significantly detrimental effect on coating solubility and bone apposition but do not perform mechanical tests [134, 135]. While mechanical integrity of the interface between relatively insoluble sintered HA and bone indicates that only a threshold level of calcium release may be required, too much calcium may also be detrimental. In long term experiments, HA-coated implants were mechanically more stable than implants coated with amorphous calcium phosphate, and biological deposits on HA-coated implants with coating crystallinities of 43% or less did not exhibit the mineralized proteoglycan layer typical of PSHA coatings [121, 182].

While coating crystallinity did not affect on the degree of bone apposition, it appears to have influenced the microstructure of the apatite deposits. The unannealed PSHA coating, with a higher percentage of amorphous calcium phosphate, exhibited a high number density of deposited biological apatite crystallites shortly after implantation. The annealed-PSHA coatings required up to three days to demonstrate similar apposition. Moreover, the microstructure of the apatite deposits on the IBAD-HA coatings differed from that of deposits on the PSHA coatings. Larger crystallites which were observed directly apposed to the PSHA coatings were separated from the IBAD-HA coatings by a diffuse layer of morphologically indistinct deposits which contain Ca and P according to XEDS. The observation of these calcium and phosphorus-containing deposits in conjuction with discrete apatite crystallites and the similarity of their morphology to other amorphous biological CaP deposits indicate that the morphologically indistinct deposits comprise a CaP precursor phase [178].

Coating solubility may also have influenced the evolution of the microstructure of the apatite deposits. The morphologically indistinct deposits observed apposed to the PSHA coatings at early time periods were largely replaced by larger crystallites by 10 days.

The observations of different types of apatite crystallite organization in the preliminary study indicate that it is unlikely that the crystallites observed at 10 days are the result of some kind of phase transition within the deposits. The difference in microstructure between 6 and 14 days in the preliminary study is not the result of the migration of deposited crystallites but rather an indication of how the crystallites were organized as they were deposited. It was hypothesized that collagen-mediated deposition would result in a different crystallite organization than simple precipitation within the proteins deposited on the surface, and evidence for that was observed in the periodic deposits seen after 10 days on the annealed-PSHA samples. Similarly, it is more likely that the crystallites observed at 10 days are the product of dissolution of the initial CaP deposits, followed by reprecipitation of the larger, discrete apatite crystallites.

After 10 days *in vivo*, the annealed-PSHA coatings were apposed by deposits having the periodic microstructure of bone. These were not observed on the unannealed PSHA coatings. In contrast to these observations, the literature reports that the tissue immediately apposing a PSHA coating is collagen free [58, 121]. Others report the direct apposition of bone to dense HA implants after long term implantation, but observe an apatite-rich transition layer between bone and dense HA at shorter time periods [114, 125].

The perpendicular orientation of the apatite networks to the coating surface parallel other observations of bone apposition to dense HA implants [171]. In contrast, collagen indirectly bound indirectly to implants via a mineralized layer tends to be oriented parallel to the implant surface [183]. This is likely related to the presence of the collagen-free binding zone, which is primarily composed of glycosaminoglycans and biological apatite. An important component of the extracellular matrix, proteoglycans have a high affinity for collagen, and lower interfacial energy ought to be achieved by having the collagen maximize the surface area in contact with the proteoglycan layer. This thermodynamic argument offers a clue to the interaction of collagen with the annealed-PSHA coating. The

apatite nucleation sites in collagen are located in the hole zones, the places where the C- and N-termini of the collagen molecule meet [59, 67]. This is then the most thermodynamically favored site for collagen to bind hydroxyapatite, and the collagen molecule orients itself so that its ends bind the PSHA coating. This mechanism does not explain why the collagen is observed directly apposed to the annealed-PSHA and not to the unannealed-PSHA coatings, however.

The influence of coating solubility is also reflected in the microstructure of the apatite deposits on the IBAD-HA coatings. After 10 days, the microstructure of the deposits immediately apposed to these coatings is closely related to the diffuse deposits observed on the PSHA coatings at earlier time periods. While larger, more discrete crystallites are visible, they are located at the outer regions of these deposits, not within them. In addition, larger crystallites are not seen in direct contact with the IBAD-HA coating, in contrast to the PSHA coatings. While the surface roughness of the PSHA and IBAD-HA coating were significantly different, on the size scale of an individual apatite crystallite (about 100 x 60 x 4 nm) they are roughly the same. An individual crystallite interacts with one or two HA grains, not the tortuous surface of the PSHA coating. Thus, it is possible to discuss the influence of surface chemistry on the morphology of biological apatite deposits independent of surface roughness. If cell-mediated deposition had been observed, this would not be the case.

Two questions in the recent literature inquire 1) whether HA is necessary for bone bonding or merely facilitates/accelerates it, and 2) whether HA influences bone bonding through chemical or mechanical interactions. The influence of coating solubility on the microstructure of apatite deposits suggests a way to answer both of these questions.

That the apatite deposits on the IBAD-HA coating resemble the deposits on the PSHA coatings at three hours and three days supports the theory that the coating influences the timing of apatite deposition. Note, however, that the coating does not change the

ultimate magnitude of that response -- there were no significant differences in the fraction of the surface apposed by bone after ten days. Instead, there is a difference in the maturity of the biological deposits (see mechanism, below). Moreover, the degree of apatite deposition is not a guarantee of clinical success. Laboratory studies of bone bonding should use mechanical criteria to quantify bone bonding rather than histological criteria such as percent apposition.

This study supports the hypothesis that apatite deposition does not follow only from coating dissolution and reprecipitation, indicating that the chemical influence of HA on bone bonding is more complicated than a simple relationship between solubility and the degree of apatite deposition [129, 140]. In this study, a completely insoluble coating and two soluble coatings did not exhibit significantly different degrees of bone apposition after as few as three days. In addition, morphologically similar biological deposits were observed on both the soluble and insoluble coatings. However, the difference in the time periods at which these features were observed suggests that the initial microstructure of the deposits and the evolution of that microstructure is at least partially mediated by the chemistry of the HA coating. The lack of small apatite crystallites, such as those observed on PSHA coatings after three hours (cf. Figure 3.22), in the vicinity of the IBAD-HA coatings also supports this hypothesis. It is most likely that HA influences bone bonding through *both* mechanical and chemical interactions.

While evidence of collagen was observed in this study, cells were not. As a result, this paper will not provide a complete discussion of the biological processes which lead to bone bonding to HA-coated implants. However, a discussion of the time course of the apatite deposition which is part of that process is certainly warranted. Initially, small apatite crystallites and poorly crystalline CaP phases precipitate in the vicinity of the coating. The number density of crystallites in a given area may depend on the calcium release from the coating. As more crystallites are deposited, they begin form aggregates,

some of which are directly apposed to the coating. Further deposition, in addition to remodeling of the deposited material, results in the deposition of larger crystallites. As deposition continues, the aggregates increase in size until they merge. At later times, remodeling of the deposited material, in addition to the presence of ECM proteins deposited by newly-arrived cells, results in dense deposits of randomly oriented crystallites. If collagen is present, it will mineralize to form oriented crystallite networks reminiscent of those in bone. The binding of collagen directly to the implant surface, rather than indirectly via a mineralized matrix of proteoglycans, may depend on the crystallinity of the implant coating. Moreover, while cells were not observed, cells are required to produce collagen, and the orientation of the ordered crystallite arrangements with respect to the coating surface implies a preferred orientation of those cells (which produced the requisite collagen) with respect to the surface of the coating.

Following page

Figure 3.19: TEM micrograph of the HA coating on an unimplanted PSHA-coated Ti-6Al-4V rod.

Figure 3.20: TEM micrograph of the HA coating on an IBAD-HA coated implant 10 days post-implantation.

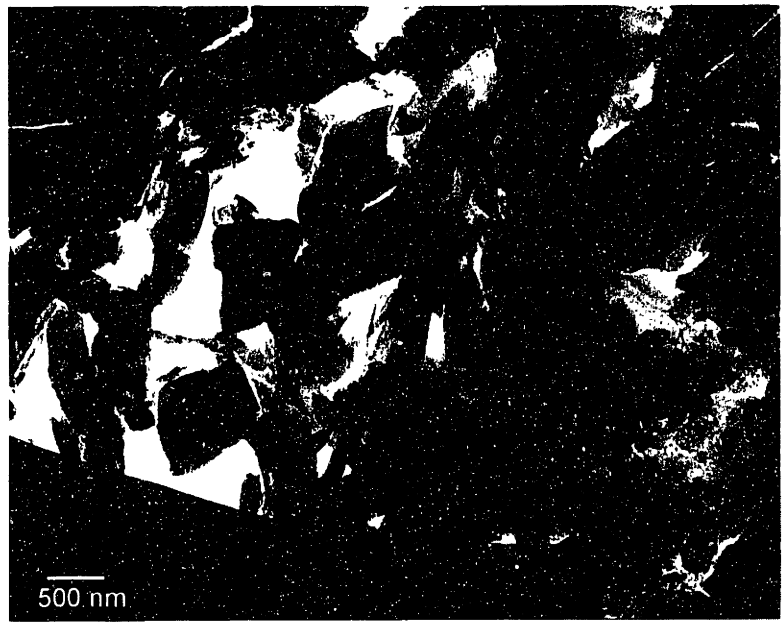

Figure 3.19

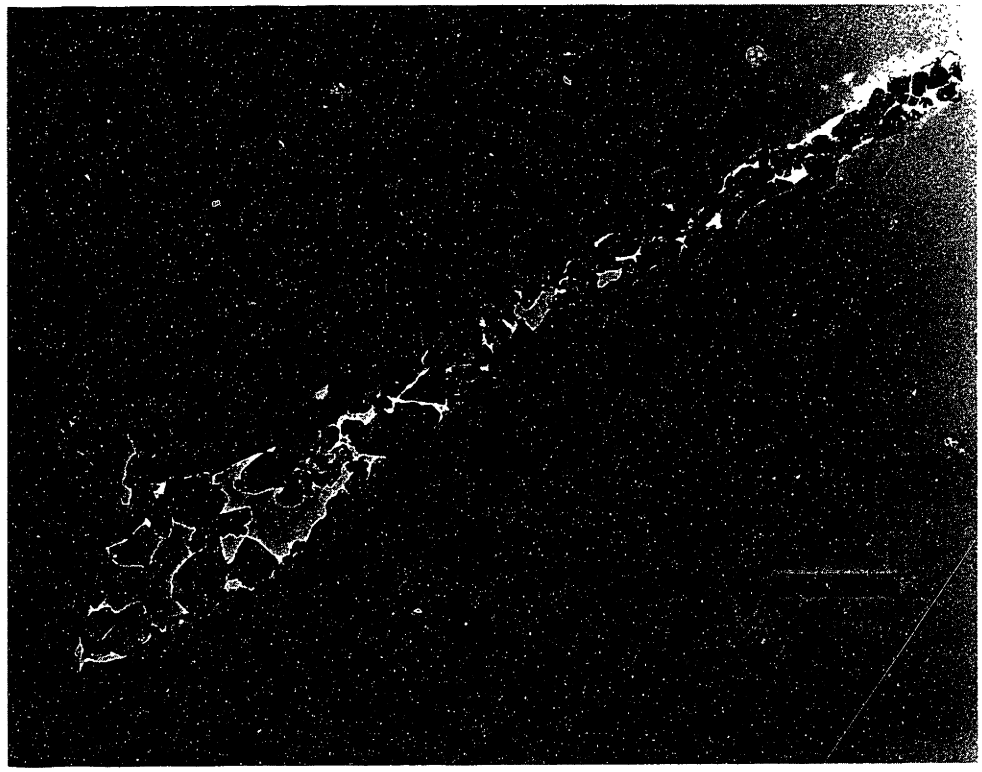

Figure 3.20

Following page

Figure 3.21: TEM micrograph of tissue apposing a PSHA-coated implant 3 hours post-implantation, showing numerous small crystallites apposing the coating.

Figure 3.22: TEM micrograph of tissue apposing an annealed-PSHA coated implant 3 hours post-implantation, showing a few small crystallites apposing the implant and a thin border surrounding its periphery.

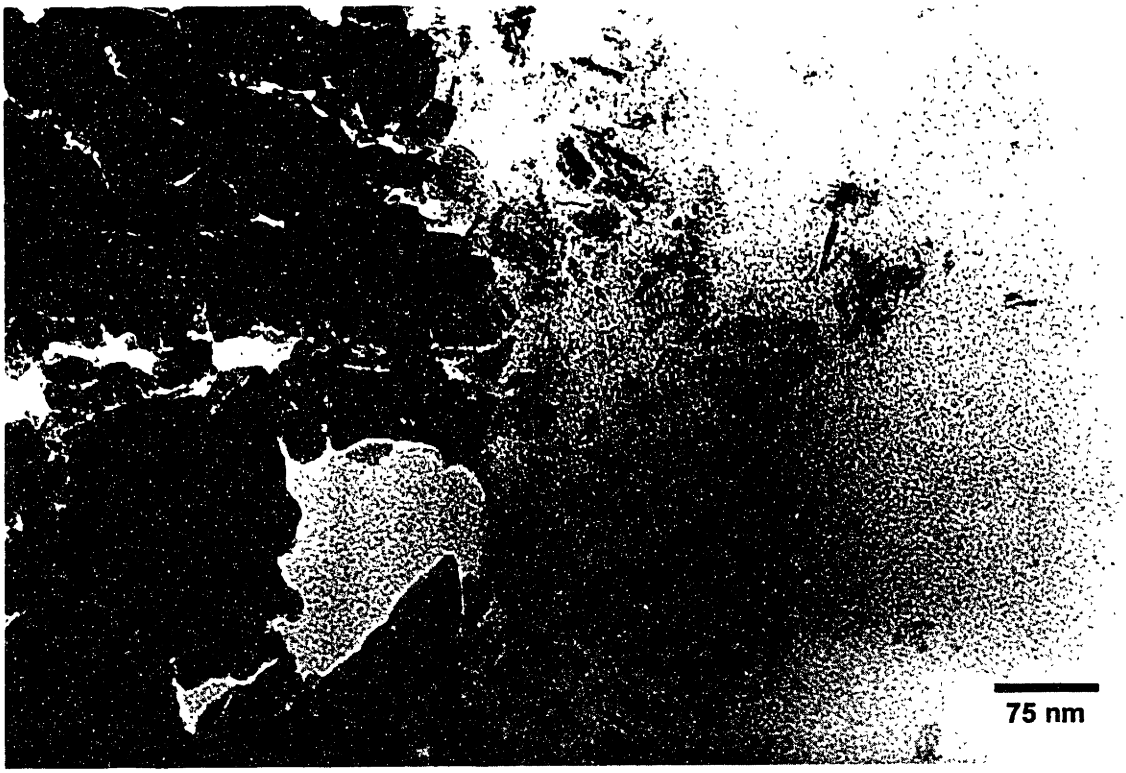

Figure 3.21

Figure 3.22

Following page

Figure 3.23: TEM micrograph of tissue apposing a PSHA coated implant 3 days post-implantation, showing a poorly crystalline CaP phase apposing the coating.

Figure 3.24: TEM micrograph of tissue apposing a PSHA coated implant 3 days post-implantation, showing a speckled network of stained tissue, perhaps proteins on which calcium phosphate precipitates are beginning to nucleate.

Figure 3.23

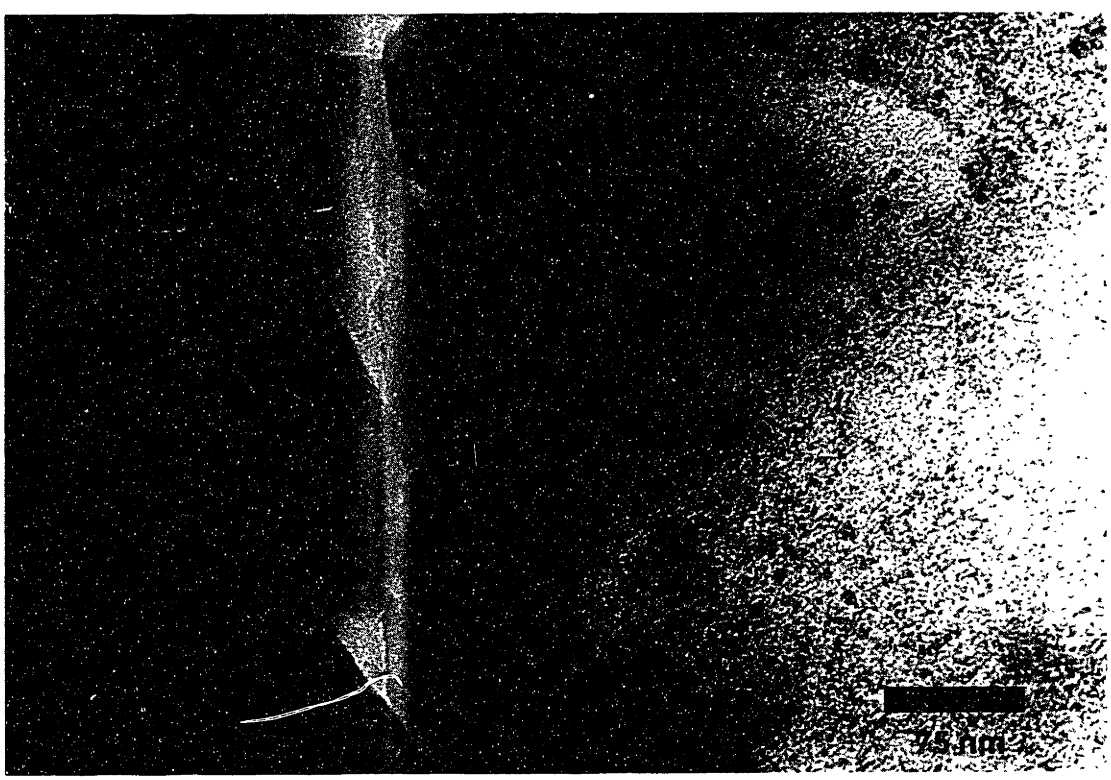

Figure 3.24

Following page

Figure 3.25: TEM micrograph of tissue apposing an annealed-PSHA coated implant three days post-implantation. Larger crystallites can be distinguished within the low-contrast apatite deposits (arrows).

Figure 3.26: TEM micrograph of tissue apposing an annealed-PSHA coated implant three days post-implantation, showing a somewhat denser aggregate of apatite crystallites than that observed after 3 hours.

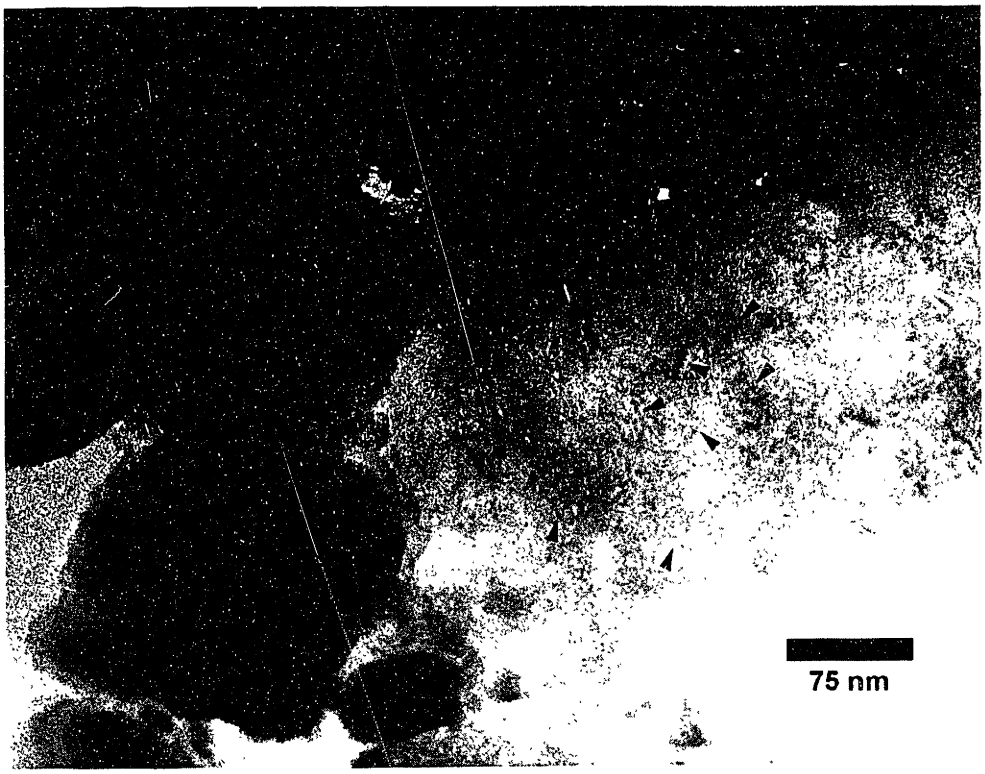

Figure 3.25

Figure 3.26

Following page

Figure 3.27: TEM micrograph of tissue apposing an annealed-PSHA coated implant three days post-implantation, showing a stained border surrounding the implant and directly apposed to it in several places.

Figure 3.28: TEM micrograph of tissue apposing an annealed-PSHA coated implant three days post-implantation, showing stained electron dense globules of various sizes.

Figure 3.27

Figure 3.28

Following page

Figure 3.29: TEM micrograph of tissue apposing a PSHA coated implant 10 days post-implantation.

Figure 3.30: TEM micrograph of tissue apposing a PSHA coated implant 10 days post-implantation, showing apatite deposition primarily comprising larger, discrete crystallites.

Figure 3.29

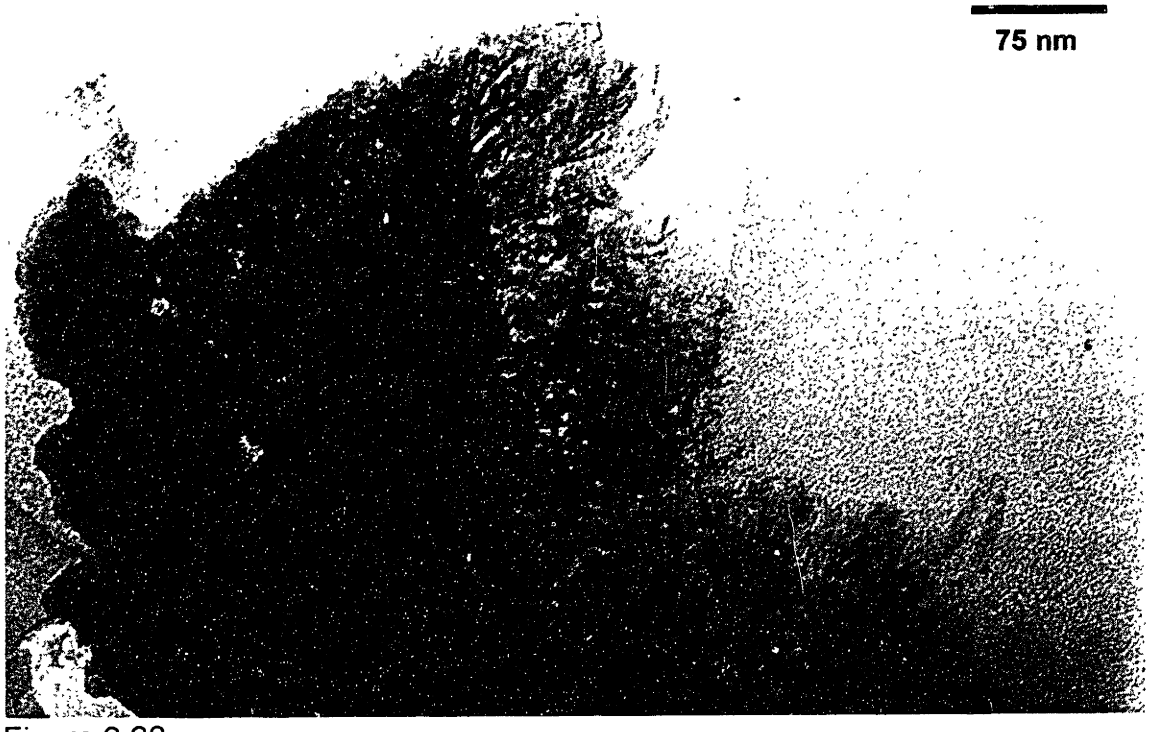

Figure 3.30

Following page

Figure 3.31: TEM micrograph of tissue apposing an annealed-PSHA coated implant 10 days post-implantation, showing apatite deposition primarily comprising a random array of discrete crystallites.

Figure 3.32: TEM micrograph of tissue apposing an annealed-PSHA coated implant 10 days post-implantation, showing apatite crystallites deposited in periodic arrays along the implant surface.

Figure 3.31

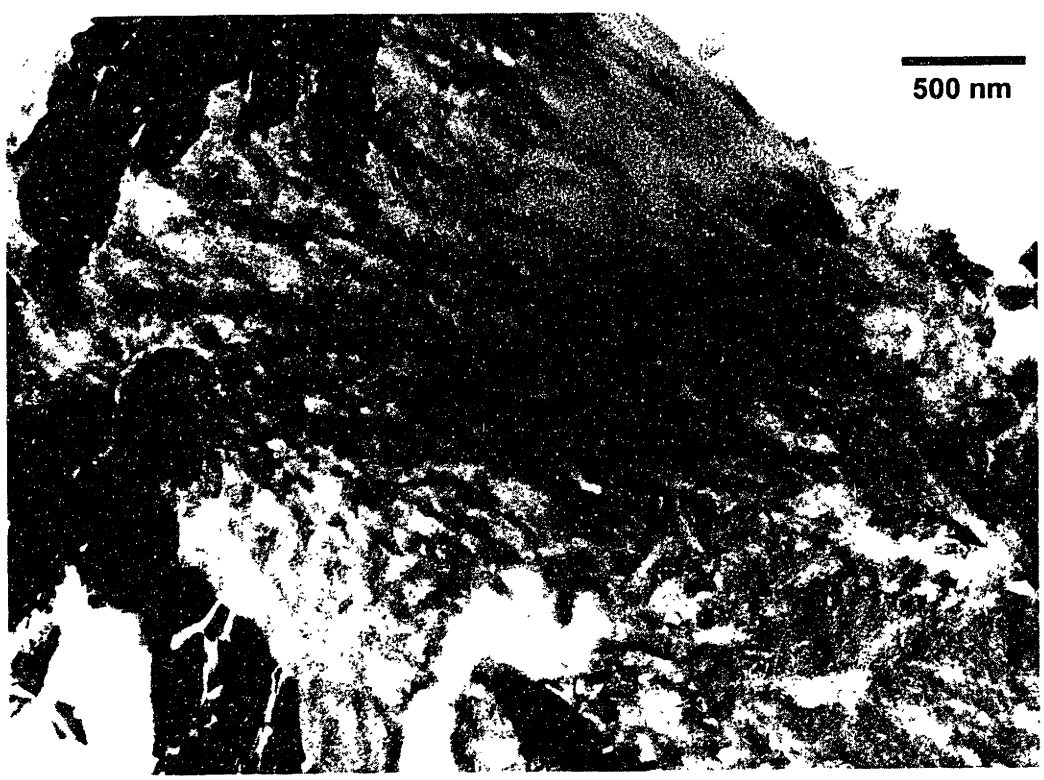

Figure 3.32

Following page

Figure 3.33: TEM micrograph of tissue apposing an annealed-PSHA coated implant 10 days post-implantation, showing in more detail the periodic arrangement of crystallites perpendicular to the surface of the coating.

Figure 3.34: TEM micrograph of tissue apposing an IBAD-HA coated implant 10 days post-implantation, showing both morphologically indistinct CaP deposits and larger, discrete apatite crystallites. The underfocused image enhances the contrast of the individual crystallites.

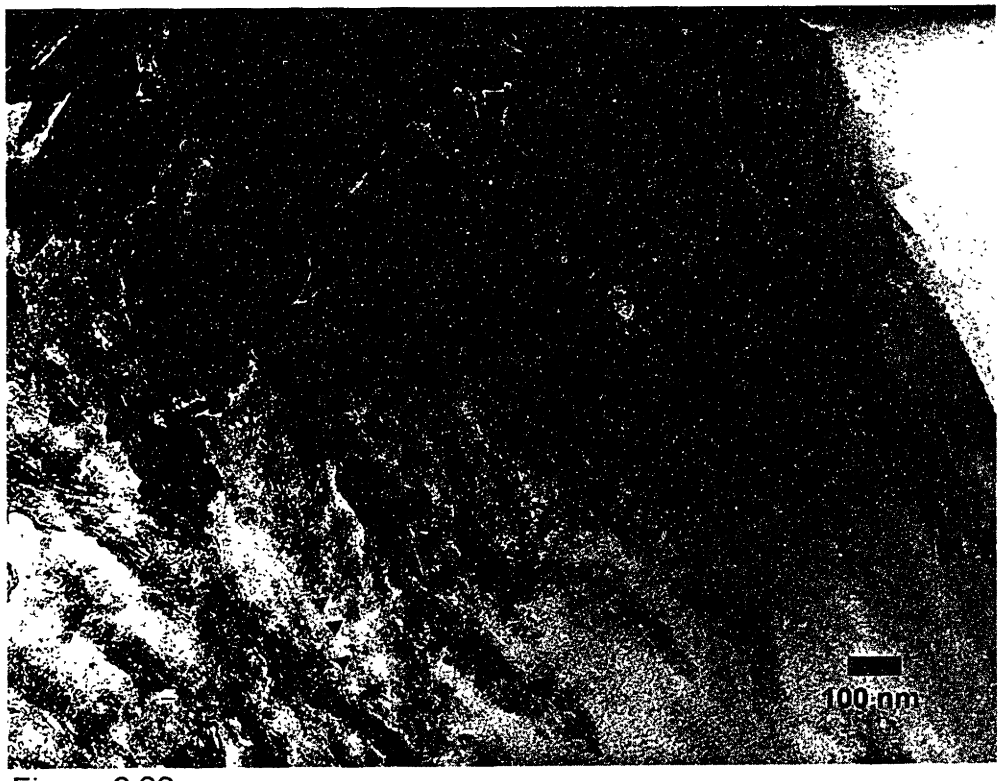

Figure 3.33

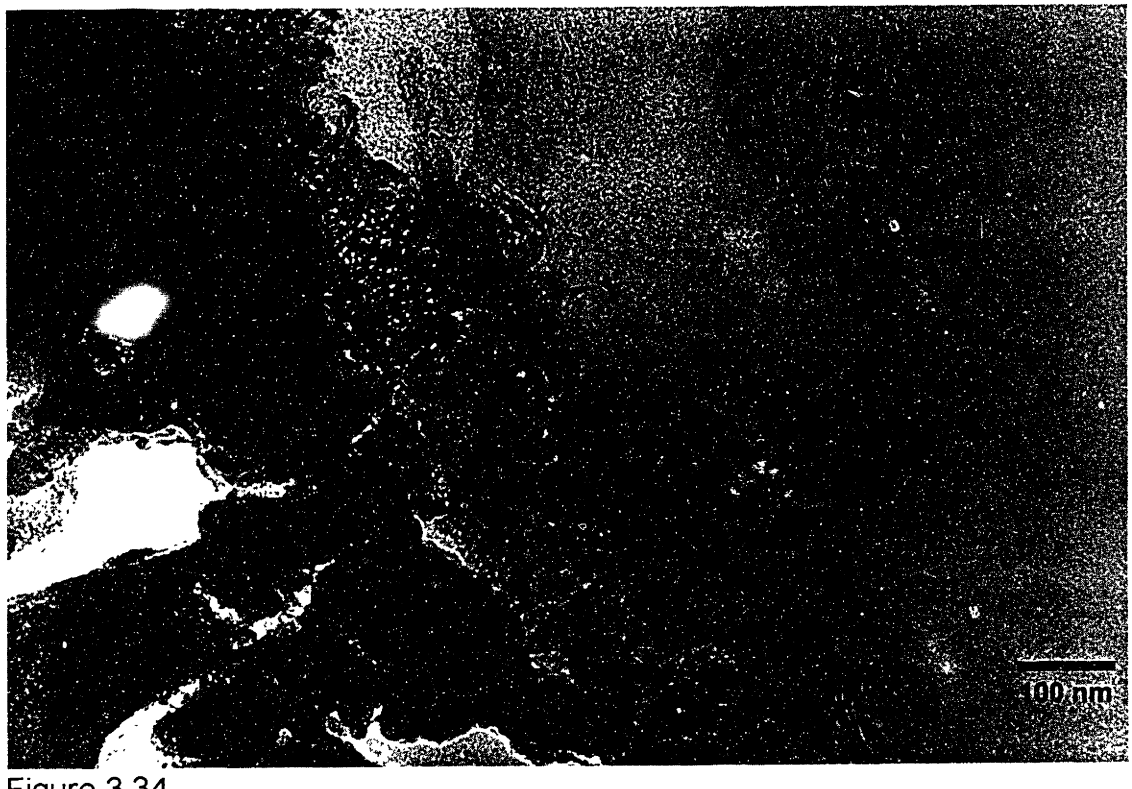

Figure 3.34

Chapter 4

Microstructure of the Oxide Scale on Zr-2.5Nb

4.1.1 Oxidation of zirconium alloys

Oxidized zirconium (OZ) was originally characterized by researchers interested in the use of zirconium as a fuel cladding material in Canadian CANDU nuclear reactors. Zirconium alloys are used as structural components in water-cooled reactors because they have, in addition to beneficial mechanical properties, high corrosion resistance and a favorable neutron cross-section [34]. Zirconia scales have also exhibited high scratch resistance on both flat and curved zirconium substrates, and prosthetic knees formed from oxidized zirconium demonstrate superior wear properties to the Co-Cr-Mo alloys commonly used for prosthetic knees under simulated wear conditions [35]. Zr-2.5Nb has a relatively low elastic modulus (97 GPa), and the oxidized metal is biocompatible and does not corrode or release metal ions *in vivo* [184].

The elements of the oxide microstructure which contribute to the favorable wear properties of OZ have not been extensively characterized, especially because most of the early wear testing of zirconia focused on cubic zirconia [185]. Cracking in the oxide layer is minimized because the oxide grows with a columnar grain structure which is rendered in compression by the predominant growth stresses [40, 41]. Dissolved oxygen in the substrate also enhances the toughness of the alloy, which may enhance the tribological properties of the overlying scale [186, 187]. One study on OZ microstructure determined

that thicker oxide coatings did not enhance wear resistance, despite the increase in hardness with scale thickness [187]. Moreover, the microstructure of the oxide varies greatly with oxidation conditions [188, 189]. Thus, the wear properties of OZ might be expected to vary with elements such as the time, temperature, and atmosphere of oxidation.

TEM provides a method of visualizing both the oxide/metal interface and the thickness of the oxide scale, enabling an accurate description of the oxide microstructure. Most TEM investigations have been conducted by researchers connected to the nuclear power industry; consequently, a large number of TEM studies concern oxidation in steam. The original alloys developed for the nuclear power industry were the Zircaloys (1-4), Zr-Sn alloys which may contain Cr and/or Ni, depending on the formulation. While studies of oxidized Zr-Nb alloys have been conducted since the late 1950's, the field has expanded with the recent development of Zr-2.5Nb for use both in pressure tubes and as fuel cladding [34].

Mechanistic studies of oxidation in zirconium alloys show two oxidation domains separated in time by a transition. Before the transition, a uniform oxide scale with few pores or cracks forms on the metal. This blue-black oxide is protective, in contrast to the white post-transition oxide, which is characterized by large pores and cracks in the microstructure. These form a continuous network from the surface to the metal interface, leading to "breakaway" oxidation [190, 191]. The transition has been ascribed to mechanical failure of the inner layers of the oxide under high compressive growth stresses [192]. In device applications, oxidation is controlled to produce a thin layer of the protective pre-transition oxide; thus, the later phases of oxidation are not a concern in this study.

For Zircaloys, the pre-transition oxide is columnar and primarily monoclinic. A small amount of tetragonal zirconia is also present. Small pores parallel to the interface and larger cavities are also observed. After oxidation at 520°C, a nodular oxide comprising

equiaxed grains is observed; it is not observed at 420°C. It contains large pores and cavities but no tetragonal zirconia [190]. Others observe equiaxed tetragonal grains after oxidation in oxygen, but not steam. In addition, an amorphous interlayer is observed between the oxide and the metal. The initial oxide grains appear to form within this layer as equiaxed tetragonal crystallites, which transform to the monoclinic oxide, followed by columnar growth [41]. The combination of texture and columnar growth in the oxide minimizes compressive stresses in the scale resulting from the difference in molar volume between the oxide and metal [193]. At very high temperatures (>750°C), a white oxide is formed which incorporates numerous pores and cracks visible at the light microscopic level [194]. While higher temperature oxides are typically formed in dry air instead of steam, as in the lower temperature studies, it is still possible to speculate that at higher temperatures there may be no "transition" - only the post-transition oxide forms. Kinetic studies would be necessary to demonstrate this definitively, although TEM investigation of these samples would have helped.

The proportion of tetragonal oxide within the scale decreases with oxidation temperatures and time [193, 195]. Initial concentrations of tetragonal zirconia can be as high as 40%, decreasing to only about 25% before the transition and to about 7% afterwards. However, the amount of tetragonal zirconia at the interface does not vary with time, indicating that the tetragonal zirconia is transforming to monoclinic during oxidation [193, 196]. Intermetallic precipitates containing Fe and Cr are also incorporated into the oxide [41, 196]. The tetragonal grains are stabilized by high pressures or small grain sizes, less than about 30 nm [196]. Extensive work on tetragonal phases in the oxide has also clarified the controversy over the presence of cubic zirconia in the scales. While the tetragonal and cubic phases are nearly impossible to distinguish by diffraction, Raman spectroscopy can differentiate between the two and was used in the above studies [193, 196].

Oxidation of zirconium-niobium alloys is similar to that of the Zircaloys. The oxide is primarily composed of a columnar monoclinic phase, with evidence for a second phase composed of tetragonal zirconia or a mixed oxide compound, $6ZrO_2 \cdot Nb_2O_5$ [189, 197]. The oxidation kinetics exhibit a transition from parabolic to linear, accompanied by the formation of a white oxide [191, 198].

However, there are differences in both the microstructure of the oxide scale on Zr/Nb alloys and the mechanism of oxidation. Differences in oxidation mechanism between the Zircaloys and Zr-Nb alloys indicate a dependence on alloy composition which is typical of alloy oxidation. For example, studies of the microstructure of the oxide/metal interface make no mention of the amorphous layer observed on the Zircaloys [188, 197]. However, because of the low solubility of Nb in Zr at low temperatures, Zr-Nb alloys have a two phase microstructure comprising hexagonal α-Zr and cubic β-Nb at room temperature (Figure 4.1). It is expected that the two phases will oxidize differently. Alloys annealed at temperatures above the Zr-Nb eutectoid at 620°C include a β-Zr phase instead of the β-Nb phase. Cubic β-Zr can dissolve up to 19% Nb. These alloys appear to preferentially oxidize in the Nb-enriched β–Zr regions, leading to oxide "stringers" penetrating into the β grains [197]. However, others have observed delayed oxidation of the β phase [199?]. During oxidation at lower temperatures, the β phase partially transforms to ω-Zr and forms an amorphous oxide [197, 199].

4.1.2 Objectives

The first goal of this study was to characterize the ultrastructure of the interface zone of oxidized zirconium (OZ) currently being used for the femoral component in TKA. This also includes a study of the microstructure of thermally grown zirconium oxide and characterization of the phases present. The second goal was then to identify elements of the microstructure of OZ which contribute to its favorable tribological properties.

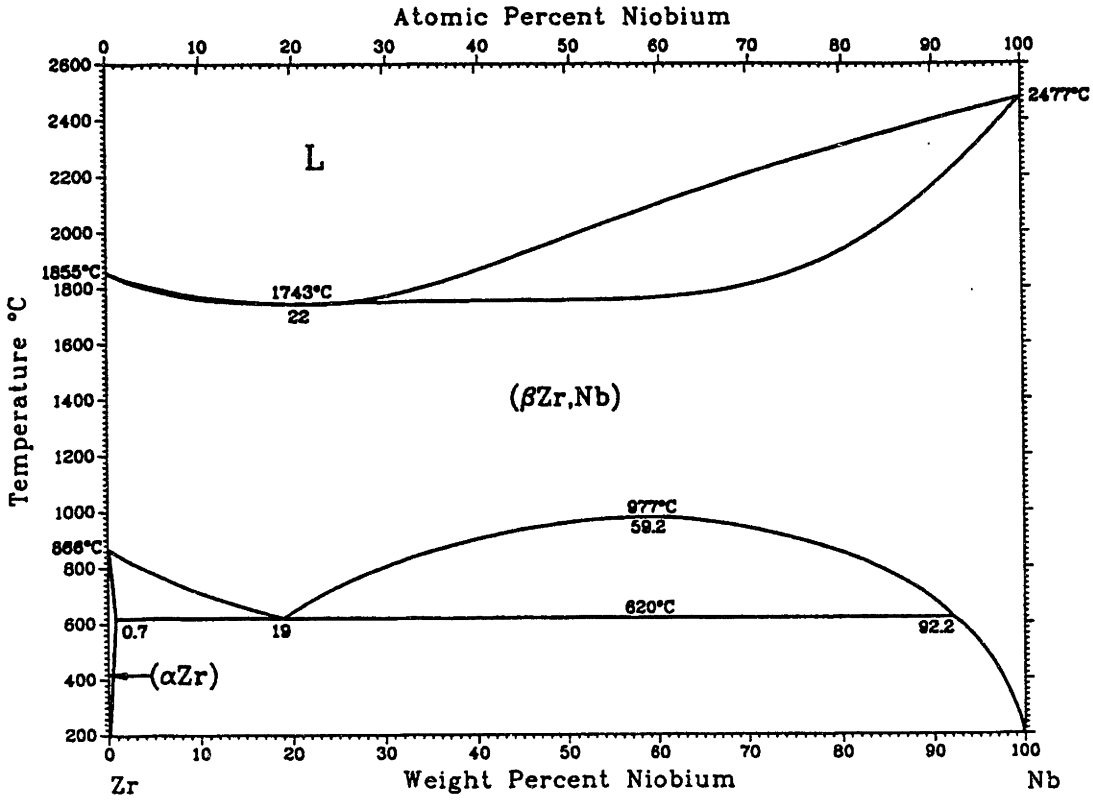

Figure 4.1: Equilibrium phase diagram for the Nb/Zr system [200].

4.2 Materials and Methods

Coupons sliced from Zr-2.5Nb rod (<25-34 ppm Si, 415-620 ppm Fe, 33-39 ppm Al) were oxidized at Smith and Nephew, Inc., (Memphis, TN) in a dry air (Table 4.1). Samples were prepared in several different ways for TEM. Undergraduate students Matthew Van Eman and Wendy Mao prepared a number of samples from circular coupons. These were cut in half along a diameter, and the semi-circles were epoxied together using Hardman's Green epoxy. These sandwiches were then sectioned. Each section was mounted on a brass platen and polished by hand using 600 grit SiC paper until level. Small grooves 3 mm across and 200-300 μm deep were drilled into the sections using an ultrasonic disc cutter, ensuring that the epoxy line was a diameter. The section was then mounted groove side down on a brass platen and polished mechanically using 320 grit SiC

paper until the grooves were exposed. It was polished by hand on 600 grit SiC paper until it was about 100 micrometers thick and with 6 and 1 μm diamond pastes until it was about 40-50 μm thick. A copper slot grid was mounted on the sample with 5-minute epoxy, and the sample was ion-milled on a cold stage to electron transparency. One sample (oxidized three hours at 593°C) was tripod polished according to the procedure described by Anderson [201, 202]. A full discussion of the tripod polishing technique used in this laboratory is in Appendix A.

Oxidation Conditions of Zr-2.5Nb Samples

Temperature (°C)	Time (hours)	Surface
635	1	Longitudinal
635	1	Transverse
593*	0.75	Transverse
593**	1	Transverse
593	3	Transverse
593	4	Longitudinal
593	4	Transverse

*Samples prepared by Wendy Mao according to procedure described in [189]
**Samples prepared by Matthew Van Eman as described in [189]

Table 4.1: Oxidation conditions of Zr-2.5Nb samples prepared for TEM.

In the second method, the samples provided by Smith and Nephew had been machined into small rectangular slices before oxidation, enabling preparation of samples which included both the transverse and longitudinal faces of the material. Slices about 250 μm thick and about 1 cm^2 were cut from the transverse and longitudinal faces of the sample. These were then scored at 2.3 mm intervals using a low speed diamond saw (Buehler) lubricated with water. The opposite face of each slice was polished until the

score marks were exposed to release thin strips including both the oxide and a thin layer of the underlying metal substrate. The strips were coated with 100 Å evaporated gold, sandwiched between two tantalum hemicylinders such that the oxide faces were touching, and encased in a 3 mm (o.d.) stainless steel tube with Hardman Green epoxy. This was in turn encased in a 3 mm (i.d.) brass tube with 5 minute epoxy to reduce burring during sectioning. Cross-sections, approximately 400 μm thick, were cut on a low speed diamond saw lubricated with water and the steel-encased sample carefully removed from the brass with a beveled piece of the steel tubing. This was then mounted on a 1 cm glass platen and polished on a Buehler Minimet automatic polishing machine on a plate embedded with 45 μm diamond particles until smooth. The sample was then flipped on the platen, first measuring the thickness of the platen, with a minimal amount of crystal bond to guarantee the accuracy of final thickness measurements of the sample. The sample was polished to a 250 μm thickness on the 45 μm diamond plate, to 150 μm using a 30 μm diamond plate, and to 120 μm on a 15 μm plate. A nylon polishing cloth (Buehler) charged with 6 μm diamond paste and lubricated with water was used to polish the sample to a 6 μm finish; a 1 μm finish was achieved with diamond paste on a napped polishing cloth (Microcloth™, Buehler). The thickness of the sample was carefully measured, and the sample dimpled from the rougher side using 3 μm diamond paste until it was 25 μm thick. The sample was thinned another 20 μm with 1 μm paste. A copper slot grid was mounted with the slot parallel to the oxide/metal interface with 5-minute epoxy and the sample ion-milled on a cold stage (Gatan) to electron transparency. The sample was milled at a 15° angle until hole appeared, after which it was milled at a 12° angle until the sample was sufficiently thin (25-30 hours) [203].

The samples were examined by TEM in JEOL JEM 2000CX and 2010 instruments, and electron diffraction and dark field microscopy were used to study the microstructure of the oxide and its interface with the metal. Both selected area electron diffraction and

electron microbeam diffraction were used to identify the phases present in the samples. For reference, the electron diffraction patterns of the monoclinic oxide and ω-Zr were simulated using Cerius2, a software package produced by Molecular Simulations, Inc; the scattering factors for x-ray and electron diffraction were not significantly different. Elemental analysis was performed via x-ray energy dispersive spectroscopy (XEDS) in a VG HB603 STEM. Elemental maps generated by the Link software system attached to the XEDS detector were converted to TIFF format using a program written by Dr. Anthony Garratt-Reed. These images were then colorized in Adobe Photoshop to facilitate spatial localization of zirconium, oxygen, and niobium. Some elemental analysis was also performed in the JEM 2010. However, because the detector had not yet been calibrated and the standard copper holder (rather than the low emission Be holder) was used to mount the sample, analysis in the JEM 2010 was limited to identification of elements present in the sample, not their proportions.*

Thermodynamic stability diagrams showing the stability of Zr and Nb with respect to oxygen and the thermodynamically stable oxide phases were compiled using equations calculated by Dr. Julia Duncan using Outokumpu HSC Chemistry for Windows 2.0.

4.3 Results

Pre-oxidation processing of the metal results in an anisotropic microstructure within the metal. As the metal is rotary-forged into rods prior to oxidation, the metal microstructure is elongated along the long axis of the rod (Figure 4.2). This results in a significant difference in microstructure between the transverse and longitudinal directions of the metal. In the longitudinal direction, the microstructure comprises large, elongated grains about 1 μm across alternating with smaller grains several hundred nanometers across (Figure 4.3). XEDS shows that these smaller grains contain a higher concentration of Nb

* The samples produced by the above procedure are too thick to fit in the Be holder, which is also the double tilt holder for this particular microscope.

than the larger grains and thus correspond to β-Zr grains (Figure 4.4) (see below). The extensive cold work also generates a large dislocation density in the metal (Figure 4.5).

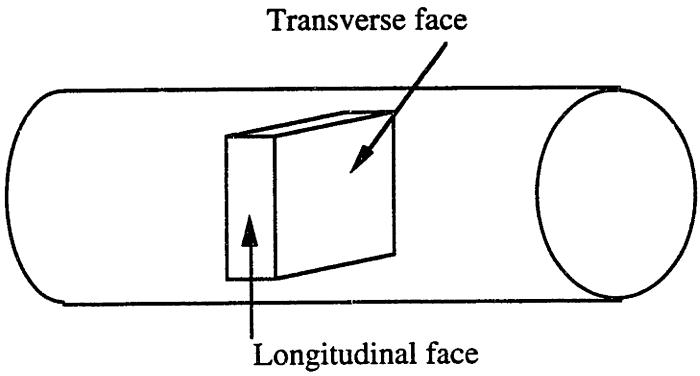

Figure 4.2: Directions in rod of Zr-2.5 Nb due to processing of alloy barstock.

The Zr-2.5wt.% Nb alloy falls in a two phase region in the Zr-Nb phase diagram (see Figure 4.1). Consequently, the microstructure comprises grains of both α-Zr, containing less than 1% Nb, and a high-niobium phase. Above the eutectoid temperature, the second phase is β-Zr, containing up to about 20% Nb (for the Zr-2.5Nb alloy). Below it, the second phase comprises metallic niobium, which can dissolve up to 10% Zr at 615°C. Within the metal, β–Zr grains were identified by both electron diffraction and elemental analysis. In general, the β grains were somewhat smaller than the α grains and measured 0.5 μm x 1-2 μm in the longitudinal direction. The metal microstructure was not viewed in cross-section; as a consequence of the sample preparation protocol, the metal microstructures on the transverse and longitudinal samples were related to each other by a 90 degree rotation in the plane of the sample. Alternation of the α and β grains indicates that the Nb-rich β grains probably form in sheaths around the α grains [204]. In this study, variations in oxide microstructure and growth kinetics were correlated to these differences in metal microstructure.

The oxide exhibited two morphologies. The bulk of the oxide had a columnar microstructure with grains ranging in width from 20-100 nm (Figure 4.6). Statistical analysis of covariance (ANOVA) showed a significant effect of oxidation temperature, location within the oxide (air/oxide interface, metal/oxide interface), and metal microstructure on grain size (Figure 4.7). A significance level of $p < 0.025$ was chosen because significance was tested with two 2x2 ANOVA tests, rather than one 2x2x2 [205]. The dependence of grain width on temperature and metal microstructure (longitudinal versus transverse) parallels the growth kinetics of the oxide. Not only did oxidation rate increase with temperature, it was also faster on the transverse face of the metal than on the longitudinal face [36].

The columnar oxide was continuous through the entire oxide scale, and the top of the scale exhibited scalloping. The scallops were concave towards the oxide/metal interface and corresponded to the grain boundaries between columns. The grains themselves were typically arranged in a staggered fashion (like brickwork courses) where parallel grains did not have parallel termini. These features were identified by contrast variations in the micrographs. There were frequent exceptions to the staggered arrangement of grains, however, where the ends of three or four grains were coplanar, although the planes of the spanning grain boundary were not typically parallel to the metal/oxide interface (Figure 4.8). Moreover, adjacent grains with coplanar grain boundaries tended to exhibit similar image contrast. In general, oxide grain termini did not appear to correlate with features in the metal substrate such as prior grain boundaries. However, the metal grain boundaries may nevertheless have been preserved in the microstructure of the oxide. Figure 4.9 shows a difference in phase contrast in the oxide which resembles a grain boundary. While the boundary between the two regions is clear, a few oxide grains lie across it. Elemental analysis showed that the columnar oxide did not contain detectable amounts of niobium (<1-2%).

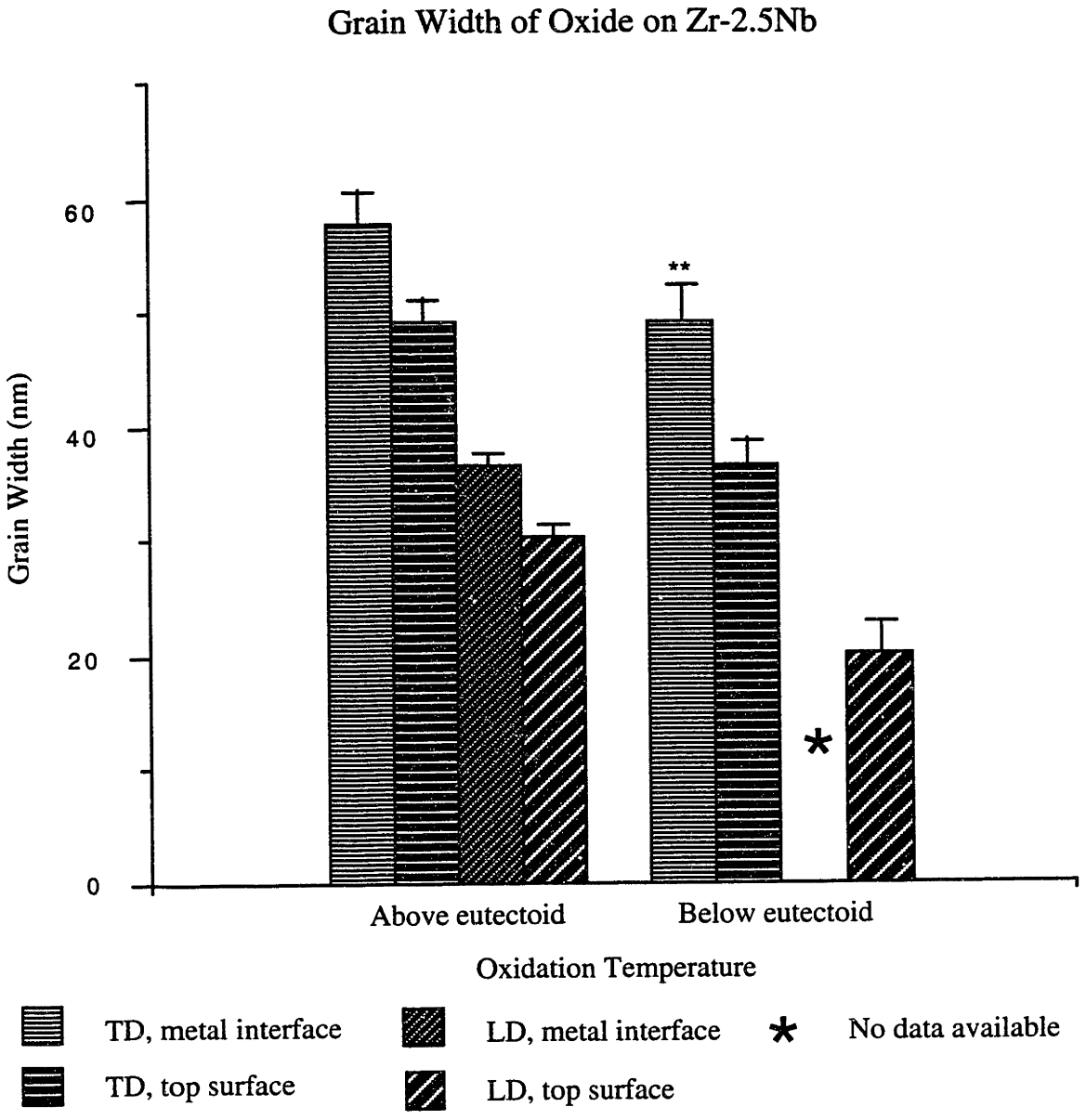

Figure 4.7: Dependence of grain width in the oxide scale grown on Zr-2.5Nb on substrate microstructure and oxidation temperature. TD=transverse direction; LD=longitudinal direction; top surface=oxide/air interface. **Sample oxidized for three hours.

Higher Nb content was observed in regions which coincided with a second oxide microstructure. Figure 4.10 shows one located within 0.5 μm of the oxide/air interface;

this microstructure was primarily seen in the upper (i.e.: close to the oxide/air interface) and middle sections of the oxide scale; it was not observed at the oxide/metal interface (e.g. in formation; see below). The grains of this oxide were smaller and more equiaxed, and they tended not to follow the columnar organization of the surrounding oxide. While the regions of equiaxed oxide grains tended to have a relatively smooth interface with the surrounding columnar oxide, elemental analysis revealed that the trailing side (away from the oxide/air interface) of the high niobium regions tended to have niobium "fingers" reaching in the direction of the oxide/metal interface. These fingers were entirely contained within the equiaxed oxide microstructure. The equiaxed regions in scales on both the longitudinal and transverse surfaces were about 0.3-0.5 μm across and achieved lengths of 1 μm or more, about the same size as the β-Zr grains in the metal. While the shape and orientation of these regions tended to parallel that of the β-Zr grains in the allot, not enough of these features were observed to establish a definitive relationship. The equiaxed regions did not form a continuous network within the scale, rather, they were morphologically isolated from one another within a continuous matrix formed by the columnar oxide.

Two different interfacial features were observed in all samples. The first was a direct interface between the oxide and the metal, with no intervening layer (cf. Figure 4.6). This interface was scalloped such that the scallops were concave away from the metal and contained no cracks or voids. In Figure 4.6, an oxidized structures can be observed which may either correlate with internal or grain boundary oxidation. The second interfacial feature consisted of small grains, 250-300 nm across, which typically lay along the width of several oxide grains. They extended approximately 100 nm into the metal, from which they were distinguished by the larger size of the metal grains (Figure 4.11). With one exception, elemental analysis showed no excess niobium in these interfacial grains with respect to the alloy or the oxide. Their oxygen content relative to that in the oxide scale or the adjacent alloy could not be determined. However, microdiffraction of the interfacial

grains revealed that they probably consist of α-Zr, but the measured d-spacings were about 0.13-0.15 Å shorter than those given in the literature.

Indexing of electron diffraction patterns from Zr-Nb alloys and their oxides is complicated by the large number of possible phases. Zirconium metal exhibits two and possibly three different polymorphs in this experiment, the α and β phases shown on the phase diagram and an ω phase which is metastable at low temperatures and pressures and does not appear on the equilibrium phase diagram. ZrO_2 has three different polymorphs. The monoclinic phase predominates at almost all temperatures and compositions. The tetragonal and cubic phases are only stable at higher temperatures and pressures, but they can also be stabilized by impurity additions such as yttrium or magnesium. In addition, Nb forms several oxides, including NbO, NbO_2, and Nb_2O_5, depending on the partial pressure of oxygen. At atmospheric pressure, the pentoxide is the most stable oxide. The zirconia-niobia phase diagram is also quite complex, due to the formation of a line compound, $6ZrO_2 \cdot Nb_2O_5$, at about 90% (monoclinic) zirconia (Figure 4.12). Fortunately, niobium metal appears in this experiment with only one (bcc) polymorph. Table 4.2 shows some of the allowed x-ray reflections from some of these phases. Note especially the reflections around 2.95 Å. This reflection provides the best means of distinguishing the tetragonal and monoclinic phases of ZrO_2, yet it also appears in the diffraction patterns of cubic zirconia (not shown) and the mixed oxide! Fortunately, the cubic and tetragonal phases can be distinguished via Raman spectroscopy, and the cubic phase does not appear to form in this system [196].

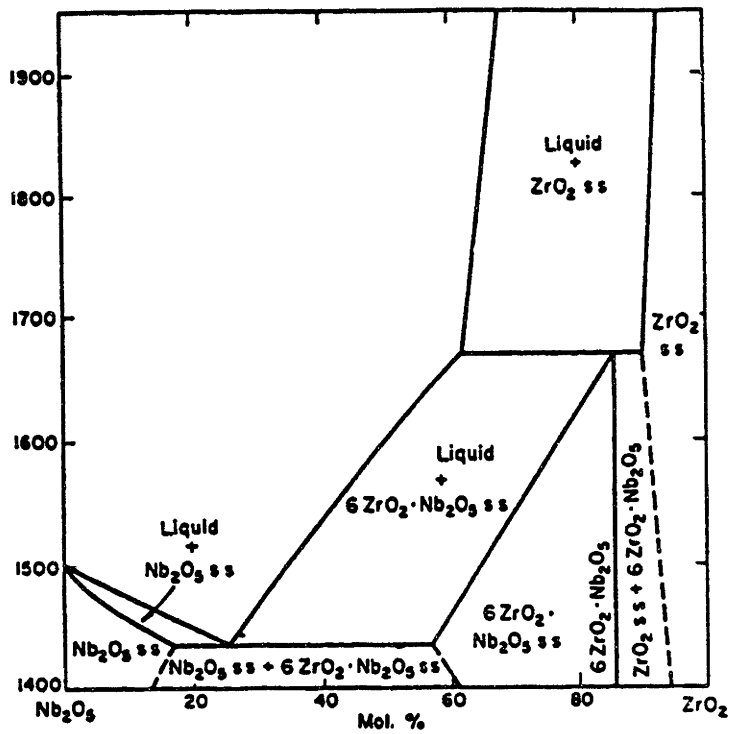

Figure 4.12: Equilibrium phase diagram of the zirconia/niobia system [206].

Both x-ray and selected area electron diffraction showed that both the columnar and equiaxed oxides comprised primarily monoclinic zirconia, with small amounts of tetragonal zirconia (Figure 4.13) [207]. While the d-spacings for planes in the tetragonal oxide are very similar to those for the monoclinic oxide, the tetragonal phase can be distinguished from the monoclinic by the (111) planes, which have a d spacing (2.96 Å) between those for the monoclinic (111) and (-111) planes (2.84 and 3.16 Å, respectively). In the columnar oxide, strong crystallographic texture was also revealed by heightened intensities of both the $(111)_m$ and $(111)_t$ reflections. The texture corresponds to a fiber texture with the [111] axis along the length of the elongated columnar grains. The equiaxed oxide did not exhibit an oriented texture.

Scattering Planes in Oxidized Zirconium Phases

Zirconia (monoclinic)			Zirconia (tetragonal)			$6ZrO_2 \cdot Nb_2O_5$		
d(A)	I	hkl	d(A)	I	hkl	d(A)	I	hkl
3.69	14	110	2.96	100	111	3.61	9	101
3.64	10	011	2.60	18	002	2.95	100	111
3.16	100	-111	2.54	25	200	2.64	17	002
2.84	68	111	1.83	65	202	2.56	18	020
2.62	21	200	1.81	35	220	2.48	12	200
2.61	11	020	1.57	25	113	1.84	23	022
2.54	13	002	1.54	45	311	1.81	21	202
2.21	12	-112	1.49	12	222	1.78	28	220
1.84	18	220				1.54	22	131
1.81	22	022						
1.80	13	-221						
1.65	11	310						
1.54	8	131						

Table 4.2: Permitted scattering planes and relative scattered intensities for oxidized zirconium phases [96, 206].

Electron diffraction demonstrated that the tetragonal oxide is present throughout the oxide thickness in both the columnar and equiaxed areas. In addition, tetragonal grains appear to have the same morphology and appearance as the monoclinic grains; they could only be distinguished by electron diffraction. Elemental analysis in the JEM 2010 showed the same amount of niobium in the columnar tetragonal grains as in monoclinic grains in an adjacent area of the scale. Thus, it is unlikely that the oxide identified as tetragonal in these regions of the scale is actually composed of the mixed oxide $6ZrO_2 \cdot Nb_2O_5$. However, the large amounts of niobium in the equiaxed regions of the scale make distinction of the two phases difficult, and it is highly likely that the mixed oxide is present in the equiaxed regions of the scale.

Within the oxide, small, flat lower contrast structures parallel to the metal surface were observed between individual columnar grains. These were fairly common in the inner sections of the oxide; they were observed very infrequently at the top surface (Figure 4.14). They were frequently associated with small, equiaxed grains within the oxide columns. These smaller grains do not show excess niobium with respect to the rest of the oxide, and electron microdiffraction revealed that they probably comprise monoclinic zirconia. Longer structures extending across two or three grains (columns) were also observed. In the thicker areas of the wedge-shaped TEM specimens, these features were filled with aperiodic material which failed to exhibit long range order (LRO) in HRTEM observations. Closer to the thin edge of the samples, these features appeared empty. However, because non-crystalline phases tend to mill faster than crystalline phases, any material that was once contained within these structures was probably eroded in the ion-mill.

XEDS of these features in the STEM showed peaks corresponding to both tantalum and silicon; the latter is an impurity element in the alloy. The resolution of the detector is not good enough to distinguish between the Ta Mα line at 1.71 keV and the Si Kα line at 1.74 keV. Therefore, in order to distinguish the tantalum, which could have sputtered onto the sample during ion milling, from the silicon, additional XEDS of the Ta hemicylinders was performed. Comparison of the relative intensities of the Ta Lα and Mα lines enabled the identification of Si . In addition, XEDS showed that no silicon was present in the adjacent columnar oxide. Thus, the small "cracks" are most likely filled with an aperiodic silicate phase. However, the diffusion pump in the ion mill uses a silicone based oil, so the remote possibility exists that the Si was incorporated during milling. This is unlikely because Si was only observed in the aperiodic material, not in the bulk of the oxide.

Similar low-contrast features extending across 5 or more grains were also observed (Figure 4.15). In some regions, especially in the thicker areas of the sample, these features

contained some aperiodic material. These features were sometimes associated with the leading edge of areas containing the small, equiaxed oxide grains discussed above. These "defects" appeared to be quite stable and do not appear detrimental to oxide integrity. Despite long exposure times in both the electron beam and the argon plasma used for sample thinning, they did not appear to propagate, and thin areas of oxide which were attached to the bulk over very small areas did not come detached from the sample. In addition, similar large electron-translucent features were observed in thicker areas of the sample which were not otherwise electron transparent, indicating that these features were probably not caused by electron beam damage to the material. Some of these features are located quite close to the oxide/metal interface.

Within the metal, intragranular areas were observed where niobium was observed to have segregated from the zirconium (Figure 4.16). The Nb segregated into small laths about 45 nm wide alternating in a lamellar fashion with laths which exhibited microdiffraction patterns corresponding to α-Zr. Electron diffraction and dark field microscopy showed that the Zr-rich lamellae probably originated from a single metal grain (Figure 4.17). Because the feature in Figures 4.16 and 4.17 was close to the hole in the TEM sample, it is difficult to locate this feature with respect to the oxide/metal interface, but it is definitely within a micrometer, probably closer. The Zr-rich lamellae also contained about 20% oxygen; the Nb-rich lamellae contained about 75% niobium, indicating that the lamellae probably contain a Nb-enriched β-Zr phase (βenr). Both the neighboring metal grains (farther from the oxidation front) and the Nb-rich lamellae contained almost no oxygen.

Following initial identification of the lamellae, subsequent searching of the oxide/metal interface of the high temperature/longitudinal oxide revealed that this was a relatively common alloy interface feature. The Nb-rich lamellae extend into the oxide from the metal (Figure 4.18). XEDS not only revealed the segregation of the niobium and

zirconium but also showed that some of the niobium-rich lamellae did not themselves contain oxygen (Figure 4.19). The extension of these oxygen-poor lamellae across the oxide/metal interface indicates that oxidation is delayed with respect to the location of the oxidation front. Elemental analysis also confirmed that the segregation began in the metal and continued across the metal/oxide interface into the oxide, and similar features were observed entirely contained within the oxide. In Figure 4.18, the high niobium region in the metal adjacent to the segregated area is probably a β-Zr grain.

Diffraction from the oxidized lamellae showed that they include monoclinic zirconia and either tetragonal zirconia or the mixed zirconia/niobia ($6ZrO_2 \cdot Nb_2O_5$) phase (or both). Electron diffraction also confirmed the presence of zirconia both in-between the capillaries and on either side of the oxidized segregated region. Selected area diffraction and microdiffraction of the unoxidized capillaries showed a reflection (d=1.996 Å) which does not correspond to strong reflections from any of the oxide or alloy phases [206]. While it does correspond to a weak reflection from ω-Zr, (111), the high forging and oxidation temperatures make the thermal formation of ω, a metastable phase, unlikely [208]. Published time-temperature-transformation diagrams of eutectoid Zr-Nb show that ω-Zr is only stable below 532°C (Figure 4.20) [209]. The TTT diagram also demonstrates that any ω present in the original bar stock was transformed to β-Zr when the sample was heated to the oxidation temperature. While athermal ω can form within β-Zr on cooling from above the ω-start temperature at 532°C, the samples in this study were cooled too quickly to allow this transformation [210].

The features described above originated in elongated β-Zr grains oriented obliquely to the oxide/metal interface. However, most of the elongated β-Zr grains in the longitudinally oriented samples are oriented parallel to the interface. These present a much longer cross-section (by a factor of at least 2) to the advancing oxidation front. Some of these grains appear to oxidize to form the equiaxed oxides described above. However,

they sometimes exhibit segregation similar to that described above (Figure 4.21). Near the air/oxide interface, regions were observed within the columnar oxide which nevertheless exhibited high niobium concentrations and segregation of the zirconium and niobium (Figure 4.22). Initial observations suggested they have the same microstructure and composition as the oxide of the α-Zr. However, they can be identified in TEM by the small lamellar grains. Of course, elemental composition had to be confirmed by microanalysis (Figure 4.22c). The microstructure of this oxide is much more disorganized than that resulting from oxidation of the obliquely oriented β-Zr grains. This microstructure appears to originate before proper oxide formation occurs at the oxide/metal interface, as in Figure 4.21.

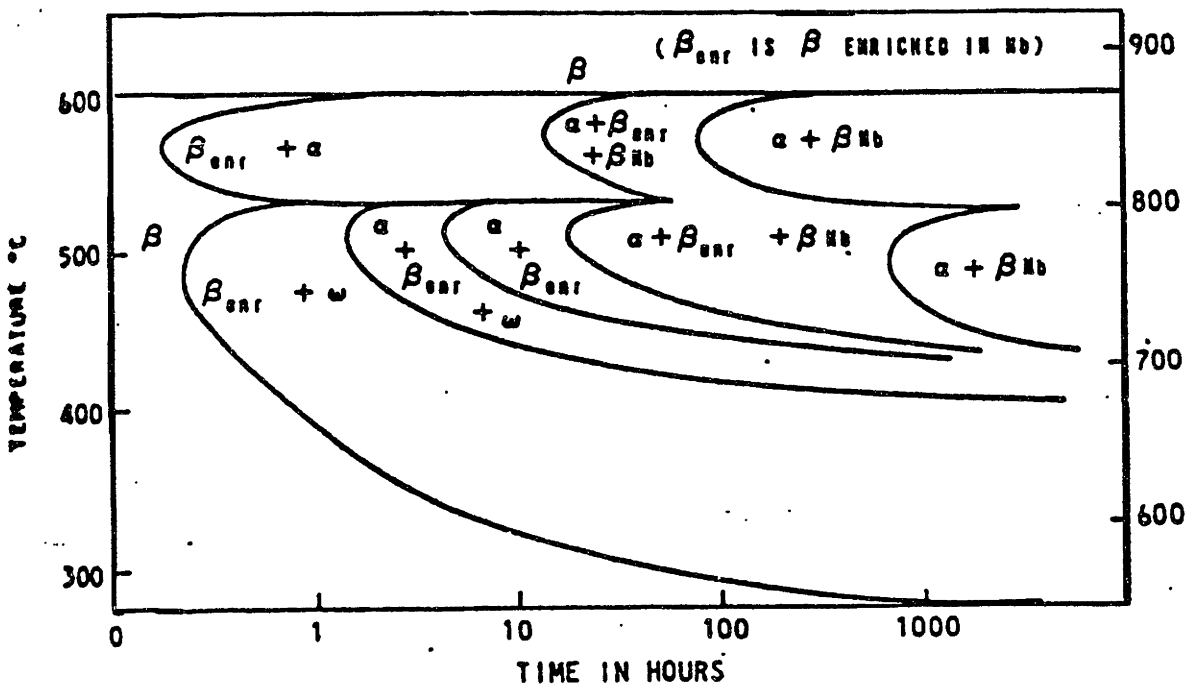

Figure 4.20: Time-temperature-transformation diagram for Zr-20Nb [209].

Similar segregation was also observed in oxide scales on the transversely oriented samples. A somewhat different segregated microstructure was also observed (Figure 4.23). The segregated microstructure comprised grains with a slightly different microstructure from that of the surrounding oxide, with grain boundaries strictly parallel to each other and very narrow grain widths. The overall widths of the Nb-enriched features are smaller than the average width of the β-Zr grains in the metal.

4.4 Discussion

One of the unique properties of the Zr-ZrO_2 system, and the one which has made it of interest to both the nuclear reactor and orthopedic industries, is the high integrity of the interface between the oxide and the substrate. The results described here provide multiple reasons why the oxide in this system should be adherent. There are no voids or pores in the interface which could lead to spallation or other catastrophic failure. The columnar oxide may also be more resistant to shear across the grain boundaries, decreasing the propensity for intra-oxide spallation under wear.

Some features were observed which were apparently inconsistent with the demonstrated wear performance of this material. Most notable among these are the low-contrast features of various sizes observed throughout the thickness of the scale. In most cases, these features are filled with amorphous material. Features similar to the smaller low-contrast laths have been observed in other oxidation experiments using Zr-2.5Nb alloys with similar impurity levels [188]. That these features exhibit enhanced concentrations of impurity atoms, particularly with respect to the surrounding oxide, indicates that they are probably an amorphous oxide phase. These features may act as getters for impurity atoms which are insoluble in the oxide. While our observations indicate that the larger features are probably not artifacts of sample preparation, experiments similar to those conducted in [188] would be necessary to confirm this.

The variation of oxide grain width with depth in the oxide scale, alloy microstructure, and oxidation temperature was also somewhat intriguing. This phenomenon has been observed previously, but no explanation was proposed at that time [211]. One possible explanation for this variation is the decrease in the growth rate resulting from the parabolic variation of oxidation rate with time [207]. Moreover, the oxidation rate is faster on the transverse face of the metal than on the longitudinal face, and, of course, the oxidation rate also increases with temperature [207]. Most of these relationships are paralleled in the oxide grain widths. Grain widths are larger on the transverse face of the metal and for oxides grown at the higher temperature. However, the oxidation rate is faster at the initial stages of oxidation, yet the oxide formed at this stage, the upper layer of the scale, has smaller grains than the oxide at the bottom of the scale. Thus, a simple kinetic argument is inadequate to explain this phenomenon. However, slower growing crystallites may have more time to make lateral adjustments to minimize growth stresses or increase the degree of epitaxy, implying that a combination of thermodynamic and kinetic effects may describe the variation of grain width with depth in the oxide scale.

In addition, lateral grain boundaries in an inward growing scale such as that on Zr-2.5Nb may form if internal oxide grains nucleate in an oxygen saturated alloy in advance of the advancing scale front and are overtaken by it. If the internal grain is not favorably oriented for rapid growth, when it is overtaken by the oxidation front renucleation will take place to form an adjacent oxide grain. There are many features in an alloy which disturb the periodicity of the atomic arrangement and may thus become nucleation sites for internal oxide formation. Indeed, prior cold work in the alloy has led to an extensive network of dislocations and subgrain boundaries visible via TEM. Because a dislocation is also a localized area of higher elastic energy and chemical potential, it can serve as a nucleation

site for the oxide, resulting in internal oxide formation ahead of the advancing oxide scale front.

At small concentrations of Nb, Nb increases the oxidation rate [212]. Indeed, some investigators note an increased rate of oxidation at the β-grains in Zr-2.5Nb pressure tube alloys, resulting in oxide ridges at the interface [197, 213]. It is therefore somewhat odd that, in this investigation, segregation within the β-grains led to unoxidized Nb-rich lamellae in an oxidized zirconium matrix. However, delayed oxidation with respect to the oxidation front has been observed in Nb-enriched Zr phases in Zr-2.5Nb alloys [211]. It thus appears that higher concentrations of Nb actually slow the oxidation rate, perhaps via a doping effect. Using the Kroger-Vink notation, Nb^{5+} is incorporated into the oxide scale as follows:

$$Nb_2O_5 + V_O^{\cdot\cdot} \xrightarrow{ZrO_2} 2Nb_{Zr}^{\cdot} + 5O_O^x \qquad \text{(Eqn. 4.1)}$$

The reduction in the concentration of oxygen vacancies reduces diffusion of oxygen through the oxide, reducing the oxidation rate. The question of whether niobium is actually incorporated into the scale as a pentavalent cation is crucial, however, because lower valencies of niobium either leave the oxygen vacancy concentration unchanged (as for Nb^{4+}) or even increase it, as follows:

$$NbO \xrightarrow{ZrO_2} Nb_{Zr}^{''} + O_O^x + V_O^{\cdot\cdot} \qquad \text{(Eqn. 4.2)}$$

The question, then, is which of these cations form. Figure 4.24 shows the relative stabilities of the various Nb cations at 600° and 635°C. While Nb_2O_5 is the most stable oxide phase, Nb^{5+} will not form unless sufficient oxygen is present. Because of the diffusion of oxygen through the scale to the alloy, it is most likely that pentavalent niobium

is incorporated into the oxide, and not tetra- or divalent species (see below). It should also be noted in Figure 4.24 that zirconium is stable with respect to oxidation at partial pressures less than log PO_2 = -53.2 at 635°C and -56 at 600°C.

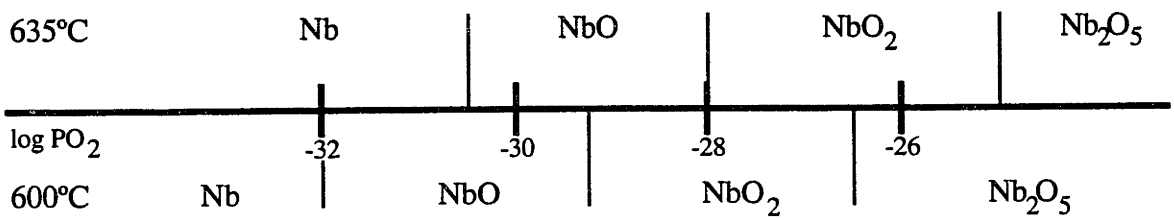

Figure 4.24: Stability diagram of niobia phases with respect to oxygen partial pressure at 600°C and 635°C.

The diffusion of oxygen into the β-phase has a second, related, effect on the alloy microstructure. Because of the low solubility of oxygen in β-Zr, diffusion of oxygen into β-Zr causes a transformation to α-Zr+β-Nb [214].* Oxygen dissolved into the α-Zr stabilizes the phase with respect to the phase transformation to β-Zr [214]. At lower temperatures, β-Zr decomposes to ω-Zr+β-Zr(enr), β-Zr enriched with Nb [197]. Others have observed a fine columnar structure near the metal/oxide interface comprising α-Zr and an oxide (the oxygen stabilizes α-Zr, raising the temperature of the transition to β-Zr). It was proposed that the diffusion of oxygen into the alloy led to the formation of an α+β+oxide microstructure predicted by the ternary phase diagram [198]. Within the alloy, the oxide formed by internal oxidation is expected to consist of ZrO_2; in the scale, the mixed oxide, $6ZrO_2 \cdot Nb_2O_5$, is expected to form as the niobium oxidizes and that oxide reacts with the surrounding ZrO_2.

Thus, one can propose an oxidation mechanism for the β-Zr grains which leads to the segregated microstructure observed. As oxygen diffuses into the β-grains, they begin

* β-Nb is not a special phase of niobium - there is no α-Nb. Instead, it indicates a Nb phase which can dissolve up to about 7% Zr, depending on temperature; likewise, β(enr) indicates β-Zr in which greater than 20% Nb is dissolved.

to transform into a two phase system comprising α-Zr and a bcc Zr-Nb solid solution which is depleted in Zr to some extent. Oxygen continues to diffuse into the newly formed α grains, and they also begin to oxidize.

In the meantime, oxygen is not very soluble in remaining bcc Zr-Nb solid solution and does not diffuse into it in advance of the oxidation front [57]. While the solubility of oxygen is small, it is enough to allow the formation of Nb^{5+} and the eventual reaction of Nb_2O_5 with ZrO_2 to form the mixed oxide, $6ZrO_2 \cdot Nb_2O_5$. Moreover, the concentration of Nb is great enough in this phase (about 75% by XEDS) that its oxide will be in the two-phase mixed oxide/Nb_2O_5 region of the phase diagram. The diffusion of Nb^{5+} through niobia is fast, and as oxygen diffuses in from the oxide, Nb^{5+} will diffuse from the newly formed oxide into the zirconia scale, resulting in the doping effect described above [215]. This reduces both oxygen diffusion and the oxidation rate and results in the unoxidized, Nb-enriched capillaries observed at the oxide/metal interface.

There is a second product of β-Zr oxidation, the equiaxed oxide. It is not surprising that this Nb-enriched oxide should have formed with a different microstructure from the columnar oxide which dominates the scale (and which contains almost no Nb). The microstructure of an oxide depends upon its composition. It is not even unexpected that the oxide should have been observed at the air/oxide interface and in the interior regions of the oxide but not at the metal/oxide interface. In oxides on the longitudinal surface of the alloy, the oxide scale is thin enough (on the scale of the α-grain width) that if Nb-enriched oxide exists in the top or middle regions of the oxide, then the oxidation front may not penetrate through the α-grains to another row of β-grains before the material is removed from the furnace. If the β-Zr grains are oriented obliquely to the surface, this will not be true, however.

However, a significant amount of β-oxidation was observed at the metal/oxide interface on one of the samples, and the equiaxed oxide was not observed in formation.

Again, this is to be expected -- one mechanism of oxide formation ought to be favored, either thermodynamically or kinetically, over another. It is unlikely that one would observe two mechanisms occurring at the same time in the same sample. As a result, however, it is simplistic to say in the above paragraph that equiaxed oxide is not observed near the metal/oxide interface or in formation simply because the oxidation front has not penetrated to the originating β-grain. Moreover, evidence for oxygen-driven segregation of Nb in the β-Zr grains was observed in the upper regions of the oxide.

It is unfortunate that no good TEM specimens including the metal/oxide interface were produced from samples oxidized for four full hours below the eutectoid. While no segregation was observed at the interface in samples oxidized for shorter times, if the segregation is limited by kinetics, it might have required the extra hour to proceed at the lower temperature. However, very good images of the upper regions of the oxide were obtained for these samples, and these have one very telling feature -- the Nb-enriched lamellae extending toward the metal/oxide interface (Figure 4.10). The area of the equiaxed oxide which oxidized later (because it is further from the air/oxide interface) exhibits segregation of niobium into a Nb-enriched and a Nb-poor (Zr-enriched) region. It may indeed be that the kinetics of the oxygen-driven transformation from β-Zr to α-Zr + β-Nb are slow enough at the lower oxidation temperature to prevent it from occurring. Even so, there may be enough time for some segregation of niobium as oxygen diffuses into the lower regions (towards the metal/oxide interface) of the β-grain.

Moreover, this transformation from β-Zr to α-Zr + β-Nb is still thermodynamically favored below the eutectoid temperature. The degree of undercooling required to overcome the activation energy probably depends on the amount of dissolved oxygen in the alloy. Because of this, and because this transformation does not take place above the eutectoid, the mechanism which leads to formation of the equiaxed oxide will be described with the assumption that this transition does not take place. Even if this phase transition occurs at

the lower temperature, the mechanism described below just takes place in parallel with the oxidation of the individual Zr and Nb grains, which are small because of the short oxidation times.

We then assume that the β-phase oxidizes without transforming. While the zirconium is the more stable oxide, oxidation of niobium is kinetically favored, so both components oxidize [214]. The mixed oxide phase also forms, either as a result of reactions between the niobia and zirconia or the diffusion of niobium from the unoxidized portions of the grain into the oxide. The oxidation rate is still limited by diffusion of oxygen into the scale so the niobia cannot "overgrow" the zirconia grains. Instead, as oxygen diffuses into the β-Zr grain, growth of niobia grains is favored at the oxidation front, but internal oxidation results in the formation of zirconia within the alloy grain. The zirconia grains stop the growth of the niobia grains and vice versa. The combination of internal oxidation of zirconia and formation of niobia at the oxidation front leads to the formation of small, equiaxed oxide grains. As the oxidation front advances through the β-Zr grain, this process repeats several times. Any niobium dissolved in the zirconia grains will slow oxygen diffusion and impede the progress of the oxidation front, presenting the possibility of a small amount of niobium segregation within the grain.

The mechanism described above may explain why an equiaxed oxide is observed in the middle regions of the same oxide scales where segregation occurred at the metal/oxide interface. The segregation takes longer to proceed and cannot take place in the early stages of oxidation.

The oxidation of the Nb-rich phases in the alloy also illustrates the variation of oxide microstructure with oxidation temperature. At lower oxidation temperatures (below 500°C), the β-Zr,Nb solid solution phase has been reported to oxidize to form a either tetragonal Nb sub-oxide based on Nb_6O or an amorphous oxide [211]. Which of these oxides is formed appears to depend on the location of the oxide within the scale and the

concentration of Nb in the originating phase. Neither of these features was observed in the higher temperature oxides formed in this experiment. Instead, β-phase oxidation results in either the equiaxed oxide or the Nb segregation phenomenon discussed above. At both lower and higher temperatures, however, it has been reported that the Nb exhibits delayed oxidation [211]. The sub-oxide may be observed at lower oxidation temperatures because the kinetics may be too slow to allow the formation of stoichiometric oxides. This is consistent with the observation of an amorphous oxide closer to the surface of oxide scales grown at lower temperatures -- as oxygen continues to diffuse through the scale, the sub-oxide continues to oxidize [211]. The observation of segregated, columnar-like oxide grains near the surface of scales formed in this experiment indicates that a similar mechanism does not operate at higher temperatures. That is, oxidation following segregation in the alloy probably does not result in the equiaxed oxide with time; the equiaxed oxide forms via a separate mechanism.

The difference in temperature may also change the oxidation rate of the β-phase. It has already been shown that the difference in temperature causes a difference in oxidation mechanism; the higher temperature mechanisms may have higher activation energies than the lower temperature mechanism. Thermodynamic effects would then dictate which mechanism predominates at which temperature; otherwise, the same mechanism would occur at all temperatures. The formation of ω-Zr provides a thermodynamic "switch" for the two mechanisms. At lower temperatures, the decomposition products of the metastable β-phase are ω-Zr and a Nb-enriched β-phase. The ω is metastable and oxidizes at a faster rate than α-Zr [216]. In combination with the quick oxidation of niobium, this leads to accelerated oxidation of the β-phases with respect to α-Zr at lower temperatures. In contrast, ω is not stable at higher temperatures. Instead, decomposition of the β-phase produces α-Zr and a Nb-enriched phase. As a result, the overall mechanism of β-phase oxidation will be different because the intermediate products are different. The α-Zr

product can be expected to oxidize at the same rate as the "native" α-Zr phase. It has already been noted that the Nb-enriched decomposition product exhibits delayed oxidation with respect to α-Zr. Again, the delay is not great, and the unoxidized Nb laths only extend about 100 nm into the oxide (behind the oxidation front). If the scale is 6 μm thick, this translates to about a 1 second delay at 635°C and 4 seconds at 597°C. It is enough, however, to generate a relatively even oxide/metal interface in comparison to oxides grown at lower temperatures on alloys with lower dislocation densities.

That the high-Nb regions in the oxide scale probably originate in the β-Zr grains indicates that elements of the alloy microstructure are maintained in the oxide microstructure. The microstructural features observed in Figure 4.9 also support this hypothesis; the difference in contrast may result from the difference in crystallographic orientation between the originating alloy grains. On the other, the ends of the grains in the oxide do not appear to derive from grain boundaries in the metal. While the average grain lengths were not calculated statistically, they range from 60 to several hundred nanometers. Moreover, the regions where the columnar grain termini were collinear did not extend beyond a few grains, about 260 nm, while the originating alloy grains are at least 500 nm wide and at least 1 μm long. Thus, the oxide preserves a history, albeit incomplete, of the originating alloy.

Following page

Figure 4.3: STEM micrograph (bright field) of Zr-2.5Nb oxidized for one hour at 635°C (transverse face) showing alpha and beta zirconium grains in alloy substrate

Figure 4.4: XEDS map of alloy shown in Figure 4.2, showing distribution of niobium between alpha and beta zirconium.

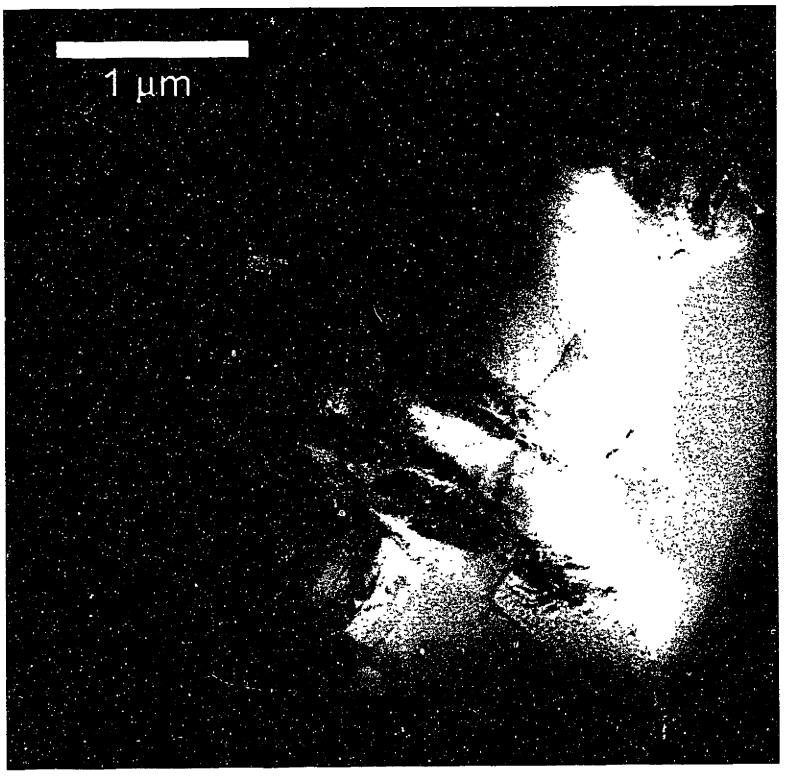

Figure 4.3

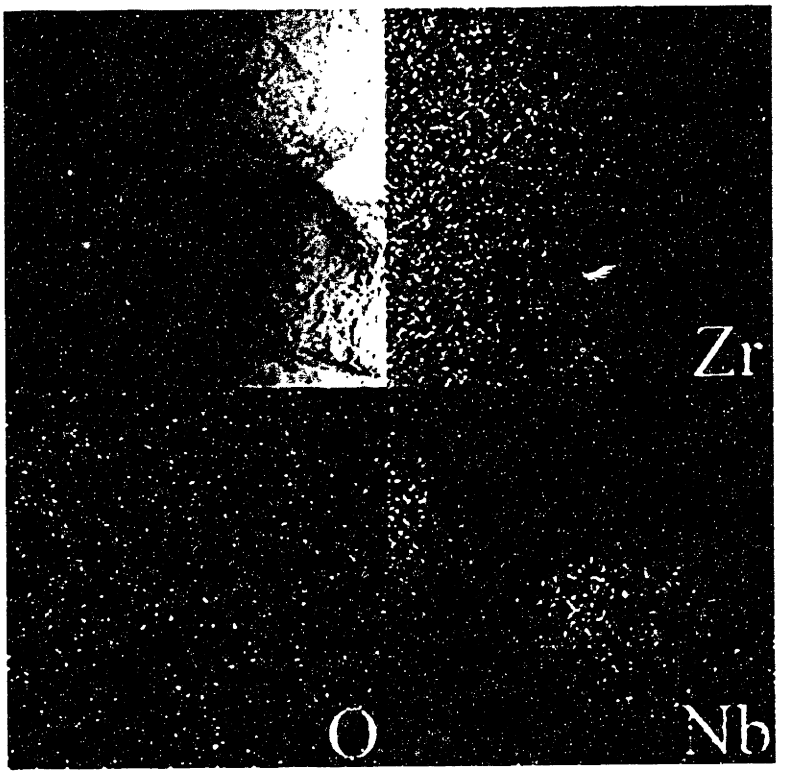

Figure 4.4

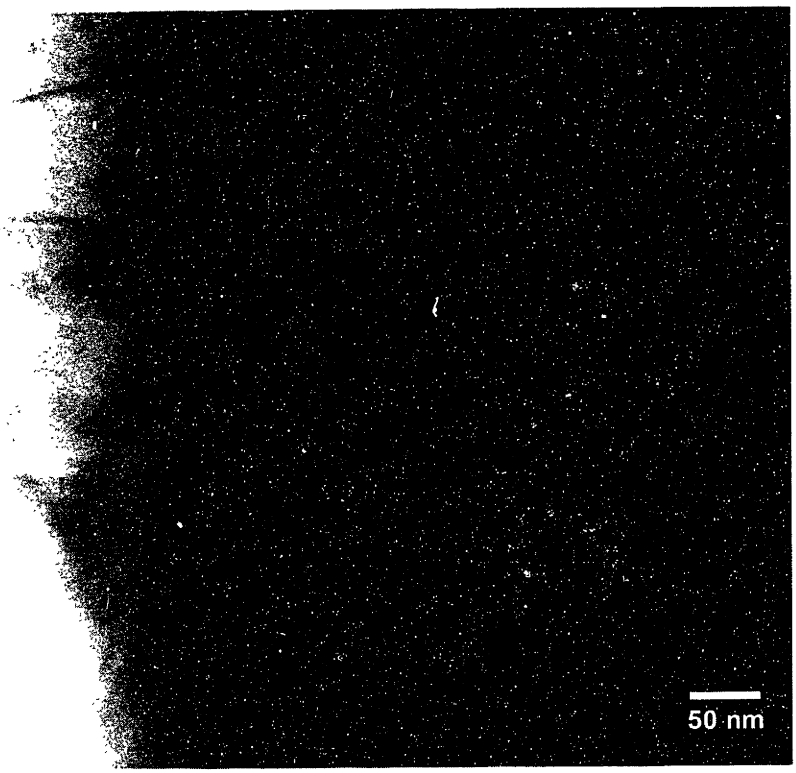

Figure 4.5: TEM micrograph of Zr-2.5Nb oxidized for one hour at 635°C (transverse face) showing dislocations in alloy substrate.

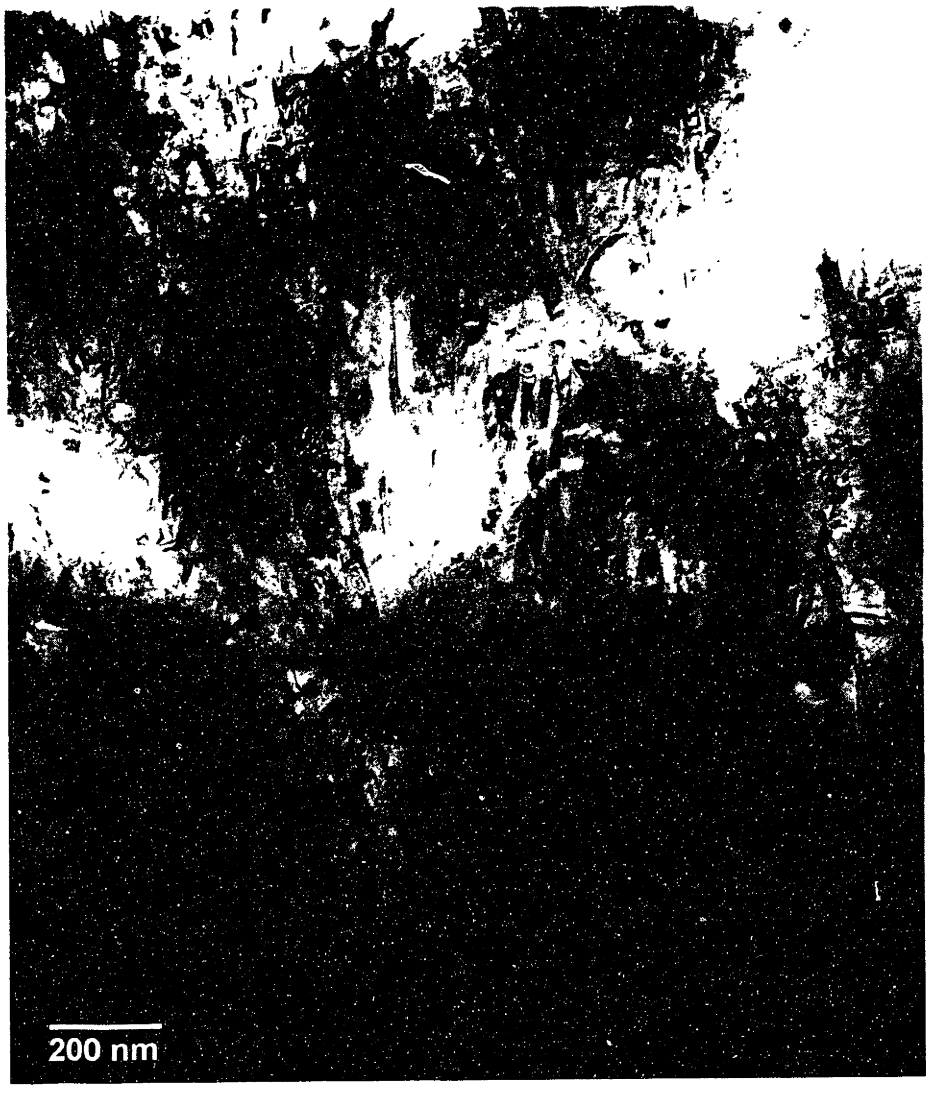

Figure 4.6: TEM micrograph of Zr-2.5Nb oxidized for 45 minutes at 593°C. At this scale, almost the entire oxide scale and its interface with the alloy is visible in the micrograph.

Following page

Figure 4.8: TEM micrograph of Zr-2.5Nb oxidized for one hour at 635°C, showing lateral grain boundaries both continuous and staggered from grain to grain.

Figure 4.9: STEM micrographs of Zr-2.5Nb oxidized for four hours at 593°C (transverse face) showing microstructure of alloy maintained even near the top of the oxide (L-bright field, R-annular dark field).

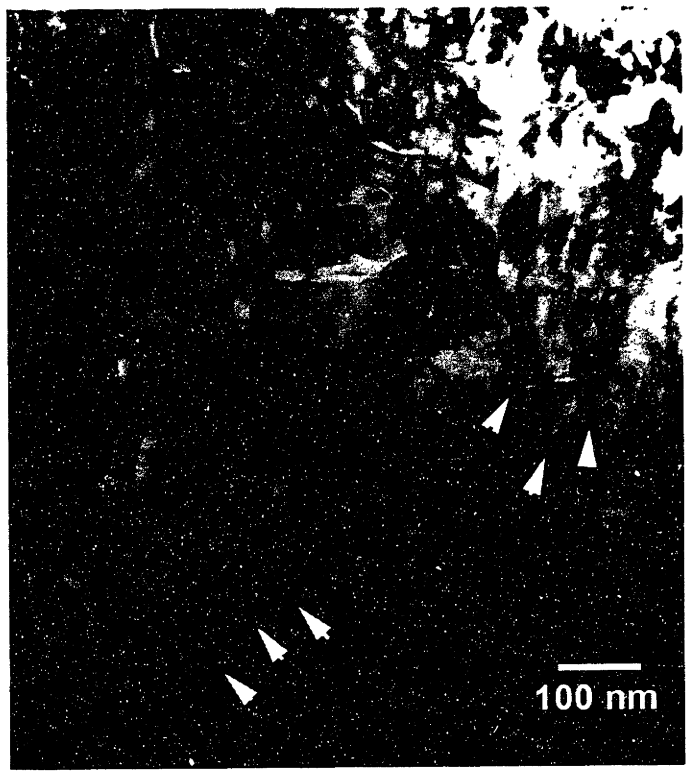

Figure 4.8

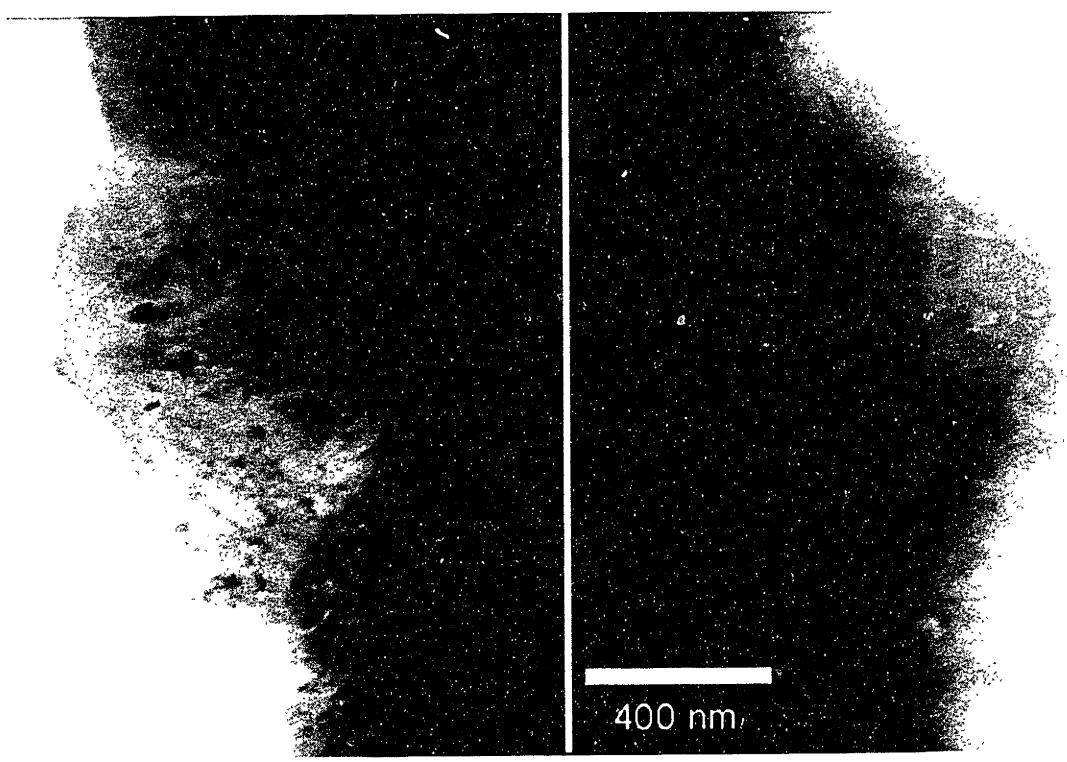

Figure 4.9

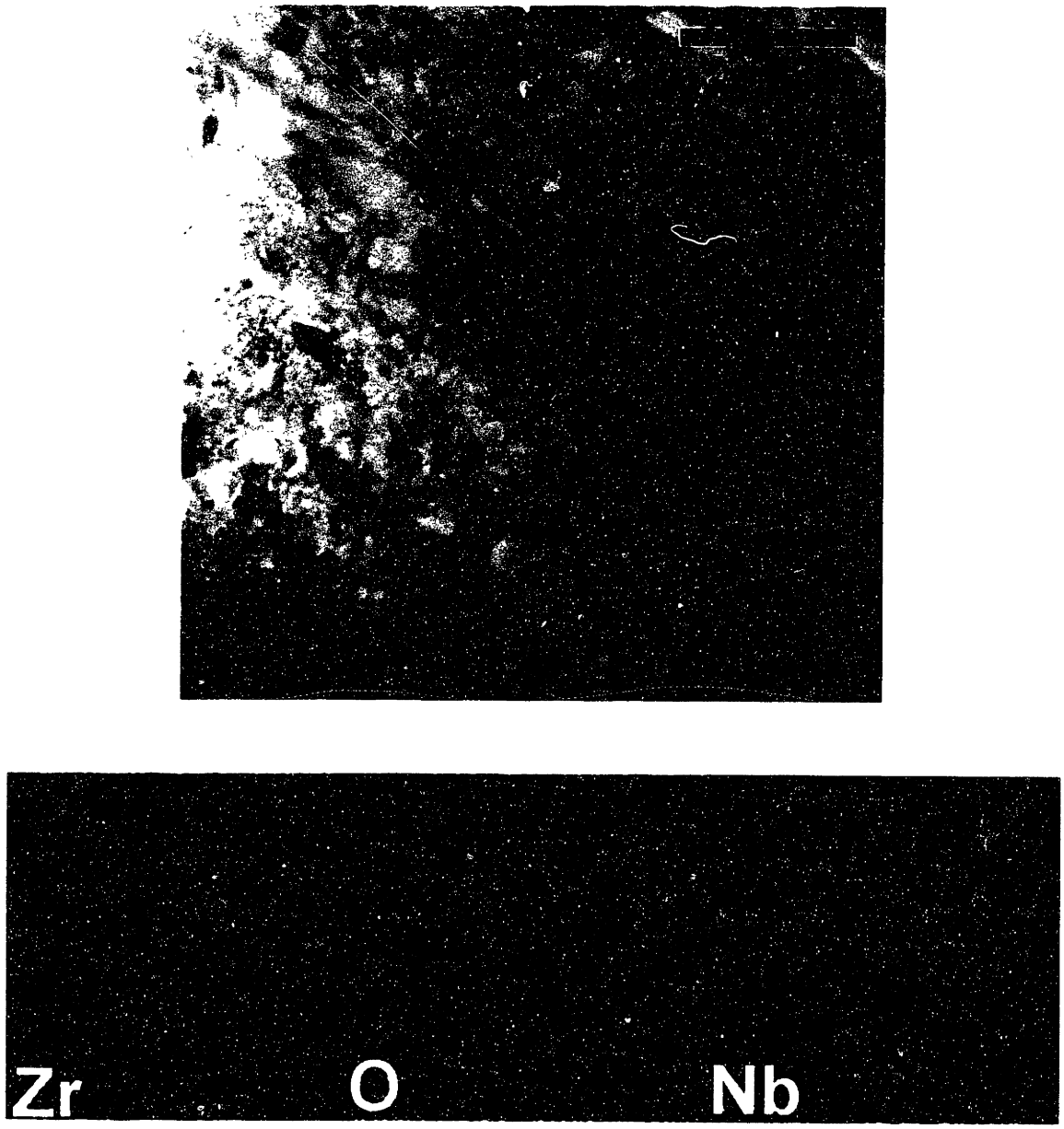

Figure 4.10: a) STEM micrograph of Zr-2.5Nb oxidized for four hours at 593°C (transverse face) showing equiaxed oxide microstructure near top of oxide scale; b) XEDS map of the same area, showing enhanced Nb content in equiaxed grains.

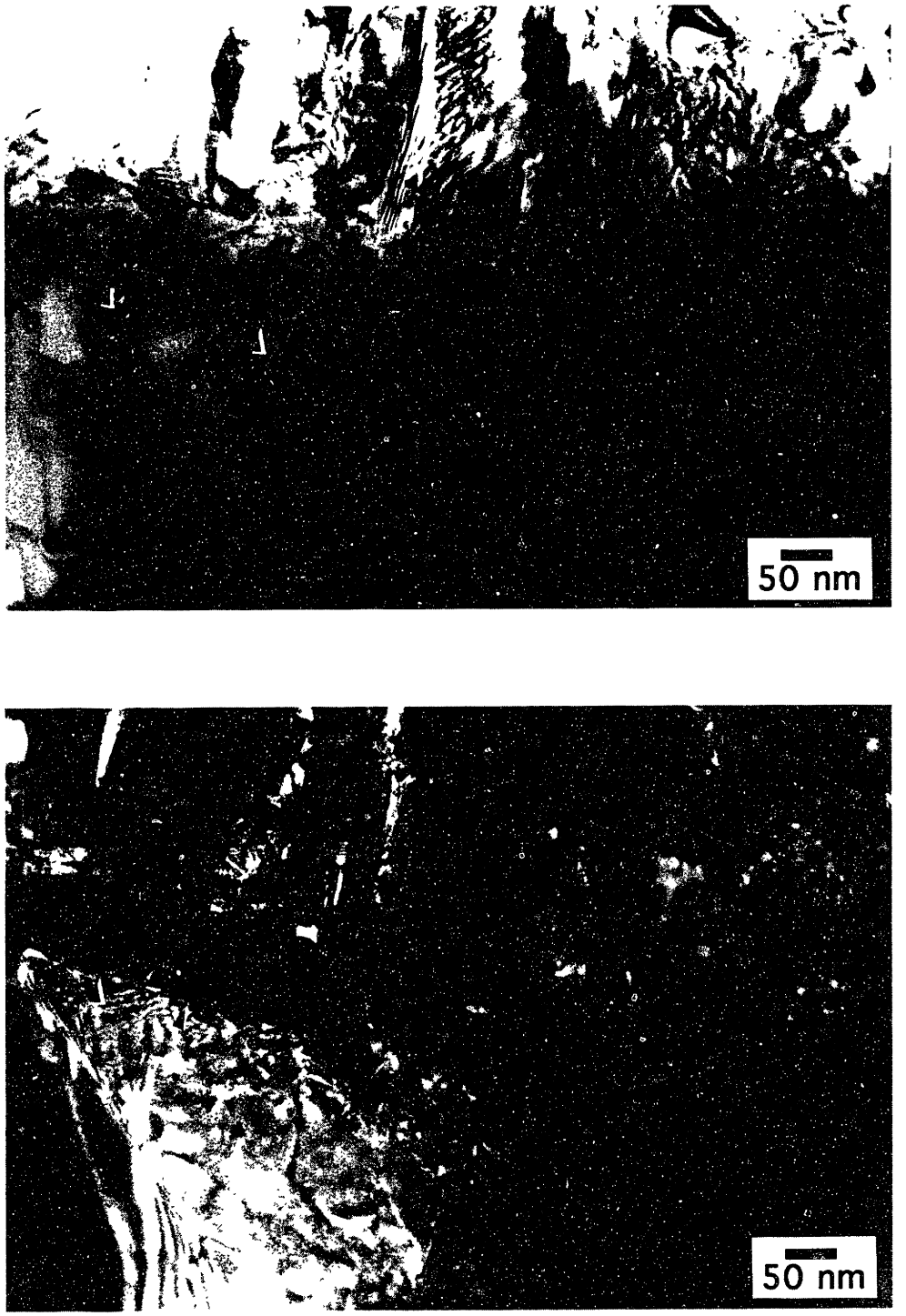

Figure 4.11: a) Bright field and b) dark field TEM micrographs of Zr-2.5Nb oxidized for one hour at 635°C (transverse face). The arrows indicate small metallic grains at the oxide/metal interface.

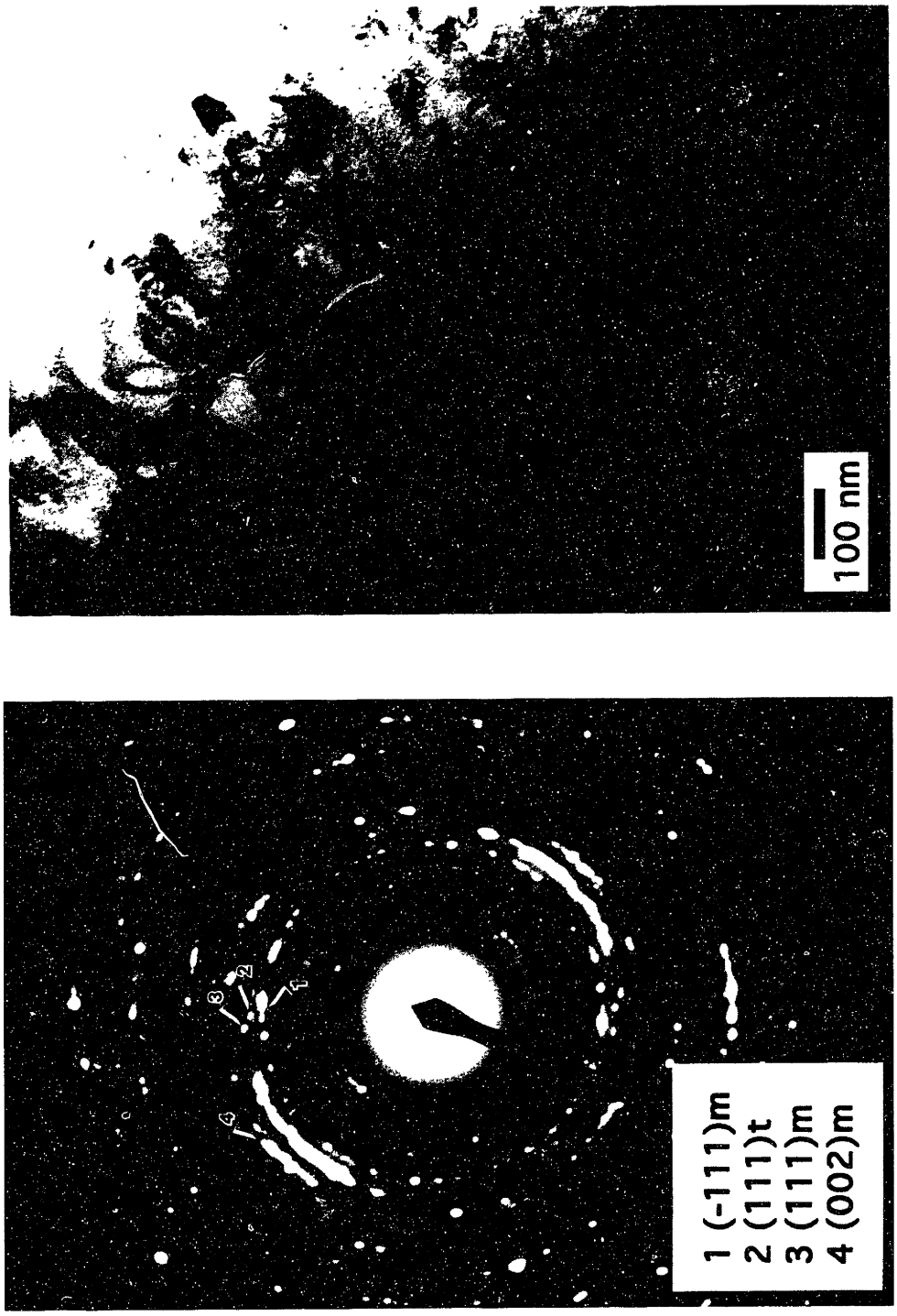

Figure 4.13: a) TEM micrograph of Zr-2.5Nb oxidized for one hour at 635°C (longitudinal face) b) SAED pattern including sampling from about four times the area in a), showing the presence of the tetragonal (and maybe the mixed) oxide and texture in the oxide parallel to the columnar grains shown in (a).

Following page

Figure 4.14: TEM micrographs of Zr-2.5Nb oxidized for four hours at 593°C (transverse face) showing an equiaxed grain within the columnar microstructure adjacent to a lower-contrast feature filled with aperiodic material.

Figure 4.15: TEM micrograph of Zr-2.5Nb oxidized for one hour at 635°C (transverse face, showing a large low-contrast feature extending across several grains.

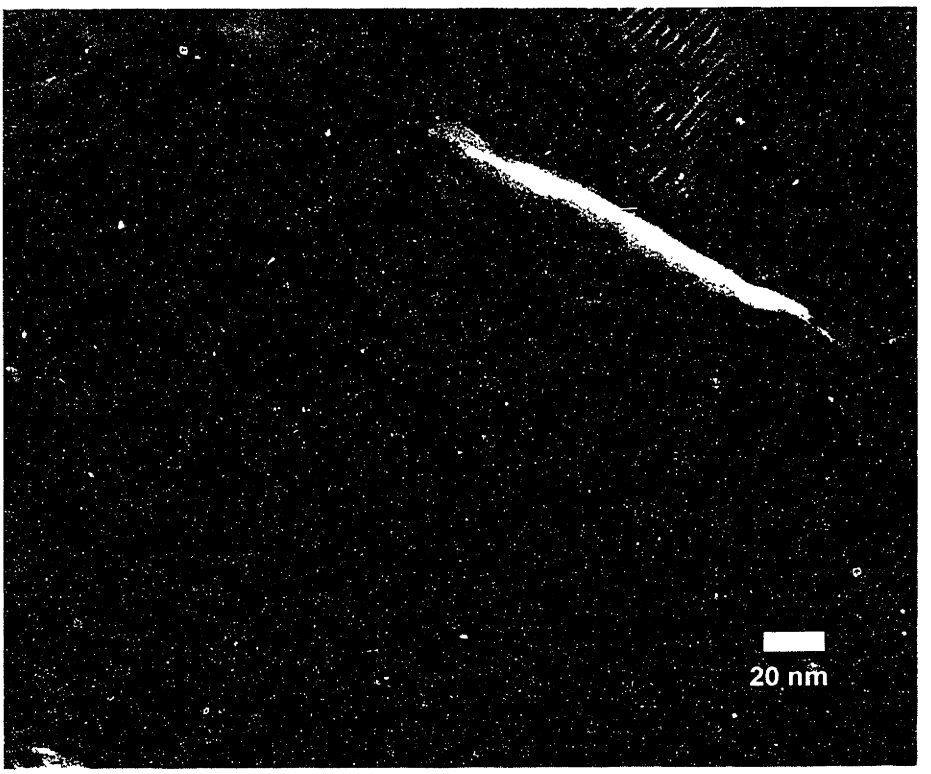

Figure 4.14

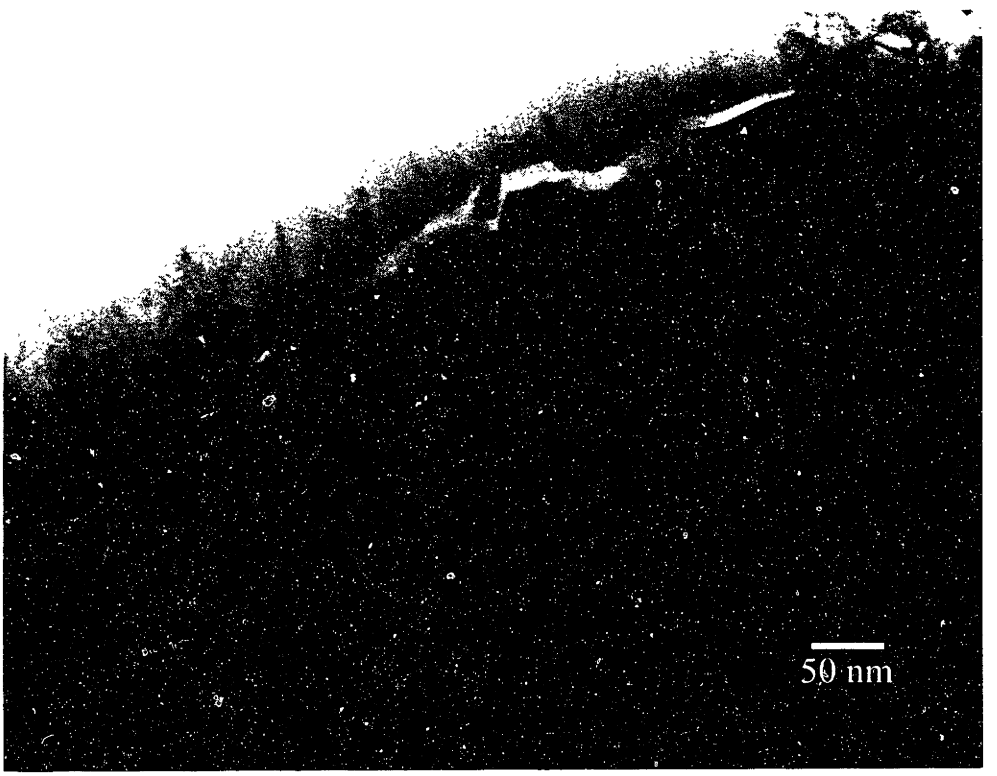

Figure 4.15

Following page

Figure 4.16: a) STEM micrograph of Zr-2.5Nb oxidized for one hour at 635°C (longitudinal face) b) XEDS maps showing the distribution of zirconium and niobium in (a).

Figure 4.17: Dark field TEM image including the area shown in Figure 4.16.

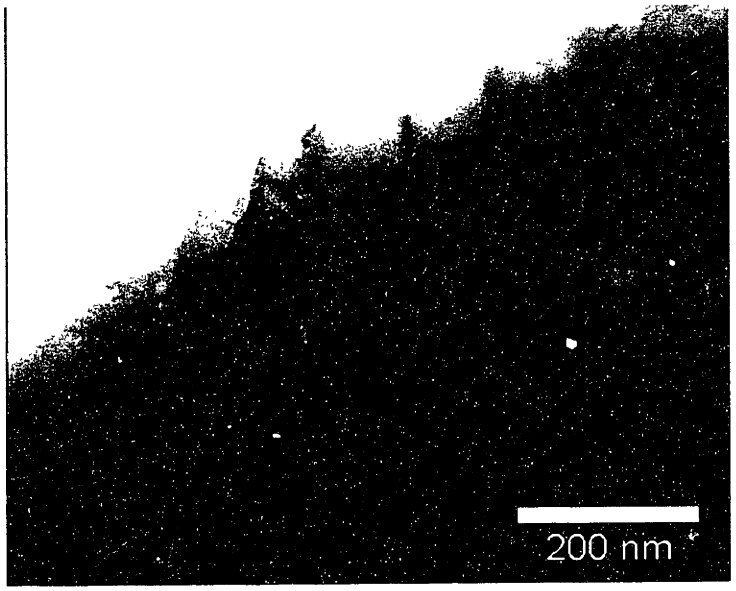

Figure 4.16a

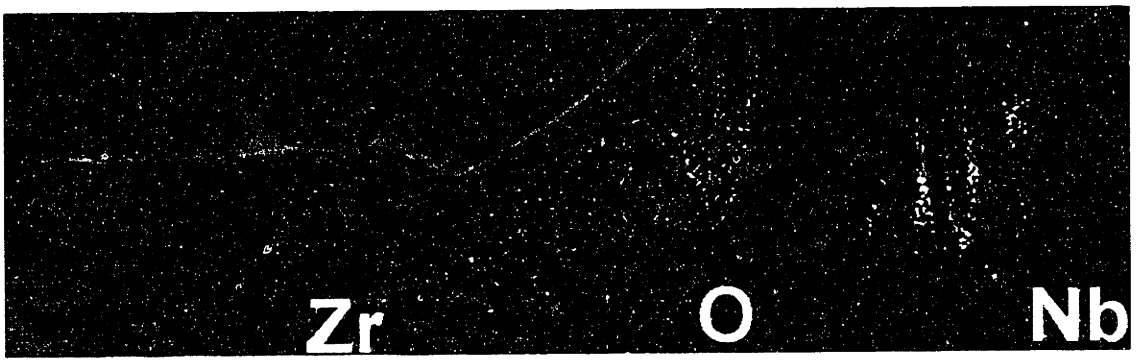

Figure 4.16b

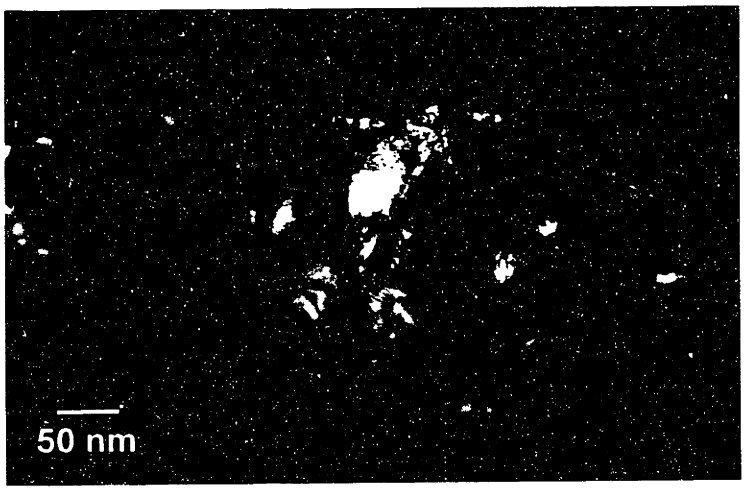

Figure 4.17

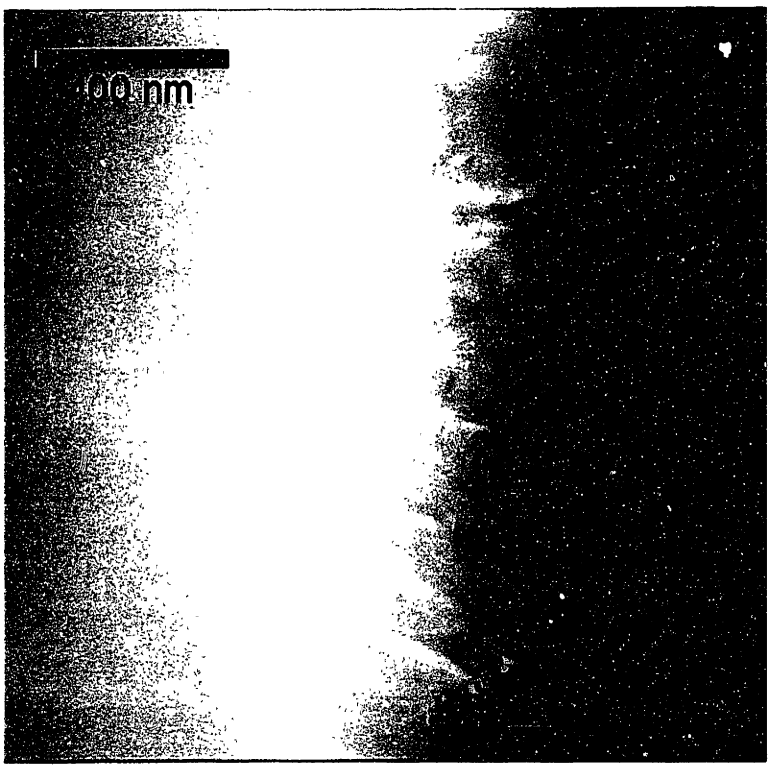

Figure 4.18

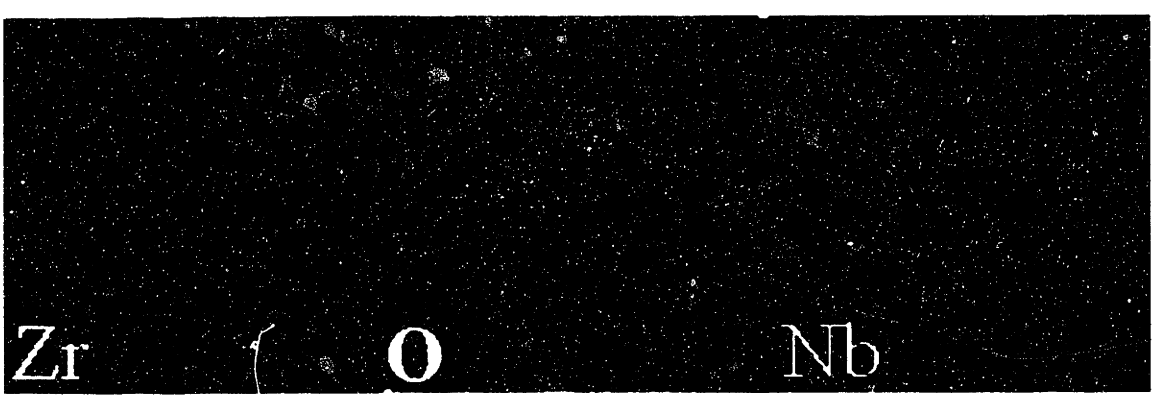

Figure 4.19

Figure 4.18: STEM micrograph of Zr-2.5Nb oxidized for one hour at 635°C (longitudinal face, dark field). The lighter tendril-like features are unoxidized niobium lamellae reaching from within the alloy into the oxide.
Figure 4.19: XEDS maps of the area in Figure 4.18 showing the distribution of niobium and zirconium and the location of the oxide/metal interface.

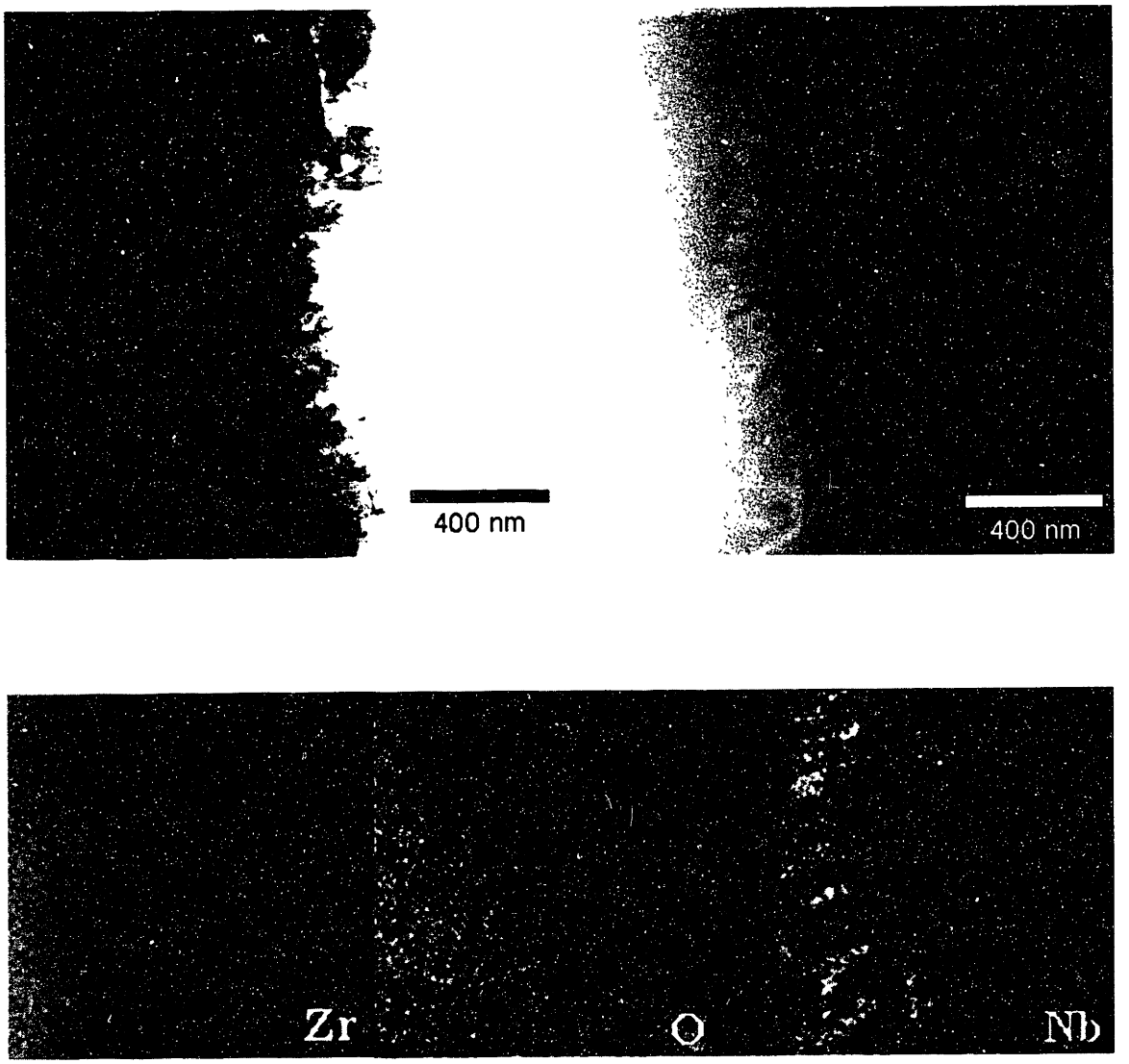

Figure 4.21: a,b) STEM micrographs of Zr-2.5Nb oxidized for one hour at 635°C (longitudinal face) showing segregated microstructure in a grain at the oxide/metal interface (a -bright field, b-annular dark field); c) XEDS maps of the area in (a) and (b) showing distribution of Zr and Nb.

Figure 4.22: a) Bright field STEM micrograph of Zr-2.5Nb oxidized for one hour at 635°C (longitudinal face) showing two small capillary-like grains within the columnar microstructure near the top of the oxide (arrows); b) XEDS maps of the area in (a) showing distribution of zirconium and niobium.

Figure 4.23: a) STEM micrograph of Zr-2.5Nb oxidized for one hour at 635°C (transverse face) showing segregated microstructure close to the oxide/metal interface b) XEDS map of (a) showing distribution of Nb.

Chapter 5

Final Comments on Device Design for Total Joint Arthroplasty

5.1 Cementless Fixation as a Quasi-Tissue Engineering Approach to Joint Replacement

This thesis comprises three related investigations of materials used for prosthetic applications in orthopedics. The first, bone substitute materials, actually serve as prosthetic bone, filling in the space where bone is absent due to surgery or disease. The second and third studies concern applications more commonly described as prosthetic, the replacement of the two joints of the femur -- the hip at the proximal end and the knee at the distal end. The initial approach to the problem of replacing any part of the body is the same. One must ask what tissues are present and what functions are performed. The engineer must then determine which functions a prosthesis must replace and design a device which can perform those functions. In the hip, for example, the functions which are performed by the various components are articulation, support, circulation, and motion. The muscles remain intact after joint replacement, and the synthetic prosthesis does not require a blood supply, so the engineer must determine how to put together a device which articulates against either a natural (cartilage) or synthetic (UHMWPE) surface and supports the weight of the body -- both in motion and at rest. The preceding argument is a simplified description, but it outlines the basic engineering approach to prosthesis design.

Tissue engineering, in turn, seeks to create materials which will enable the body to restore all the functions which were performed in the missing tissue(s). This is the design philosophy behind "artificial skin," where a collagen-glycosaminoglycan (collagen-GAG) scaffold is eventually replaced by dermis and epidermis produced *in situ*. Even so, the prosthesis does not replace all the functions of skin - it has neither sweat glands nor follicles [217]. Over short times, devices produced using the tissue engineering approach may actually serve as a prosthesis. To return to the example of artificial skin, the device helps protect the underlying tissue from both bacterial invasion and dehydration via evaporation. Over longer time scales, however, instead of replacing the missing tissue(s), the tissue engineering approach seeks to regenerate it.

The present study is not a tissue engineering thesis, and the somewhat cursory discussion provided above will have to be sufficient. However, it does offer a description of the approach which has been taken to implant fixation in this thesis. That is, even though it is currently not feasible to tissue engineer an entire hip joint, it is possible to apply a tissue engineering approach to specific features of the joint. The use of HA coatings enables the formation of both a chemical and mechanical bond between the implant and the bone rather than the purely mechanical one formed by the use of PMMA bone cement. Moreover, the interface formed by this bond can be self-maintaining. In case of injury or added stress (such as weight gain), the body is able to respond via remodeling. Even if the HA coating is not used, it is important to consider the body's response during implant design. Stress shielding is one example of a biological response to an implant which has, at first glance, nothing to do with the functions the implant was supposed to perform. Particle disease is an even better example because ideally functioning implants do not induce it. Thus, the questions asked by the tissue engineering approach are important even if the goals of tissue engineering are not part of the design process.

While the work in this thesis concentrated on cementless fixation via HA coatings, OZ also shows promise for cementless applications. In animal models, OZ implants exhibit superior bone apposition over cpTi after six months, indicating that the calcium phosphate-free oxide is still osteoconductive [35, 184, 218]. Moreover, prior investigators have found evidence of bone apposition to pure zirconium [153]. In addition, both porous (~100 μm) and grit blasted (1-5 μm roughness) Ti-6Al-4V implants exhibit increased bone apposition and interfacial strength over smooth implants, indicating that grit-blasting a zirconium surface may further enhance osteoconduction [141, 219-222]. This creates two more possibilities for cementless knee designs, either a) entirely composed of OZ or b) combining an OZ surface articulating against UHMWPE with a grit-blasted zirconium metal surface which is apposed to bone. The favorable wear properties of OZ against articular cartilage also suggest its use in hip arthroplasty [223].

One interesting aspect of tissue engineering has been almost completely ignored by this thesis -- the use of bone substitute materials is a tissue engineering approach to large scale bone injuries. Like the artificial skin, BSMs serve an immediate space filling and support function, but are ultimately designed to be replaced by natural bone. The optimal rate of remodeling is a subject of debate which has led to the wide variety of BSMs (with different properties, including degradation rate) on the market. In this experiment, however, the bone substitute materials served primarily as a control for the experiments conducted in Chapter 3 and as a medium for investigating the architecture of bone mineral.

5.2 Conclusions

1) The LVHRSEM can be used to elucidate details about the three-dimensional architecture of bone which can be viewed in cross section via TEM.

2) The mineral phase in bone is organized in a hierarchical microstructure which parallels the organization of collagen. Although the organic (collagenous) phase of bone serves as a template for the deposition of bone mineral, the mineral forms a continuous matrix as well.

3) The differences in crystallite morphology and arrangement between naturally derived and synthetic bone substitute materials can be attributed to the formation of naturally-derived bone mineral on an anisotropic collagen substrate

4) Small crystallites of biological apatite and other poorly crystallite CaP phases are deposited at the surface of an HA-coated implant within three hours. Over successive days, the crystalline deposits increase in number density and merge. Both types of deposits are eventually remodeled to form randomly oriented arrays of larger crystallites. If collagen is present, the crystallites will be deposited onto the collagen matrix to form bone.

5) Bone apposition to an implant is not a sufficient indicator of the mechanical integrity of the interface between biological tissue and an HA-coated implant.

6) While crystallinity does not have a significant effect on the ultimate degree of apatite deposition at an HA-coating, it does influence both the kinetics of deposition and the microstructure of the deposits.

7) The oxide scale on Zr-2.5Nb is comprised primarily of a columnar oxide. The grain widths within the oxide are dependent on temperature, location within the oxide, and the microstructure of the alloy substrate. An equiaxed microstructure

within the oxide scale and a Nb-segregated microstructure near the oxide/metal interface could both be correlated with a high-Nb β-Zr originating phase in the Zr-2.5Nb alloy.

8) The interface between Zr-2.5Nb and its oxide is continuous, with no voids or cracks which might be detrimental to oxide adhesion. Crack-like features of varying sizes were identified within the scale. These features are filled with amorphous material and do not serve as nucleation sites for cracks in the oxide scale.

9) Monoclinic and tetragonal zirconia were both detected in the oxide scale on Zr-2.5Nb via electron diffraction. A mixed $6ZrO_2 \cdot Nb_2O_5$ phase may also have been detected. Both the monoclinic and tetragonal phases exhibit crystallographic texture parallel to the direction of the oxide columns.

5.3 Future Work

5.3.1 Architecture of bone and bone substitute materials

Dr. Anuj Bellare is currently using ultra-small angle x-ray scattering to investigate the spacing of the periodic aggregates of bone mineral observed in anorganic bone using the National Synchrotron Light Source at Brookhaven National Laboratories. He has previously reported a difference in the periodicity of whole and demineralized bone, and anorganic bone seemed a logical next step [224].

Whole bone samples were also prepared for TEM during this experiment, and, while it was not reported, some LVHRSEM observations of freeze-dried whole bone were also performed. The use of whole bone also suggests the use of both heavy metal and immunostains in future experiments to localize various matrix elements and to confirm the

orientation of the crystalline aggregates parallel to collagen fibrils. Comparison of immunogold stains for collagen in both the LVHRSEM and TEM might also be informative. The use of whole bone will also enable higher resolution observations of cement lines than have previously been reported in the literature.

The varying microstructures of naturally derived and synthetic BSMs suggest that cells ought to interact differently with them. *In vitro* tests of cell proliferation and migration would help determine whether such differences exist and how they influence *in vivo* responses to these materials.

5.3.2 Biological response to HA-coated Ti-6Al-4V

There is a lot of material left from the *in vivo* experiment. Further SEM of these samples may reduce the standard deviations such that a significant difference is found between the various sample groups. In addition, more TEM can be performed, including immunostaining. Various immunohistological stains may also be informative.

The samples from dog 3004 should be walked over to the machine shop. Someone ought to be able to get those samples out of the glass.

Unfortunately, the best way to preserve the IBAD-HA/bone interface in TEM sections will probably be to leave the titanium in the sample. This is certainly so for the uncoated Ti-6Al-4V samples. With practice, it is definitely possible to produce microtomed sections including the Ti-alloy substrate, and, hopefully, someone will try this or some other sample preparation technique to produce these samples. This may also enable statistically relevant experiments in the TEM.

Implant experiments with rougher IBAD-HA coatings will be better equipped to truly evaluate the biological response to this material under more clinically realistic conditions.

5.3.3 Oxidized zirconium

Some data which may prove useful to the investigation of oxidized zirconium were not collected. The grain size at the oxide/metal interface was not measured for the samples oxidized for 4 hours at the lower temperature. In addition, good images of the interface on the longitudinal face of the oxidized samples would show whether the oxidation observed at high temperatures occurs below the eutectoid.

More work should be done to definitively locate the ω-Zr phase in the segregated alloy microstructure and elsewhere.

A supply of overoxidized (10 hours at 635°C) and oxidized cast Zr-alloy samples have also been provided by Smith and Nephew, Inc. Both TEM and cross-sectional SEM observations should be performed on these samples. The oxide scale on the overoxidized samples should contain white stoichiometric ZrO_2 [190]. Overoxidized samples tend not to exhibit good oxide adhesion, and the reasons for this may be revealed by the oxide microstructure. Other studies of post-transition oxides would also aid the understanding of the microstructure of pre-transition oxide scales on Zr-2.5Nb.

Smith and Nephew, Inc. supplied us with some grit-blasted OZ cylenders for *in vivo* experiments similar to those conducted in Chapter 3. At some point both mechanical and histological evaluation of the interface between bone and these materials should be investigated.

Appendix A

Tripod Polishing of TEM Specimens

The general method for producing TEM specimens by tripod polishing is given in several places [202, 225]. These procedures are quite well written and the authors, especially Ron Anderson at IBM, are very happy to answer questions over the phone. The technical support staff at South Bay Technology, which holds the license to produce the polisher, is also quite helpful. Thus, it is not the intention here to provide a complete discussion of tripod polishing but to outline a general procedure which can be attempted to produce TEM specimens of samples with several interfaces. It should be noted that this technique still requires some refining - no completely successful TEM specimen has been produced from it at yet. Moreover, the polisher in use in the Hobbs' group at MIT is not a South Bay instrument. In the spirit of fun which pervades the two Benedict/Anderson papers on tripod polishing, this thesis offers a few comments on the procedure and its modifications for the Hobbs' group polisher.

The polisher as produced, probably by the machine shop at MIT, must be modified to prevent erosion of the aluminum feet. Slices from 1/2" delrin barstock attached to the bottoms of the feet with any cyanoacrylate glue (KrazyGlue™, Elmer's Products, Inc., Columbus, OH) will accomplish this quite well. However, cyanoacrylate glue is not particularly resistant to shear, and the delrin feet will shear off during polishing. Before

they are reattached, both surfaces to be glued should be cleaned with acetone or polished to remove the residual adhesive.

In addition, a glass platen is required for polishing. A brass platen can be easily modified by attaching a 1/4"x8" glass plate to the top using a Met-Grip liner from Buehler. The glass can be custom ordered from any auto glass shop. I used Harvard Glass in Somerville, MA, near the intersection of Webster and Cambridge Streets. Note also that polishing should be done with the wheel at its minimum speed.

Benedict and Anderson recommend an "O-Cel-O" sponge produced by Betty Crocker to clean the polishing papers. However, any brand or type of sponge will suffice. Furthermore, the producers of Mr. Clean™ cleanser, recommended by Dr. Benedict to clean the cloth covered wheel used for colloidal silica, have merged with those of Top Job™. The resulting product cleans quite well; it should be diluted to about 1/4 capful per 500 mL water.

Polishing papers are mounted on the glass-topped platen with surface tension. That is, a large quantity of water is put on the glass, the paper is put on top of that, and the excess water is removed with a squegee (available at any hardware store, such as Economy Hardware on Massachusetts Ave. in Cambridge, MA). The table is then rotated at top speed for about a minute to remove the last of the excess water.

Before attaching a sample to the polisher stage, the polisher should be leveled and polished. The third leg of the polisher, near the sample stage, is superfluous and should be retracted to a level above the that of the rear legs and the stage. The sample is then attached to an edge of the stage using crystal bond. If the sample has a curved interface, the sample should be attached such that the direction of curvature of the interface is the inverted with respect to the wheel. The stage is then attached to the polisher such that the sample is oriented at 90 degrees to the perpendicular from the stage to the rear legs of the polisher. Using a polishing wheel, the sample is polished using 30, 15, 6, and 1 μm diamond film to

a 1 μm finish. If the sample is being wedge polished, it should be finished with colloidal silica. The polisher should be held such that the general direction of the interface is parallel to the direction of motion. The polisher should be moved on the wheel during polishing or else the paper will rip. The polisher should be leveled before polishing and periodically during polishing. The glass platen should be cleaned with the Mr. Clean/Top Job™ solution before mounting the diamond papers or dust on the platen will keep the papers from lying completely flat. Colloidal silica is used on a cloth covered wheel (Microcloth, Buehler) which is cleaned with copious amounts of Mr. Clean/Top Job™ following polishing, as is the sample. Following polishing, the sample is removed from the polisher and set aside while the polisher is prepared for second side polishing. It is recommended for wedge polishing to put a slot grid on the sample before removing it from the stage. A solvent resistant epoxy such as Hardman Green should be used to attach it. It is crucial to record the thickness of this grid before attachment (see below).

Because the wedge polishing technique tends to polish the stage, a slice of 1/2" glass rod should be attached to the aluminum stage of the tripod polisher using crystal bond (Aremco). It is crucial not to use cyanoacrylate glues to attach the glass slice to the stage. This is not meant to be a permanent bond. This apparatus should then be polished and leveled. It is probably not necessary to mount the glass slice at the edge of the aluminum stage. The sample is then mounted, polished side down, at the edge of the glass slice using a very large drop of cyanoacrylate glue. The excess glue protects the edges of the sample during polishing. The sample should be mounted so the direction of curvature of the sample is the same as that of the wheel. If a grid is mounted on the polished side of the sample, it should be "bounced" in the cyanoacrylate glue several times before being pressed to the stage to prevent formation of air bubbles. The drop of glue will take about an hour to set.

If the sample is being wedge polished, one should be careful to set the micrometers on the legs so the bottom of the wedge at the bottom of the sample, not the bottom of the copper grid which is attached to it. The sample is polished to a 30 μm finish on the corresponding paper, then on 15 μm paper to 4/1000", followed by 3 μm paper to 30-40 μm. After this, the sample is polished with 1 μm paper until the wedge is about 0.5 mm into the grid. A final polish is performed with colloidal silica. The glass slide is removed from the aluminum stage and placed in a petrie dish with acetone. The acetone is changed occasionally and the sample monitored until gentle tapping of the thick edge of the sample with a tweezer will dislodge the sample. When it is dry (about 30 seconds), it is ready for TEM observation. South Bay Technology promotes the use of the Post-It note unit (PINU, or piw, Post-It width) for the measurement of thickness. It is recommended here because otherwise the stage must be removed from the polisher to measure sample thickness, and it is almost impossible to achieve the exact same orientation when the stage is remounted. This will lead to beveling in the sample, especially during wedge polishing. One PINU is approximately 90 μm. Several Post-It notes (still stuck together, not separated) held together can be used to measure multiple PINUs. Post-It Notes™ (3M, St. Paul, MN) are available cheaply from any office supply store.

If wedge polishing turns out to be too inefficient, the tripod polisher can be used simply to achieve a surface finish. Final thinning is accomplished in the ion mill. The first side of the sample is polished as described above, but without the colloidal silica. No grid is necessary. The sample is mounted on the glass slice as described above and polished to 30-40 μm as described above. The 1 μm paper is only used to achieve a surface finish, and then a grid is attached to the sample with a solvent resistant epoxy. The sample is detached from the glass slide as described above and ion milled as described in Chapters 3 and 4.

One final comment on the Benedict/Anderson papers. The authors note that many of the materials crucial to this procedure, such as sponges, squeegees, and Mr. Clean™, are quite cheap, implying that this technique ought to be accessible to any laboratory group. Additionally, although this is not mentioned in the articles, Post-It notes are also quite inexpensive. However, the otherwise optimistic laboratory manager should note that diamond film is correspondingly dear, as is the polisher itself. Conventional polishing tables should be modified to run evenly at low speeds, or a special polishing apparatus can be purchased from South Bay at a price close to that of the tripod polisher.

A representative from South Bay Technology presented the polisher at MIT in the summer of 1996. His advice is presented below:

•You should remove a thickness of at least three times the grit size of the previous step to remove the damage induced by that step. Thus, you have to remove 90 μm of material with the 15 μm diamond film to remove the damage induced by the 30 μm film, etc.

•The sample should be placed at the 12 o'clock position on the polishing wheel for polishing with colloidal silica. The 9 o'clock position is the position of lowest stress, the 6 o'clock position will maximize the specimen polishing rate.

•Polish the first side until the sample is about 1 PINU thick.

•Side-to-side tilt adjustments on the micrometer should be made 1-5 divisions at a time. You should then wait for the bevel to move all the way across the sample before making further adjustments. Front -to-back adjustments require a 20-25 division advance of both micrometers.

One final piece of advice - do not remove the sample from the polisher during second side polishing. If you have a way to measure thickness without doing so, great. Otherwise, wedge polish or estimate. If you are wedge polishing, just polish the edge of the wedge to somewhere in the middle of the sample.

Appendix B

Surgical Technique for HA-Coated Ti-6Al-4V Cylinders

HA COATED PROSTHESIS REPLACEMENT IN DOG FEMUR
H-P. HSU, M.D.

A. FOR PROXIMAL FEMUR

The animal is placed on its side and positioned so that the operative leg can be dropped over the belly side of the table for femoral exposure. A generous area around the hip and knee are shaved and cleaned, and the entire extremity is prepped. The entire area is draped and the initial drapes are attached to the skin with skin staples.

SKIN EXCISION, EXPOSURE

A curvilinear incision is made, the midpoint of which is centered just posterior to the greater trochanter, traveling distally and anteriorly. The entire skin incision is approximately 15 cm. The skin and soft tissues are dissected to the deep investing fascia. The fascia lata is incised along the cranial edge of the biceps femoris muscle as far as the skin incision allows. The biceps femoris is separated and retracted to posterior. A fatty interval is identified just anterior to the greater trochanter, which makes the internal the gluteus superficialis, the tensor fascia lata muscles, and gluteus medius. There are two to three vessels in that area which should be identified and cauterized.

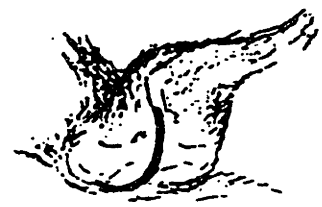

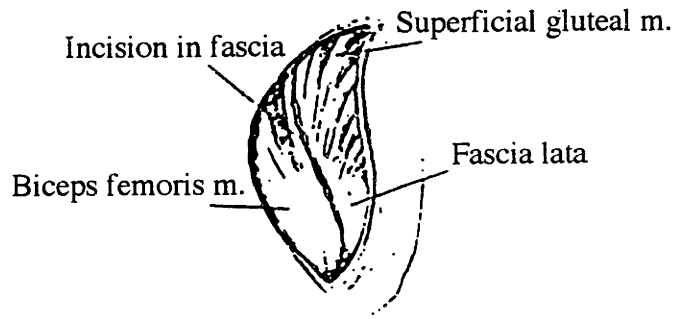

At this point, the traverse incision is made in the two thirds gluteus superficialis carried to the great trochanter and posterior half is tagged and retracted. (The sciatic never is identified as it emerges from the caudal edge of the gluteus medius, crossed obliquely over the caudal rim of the acetabulum, and continues distally to the femur.) This nerve must be protected through out the approach and must be operated carefully. The one-third tendious insertion of the gluteus medius is transacted near the trochanter so that some tendinous tissue is retained on both sides of the incision. The caudal side is tagged and reflected. All bleeding points are cauterized. The free gluteus muscles are retracted dorsally out of the field. The leg in a full position out of the internal rotation. The proximal femoral trochanteric fossa and common insertion of the obturator is cut at its musculotendious junction, and the external obturator tendon and gemelli tendon are cut at their insertion in the trochanteric fossa. The Frris-Smith rongeur is used to remove the remaining tendons of obturator and gemelli from the deep trochanteric fossa. A 6 mm in diameter drill bit is used to make 15 mm depth hole in the subchondral bone with drill sleeve. Another 6.35 mm in diameter drill bit is used to make the hole a little bigger, then a special reamer is used to finish the hole. The irrigation is used and must be maintained the whole drilling procedure.

The proximal hole is completed at the trochanteric fossa, and the implant is placed in the finish hole by the holder, and a drive is used to fix the prosthesis fit and tightly.

The wound is irrigated with saline and the tendon of external obturator is sutured to the remaining tendon of internal obturator. The gluteus medius and superficialis are replaced back with 0-vicryl sutures. The subcutaneous tissues are closed with 2-0 and 3-0 vicryl and skin is closed with a nylon suture.

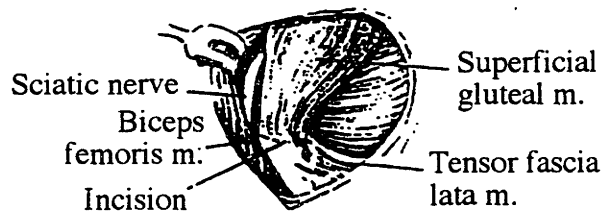

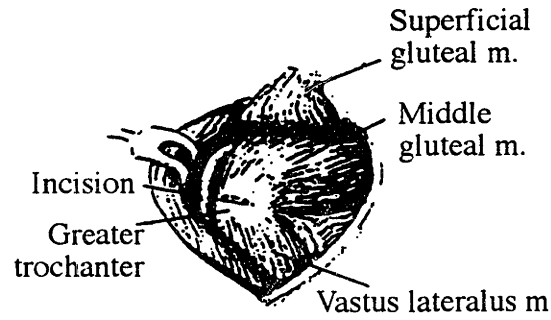

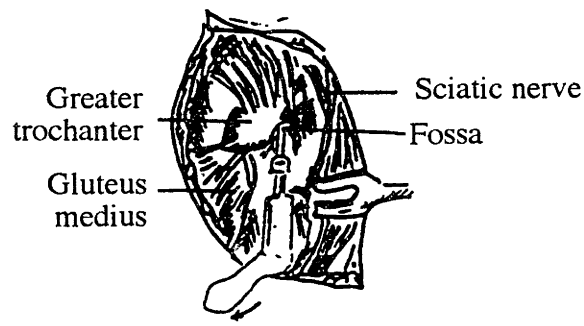

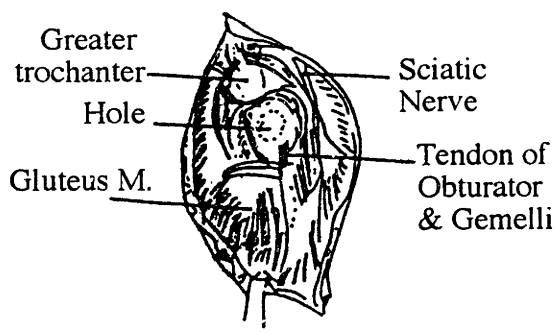

HA COATED PROSTHESIS REPLACEMENT ON THE DISTAL FEMUR AND PROXIMAL TIBIA

HU-PING HSU, M.D.

POSITION

The animal is placed on its back and positioned so that the operative leg can be moved over the belly for easy exposure of distal femur and proximal tibia. A generous area around the knee is shaved and cleaned, and the entire extremity is prepped. The entire area is draped and the initial drapes are attached to the skin with skin staples.

SKIN EXCISION, EXPOSURE

A Straight medial side incision is made, the midpoint of which is centered to the knee joint line. The entire skin incision is approximately 3.5-4.0 cm. The skin and soft tissue are dissected to the deep investing fascia. There was one branch of popliteal artery in that area which should be identified. The branch is transited through the surface of the medial distal femur (Do not cauterize). At this point above 10 mm, a small longitudinal incision is made at the front portion of superior attachment of the MCL. To release the periosteum to expose the distal femoral condylar surface. It is important to make this drill point at the level of the posterior portion of the anterior edge of distal femur about 14 mm. The 5 (emended 2, 6, 6.4) in diameter drill is used to make 10 mm (emended 32) depth hole which is flushed with saline. The HA coated cylinder shape implant is placed in the hole by the force gauge. It is for measure the pushed force.

Other important drilling position is made at proximal medial tibia. The point of which is posterior portion from the tibial tuberosity about 20-25 mm and inferior from the medial tibial plateau about 10 (emended 20) mm. Same size hole is made under the periosteum with 5 (emended 6.4) in diameter drill. The blood clots and soft tissue are removed with flushed sterile saline. The different material cylinder shape implant is placed by force gauge.

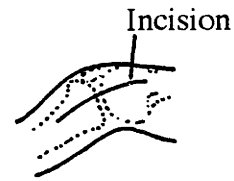

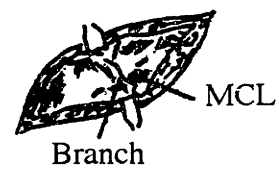

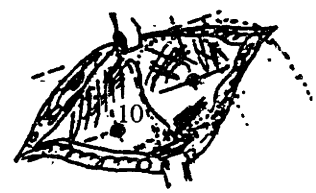

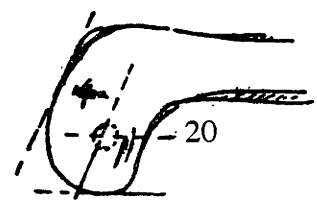

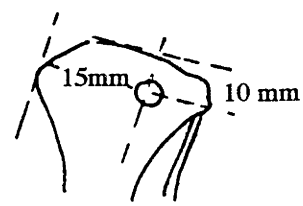

The whole surgical procedure is kept wet by sterile saline sponges, and the irrigation is used and must be maintained during the drills. The blood clots of the holes are flushed and cleaned by saline and wet sponges.

The periosteum and investing fascia are closed with 2-0 interrupted sutures. The superficial fascia and subcutaneous tissue are close by 3-0 sutures also. 3-0 Nylon sutures are used for the skin close. The anesthesia is reversed, and AP and Lateral X-Ray of knee are taken. The animal returned to its cage.

Appendix C

Ultramicrotomy of Metallic Samples for TEM

Ultramicrotomy is probably one of the most efficient techniques for the preparation of large quantities of TEM specimens. One basically uses a diamond knife to slice sections from a block. A trough attached to the knife, filled with a solvent such as water, is used to collect the sections, from which they can be lifted onto grids.

Manuals on ultramicrotomy are easily found in any academic library, and most electron microscope or histology facilities employ at least one person who can demonstrate the technique to a new microscopist. However, most people who practice ultramicrotomy do not microtome metals. This appendix is basically the advice of someone who used the time-honored technique of trial and error (and a little luck) to make a number of passable samples.

First, I have heard rumors that a knife with a different included angle than that which is normally used should be utilized for microtomy of metals. This may be so, and the technical consultant at your neighborhood knife dealership, such as DuPont or Diatome, will be happy to talk to you about this. I used a 45° knife from DuPont. I also marked the living daylights out of it. DO NOT DO THIS UNLESS YOU HAVE A KNIFE YOU CAN TRASH!

Second, through this entire discussion you should remember one very important thing about microtomed samples. Sections are not sliced from the block; they are fractured.

Thus, a microtomed sample will always have a burr. While one does not normally notice the burr on plastic samples, on metallic samples it is fairly obvious.

Samples microtomed in this study and related studies included Ti-6Al-4V rod, anodized aluminum, and oxidized zirconium. The microtomy technique given here is specific to Ti-alloy rod. The embedding technique is useful for all of these samples. Spurr's is recommended for PSHA-coated samples; Araldite embedding is described below.

The recipe for PolyBed/Araldite (Polysciences) is 10 g Polybed, 5.5 g Araldite, 18 g dodecenyl succinic anhydride (DDSA), and 0.5 g 2,4,6-tri(dimethylaminomethyl)phenol (DMP-30). The mixture should be stirred before adding the DMP-30 and then again afterwards. It can be stored in syringes according to the manufacturer's instructions. It is cured for 24 hours at 60°C. I do not recommend pulling vacuum on this epoxy because it makes air bubbles. Rather, use graded solutions of the epoxy in propylene oxide to infiltrate the sample.

Once the rod is embedded, cut it into 5-7 mm sections using a low speed diamond saw (Figure C.1 - Step 1). These sections are then cut on the same saw parallel to the axis of the cylinder to form 1-1.5 mm slices (Steps 2,3). The slices should be cut such that there is significant curvature along the side of the sample. The slices are then sliced again (again on the low speed saw) parallel to the original axis to make 1x1 mm slivers (Steps 4,5). The goal is to form a metallic sliver with a triangular cross-section. This is the reason for curvature along the side of the sample. If there is no curvature, the slice can be oriented on the saw such that the cut will produce a triangular cross-section. This sliver is then re-embedded.

Slicing slivers from the slices is not trivial. The slice will not support itself if it is simply mounted on a block for sawing. An extra piece of ceramic should be used to brace the slice. It should be placed such that the direction of sawing is into the brace (Step 4 - the

larger block on which the two pieces are mounted is not shown). Alternately, two extra pieces of ceramic can be used, one on each side. An unchipped blade mounted on a saw running at low speed with a low sample advance rate will prevent the sample from coming off the block.

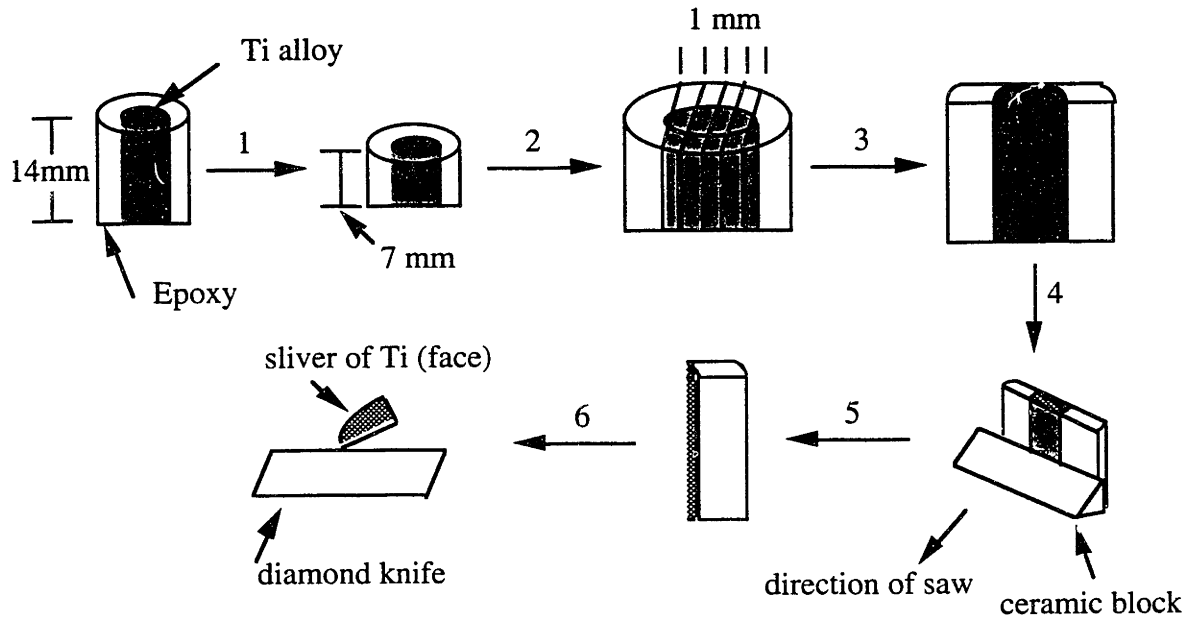

Figure C.1: Illustration of how to trim Ti-alloy cylinder for microtomy. The steps (1-6) are described in the text.

The samples are then re-embedded and microtomed. It will not be possible to face off the blocks using a glass knife. An old diamond knife should be used instead. Shallow angles (I used 4°) will minimize the size of the burr which is formed. If the sample is oriented such that the leading "edge" of the sample is actually a corner, curling will be minimized (Step 6). Slices should be collected on folding grids because they are not tremendously adherent to the copper, even with polyisobutylate adhesive. Because the slice will catch on the edge of the blade or sink to the bottom of the trough, the samples cannot be collected from the trough with the grid an alternative collection method is needed. Take a glass slide and make a small square (0.7 x 0.7 cm) on it with nail polish. Put a drop

of water on the square. Lift the sample from the edge of the knife with an eyelash tool and put it on the drop of water. Before it sinks to the side of the drop, collect it on the grid. If the slice sinks, it can be moved back to the top of the drop with the eyelash tool. Note that the epoxy will probably be lost from the sample at some point during microtomy. Unless there is something important left in the epoxy, this is not a problem [207].

Appendix D

Other Data From the Investigation of the Oxide Scale on Zr-2.5Nb

D.1 Introduction

The purpose of this appendix is to present some data, which, while not timely enough to be included in the chapter, were definitely interesting enough to be fully described in this appendix.

D.2 Methods

The data described below are the results of two experiments. The first is the TEM investigation which is described fully in Chapter 4. The second is an in-situ oxidation/XRD experiment conducted by Meri Treska with the author's assistance. A sample of Zr-2.5Nb barstock provided by Smith and Nephew, Inc. was machined into a 1x10x15 mm slice whose face included a longitudinal cross-section of the material. One face was polished to a 600 grit finish with SiC paper (Buehler). The sample was inserted into a hot stage provided by Rigaku for their RU200 instrument and aligned with the x-ray (Cu Kα) beam. The x-ray diffractometer was operated at 50 kV and 200 mA. The chamber including the stage was flooded with helium and heated to 635°C; XRD spectra were read for $2\theta = 25°$-$65°$ at room temperature, 200°C, 400°C, and 635°C. Air was allowed to enter the chamber, and the sample was allowed to oxidize for about 2 hours,

with spectra read every 30 minutes (one spectrum took 8 minutes scanning at 5°/min, adding up to an extra 32 minutes). The sample was then cooled to room temperature, with spectra taken at the same temperatures as during heating, with an additional spectrum read after the sample had been at room temperature for 12 hours. The fraction of tetragonal zirconia in the scale was determined by comparison of the integrated intensities of the (111) peaks for the monoclinic and tetragonal phases, accounting for polarization.

D.3 Results and Discussion

The development of the tetragonal phase in the oxide scale is tracked in Figure D.1. That the initial fraction of the tetragonal phase is very high and decreases over both oxidation and cooling indicates that at least some tetragonal zirconia is converted to monoclinic zirconia during the formation and cooling of the scale. However, tetragonal zirconia continues to be formed throughout oxidation because the TEM experiment demonstrated that the tetragonal phase was present in the scale near the oxide/metal interface as well as at the outer surface of the scale. The rate of formation of the monoclinic oxide with respect to the tetragonal oxide also appears to increase as oxidation proceeds.

While searching for examples of β-phase oxidation in the transverse oxide formed at 635°C, a lamellar microstructure was observed which differed from that observed in Figures 4.18 or 4.23 (Figure D.2). The microstructure is lamellar, like that in Figure 4.23, but the orientation of the lamellae is oblique to that of the oxide columns. XEDS analysis showed that the area of the lamellar microstructure contained higher concentrations of Nb than the surrounding oxide. HRTEM revealed that the lamellae comprised two alternating phases, one with a lattice fringe spacing of 2.8 Å and the other with a fringe spacing of 3.1 Å. The orientation of the fringes is consistent between the alternate lamellae. The error in the measurement of lattice spacings from the micrograph is at least 0.1 Å. However, comparison with the SAED pattern of the area indicates that both monoclinic

zirconia and an oxide phase with a reflection at 2.95 (either tetragonal zirconia or the mixed $6ZrO_2 \cdot Nb_2O_5$ phase) are present. The presence of Nb indicates that the mixed oxide is probably present. Without XEDS analysis in the STEM (the analysis described above was performed in the JEM 2010), it is impossible to determine the distribution of Nb among the lamellae.

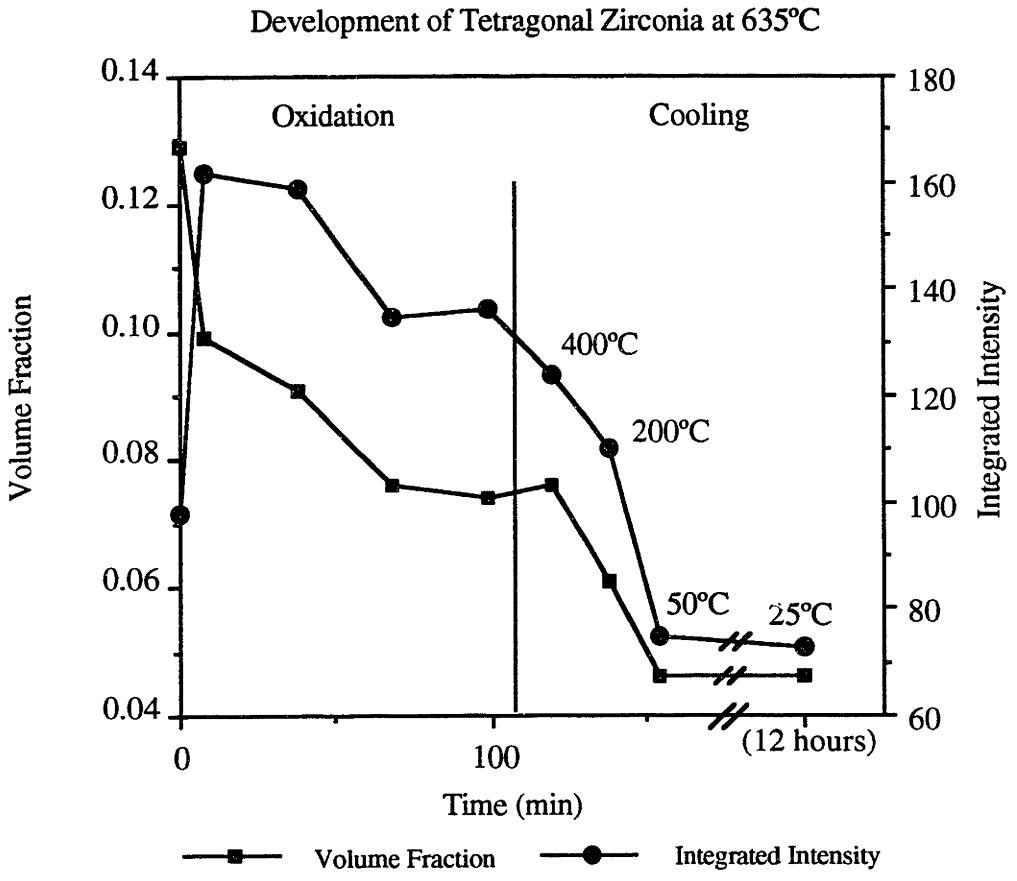

Figure D.1: Chart showing development of tetragonal zirconia within oxide scale during oxidation at 635°C in air on the longitudinal face of Zr-2.5Nb barstock.

The microstructure observed probably results from one of two phenomena. It may result from the same β to $\beta + \alpha$ transformation described in detail in Chapter 4. If this is so, then there is a factor contributing to crystallographic texture in the transformed phases.

That is, there may be a preferential orientation of the transformed phases with respect to the originating phase. Alternately, the microstructure may result from the transformation of tetragonal zirconia to monoclinic zirconia. The alternating (abababab) arrangement of the lamellae is common in martensitic transformations. Elemental analysis would confirm one of these hypotheses; however, the presence of Nb tends to favor the former.

Following page

Figure D.2: TEM micrograph of oxide scale grown at 635°C (transverse surface) showing lamellar grains oriented obliquely to the column in which they are located.

Figure D.3: HRTEM micrograph of lamellar grains in Figure D.2, showing alternation of two phases. (a) denotes phase with lattice fringes spaced at 2.8Å, (b) denotes phase with lattice fringes spaced at 3.1Å.

Figure D.2

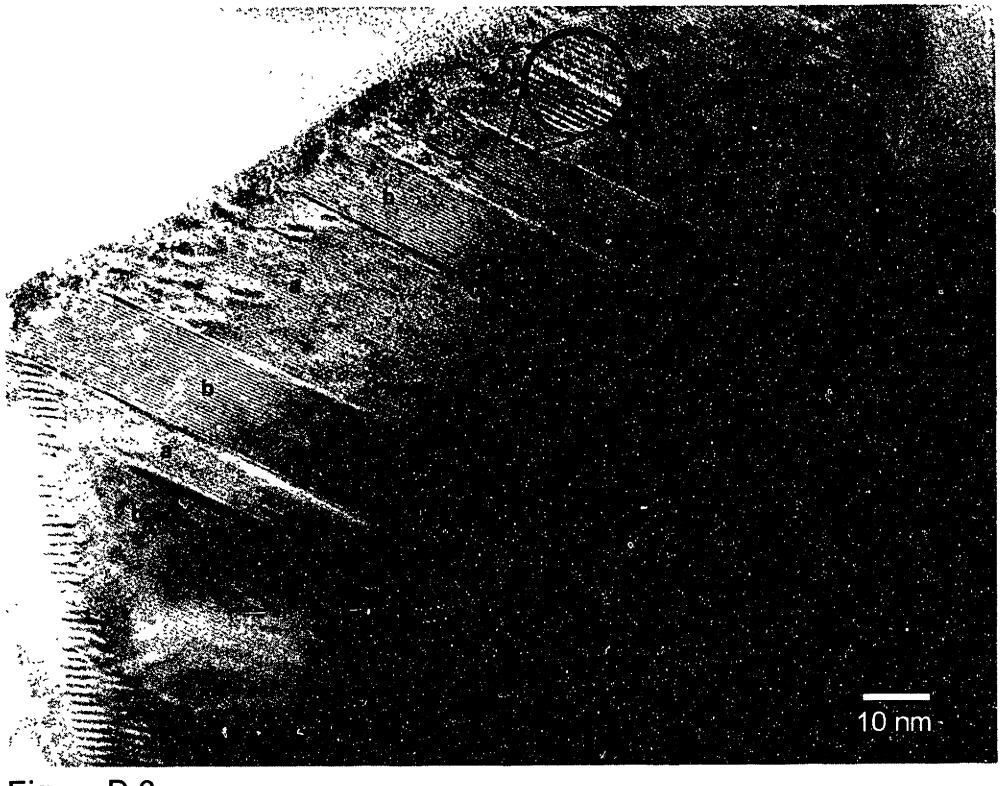

Figure D.3

References

1) R. Fulghum, *All I Really Need to Know, I Learned in Kindergarten..* 1989, New York, NY: Villard Books.

2) W.H. Harris and C.B. Sledge. Total hip and total knee replacement (First of two parts). *New Engl. J. Med.* **323**:725-731 (1990)

3) W.H. Harris and C.B. Sledge. Total hip and total knee replacement (Second of two parts). *New Eng. J. Med.* **323**:801-807 (1990)

4) M. Spector. Prostheses: materials, design, and strategies for implant fixation, in *Orthopedic Knowledge Update 3* . 1990, Amer. Acad. Orthop. Surg.: p. 185-205.

5) J.P. Paul. Forces transmitted by joints in the human body. *Proc. Inst. Mech. Engrs.* **181**:8 (1967)

6) R.G.T. Geesink, K. de Groot, and C.P.A.T. Klein. Chemical implant fixation using hydroxyl-apatite coatings. *Clin. Orthop.* **225**:147-170 (1987)

7) R.J. Haddad Jr., S.D. Cook, and K.A. Thomas. Biological fixation of porous-coated implants. *J. Bone Joint Surg.* **69-A**:1469-1476 (1987)

8) L.L. Hench and J. Wilson. Bioceramics. *MRS Bulletin.* **16**:62-74 (1991)

9) W.L. Jaffe and D.F. Scott. Total hip arthroplasty with hydroxyapatite-coated prostheses. *J. Bone Joint Surg.* **78-A**:1918-1934 (1996)

10) S.D. Cook, K.A. Thomas, J.F. Kay, and M. Jarcho. Hydroxyapatite-coated porous titanium for use as an orthopedic biologic attachment system. *Clin. Orthop.* **230**:303-312 (1988)

11) R.G.T. Geesink. Hydroxyapatite-coated total hip prostheses. *Clin. Orthop.* **261**:39-58 (1990)

12) R.L. Buly and T.P. Sculco. Recent advances in total knee replacement surgery. *Curr. Opin. Rheum.* **7**:107-113 (1995)

13) F.C. Ewald and P.S. Walker. The current status of total knee replacement. *Rheum. Dis. Clin. North Am.* **14**:579-590 (1988)

14) J.A. Williams, *Engineering Tribology.* 1994, Oxford, England: Oxford University Press.

15) S. Goodman and L. Lindgren. Polyethylene wear in knee arthroplasty. *Acta Orthop. Scand.* **63**:358-364 (1992)

16) H.-G. Willert and M. Semlitsch. Reactions of the articular capsule to wear products of artificial joint prostheses. *J. Biomed. Mat. Res.* **11**:157-164 (1977)

17) R.M. Rose, A. Crugnola, M. Ries, W.R. Cimino, I. Paul, and E.L. Radin. On the origins of high in vivo wear rates in polyethylene components of total joint prostheses. *Clin. Orthop.* **145**:277-286 (1979)

18) A. Wang, D.C. Sun, C. Stark, and J.H. Dumbleton. Wear mechanisms of UHMWPE in total joint replacements. *Wear.* **181-183**:241-249 (1995)

19) N.P. Suh. An overview of the delamination theory of wear. *Wear.* **44**:1-16 (1977)

20) B. Weightman and D. Light. The effect of the surface finish of alumina and stainless steel on the wear rate of UHMW polyethylene. *Biomaterials.* **7**:20-24 (1996)

21) J.R. Cooper, D. Dowson, and J. Fisher. Macroscopic and microscopic wear mechanisms in ultra-high molecular weight polyethylene. *Wear.* **162-164**:378-384 (1993)

22) H. Caulier, S. Vercaigne, I. Naert, J.P.C.M. van der Waerden, J.G.C. Wolke, W. Kalk, and J.A. Jansen. The effect of Ca-P plasma-sprayed coatings on the initial bone healing of oral implants: An experimental study in the goat. *J. Biomed. Mat. Res.* **34**:121-128 (1997)

23) G.W. Blunn, A.B. Joshi, P.A. Lilley, E. Engelbrecht, L. Ryd, L. Lidgren, K. Hardinge, E. Nieder, and P.S. Walker. Polyethylene wear in unicondylar knee prostheses. *Acta Orthop. Scand.* **63**:247-255 (1992)

24) N. Chang. S.M. thesis, 1998. *The Effect of Molecular Orientation on the Wear of Ultra-High Molecular Weight Polyethylene.* Massachusetts Institute of Technology, Cambridge, MA.

25) J.A. Davidson. Characteristics of metal and ceramic total hip bearing surfaces and their effect on long term ultra high molecular weight polyethylene wear. *Clin. Orthop.* **294**:361-378 (1993)

26) A.M. Patel and M. Spector. Tribological evaluation of oxidized zirconium using an articular cartilage counterface: a novel material for potential use in hemiarthroplasty. *Biomaterials.* **18**:441-447 (1997)

27) M. Mosleh and N.P. Suh. Wear particles of polyethylene in biological systems. in *51st Annual STLE Meeting*. 1996: p. 1-6.

28) P. Kumar, M. Oka, K. Ikeuchi, K. Shimizu, T. Yamamuro, H. Okumura, and Y. Kotoura. Low wear rate of UHMWPE against zirconia ceramic (Y-PSZ) in comparison to alumina ceramic and SUS 316L alloy. *J. Biomed. Mat. Res.* **25**:813-828 (1991)

29) B. Derbyshire, J. Fisher, D. Dowson, C. Hardacker, and K. Brummit. Comparative study of the wear of UHMWPE with zirconia ceramic and stainless steel femoral heads in artificial hip joints. *Med. Eng. Phys.* **16**:229-236 (1994)

30) H. Oonishi, M. Aono, N. Murata, and S. Kushitani. Alumina versus polyethylene in total knee arthroplasty. *Clin. Orthop.* **282**:95-104 (1992)

31) V.O. Saikko. Wear of the polyethylene acetabular cup: The effect of head material, head diameter, and cup thickness studied with a hip simulator. *Acta Orthop. Scand.* **66**:501-506 (1995)

32) Y. Ichikawa, Y. Akagawa, H. Nikai, and H. Tsuru. Tissue compatibility and stability of a new zirconia ceramic *in vivo*. *J. Prosthet. Dent.* **68**:322-326 (1992)

33) S.E. White, L.A. Whiteside, D.S. McCarthy, M. Anthony, and R.A. Poggie. Simulated knee wear with cobalt chromium and oxidized zirconium knee femoral components. *Clin. Orthop.* **309**:176-184 (1994)

34) D.G. Franklin and P.M. Lang. Zirconium alloy corrosion: A review based on an International Atomic Energy Agency (IAEA) meeting, in *Zirconium in the Nuclear Industry: Ninth International Symposium, ASTM STP 1132,* C.M. Eucken and A.M. Garde, ed. 1991, American Society for Testing and Materials: Philadelphia, PA. p. 3-32.

35) J.A. Davidson, C.M. Asgian, A.K. Mishra, and P. Kovaks. Zirconia (ZrO2)-coated zirconium-2.5Nb alloy for prosthetic knee bearing applications. *Bioceramics* . **5**:389-401 (1993)

36) M. Treska. unpublished results.

37) M. Treska and L.W. Hobbs. *In situ* stress determination at high temperature in metal/oxide system by x-ray diffraction. (in preparation)

38) A. Aubry, F. Armanet, G. Beranger, J.L. LeBrun, and G. Maeder. Measurement of residual stresses by x-ray diffraction in a Ni/NiO system obtained by high temperature oxidation. *Acta Metall.* **36**:2779-2786 (1988)

39) P.Y. Hou and R.M. Cannon. The stress state in thermally grown NiO scales. in *Fourth International Symposium of High Temperature Corrosion.* 1996: p.

40) B. Wadman, Z. Lai, H.-O. Andren, A.-L. Nystrom, P. Rudling, and H. Petterson. Microstructure of oxide layers formed during autoclave testing of zirconium alloys, in *Zirconium in the Nuclear Industry: Tenth International Symposium, ASTM STP 1245,* A.M. Garde and E.R. Bradley, ed. 1994, Amer. Soc. for Testing and Materials: Philadelphia, PA. p. 579-598.

41) F. Garzarolli, H. Seidel, R. Tricot, and J.P. Gros. Oxide growth mechanism on zirconium alloys, in *Zirconium in the Nuclear Industry: Ninth International Symposium, ASTM STP 1132,* C.M. Euken and A.M. Garde, ed. 1991, Amer. Soc. for Testing and Materials: Philadelphia, PA. p. 395-415.

42) M. Spector. Anorganic bovine bone and ceramic analogs of bone mineral as implants to facilitate bone regeneration. *Clin. Plas. Surg.* **21**:437-444 (1994)

43) R.Z. LeGeros, C. Bautista, D. Styner, J.P. LeGeros, T.V. Vijiayaraghavan, M. Retino, and A. Valdecanas. Comparative properties of bioactive bone graft materials. in *Bioceramics*, Vol. 8. J. Wilson, L.L. Hench, and D. Greenspan, ed. 1995, Oxford, England: Alden Press.

44) A.C. Wetzel, H. Stich, and R.G. Caffesse. Bone apposition onto oral implants in the sinus area filled with different grafting materials. *Clin. Oral. Impl. Res.* **6**:155-163 (1995)

45) J.R. Wagner. Clinical and histological case study using resorbable hydroxylapatite for the repair of osseous defects prior to endosseous implant surgery. *J. Oral Implantol.* **15**:186-192 (1989)

46) A. Corsair. A clinical evaluation of resorbable hydroxylapatite for the repair of human intra-osseous defects. *J. Oral Implantol.* **16**:125-128 (1990)

47) L.F.A. Stassen, W.S. Hislop, D.M. Still, and K.F. Moos. Use of anorganic bone in periapical defects following apical surgery - a prospective trial. *Brit. J. Oral Maxillofac. Surg.* **32**:83-85 (1994)

48) J.M. Lane, F. Betts, A.S. Posner, and D.W. Yue. Mineral parameters in early fracture repair. *J. Bone Joint Surg.* **66-A**:1289-1293 (1984)

49) M.J. Yaszemski, R.G. Payne, W.C. Hayes, R. Langer, and A.G. Mikos. Evolution of bone transplantation: molecular, cellular and tissue strategies to engineer human bone. *Biomaterials.* **17**:175-185 (1996)

50) R.Z. LeGeros, O.R. Trautz, J.P. LeGeros, E. Klein, and W.P. Shirra. Apatite crystallites: Effects of carbonate on morphology. *Science.* **155**:1409-1411 (1967)

51) H. Ji and P.M. Marquis. Effect of heat treatment on the microstructure of plasma-sprayed hydroxyapatite coating. *Biomaterials.* **14**:64-68 (1993)

52) L.G. Ellies, D.G.A. Nelson, and J.D.B. Featherstone. Crystallographic changes in calcium phosphates during plasma-spraying. *Biomaterials.* **13**:313-316 (1992)

53) M.J. Filiaggi, R.M. Pilliar, and N.A. Coombs. Post-plasma-spraying heat treatment of the HA coating/Ti-6Al-4V implant system. *J. Biomed. Mat. Res.* **27**:191-198 (1993)

54) Z. Zyman, J. Weng, X. Liu, X. Li, and X. Xhang. Phase and structural changes in hydroxyapatite coatings under heat treatment. *Biomaterials.* **15**:151-155 (1994)

55) J. Moradian-Oldak, S. Weiner, L. Addadi, W.J. Landis, and W. Traub. Electron imaging and diffraction study of individual crystals of bone, mineralized tendon and synthetic carbonate apatite. *Conn. Tiss. Res.* **25**:219-228 (1991)

56) V. Ziv, I. Sabanay, T. Arad, W. Traub, and S. Weiner. Transitional structures in lamellar bone. *Microsc. Res. Tech.* **33**:203-213 (1996)

57) A. Ascenzi and A. Benvenuti. Orientation of collagen fibers at the boundary between two successive osteonic lamellae and its mechanical interpretation. *J. Biomechanics.* **19**:455-463 (1986)

58) T. Kitsugi, T. Yamamuro, T. Nakamura, and M. Oka. Transmission electron microscopy observvations at the interface on bone and four types of calcium phosphate ceramics with different calcium/phosphorus molar ratios. *Biomaterials.* **16**:1101-1107 (1995)

59) S. Weiner and W. Traub. Bone structure: From Ångstroms to microns. *FASEB Journal.* **6**:879-885 (1992)

60) A.L. Arsenault. Crystal-collagen relationships in calcified turkey leg tendons visualized by selected-area dark field electron microscopy. *Calcif. Tiss Int.* **43**:202-212 (1988)

61) D.D. Lee and M.J. Glimcher. Three-dimensional spatial relationship between the collagen fibrils and the inorganic calcium phosphate crystals of pickerel (*Americanus* americanus) and herring (*Clupea* harengus) bone. *J. Mol. Bio.* **217**:487-501 (1991)

62) M. Spector. High resolution electron microscope study of lattice images in biological apatites. *J. Microsc.* **103**:55-62 (1975)

63) S.A. Jackson, A.G. Cartwright, and D. Lewis. The morphology of bone mineral crystals. *Calcif. Tiss. Int.* **25**:217-222 (1978)

64) K.R. St. John, L.D. Zardiakas, R.C. Terry, R.D. Teasdall, S.E. Cooke, and H.M. Mitias. Histological and electron microscopic analysis of tissue response to synthetic composite bone graft in the canine. *J. Appl. Biomat.* **6**:89-97 (1995)

65) D.D. Lee, W.J. Landis, and M.J. Glimcher. The solid, calcium-phosphate mineral phases in embryonic chick bone characterized by high-voltage electron diffraction. *J. Bone Min. Res.* **1**:425-432 (1986)

66) F.L.G. Cuisinier, P. Steuer, A. Brisson, and J.C. Voegel. High resolution electron microscopy study of crystal growth mechanisms in chicken bone composites. *J. Crystal Growth.* **156**:443-453 (1995)

67) W.J. Landis and M.J. Song. Early mineral deposition in calcifying tendon characterized by high voltage electron microscopy and three-dimensional graphic imaging. *J. Struct. Bio.* **107**:116-127 (1991)

68) T. Ichijo, Y. Yamashita, and T. Terashima. Observations on structural features and characteristics of biological apatite crystals 4. Observation on ultrastructure of human bone crystals. *Bull. Tokyo Med. Dent. Univ.* **40**:93-112 (1993)

69) W.J. Landis, K.J. Hodgens, M.D. McKee, A. Nanci, M.J. Song, S. Kiyonaga, J. Arena, and B. McEwen. Extracellular vesicles of calcifying turkey leg tendon characterized by immunocytochemistry and high voltage electron microscopic tomography and 3-D graphic image reconstruction. *Bone Min.* **17**:237-241 (1992)

70) W.J. Landis, M.J. Song, A. Leith, L. McEwen, and B.F. McEwen. Mineral and organic matrix interaction in normally calcifying tendon visualized in three dimensions by high-voltage electron microscopic tomography and graphic image reconstruction. *J. Struct. Bio.* **110**:39-54 (1993)

71) W.J. Landis, K.J. Hodgens, J. Arena, M.J. Song, and B.F. McEwen. Structural relations between collagen and mineral in bone as determined by high voltage electron microscopic tomography. *Microsc. Res. Tech.* **33**:192-202 (1996)

72) W.J. Landis, J. Moradian-Oldak, and S. Weiner. Topographic imaging of mineral and collagen in the calcifying turkey tendon. *Conn. Tiss. Res.* **25**:181-196 (1991)

73) D.D. Lee and M.J. Glimcher. The three-dimensional spatial relationship between the collagen fibrils and the inorganic calcium-phosphate crystals of pickerel and herring fish bone. *Conn. Tiss. Res.* **21**:247-257 (1989)

74) J. Christoffersen and W.J. Landis. A contribution with review to the description of mineralization on bone and other calcified tissues *in vivo*. *Anat. Rec.* **230**:435-450 (1991)

75) A.L. Arsenault, B.W. Frankland, and F.P. Ottensmeyer. Vectorial sequence of mineralization in the turkey leg tendon determined by electron microscopic imaging. *Calcif. Tiss. Int.* **48**:46-55 (1991)

76) A.L. Arsenault. Image analysis of collagen-associated mineral distribution in cryogenically prepared turkey leg tendons. *Calcif. Tiss. Int.* **48**:56-62 (1991)

77) E. Bonucci. Comments on the ultrastructural morphology of the calcification process: An attempt to reconcile matrix vesicles, collagen fibrils, and crystal ghosts. *Bone Min.* **17**:219-222 (1992)

78) A.L. Arsenault. Structural and chemical analyses of mineralization using the turkey leg tendon as a model tissue. *Bone Min.* **17**:253-256 (1992)

79) W. Traub, T. Arad, and S. Weiner. Growth of mineral crystals in turkey tendon collagen fibers. *Conn. Tiss. Res.* **28**:99-111 (1992)

80) A.L. Boskey, B.D. Boyan, and Z. Schwartz. Matrix vesicles promote mineralization in a gelatin gel. *Calcif. Tiss. Int.* **60**:309-315 (1997)

81) U. Plate, T. Tkotz, H.P. Wiesmann, U. Stratmann, U. Joos, and H.J. Höhling. Early mineralization of matrix vesicles in the epiphyseal growth plate. *J. Microsc.* **183**:102-107 (1996)

82) G. Boivin, C. Anthoine-Terrier, and K.J. Obrant. Transmission electron microscopy of bone tissue. *Acta Orthop. Scand.* **61**:170-180 (1990)

83) J.E. Davies, N. Nagai, N. Takeshita, and D.C. Smith. Deposition of cement-like matrix on implant materials, in *The Bone Biomaterial Interface*, J.D. Davies, ed. 1991, University of Toronto Press: Toronto. p. 285-294.

84) J. Sela, Z. Schwartz, D. Amir, L.D. Swain, and B.D. Boyan. The effect of bone injury on extracellular matrix vesicle proliferation and mineral formation. *Bone Min.* **17**:163-167 (1992)

85) Y. Takano, C.H. Turner, and D.B. Burr. Mineral anisotropy in mineralized tissues is similar among species and mineral growth occurs independently of collagen orientation in

rats: Results from acoustic velocity measurments. *J. Bone. Min. Res.* **11**:1292-1301 (1996)

86) D.M. Kohler, M.A. Crenshaw, and A.L. Arsenault. Three-dimensional analysis of mineralizing turkey leg tendon: Matrix vesicle-collagen relationships. *Matrix Biology.* **14**:543-552 (1994)

87) W.J. Landis, K.J. Hodgens, M.J. Song, J. Arena, S. Kiyonaga, M. Marko, C. Owen, and B.F. McEwen. Mineralization of collagen may occur on fibril surfaces: Evidence from conventional and high-voltage electron microscopy and three-dimensional imaging. *J. Struct. Bio.* **117**:24-35 (1996)

88) A. Boyde. Scanning electron microscopic studies of bone, in *The Biochemistry and Physiology of Bone,* G.H. Bourne, ed. 1976, Academic Press: New York, NY. p. 580.

89) A. Boyde and S.J. Jones. Scanning electron microscopy of bone: Instrument, specimen, and tissue. *Microsc. Res. and Tech.* **33**:92-120 (1996)

90) D.L. Vezie, E.L. Thomas, and W.W. Adams. Low-voltage, high resolution scanning electron microscopy: a new characterization technique for polymer morphology. *Polymer.* **36**:1761-1779 (1995)

91) V. Benezra, L.W. Hobbs, and M. Spector. Ultrastructure and architecture of bone mineral and selected synthetic bone substitutes revealed by low voltage high resolution SEM. *Transactions of the Society for Biomaterials.* **20**:140 (1997)

92) Impladent, *Company literature.* 1996, Holliswood, NY.

93) CeraMed Dental Products, *Company literature.* 1996, Lakewood, CO.

94) E. Rubin and J.L. Farber, ed. *Pathology.* 1988, J.B. Lippincott: Philadelphia, PA.

95) M. Spector. Charakterisierung biokeramischer Kalziumphosphatimplante. *Hefte zur Unfallheilkunde.* **216**:11-22 (1991)

96) J.V. Smith, ed. *X-ray Powder Diffraction File.* 1967, American Society for Testing and Materials: Philadelphia, PA.

97) K.S. Prostak and S. Lees. Visualization of crystal-matrix structure. *In situ* demineralization of mineralized turkey leg tendon and bone. *Calcif. Tiss. Int.* **59**:474-479 (1996)

98) F.L. Losee and L.A. Hurley. Bone treated with ethylenediamine as a successful foundation material in cross-species bone grafts. *Nature.* **177**:1032-1033 (1956)

99) W.J. Landis, M.C. Paine, and M.J. Glimcher. Electron microscopic observations of bone tissue prepared anhydrously in organic solvents. *J. Ultrastr. Res.* **59**:1-30 (1977)

100) W.J. Landis and M.J. Glimcher. Electron diffraction and electron probe microanalysis of the mineral phase of bone tissue prepared by anhydrous techniques. *J. Ultrastr. Res.* **63**:188-223 (1978)

101) S. Weiner, T. Arad, and W. Traub. Crystal organization in rat bone lamellae. *FEBS Lett.* **285**:49-54 (1991)

102) P. Fratzl, N. Fratzl-Zelman, K. Klaushofer, G. Vogl, and K. Koller. Nucleation and growth of mineral crystals in bone studied by small-angle x-ray scattering. *Calcif. Tiss. Int.* **48**:407-413 (1991)

103) D.E. Newbury, D.C. Joy, P. Echlin, C.E. Fiori, and J.I. Goldstein, *Advanced Scanning Electron Microscopy and X-Ray Microanalysis.* 1986, New York, NY: Plenum Press.

104) E.P. Katz, E. Wachtel, M. Yamauchi, and G.L. Mechanic. The structure of mineralized collagen fibrils. *Conn. Tiss. Res.* **21**:149-158 (1989)

105) S. Weiner, T. Arad, I. Sabanay, and W. Traub. Rotated plywood structure of primary lamellar bone in the rat: Orientations of the collagen fibril arrays. *Bone.* **20**:509-514 (1997)

106) E.B. Hunziker, W. Herrmann, L.M. Cruz-Orive, and A.L. Arsenault. Image analysis of electron micrographs relating to mineralization in calcifying cartilage: Theoretical considerations. *J. Elect. Microsc. Tech.* **11**:9-15 (1989)

107) M. Spector. Basic Principles of Tissue Engineering, in *Tissue Engineering: Applications in Periodontics and Oral Surgery,* S. Lynch, ed. 1998, Quintessence Publishing Co., Inc.: Carol Stream, IL.

108) A.J. Hodge. Molecular models illustrating the possible distributions of 'holes' in systematically staggered arrays of type I collagen molecules in native-type fibrils. *Conn. Tiss. Res.* **21**:137-147 (1989)

109) D.G. Smiler, P.W. Johnson, J.L. Lozada, C. Misch, J.L. Rosenlicht, O.H. Tatum, and J.R. Wagner. Sinus lift grafts and endosseous implants. Treatment of the atrophic posterior maxilla. *Dent. Clin. North Am.* **36**:151-188 (1992)

110) L. Jaber, C. Mascrés, and W.B. Donohue. Reaction of the dental pulp to hydroxyapatite. *Oral Surg. Oral Med. Oral Pathol.* **73**:92-98 (1992)

111) W.S. Hislop, P.M. Finlay, and K.F. Moos. A preminiary study into the uses of anorganic bone in oral and maxillofacial surgery. *Brit. J. Oral. Maxillofac. Surg.* **31**:149-153 (1993)

112) J.L. Ricci, N.C. Blumenthal, J.M. Spivak, and H. Alexander. Evaluation of a low-temperature calcium phosphate particulate implant material: physical-chemical properties and in vivo bone response. *J. Oral Maxillofac. Surg.* **50**:969-978 (1992)

113) G. Daculsi, R.Z. LeGeros, H. Heughebaert, and I. Barbieux. Formation of carbonate-apatite crystals after implantation of calcium phosphate ceramics. *Calcif. Tiss. Int.* **46**:20-27 (1990)

114) M. Neo, T. Nakamura, C. Ohtsuki, T. Kokubo, and T. Yamamuro. Apatite formation on three kinds of bioactive material at an early stage *in vivo*: A comparative study by transmission electron microscopy. *J. Biomed. Mat. Res.* **27**:999-1006 (1993)

115) V. Benezra, L. Hoang, L.W. Hobbs, G.H. Nancollas, M. Kearney, and M. Spector. Ultrastructural and immunohistochemical studies of the early response of bone to HA-coated Ti-6Al-4V *in vivo. Transactions of the Society for Biomaterials.* **18**:69 (1995)

116) V. Benezra, M. Spector, and L.W. Hobbs. Characterization of mineral deposits on plasma-sprayed HA-coated Ti-6Al-4V. *Materials Research Society Symposium Proceedings.* **414**:165-170 (1996)

117) H.J. Höhling, H. Steffens, G. Stamm, and U. Mays. Transmission electron microscopy of freeze-dried, unstained epiphysial cartilage of the guinea pig. *Cell Tiss. Res.* **167**:243-263 (1976)

118) M. Spector, R. Prabhakar, A. Bignami, P.A. Lalor, J. Bearcroft, N. Beals, and G.H. Nancollas. Early bone-bonding response to plasma-sprayed hydroxyapatite coatings of different compositions in the canine. *Transactions of the Society for Biomaterials.* **18**:122 (1995)

119) K.A. Thomas, J.F. Kay, S.D. Cook, and M. Jarcho. The effect of surface macrotexture and hydroxylapatite coating on the mechanical strengths and histologic profiles of titanium implant materials. *J. Biomed. Mat. Res.* **21**:1395-1414 (1987)

120) G.L. DeLange, C. DePutter, and F.L.J.A. De Wijs. Histological and ultrastructural appearance of the hydroxyapatite-bone interface. *J. Biomed. Mat. Res.* **24**:829-845 (1990)

121) J.D. de Bruijn, J.S. Flach, K. de Groot, C.A. van Blitterswijk, and J.E. Davies. Analysis of the bony interface with various types of hydroxyapatite *in vitro. Cells and Materials.* **3**:115-127 (1993)

122) J.D. de Bruijn, C.A. van Blitterswijk, and J.E. Davies. Initial bone matrix formation at the hydroxyapatite interface *in vivo. J. Biomed. Mat. Res.* **29**:89-99 (1995)

123) F.B. Bagambisa, U. Joos, and W. Schilli. Mechanisms and structure of the bond between bone and hydroxyapatite ceramics. *J. Biomed. Mat. Res.* **27**:1047-1055 (1993)

124) B.M. Tracy and R.H. Doremus. Direct electron microscopy studies of the bone-hydroxylapatite surface. *J. Biomed. Mat. Res.* **18**:719-726 (1984)

125) M. Neo, S. Kotani, T. Nakamura, T. Yamamuro, C. Ohtsuki, T. Kokubo, and Y. Bando. A comparative study of ultrastructures of the interfaces between four kinds of surface-active ceramic and bone. *J. Biomed. Mat. Res.* **26**:1419-1432 (1992)

126) J. Hemmerlé and J.-C. Voegel. Ultrastructural aspects of the intact titanium implant-bone interface from undecalcified ultrathin sections. *Biomaterials.* **17**:1913-1920 (1996)

127) S.R. Radin and P. Ducheyne. The effect of calcium phosphate ceramic composition and structure on *in vitro* behavior. II. Precipitation. *J. Biomed. Mat. Res.* **27**:35-45 (1993)

128) P. Ducheyne, S. Radin, and L. King. The effect of calcium phosphate ceramic composition and structure on *in vitro* behavior. I. Dissolution. *J. Biomed. Mat. Res.* **27**:25-34 (1993)

129) P. Ducheyne, J. Beight, J. Cuckler, B. Evans, and S. Radin. Effect of calcium phosphate coating characteristics on early post-operative bone tissue ingrowth. *Biomaterials*. **11**:531-540 (1990)

130) J. Morgan, K.R. Holtman, J.C. Keller, and C.M. Stanford. *In vitro* mineralization and implant calcium phosphate-hydroxyapatite crystallinity. *Implant Dentistry*. **5**:264-271 (1996)

131) K. Hayashi, T. Inadome, T. Mashima, and Y. Sugioka. Comparison of bone-implant interface shear strength of solid hydroxyapatite and hydroxyapatite-coated titanium implants. *J. Biomed. Mat. Res.* **27**:557-563 (1993)

132) C.P.A.T. Klein, P. Patka, H.B.M. van der Lubbe, J.G.C. Wolke, and K. de Groot. Plasma-sprayed coatings of tetracalciumphosphate, hydroxyl-apatite, and α-TCP on titanium alloy: An interface study. *J. Biomed. Mat. Res.* **25**:53-65 (1991)

133) C.P.A.T. Klein, P. Patka, J.G.C. Wolke, J.M.A. de Blieck-Horgervorst, and K. de Groot. Long-term in vivo study of plasma-sprayed coatings on titanium alloys of tetracalcium phosphate, hydroxyapatite and α-tricalcium phosphate. *Biomaterials*. **15**:146-150 (1994)

134) C.P.A.T. Klein, J.G.C. Wolke, J.M.A. de Blieck-Horgervorst, and K. de Groot. Features of calcium phosphate plasma-sprayed coatings: An *in vitro* study. *J. Biomed. Mat. Res.* **28**:961-967 (1994)

135) C.P.A.T. Klein, J.G.C. Wolke, J.M.A. de Blieck-Horgervorst, and K. de Groot. Calcium phosphate plasma-sprayed coatings and their stability: An *in vivo* study. *J. Biomed. Mat. Res.* **28**:909-917 (1994)

136) J. Chen, W. Tong, Y. Cao, J. Feng, and X. Zhang. Effect of atmosphere on phase transformation in plasma-sprayed hydroxyapatite coatings during heat treatment. *J. Biomed. Mat. Res.* **34**:15-20 (1997)

137) B.C. Wang, E. Chang, T.M. Lee, and C.Y. Yang. Changes in phases and crystallinity of plasma-sprayed hydroxyapatite coatings under heat treatment: A quantitative study. *J. Biomed. Mat. Res.* **29**:1483-1492 (1995)

138) B.E. Tucker, C.M. Cotell, R.C.Y. Auyeung, M. Spector, and G.H. Nancollas. Pre-conditioning and dual constant composition dissolution kinetics of pulsed laser deposited hydroxyapatite thin films on silicon substrates. *Biomaterials*. **17**:631-637 (1996)

139) M. Jarcho. Biomaterial aspects of calcium phosphates. *Dent. Clin. North Am.* **30**:25-47 (1986)

140) R.Z. LeGeros, I. Orly, M. Gregoire, and G. Daculsi. Substrate surface dissolution and interfacial biological mineralization, in *The Bone Biomaterial Interface,* J.D. Davies, ed. 1991, University of Toronto Press: Toronto. p. 76-88.

141) K.A. Thomas and S.D. Cook. An evaluation of variables influencing implant fixation by direct bone apposition. *J. Biomed. Mater. Res.* **19**:875-901 (1985)

142) D. Buser, R.K. Schenk, S. Steinemann, J.P. Fiorellini, C.H. Fox, and H. Stich. Influence of surface characteristics on bone integration of titanium implants. A histomorphometric study in miniature pigs. *J. Biomed. Mat. Res.* **25**:889-902 (1991)

143) K. Gomi and J.E. Davies. Guided bone tissue elaboration by osteogenic cells *in vitro*. *J. Biomed. Mat. Res.* **27**:429-431 (1993)

144) S.H. Maxian, J.P. Zawadsky, and M.G. Dunn. Mechanical and histological evaluation of amorphous calcium phosphate and poorly crystallized hydroxyapatite coatings on titanium implants. *J. Biomed. Mat. Res.* **27**:717-728 (1993)

145) M.T. Walenciak, M.C. Zimmerman, R.D. Harten, J.L. Ricci, and D.T. Stamer. Biomechanical and histological analysis of an HA coated, arc deposited CPTi canine hip prosthesis. *J. Biomed. Mat. Res.* **31**:465-474 (1996)

146) A. Moroni, V.L. Caja, E.L. Egger, T. Trinchese, and E.Y.S. Chao. Histomorphometry of hydroxyapatite coated and uncoated porous titanium bone implants. *Biomaterials*. **15**:926-936 (1994)

147) D.S. Pereira, J.L. Ricci, D. Scott, R.S. Cesar, W. Jaffe, M. Hawkins, Y.H. Oh, and H. Alexander. Effects of macroroughness and hydroxyapatite coating on osteointegration and osteoconduction. *Transactions of the Society for Biomaterials*. **18**:424 (1995)

148) Y. Nakashima, K. Hayashi, T. Inadome, K. Uenoyama, T. Hara, T. Kanemaru, Y. Sugioka, and I. Noda. Hydroxyapatite coating on titanium arc sprayed titanium implants. *J. Biomed. Mat. Res.* **35**:287-298 (1997)

149) T. Inadome, K. Hayashi, Y. Nakashima, H. Tsumura, and Y. Sugioka. Comparison of bone-implant interface shear strength of hydroxyapatite-coated and alumina-coated metal implants. *J. Biomed. Mat. Res.* **29**:19-24 (1995)

150) D.M. Dzidzic, I.H. Savva, D.S. Wilkinson, and J.E. Davies. Osteoconduction on, and bonding to, calcium phosphate ceramic implants. *Materials Research Society Symposium Proceedings*. **414**:147-156 (1996)

151) D.E. Steflik, P.J. Hanes, A.L. Sisk, G.R. Parr, M.J. Song, F.T. Lake, and R.V. McKinney. Transmission electron microscopic and high voltage electron microscopic observations of the bone and osteocyte activity adjacent to unloaded dental implants placed in dogs. *J. Periodontol.* **63**:443-452 (1992)

152) L. Linder, T. Albrektsson, P.-I. Branemark, H.-A. Hansson, B. Ivarsson, U. Jonsson, and I. Lundstrom. Electron microscopic analysis of the bone-titanium interface. *Acta Orthop. Scand.* **54**:45-52 (1983)

153) T. Albrektsson, H.-A. Hansson, and B. Ivarsson. Interface analysis of titanium and zirconium bone implants. *Biomaterials*. **6**:97-101 (1985)

154) C. Johansson, J. Lausmaa, M. Ask, H.-A. Hansson, and T. Albrektsson. Ultrastructural differences of the interface zone between bone and Ti-6Al-4V or commercially pure titanium. *Biomaterials.* **11**:3-8 (1989)

155) D.E. Steflik, A.L. Sisk, G.R. Parr, L.K. Gardner, P.J. Hanes, F.T. Lake, D.J. Berkery, and P. Brewer. Osteogenesis at the dental implant interface: High-voltage electron microscopic and conventional transmission electron microscopic observations. *J. Biomed. Mat. Res.* **2**:791-800 (1993)

156) M.A. Listgarten, D. Buser, S.G. Steinemann, K. Donath, N.P. Lang, and H.P. Weber. Light and transmission electron microscopy of the intact interfaces between non-submerged titanium-coated epoxy resin implants and bone or gingiva. *J. Dent. Res.* **71**:364-371 (1991)

157) J.A. Jansen, J.P.C.M. van de Waerden, J.G.C. Wolke, and K. de Groot. Histologic evaluation of the osseous adaptation to titanium and hydroxyapatite-coated titanium implants. *J. Biomed. Mat. Res.* **25**:973-989 (1991)

158) S.G. Steinemann, J. Eulenberger, P.-A. Mäusli, and A. Schröder. Adhesion of bone to titanium, in *Biological and Biomechanical Performance of Biomaterials,* P. Christel, A. Meunier, and A.J.C. Lee, ed. 1986, Elsevier Science Publishers: Amsterdam. p. 409-414.

159) S.G. Steinemann, J. Eulenberger, P.-A. Mäusli, and A. Schröder. Adhesion of bone to titanium. in *Transactions of the European Society for Biomaterials.* 1985: p. 72.

160) D.A. Gerdeman and N.L. Hecht, *Arc plasma technology in materials science.* in Applied Mineralogy, V.D. Fréchette, *et al.*, ed. Vol. 3. 1972, New York: Springer Verlag.

161) K. de Groot, R. Geesink, C.P.A.T. Klein, and P. Serekian. Plasma sprayed coatings of hydroxylapatite. *J. Biomed. Mat. Res.* **21**:1275-1381 (1987)

162) J.C. Knowles, K. Gross, C.C. Berndt, and W. Bonfield. Structural changes of thermally sprayed hydroxyapatite investigated by Rietveld analysis. *Biomaterials.* **17**:639-645 (1996)

163) R.Y. Whitehead, W.R. Lacehead, and L.C. Lucas. Structure and integrity of a plasma sprayed hydroxylapatite coating on titanium. *J. Biomed. Mat. Res.* **27**:1501-1507 (1993)

164) Z. Zyman, Y. Cao, and X. Zhang. Periodic crystallization effect in the surface layers of coatings during plasma spraying of hydroxyapatite. *Biomaterials.* **14**:1140-1144 (1993)

165) I.M.O. Kangasniemi, C.C.P.M. Verheyen, E.A. van der Velde, and K. de Groot. *In vivo* tensile testing of fluorapatite and hydroxyapatite plasma-sprayed coatings. *J. Biomed. Mat. Res.* **28**:563-572 (1994)

166) C. Cotell. Pulsed laser deposition and processing of biocompatible hydroxylapatite thin films. *Appl. Surface. Sci.* **69**:140-148 (1993)

167) F.Z. Cui, Z.S. Luo, and Q.L. Feng. Highly adhesive hydroxyapatite coatings on titanium alloy formed by ion beam assisted deposition. *J. Mat. Sci.: Matls. in Med.* **8**:403-405 (1997)

168) F.A. Smidt. Use of ion beam assisted deposition to modify the microstructure and properties of thin films. *Internat. Mat. Rev.* **35**:61-128 (1990)

169) X. Li, J. Weng, W. Tong, C. Zuo, X. Zhang, P. Wang, and Z. Liu. Characterization of hydroxyapatite film with mixed interface by Ar+ ion beam enhanced deposition. *Biomaterials*. **18**:1487-1493 (1997)

170) C.M. Müller-Mai, C. Voigt, and U. Gross. Incorporation and degradation of hydroxyapatite implants of different surface roughness and surface structure in bone. *Scanning Microsc.* **4**:613-624 (1990)

171) M. Jarcho, J.F. Kay, K.I. Gumaer, R.H. Doremus, and H.P. Drobeck. Tissue, cellular, and subcellular events at a bone-ceramic hydroxylapatite surface. *J. Bioeng.* **1**:79-92 (1977)

172) R. Prabhakar. Early biological responde to plasma-sprayed hydroxyapatite coatings of different compositions in the canine. Biology Project Lab, Massachusetts Institute of Technology. Cambridge, MA, 1992.

173) G. Daculsi, R.Z. LeGeros, J.P. LeGeros, and D. Mitre. Lattice defects in calcium phosphate ceramics: High resolution TEM ultrastructural study. *J. Appl. Biomat.* **2**:147-152 (1991)

174) J.L. Ricci, J.M. Spivak, N.C. Blumenthal, and H. Alexander. Modulation of bone ingrowth by surface chemistry and roughness, in *The Bone Biomaterial Interface,* J.D. Davies, ed. 1991, University of Toronto Press: Toronto. p. 334-349.

175) H.B. Wen, F.Z. Cui, Q.L. Feng, H.D. Li, and X.D. Zhu. Microstructural investigation of the early external callus after diaphyseal fractures of human long bone. *J. Struct. Bio.* **114**:115-122 (1995)

176) D.A. Skoog, D.M. West, and F.J. Holler, *Fundamentals of Analytical Chemistry*. in 1988, New York, NY: Saunders College Publishing.

177) Z. Schwartz, D. Amir, B.D. Boyan, D. Cochavy, D. Muller-Mai, L.D. Swain, U. Gross, and J. Sela. Effect of glass ceramic and titanium implants on primary calcification during rat tibial bone healing. *Calcif. Tiss. Int.* **49**:359-364 (1991)

178) M. Spector. Ph.D. thesis, 1971. *A Study of the Mineral Phase Development Associated with Arterial Calcification.* Carnegie Mellon University, Pittsburgh, PA.

179) S.L. Mitchell, P.A. Villars, T.E. Orr, and M. Spector. Compressive properties of cancellous bone defects in a rabbit model treated with natural bone mineral and synthetic HA. *Transactions of the Society for Biomaterials.* **21**:234 (1995)

180) F.Z. Cui. Personal Communication, 1998.

181) S.D. Cook, J.F. Kay, K.A. Thomas, and M. Jarcho. Interface mechanics and histology of titanium and hydroxylapatite-coated titanium for dental implant applications. *Int. J. Oral Maxillofac. Surg.* **2**:15-22 (1987)

182) M. Nagano, T. Nakamura, T. Kokubo, M. Tanahashi, and M. Ogawa. Differences of bone bonding ability and degradation behaviour in vivo between amorphous calcium phosphate and highly crystalline hydroxyapatite coating. *Biomaterials.* **17**:1771-1777 (1996)

183) J.E. Davies. *In vitro* modeling of the bone/implant interface. *Anat. Rec.* **245**:426-445 (1996)

184) S.B. Goodman, J.A. Davidson, V.L. Fornasier, and A.K. Mishra. The local and systemic response to cylinders of a low modulus titanium alloy (Ti-13Nb-13Zr) and a wear resistant zirconium alloy (Zr-2.5Nb) implanted in the rabbit tibia. *Transactions of the Orthopaedic Research Society.* **39**:450 (1993)

185) P.S. Christel. Zirconia: The second generation of ceramics for total hip replacement. *Bull. Hosp. Joint. Dis. Orthop. Inst.* **49**:170-177 (1989)

186) C.N. Panagopoulos. Surface oxide strengthening of zirconium. *Mat. Lett.* **8**:216-219 (1989)

187) J.C. Haygarth and L.J. Fenwick. Improved wear resistance of zirconium by enhanced oxide films. *Thin Solid Films.* **118**:351-362 (1984)

188) R.A. Ploc and J.A. Little. Porosity in Zr-2.5-Nb Corrosion Films. in *3rd International Conference on Microscopy of Oxidation.* 1996: p. 475-487.

189) M. Van Eman, V. Benezra, and L.W. Hobbs. A preliminary report on the feasibility of oxide-zirconium alloy interface study by transmission electron microscopy, 1995.

190) H.-J. Beie, A. Mitwalsky, F. Garzarolli, H. Ruhmann, and H.-J. Sell. Examinations of the corrosion mechanism of zirconium alloys, in *Zirconium in the Nuclear Industry: Tenth International Symposium, ASTM STP 1245,* A.M. Garde and E.R. Bradley, ed. 1994, American Society for Testing and Materials: Philadelphia, PA. p. 615-643.

191) M.G. Cowgill, S.H. Wong, and W.W. Smeltzer. Breakaway oxidation transition for a zirconium-2.7 w/o niobium alloy. *J. Electrochem. Soc.* **115**:927-929 (1968)

192) D.H. Bradhurst and P.M. Heuer. The influence of oxide stress on the breakaway oxidation of Zircaloy-2. *J. Nucl. Mater.* **37**:35-47 (1970)

193) J. Godlewski. How the tetragonal zirconia is stabilized in the oxide scale that is formed on a zirconium alloy corroded at 400°C in steam, in *Zirconium in the Nuclear Industry: Tenth International Symposium, ASTM STP 1245,* A.M. Garde and E.R. Bradley, ed. 1994, American Society for Testing and Materials: Philadelphia, PA. p. 663-686.

194) M. Abrudeanu, I. Vucu, V. Dumitrescu, C. Petot, G. Petot-Ervas, P. Archambault, M. Petrescu, and N. Petrescu. Microstructure and electron microprobe study of oxide

layers obtained on zircaloy-4 by oxidation at high temperature. in *Second International Conference on Microscopy of Oxidation.* 1993: p. 387-395.

195) B.-X. Zhou. Electron microscopy study of oxide films formed on zircaloy-2 in superheated steam, in *Zirconium in the Nuclear Industry: Eighth International Symposium, ASTM STP 1023,* L.F.P. Van Swam and C.M. Eucken, ed. 1989, American Society for Testing and Materials: Philadelphia, PA. p. 360-373.

196) J. Godlewski, J.P. Gros, M. Lambertin, J.F. Wadier, and H. Weidlinger. Raman spectroscopy study of the tetragonal-to-monoclinic transition in zirconium oxide scales and determination of overall oxygen diffusion by nuclear microanalysis of O18, in *Zirconium in the Nuclear Industry: Ninth International Symposium, ASTM STP 1132,* C.M. Euken and A.M. Garde, ed. 1991, Amer. Soc. for Testing and Materials: Philadelphia, PA. p. 416-436.

197) V.F. Urbanic, P.K. Chan, D. Khatamian, and O.-T. Woo. Growth and characterization of oxide films on zirconium-niobium alloys, in *Zirconium in the Nuclear Industry: Tenth International Symposium, ASTM STP 1245,* A.M. Garde and E.R. Bradley, ed. 1994, American Society for Testing and Materials: Philadelphia, PA. p. 116-132.

198) V.F. Urbanic and W.W. Smeltzer. Oxidation properties of a zirconium-2.7 w/o niobium alloy in the temperature range 650°-1000° C. *J. Electrochem. Soc.* **119**:1527-1531 (1972)

199) Y.P. Lin, O.T. Woo, and D.J. Lockwood. Texture and phases in oxide films on Zr-Nb alloys. *Materials Research Society Symposium Proceedings.* **343**:487-492 (1994)

200) H. Okamoto, *ASM Handbook, Volume 3, Alloy Phase Diagrams.* 1992, Materials Park, OH: ASM International.

201) R. Anderson and J. Benedict. Precision ion milling of layered, multi-element specimens with high specimen preparation spatial resolution. *Materials Research Society Symposium Proceedings.* **254**:141-148 (1992)

202) J.P. Benedict, S.J. Klepeis, W.G. Vandygrift, and R. Anderson. A method for precision speimen preparation for both SEM and TEM analysis. *EMSA Bulletin.* **19**:74-79 (1989)

203) C.M. Cotell. Sc.D. thesis, 1988. *Effect of Yttrium on the Oxidation Mechanisms of Pure Chromium.* Massachusetts Institute of Technology, Cambridge, MA.

204) S.P. Mangin. S.M. thesis, 1998. *Microstructural Study of Zirconium Oxide Grown on Zirconium Alloy Substrate for Orthopaedic Applications.* Massachusetts Institute of Technology, Cambridge, MA.

205) R.L. Lieber. Experimental design and statistical analysis, in *Orthopedic Basic Science,* S.R. Simon, ed. 1994, American Academy of Orthopedic Surgeons: Park Ridge, IL. p. 623-665.

206) R.S. Roth and L.W. Coughanour. Phase equilibrium relations in the systems titania-niobia and zirconia-niobia. *J. Res. Nat. Bureau Standards.* **55**:209-213 (1955)

207) V. Benezra, S.P. Mangin, M. Treska, M. Spector, and L.W. Hobbs. Ultrastructure and adhesion of the scale on oxidized Zr-2.5Nb for total joint arthroplasty. *Trans. Soc. Biomat.* **24** (1998)

208) O.T. Woo, D.J. Lockwood, Y.P. Lin, and V.F. Urbanic. Structure of oxides grwon on Zr-20Nb alloy. *Materials Research Society Symposium Proceedings.* **357**:219-224 (1995)

209) B.A. Cheadle and S.A. Aldridge. The transformation and age hardening behavior of Zr-19wt%Nb. *J. Nucl. Mater.* **47**:255-258 (1973)

210) D.J. Cometto, G. L. Houze, and R.F. Hehemann. The omega transformation in zirconium-niobium (columbium) alloys. *Trans. AIME.* **233**:30-39 (1965)

211) Y.P. Lin. Nature of oxidised β-phases in Zr-2.5Nb alloy. in *3rd International Conference on Microscopy of Oxidation.* 1996: p. 462-474.

212) M.G. Cowgill and W.W. Smeltzer. The oxidation properties of a zirconium-2.7 w/o niobium alloy in the temperature range 300°-500° C. *J. Electrochem Soc.* **114**:1089-1095 (1967)

213) B.D. Warr, E.M. Rasile, and A.M. Brennenstuhl. Electron microscopical analyses of oxides in Zr-2.5 wt% Nb. in *Proceedings of the International Atomic Energy Agency Technical Committee Meeting on Fundamental Aspects of Corrosion on Zirconium-base Alloys for Water Reactor Environments.* 1989: p. 124-134.

214) P. Kofstad, *High Temperature Corrosion.* 1988, New York, NY: Elsevier Applied Science.

215) J. Duncan. Personal communication, 1998.

216) K.N. Choo, Y.H. Kang, S.I. Pyun, and V.F. Urbanic. Effect of composition and heat treatment on the microstructure and corrosion behavior of Zr-Nb alloys. *J. Nucl. Mater.* **209**:226-235 (1994)

217) I.V. Yannas, E. Lee, D.P. Orgill, E.M. Skrabut, and G.F. Murphy. Synthesis and characterization of a model extracellular matrix which induces partial regeneration of adult mammalian skin. *Proc. Nat. Acad. Sci. USA.* **86**:933-937 (1989)

218) S.B. Goodman, J.A. Davidson, V.L. Fornasier, and A.K. Mishra. Histological response to cylinders of a low modulus titanium alloy (Ti-13Nb-13Zr) and a wear resistant zirconium alloy (Zr-2.5Nb) implanted in the rabbit tibia. *J. Appl. Biomat.* **4**:331-339 (1993)

219) A.J.T. Clemnow, A.M. Weinstein, J.J. Klawitter, J. Koeneman, and J. Anderson. Interface mechanics of porous titanium implants. *J. Biomed. Mat. Res.* **15**:73-82 (1981)

220) C.A. Engh, J.D. Bobyn, and A.H. Glassman. Porous coated hip replacement: The factors governing bone in growth, stress shielding, and clinical results. *J. Bone Joint Surg.* **69-B**:45-55 (1987)

221) V.M. Goldberg, S. Stevenson, J. Feighan, and D. Davy. Biology of grit-blasted titanium alloy implants. *Clin. Orthop.* :122-129 (1995)

222) A. Wennerberg, T. Albrektsson, B. Andersson, and J.J. Krol. A histomorphometric and removal torque study of screw-shaped titanium implants with three different surface topographies. *Clin. Oral Implants Res.* **6**:24-30 (1995)

223) A.M. Patel and M. Spector. Oxidized zirconium for hemiarthroplasty: An *in vitro* assessment. *Bioceramics.* **8**:169-175 (1995)

224) A. Bellare and T.E. Orr. A study of mineralized bone tissue by ultra-small angle x-ray scattering. *Transactions of the Society for Biomaterials.* **24**:404 (1998)

225) J. Benedict, R. Anderson, and S.J. Klepeis. Recent developments in the use of the tripod polisher for TEM specimen preparation. *Materials Research Society Symposium Proceedings.* **254**:121-140 (1992)

THESIS PROCESSING SLIP

FIXED FIELD: ill. _____ name _____

index _____ biblio _____

▶ COPIES: (Archives) Aero Dewey Eng Hum
Lindgren Music Rotch (Science)

TITLE VARIES: ▶☐ _____

NAME VARIES: ▶☐ _____

IMPRINT: (COPYRIGHT) _____

▶ COLLATION: 230ℓ

▶ ADD: DEGREE: _____ ▶ DEPT.: _____

SUPERVISORS: _____

NOTES:

cat'r: date:

page: 537

▶ DEPT: MatSci & E

▶ YEAR: 1999 ▶ DEGREE: Ph.D.

▶ NAME: BENEZRA, Valarie
Ilene